VAN DER WAALS SHEETS FOR RECHARGEABLE METAL-ION BATTERIES

by

LAMUEL ABRAHAM DAVID

B.E., Anna University, Chennai, India, 2010
M.S., Kansas State University, KS, USA, 2011

AN ABSTRACT OF A DISSERTATION

submitted in partial fulfillment of the requirements for the degree

DOCTOR OF PHILOSOPHY

Department of Mechanical and Nuclear Engineering
College of Engineering

KANSAS STATE UNIVERSITY
Manhattan, Kansas

2015

Abstract

The inevitable depletion of fossil fuels and related environmental issues has led to exploration of alternative energy sources and storage technologies. Among various energy storage technologies, rechargeable metal-ion batteries (MIB) are at the forefront. One dominant factor affecting the performance of MIB is the choice of electrode material. This thesis reports synthesis of paper like electrodes composed for three representative layered materials (van der Waals sheets) namely reduced graphene oxide (rGO), molybdenum disulfide (MoS_2) and hexagonal boron nitride (BN) and their use as a flexible negative electrode for Li and Na-ion batteries. Additionally, layered or sandwiched structures of vdW sheets with precursor-derived ceramics (PDCs) were explored as high C-rate electrode materials.

Electrochemical performance of rGO paper electrodes depended upon its reduction temperature, with maximum Li charge capacity of 325 $mAh.g^{-1}$ observed for specimen annealed at 900°C. However, a sharp decline in Na charge capacity was noted for rGO annealed above 500 °C. More importantly, annealing of GO in NH_3 at 500 °C showed negligible cyclability for Na-ions while there was improvement in electrode's Li-ion cycling performance. This is due to increased level of ordering in graphene sheets and decreased interlayer spacing with increasing annealing temperatures in Ar or reduction at moderate temperatures in NH_3. Further enhancement in rGO electrodes was achieved by interfacing exfoliated MoS_2 with rGO in 8:2 wt. ratios. Such papers showed good Na cycling ability with charge capacity of approx. 225.$mAh.g^{-1}$ and coulombic efficiency reaching 99%.

Composite paper electrode of rGO and silicon oxycarbide SiOC (*a type of PDC*) was tested as high power-high energy anode material. Owing to this unique structure, the SiOC/rGO composite electrode exhibited stable Li-ion charge capacity of 543.$mAh.g^{-1}$ at 2400 $mA.g^{-1}$ with

nearly 100% average cycling efficiency. Further, mechanical characterization of composite papers revealed difference in fracture mechanism between rGO and 60SiOC composite freestanding paper. This work demonstrates the first high power density silicon based PDC/rGO composite with high cyclic stability.

Composite paper electrodes of exfoliated MoS_2 sheets and silicon carbonitride *(another type of PDC material)* were prepared by chemical interfacing of MoS_2 with polysilazane followed by pyrolysis . Microscopic and spectroscopic techniques confirmed ceramization of polymer to ceramic phase on surfaces on MoS_2. The electrode showed classical three-phase behavior characteristics of a conversion reaction. Excellent C-rate performance and Li capacity of 530 $mAh.g^{-1}$ which is approximately 3 times higher than bulk MoS_2 was observed. Composite papers of BN sheets with SiCN (SiCN/BN) showed improved electrical conductivity, high-temperature oxidation resistance (at 1000 °C), and high electrochemical activity (~517 mAh g^{-1} at 100 mA g^{-1}) toward Li-ions generally not observed in SiCN or B-doped SiCN. Chemical characterization of the composite suggests increased free-carbon content in the SiCN phase, which may have exceeded the percolation limit, leading to the improved conductivity and Li-reversible capacity.

The novel approach to synthesis of van der Waals sheets and its PDC composites along with battery cyclic performance testing offers a starting point to further explore the cyclic performance of other van der Waals sheets functionalized with various other PDC chemistries.

VAN DER WAALS SHEETS FOR RECHARGEABLE METAL-ION BATTERIES

by

LAMUEL ABRAHAM DAVID

B.E., Anna University, Chennai, India, 2010
M.S., Kansas State University, KS, USA, 2011

A DISSERTATION

submitted in partial fulfillment of the requirements for the degree

DOCTOR OF PHILOSOPHY

Department of Mechanical and Nuclear Engineering
College of Engineering

KANSAS STATE UNIVERSITY
Manhattan, Kansas

2015

Approved by:

Major Professor
Dr. Gurpreet Singh

Abstract

The inevitable depletion of fossil fuels and related environmental issues has led to exploration of alternative energy sources and storage technologies. Among various energy storage technologies, rechargeable metal-ion batteries (MIB) are at the forefront. One dominant factor affecting the performance of MIB is the choice of electrode material. This thesis reports synthesis of paper like electrodes composed for three representative layered materials (van der Waals sheets) namely reduced graphene oxide (rGO), molybdenum disulfide (MoS_2) and hexagonal boron nitride (BN) and their use as a flexible negative electrode for Li and Na-ion batteries. Additionally, layered or sandwiched structures of vdW sheets with precursor-derived ceramics (PDCs) were explored as high C-rate electrode materials.

Electrochemical performance of rGO paper electrodes depended upon its reduction temperature, with maximum Li charge capacity of 325 $mAh.g^{-1}$ observed for specimen annealed at 900°C. However, a sharp decline in Na charge capacity was noted for rGO annealed above 500 °C. More importantly, annealing of GO in NH_3 at 500 °C showed negligible cyclability for Na-ions while there was improvement in electrode's Li-ion cycling performance. This is due to increased level of ordering in graphene sheets and decreased interlayer spacing with increasing annealing temperatures in Ar or reduction at moderate temperatures in NH_3. Further enhancement in rGO electrodes was achieved by interfacing exfoliated MoS_2 with rGO in 8:2 wt. ratios. Such papers showed good Na cycling ability with charge capacity of approx. 225.$mAh.g^{-1}$ and coulombic efficiency reaching 99%.

Composite paper electrode of rGO and silicon oxycarbide SiOC (*a type of PDC*) was tested as high power-high energy anode material. Owing to this unique structure, the SiOC/rGO composite electrode exhibited stable Li-ion charge capacity of 543.$mAh.g^{-1}$ at 2400 $mA.g^{-1}$ with

nearly 100% average cycling efficiency. Further, mechanical characterization of composite papers revealed difference in fracture mechanism between rGO and 60SiOC composite freestanding paper. This work demonstrates the first high power density silicon based PDC/rGO composite with high cyclic stability.

Composite paper electrodes of exfoliated MoS_2 sheets and silicon carbonitride *(another type of PDC material)* were prepared by chemical interfacing of MoS_2 with polysilazane followed by pyrolysis . Microscopic and spectroscopic techniques confirmed ceramization of polymer to ceramic phase on surfaces on MoS_2. The electrode showed classical three-phase behavior characteristics of a conversion reaction. Excellent C-rate performance and Li capacity of 530 $mAh.g^{-1}$ which is approximately 3 times higher than bulk MoS_2 was observed. Composite papers of BN sheets with SiCN (SiCN/BN) showed improved electrical conductivity, high-temperature oxidation resistance (at 1000 °C), and high electrochemical activity (~517 mAh g^{-1} at 100 mA g^{-1}) toward Li-ions generally not observed in SiCN or B-doped SiCN. Chemical characterization of the composite suggests increased free-carbon content in the SiCN phase, which may have exceeded the percolation limit, leading to the improved conductivity and Li-reversible capacity.

The novel approach to synthesis of van der Waals sheets and its PDC composites along with battery cyclic performance testing offers a starting point to further explore the cyclic performance of other van der Waals sheets functionalized with various other PDC chemistries.

Table of Contents

List of Figures xi
List of Tables xxiii
Acknowledgements xxiv
Dedication xxv
Chapter 1 - Introduction 1
1.1 Motivation 1
1.2 Overview of Dissertation 5
1.3. Reference 7
Chapter 2 - Background and Literature Review 8
2.1 Concepts in Lithium ion Battery 8
2.2 Components in Li-ion Battery 10
2.2.1. Electrolyte 10
2.2.2. Electrode Material 11
Cathode Materials 13
Insertion Anode Materials 15
Alloying Anode Materials 16
Conversion Anode Material 17
2.3. Concepts in Na-ion Battery 18
2.4. Components of Na-ion Battery 19
2.4.1. Cathode 19
2.4.2. Anode 20
2.5. Graphene Synthesis and Application as Battery Electrode Material 22
2.5.1. Synthesis 23
2.5.2. Graphene as Battery Electrode 25
2.6. Molybdenum disulfide (MoS_2) Synthesis and Application as Battery Electrode Material 27
2.6.1 Synthesis 28
2.6.2. Application as Battery Electrode 29
2.7 Polymer Derived Ceramics (PDCs) 31

2.8. References 34
Chapter 3 - Reduced Graphene Oxide Paper Electrode 46
3.1. Abstract 46
3.2. Introduction 47
3.3. Experimental Section 49
3.3.1. Materials and Instrumentation 49
3.3.2. Preparation of graphene oxide 50
3.3.3. Preparation of free-standing paper 50
3.3.4. Coin Cell Assembly 51
3.4. Results And Discussion 51
3.4.1 Chemical and Structural Analysis 51
3.4.2. Initial Electrochemical Analysis 53
3.4.3. Long-Term Electrochemical Analysis 56
3.4.4. Post-Electrochemical Analysis 62
3.4.5. Mechanical Characterization 65
3.5. Conclusion 67
3.6. Acknowledgements 67
3.7. References 68
Chapter 4 - Large Area MoS_2/graphene Composite Paper Based Electrode for Room Temperature Na-ion Batteries 74
4.1. Abstract 74
4.2. Introduction 75
4.3. Materials and Instrumentation 77
4.3.1. Instrumentation 77
4.3.2. Preparation graphene oxide 79
4.3.3. Preparation of exfoliated or acid treated MoS_2 flakes 80
4.3.4. Preparation of reduced graphene oxide and MoS_2 composite paper 80
4.3.5. Coin Cell/Battery assembly 81
4.4. Results and Discussions 81
4.4.1. Material Synthesis 81
4.4.2. Electrochemical Performance 91

4.5. Conclusion 104
4.6. Acknowledgements 104
4.7. References 105
Chapter 5 - Silicon Oxycarbide/Graphene Composite Paper Electrode for Long Cycle Lithium-Ion Batteries 112
5.1. Abstract 112
5.2. Introduction 113
5.3. Methods 115
5.3.1. Preparation Of Polymer-Derived SiOC Ceramic 115
5.3.2. Preparation of Reduced Graphene Oxide and SiOC Composite Paper 116
5.3.3. Coin Cell/Battery Assembly 116
5.3.4. Instrumentation 117
5.4. Results and Discussions 118
5.4.1. Material Synthesis and Electrode Fabrication. 118
5.4.2. Electrochemical Performance 127
5.4.3. Mechanical Strength of the Composite Anode 147
5.5. Conclusion 150
5.6. Acknowledgements 151
5.7. References 152
Chapter 6 - Exfoliation of MoS_2 and Functionalization with PDC for Stable Lithium-Ion Battery Electrode 159
6.1. Abstract 159
6.2. Introduction 160
6.3. Experimental 162
6.3.1. Material Preparation 162
6.3.2. Cell Assembly and Testing 162
6.3.3. Material Characterization 163
6.4. Results and Discussion 164
6.4. Conclusion 176
6.5. References 177

Chapter 7 - Facile Synthesis and High Rate Capability of Silicon Carbonitride/Boron Nitride Composite with a Sheet-Like Morphology 183
7.1. Abstract 183
7.2. Introduction 184
7.3. Materials And Instrumentation 186
7.3.1. PREPARATION OF SiCN/BN, SiCN/BNF, SiCN/BP 187
7.3.2. PREPARATION OF PAPER ELECTRODE 188
7.3.3. COIN CELL ASSEMBLY 188
7.4. Results And Discussions 189
7.5. Conclusion 207
7.6. Acknowledgements 207
7.7. References 209
Chapter 8 - CONCLUSION 216

List of Figures

Figure 1-1 Total world energy consumption by source (2013). (Data obtained with permission from "Renewable 2014: Global Status Report" ISBN 978-3-9815934-2-6) 1
Figure 1-2 Global renewable power capacities(excluding hydro). (Reproduced with permission from REN21, Renewables Global Status Report, 2006-2012) 2
Figure 2-1 Schematic representation of discharging processes in a commonly used Li-ion battery in which graphite is used as an anode and LiCoO2 is used as the cathode. (Reproduced with permission from Sciencemag: Dunn, B. *et al.* Science, 2011, 18(334), 928) 9
Figure 2-2 SEI layer formation on anode surface inhibits dissolution of electrolyte. 10
Figure 2-3 Chemical structures of all the alkyl carbonates used in Li-ion batteries 10
Figure 2-4 Schematic representation of the different mode of Li-ion storage mechanism observed in electrode materials for Li-ion batteries. Black circles: voids in crystal structure, blue circles: metal, yellow circles: lithium. (Reproduced with permission from The Royal Society of Chemistry: Palacin, R., Chem. Soc. Rev. 2009, 38, 2565-2575) 12
Figure 2-5 Approximate range of average discharge potentials and specific capacities of some of the most common intercalation type cathodes. (Reproduced with permission from Elsevier: Nitta, N., Mater. Today, 2014, 1) 14
Figure 2-6 Schematic representation of volume expansion that occurs during alloying of Si.[66] (Reproduced with permission from Elsevier: Nitta, N., Mater. Today, 2014, 1) 16
Figure 2-7 Schematic representation of conversion reaction mechanism during ion insertion/extraction in MoS_2. (Reproduced with permission from Nature: Armand, M., *et al.*, Nature, 2008, 451, 652-657) 18
Figure 2-8 (a) Schematic representation of a typical Na-ion battery. (b) House of cards model proposed by Dunn and co-workers on sodium intercalation in hard carbon. (Reproduced with permission from Royal Society of Chemistry: Palomares, V., *et al* Energy Environmental Sci., 2012, 3, 5884-5901) 19
Figure 2-9 Voltage range and gravimetric capacities of various materials studied as cathode for Na-ion battery. (Reproduced with permission from Nature: Larcher, D. *et al*. Nat. Chem., 2015, 7, 19-29) 19

Figure 2-10 Voltage range and gravimetric capacities of various materials studied as anode for Na-ion battery. (Reproduced with permission from Nature: Larcher, D. *et al*. Nat. Chem., 2015, 7, 19-29) 21
Figure 2-11 Different procedures for synthesis of graphene like mechanical exfoliation, liquid phase exfoliation, bottom-up synthesis, epitaxial growth on SiC, epitaxaial growth on metal substrates and reduction of graphene oxide. Each method is evaluated in terms of graphene quality (G), cost aspect (C)-low value corresponds to cost of production, scalability (S), purity (P) and yield (Y). (Reproduced with permission from Nature: Raccichini, R. *et al*., Nat. Mater. 2014, 14, 271-279) 23
Figure 2-12 Schematic showing the most common pathways for producing reduced graphene oxide based electrode materials. (Reproduced with permission from Nature: Raccichini, R. *et al*., Nat. Mater. 2014, 14, 271-279) 25
Figure 2-13 Schematic shows the various applications in which graphene is used composite electrode materials. (Reproduced with permission from Nature: Raccichini, R. *et al*., Nat. Mater. 2014, 14, 271-279) 27
Figure 2-14 Schematic representation of MoS_2 structure. The atoms are bonded by covalent bonds within the layer and van der Waals force between the layers themselves 28
Figure 2-15 Schematic representation of molecular structure of different phases in step wise conversion of liquid polymer to solid ceramic 32
Figure 3-1 Material characterization. (a) Raman, (b) XRD, and (c) Electrical conductivity data of free-standing rGO papers. Data for GO paper and graphite powder is included for comparison purposes. High-resolution XPS of C1s peak corresponding to (d) 300rGO, (e) 500rGO, (f) 700rGO and (g) 900rGO. SEM cross-sectional images of (h) 300rGO, (i) 500rGO, (j) 700rGO and (k) 900rGO show the morphology of the paper. Average paper thickness was observed to be ~ (10 - 15) µm. Scale bar is 5 µm. 52
Figure 3-2 Electrochemical characterization. Comparison of first cycle charge/discharge and differential capacity curves of 300rGO, 500rGO, 700rGO and 900rGO papers cycled in (a, b) Li-ion and (c, d) Na-ion battery half-cell at 100 mA g-1anode. (e) Li charge capacity and corresponding columbic efficiency of various rGO electrodes asymmetrically cycled at varying current densities. (f) Na charge capacity and corresponding columbic efficiency of various rGO anodes asymmetrically cycled at varying current densities. (g) Na charge

capacity data for long-term symmetric cycling of 500rGO anode when cycled initially at lower current densities (see inset). Current densities and capacities are normalized w.r.t. total electrode weight and total electrode volume. 54
Figure 3-3 Long-term electrochemical cycling data for various rGO electrodes (a) LIB and (b) NIB. All the anodes were cycled at 1600 mA g-1 anode for 1000 cycles. 57
Figure 3-4 Comparison of NIB electrochemical cycling data for 500rGO paper (shown by brown color) with expanded graphite anode (on copper foil) from the literature (Black: capacity with respect to active weight and Yellow: capacity normalized with respect to the film weight, data reproduced from Wen et al.[19]). 58
Figure 3-5 Comparison of 1000th cycle charge capacity data for Li and Na half-cells presented as a function of electrode annealing temperature and C/O ratio. 59
Figure 3-6 (a) XRD data comparing ammonia reduced GO with argon reduced GO for annealing time of 2 h. Decreased interlayer spacing in NH3 over Ar reduction is clearly seen. (b) Four-point electrical conductivity of various rGO specimens prepared in this study. Ammonia-reduced specimens have higher electrical conductivity than argon-reduced specimens. 60
Figure 3-7 Figure 3.8 Electrochemical cycling data (Rate capability test) for (a) LIB and (b) NIB rGO half-cells: argon-annealed rGO compared with corresponding ammonia-annealed electrodes. 61
Figure 3-8 Post Electrochemical cycling data. (a) SEM and (b) TEM image of GO reduced at 500 °C. (c) SEM image, (d) XPS and (e) TEM image of dissembled 900rGO electrode from LIB. (f) SEM image, (g) XPS and (h) only half the paper electrode is shown, the other half was dispersed in EC/DMC solution for preparing TEM specimens). Cells were dissembled after 1050 cycles. The scale bar in (a,c,f) is 5 µm and (b,e,h) is 500 nm. 62
Figure 3-9Post Electrochemical cycling data for LIB electrodes. Digital camera image of (a) 300rGO, (b) 500rGO and (c) 700rGO free-standing anodes after cycling in a Li half-cell. (d through i) are the corresponding SEM images. Cells were dissembled in their lithiated state after 1050 cycles. 63
Figure 3-10 Post Electrochemical cycling data for NIB electrodes. Digital camera image of (a) 300rGO, (b) 700rGO and (c) 900rGO free-standing anodes after cycling in a Na half-cell. (d

through i), are the corresponding SEM images. Cells were dissembled in their sodiated state after 1050 cycles. 64
Figure 3-11 Mechanical testing data. (a) Digital camera images at various stages of the loading. (b) Engineering stress-strain plots of 300rGO, 500rGO, 700rGO and 900rGO papers, and (c) bar chart representing the calculated mean of their modulus, failure stress, and failure strain. This behavior is better captured in the media file (see Supporting Information Media File for 700rGO specimen as it fractures with a bang). 66
Figure 4-1 (a) Photographic image showing a litre of MoS_2 dispersed in DI water using superacid as stabilizer. The concentration of the dispersion is ~2 mg/mL. SEM images showing the structure and size distribution of MoS_2 (b) before and (c) after exfoliated with superacid. Average particle size was ~20 to 40 and less than 20 μm for MoS_2-raw and MoS_2-SA, respectively. The scale bar in the inset is 2 μm (d) Calculated total interaction potential energy (VT), repulsion (VDLVO), and attraction energy (VvdW) (per unit area) with increasing MoS_2 sheet separation distance (log scale) is shown. Inset: Experimentally measured zeta potential measurements, showing better dispersion stability at higher pH values. (e) Raman spectra of MoS_2 before and after exfoliation with superacid. The similarity in the relative intensity and position of the E12g and A1g peaks suggests that the structure is undistorted MoS_2. (f) The change in intensity and FWHM of MoS_2 peak at 14° 2θ in the XRD spectra suggests that MoS_2 is exfoliated after acid treatment. 83
Figure 4-2 High-resolution TEM image of superacid exfoliated MoS_2 sheets..... 84
Figure 4-3 (a) Schematic representation showing synthesis of rGO/MoS_2 composite paper. (b) Digital picture showing large area composite paper prepared through vaccum filtration. (c) SEM top-view image of 60MoS_2 paper, the insert shows the EDX spectra of spots in the SEM image indicating the material to be rGO (square) and MoS_2 (circle). (d) Corresponding SEM cross-sectional images shows the morphology of the paper. Average thickness of the paper was observed to be ~20 μm. (e) TEM images and SAED patterns of 60MoS_2. The MoS_2 sheets are observed to be wraped with graphene sheets. In SAED pattern in the insert, multiple spot pattern is observed one of which is due to the polycrystallinity of restacked rGO sheets while second set of spot pattern were due to MoS_2 sheets. (g) Thermogravimetric analysis data for MoS_2-SA, MoS_2-rGO composite paper and rGO paper. (g) Graph of conductivity vs percentage of MoS_2 in free-standing paper. 85

Figure 4-4 SEM images of (a) rGO and (b) 20MoS_2, (c) 40MoS_2 and (d) 60MoS_2-raw paper and (e-h) their corresponding SEM cross-sectional images. The inserts in (a-c) are digital photographs demonstrating the flexibility of rGO and rGO/MoS_2 paper shown in the corresponding SEM image. TEM images and SAED patterns (insert) of (i) rGO and (j-l) rGO/MoS_2 composite corresponding to the SEM images above. 86
Figure 4-5 High resolution SEM image of 60MoS_2 composite paper which shows flakes of exfoliated MoS_2 sheets overlaped with rGO sheets. 87
Figure 4-6 (a) SEM cross-sectional inmage of 60MoS_2 and EDX map of (b) carbon, (c) oxygen, (d) sulfur and (e) molybdenum. 88
Figure 4-7 X-ray photoelectron spectroscopy plot of as-synthesized MoS_2-SA and 60MoS_2 free-standing paper before and after heat treatment. 89
Figure 4-8 First and second cycle voltage profile of MoS_2/rGO composite (a) rGO, (c) 20MoS_2, (e) 40MoS_2 and (g) 60MoS_2-raw along with corresponding (b, d, f, h) differential capacity curves. 93
Figure 4-9(a) First and second cycle voltage profile of 90MoS_2 composite paper (b)along with its differential capacity curves. 94
Figure 4-10 (a) Voltage profile of 60MoS_2 free-standing anode along with its corresponding (b) differential capacity curves for the first two cycles. (b) Sodium charge capacity of all the anodes symmetrically cycled at a constant current density of 25 mAg-1 along with their cyclic efficiencies. (e) Sodium charge capacity and corresponding columbic efficiency of 60MoS_2 anode asymmetrically cycled at varying current densities. 95
Figure 4-11 Post cycle analysis of the cycled anodes: (a through e) Digital camera images of rGO, 20MoS_2, 40MoS_2, 60MoS_2 and 60MoS_2-raw composite anodes. (f through j): Low magnification SEM images, and (k through o): High magnification SEM images of the dissembled anodes. 98
Figure 4-12 (a) SEM cross-sectional inmage of 60MoS_2 and EDX map of (b) carbon, (c) oxygen, (d) sodium, (e) sulfur and (f) molybdenum. 99
Figure 4-13 Schematic representation showing the predicted mechanism for Na insertion and extraction into the MoS_2/rGO free-standing composite paper electrode. rGO provides the mechanical/ structural stability and high electrical conductivity network to the TMDC undergoing insertion and conversion reactions with Na-ions. 99

Figure 4-14 Post cycling TEM with SAED pattern and (b) XRD pattern of rGO/MoS_2 before and end of discharge cycle. 100
Figure 4-15 Tensile test setup with sample after fracture from loading. (b) Stress-strain plot for rGO, 40MoS_2 and 60MoS_2 freestanding papers. Photographic image of (c) 40MoS_2 and (d) 60MoS_2 paper tested in this study. (e, and f) are the corresponding SEM cross-sectional images showing the fractured surface. The scale bar is 20 µm. 102
Figure 5-1 Characterization of SiOC ceramic and SiOC/rGO composite papers. (a) SEM image of SiOC particles after pyrolysis of the polymeric TTCS particles. Average SiOC particle size was approximately 4 to 5 µm. The scale bar is 10 µm. (b) X-ray photoelectron spectroscopy data for cross-linked TTCS and pyrolyzed SiOC. High resolution XPS spectrum of pyrolyzed SiOC particles in the (c) Si2p region, (d) O1s region, and (e) C1s region were consistent with the polymer-derived SiOC nanodomain model. Deconvoluted peaks indicate the various bonds between Si, C and O atoms, which is distinct to pyrolyzed SiOC. (f) Raman spectrum of SiOC showed peaks that are characteristic of graphitic carbon (D-peak: 1350 cm−1 and G-peak: 1590 cm−1). (g) Attenuated Total Reflectance Fourier Transformation Infrared (ATR-FTIR) spectra of SiOC and cross-linked TTCS (ν: stretching vibration mode and δ: bending vibration mode). (h) Schematic illustration of proposed hybrid structure of the freestanding paper and the atomic structure of pyrolyzed SiOC particle. (i) SEM image of 60SiOC paper and (j) its corresponding cross-sectional images with EDX map in which Si, C, and O are indicated by red, blue and green, respectively. Insets in (i) are EDX spectra of spots shown in the corresponding SEM image indicating the material to be rGO (circle) and SiOC (square). The scale bar is 10 µm. (k) TEM SAED pattern showed multiple spot pattern due to polycrystallinity of restacked rGO sheets with faint ring pattern attributed to amorphous SiOC material. (l) XRD of cross-linked TTCS, SiOC particles, GO paper, GO/SiOC paper before and after (rGO/SiOC) thermal reduction. Complete reduction of GO to rGO is illustrated in the plot. (m) TGA curves of GO paper and GO/SiOC composite papers measured from 30 to 800 °C at a heating rate of 10 °C.min−1 in flowing air. The weight percentage of SiOC in the GO/SiOC composite is as indicated in the figure. 120
Figure 5-2 Schematic illustration showing the predicted structure of cross-linked polymeric precursor (i.e., TTCS) and polymer-derived SiOC ceramic obtained upon pyrolysis of the

cross-linked polymer at 1000°C. This type of structure is plausible based on the Raman, FTIR, XRD, and XPS data presented here and earlier work on similar systems. 122
Figure 5-3 Electrode design and fabrication. Schematic illustrating the procedure for fabrication of free-standing SiOC/graphene composite paper for use as Li-ion battery anode. The composite paper was sufficiently robust to be handled by hand and flexible enough to be rolled on to a cylinder several times without breaking. 123
Figure 5-4 Microstructure of SiOC/rGO composite papers. SEM images of (a) rGO and (b) 10SiOC, (c) 40SiOC and (d) 60SiOC paper and (e-h) their corresponding TEM images.. 123
Figure 5-5 Comparison of Raman spectra of free-standing papers before and after annealing showed no distinct change in position or relative intensity of the peaks. The ID/IG ratio remained approximately the same (~1.1 to 1.3)..... 125
Figure 5-6 Deconvoluted XPS spectrum of (a) as-prepared graphene oxide (GO) paper and (b) reduced graphene oxide (rGO) paper in the C1s region, the C-OH peak at 286.7 eV completely disappeared upon annealing proving the reduction of graphene oxide to reduced graphe..... 126
Figure 5-7 TGA curves of rGO paper and rGO/SiOC composite papers measured from 30 to 800 °C at a heating rate of 10 °C.min-1 in air. The weight percentage of SiOC in the rGO/SiOC composite was as indicated in the figure. 127
Figure 5-8 Voltage profiles along with corresponding differentiated capacity curve of (a, b) rGO, (c, d) 10SiOC, and (e, f) 40SiOC. Reduction peak at 50 mV, a secondary reduction peak at 750 mV and an oxidation peak at 133 mV are distinct to Li reaction with rGO while reduction peak at 250 mV is distinct to Li reaction with SiOC. 128
Figure 5-9 Electrochemical characteristics and proposed lithium storage mechanism. (a) Charge capacity (total electrode weight) of various paper electrodes asymmetrically cycled at increasing current densities and their cyclic efficiencies. (b) The plot shows extended cycling behavior (charge capacity versus cycle number) of anodes symmetrically cycled at 1600 mA.g−1. After 900 cycles, all anodes recovered their original capacities when they were cycled again at 100 mA.g−1. Insets show the postcycling optical and SEM images of the dissembled rGO and 60SiOC electrodes after 1020 cycles. (c) Voltage profile of 60SiOC composite and corresponding (d) differential capacity curves cycled at various current densities. (e) Schematic representing the mechanism of lithiation/delithiation in

SiOC glass particles. Majority of lithiation occurs via adsorption at disordered carbon phase uniformly distributed in the SiOC amorphous matrix. Graphene sheets serve as an efficient electron conductor and elastic support. (f) Charge capacity of 60SiOC cycled at 100 mA.g−1 at 25 °C for 10 cycles, -15 °C for 50 cycles and then back at 25 °C for 10 cycles. After cooling down to -15 °C, the cell demonstrated a stable charge capacity of ~200 mAh.g−1. The cell regained approximately 86 % of its initial capacity when returned to cycling at room temperature. 130

Figure 5-10 (a) Voltage profiles along with corresponding (b) differentiated capacity curve of 80SiOC cycled at various C-rates. The peaks at 0.33 and 0.05 V in the differentiated capacity curve are distinct to Li reaction with SiOC. The graphene interaction peak in virtually absent in the first cycle curve. 133

Figure 5-11 (a) Charge capacity of 80SiOC cycled at different rates along with their cyclic efficiencies. Even though the initial capacity was higher at 750 mAhg-1, the anode material began to disintegrate as the current density was progressively increased. This was expected, as there was insufficient graphene present to hold SiOC particles together and maintain electronic conducting network in the eelctrode. (b) SEM images of 80SiOC paper and (c) its corresponding cross-section view. (d) Digital picture of 80SiOC anode. (e) SEM image of 80SiOC, which was dissembled in the lithiated state after being cycled for 33 cycles. Arrows in the image indicate micro-cracks most likely due to cycling at high current density. 134

Figure 5-12 Experimental setup for the 4-point resistivity measurements. 137

Figure 5-13 Post electrochemical surface analysis on composite electrode. Digital camera image of (a,b) rGO-SiOC composite anodes after cycling. SEM images of (c) 10SiOC and (d) 40SiOC which were obtained in the lithiated state after being cycled for 1020 cycles..... 139

Figure 5-14 Raman data of various SiOC/rGO specimen, before and after the electrochemical testing. No considerable change in ratio of intensity was observed suggesting that the anode was largely intact even upon cycling for 1000 cycles at 1600 $mA.g^{-1}$. 140

Figure 5-15 GITT Data: (a) Charge and discharge cycles with 15 min of current pulse at 100 mAh.g-1 followed by 12 h of relaxation for SiOC at room temperature (25 °C). (b) Calculated diffusion coefficient based on the relaxation steps at the corresponding voltages. 142

Figure 5-16 (a) Charge-discharge curve derived from titration studies. (b) Polarization potential at different states of charge. Time-dependent change in the open-circuit voltage at different states of charge (SOC) during (c) insertion and (d) extraction half cycles. 143
Figure 5-17 The Density of State (DOS) for (a) lithium extraction and (b) intercalation into 60SiOC electrode at room temperature. 144
Figure 5-18 GITT Data: (a) Charge and discharge cycles with 15 min of current pulse at 100 mA.g-1 followed by 12 h of relaxation for SiOC at room temperature (-15 °C). (b) Calculated diffusion coefficient based on the relaxation steps at the corresponding voltages. 145
Figure 5-19 (a) Charge-discharge curve obtained during the experiment to obtain polarization potential. (b) Total polarization potential at different states of charge. Time dependent change in the open-circuit voltage at different states of charge (SOC) during (c) insertion and (d) extraction halves. 146
Figure 5-20 Mechanical testing data. (a) Schematic of the tensile testing setup with a photograph of rGO paper immediately after the fracture. Scale reading in the photograph indicate the change in length to be ~0.28 mm. (b) Engineering stress versus strain plots of various freestanding papers derived from load/displacement data, and (c) their corresponding modulus values. The schematic shows the predicted mechanism of fracture for rGO and 60SiOC freestanding papers. (d) The rGO paper experienced stretching and rearrangement of graphene sheets before failure. (e) For 60SiOC paper, negligible stretching or rearrangement occurred. Fracture line follows SiOC particles embedded in rGO flakes, resulting in gradual separation/tearing of the paper. The scale bar is 20 μm in all images. 148
Figure 5-21 Mechanical testing data. (a-h) Cross-sectional SEM images of rGO, 10SiOC, 40SiOC and 60SiOC freestanding papers. The scale bar is 20 µm. 149
Figure 5-22 No considerable change was observed in the Raman spectrum (Id/Ig) of the composite papers pre and post tensile testing. 150
Figure 6-1 Schematic representation showing synthesis of SiCN-MoS_2 composite from in-situ pyrolysis. Liquid-phase polysilazane functionalized MoS_2 flakes undergo organic to inorganic transformation at 1000°C in flowing nitrogen leading to SiCN-MoS_2-SiCN type morphology. Sheet like morphology is retained. 164

Figure 6-2 (Left) TGA data performed in flowing Ar gas for cross-linked polysilazane, shows polymer to ceramic transformation. The polymer to ceramic yield was approx. 78 %. (Right) TGA data performed in flowing Ar gas, shows thermal reduction of graphene oxide (GO) to reduced-graphene oxide (rGO). The yield was approx. 50 % when thermal reduction is performed at 500 °C. 165
Figure 6-3 Material characterization. SEM micrograph of (a) acid-treated MoS_2 show stacked sheets with lateral dimension of 2 μm to 5 μm. (b) SEM image of SiCN/MoS_2 and (c) its corresponding EDX map show presence of Mo (blue), Si (Green) and C (red) distributed in the composite. (d,e) TEM images of SiCN/MoS_2 sheet composite show intact morphology of MoS_2 sheets after pyrolysis. The SAED pattern in the insert corresponds to crystalline MoS_2. SEM images of SiCN/MoS_2 free-standing paper (f) cross-section, (g) top view and (h) corresponding EDX map. The insert in Figure (f) is an optical photograph of SiCN/MoS_2 free-standing and flexible paper. 166
Figure 6-4 XRD diffraction data comparison for various electrode specimens prepared in this study. Polymer-derived SiCN ceramic is amorphous while crystalline peaks for MoS_2 could be clearly visualized. 168
Figure 6-5 High-resolution X-ray photoelectron spectra of SiCN-MoS_2 composite nanosheets showing the characteristic MoS_2 and additional peaks that emerge as a result of chemical functionalization with SiCN ceramic. 168
Figure 6-6 Electrochemical data. Comparison of first, second and twentieth electrochemical cycle (voltage-capacity plots) of half-cells of (a) acid-treated MoS_2 (85 mA.g-1), (b) SiCN-MoS_2 (at 116 mA.g-1) composite and (c) SiCN-MoS_2 freestanding composite paper electrodes. (d) Electrochemical cycling performance of traditional electrodes (acid-treated MoS_2, SiCN, SiCN-MoS_2 composite) and freestanding electrode (SiCN-MoS_2 paper) for initial 20 cycles. (e) C-rate cycling performance comparison of SiCN-MoS_2 composite and SiCN-MoS_2 paper. (f) Comparison of total capacity for initial (1st and 2nd) and final (20th) cycles and contribution of various reactions for (i) acid-treated MoS_2 and SiCN-MoS_2 composite sheets. 170
Figure 6-7 Differentiated capacity with respect to corresponding operating voltage (dQ/dV) for (a) acid-treated MoS_2, (b) SiCN-MoS_2 composite and (c) SiCN-MoS_2 free-standing composite paper. 172

Figure 6-8 Post electrochemical analysis. SEM images of disassembled cells (a) acid-treated MoS_2, (b) SiCN-MoS_2 composite and (c) SiCN-MoS_2 paper electrodes after testing for 20 cycles. The insert shows digital images of corresponding electrode surfaces. (d) Elemental X-ray photoelectron spectra of the dissembled SiCN-MoS_2 composite electrode show Mo, S, and C phase modifications with additional Li peaks. 175
Figure 7-1 Schematic showing polymer to ceramic conversion and simultaneous incorporation of BN sheets in SiCN matrix. (L to R): polysilazane precursor uniformly wets BN sheets when they are stirred together. As the mixture is heated in flowing N2, polysilazane cross-links at approximately 300 °C to form long chains connected by BN sheets. Further pyrolysis at 1000 °C forms BN sheets embedded with SiCN ceramic matrix. Inset shows SEM images of composite at various stages of processing. 190
Figure 7-2 (a through e) SEM images of 'as-prepared' BN, SiCN, SiCN/BP, SiCN/BN, and SiCN/BN. (f through j) Top-view images of free-standing paper electrode made with approx. 20 wt.% rGO and (k through o) their corresponding cross-sectional images. The average paper thickness was observed to be approximately 20 to 25 µm. Scale bar is 5 µm in all images. 191
Figure 7-3(a through c): TEM images of as-obtained BN sheets, (d through i): as-synthesized SiCN/BN composite material. The insets show the SAED pattern obtained for the corresponding TEM image. SiCN/BN showed distinct pattern corresponding to BN. Scale bar is 50 nm. 192
Figure 7-4 (a) Bar chart of atomic percentage of elements present in SiCN/BN, SiCN/BNF and SiCN/BP composites obtained using XPS. (b) High-resolution XPS of B 1s, C 1s and N 1s peaks in SiCN/BN composites. (c) 11B NMR spectra showing B-N bonds in planar BN3 groups in case of SiCN/BN and SiCN/BNF and amorphous boron in SiCN/BP ceramic composites. (d) XRD comparison SiCN/BN, SiCN/BNF and SiCN/BP composites. Inset shows X-ray comparison of 'as-obtained' BN powder and SiCN/BN composite. Characteristic BN peaks were clearly observed in SiCN/BN composite. (e) Thermogravimetric analysis plots of three composites proving SiCN/BN's high thermal stability and oxidation resistance. (f) Electrical conductivity comparison of various SiCN PDCs specimen prepared in this study. rGO and BN are included to demonstrate the wide range in conductivity that can be achieved in these ceramics. 194

Figure 7-5 XPS (survey scan) comparison SiCN/BN, SiCN/BNF and SiCN/BP composites. .. 195
Figure 7-6 High-resolution XPS of C 1s and N 1s spectra of (a) SiCN and (b) SiCN/BP composites, respectively. 196
Figure 7-7 High-resolution B 1s spectrum of (a) SiCN/BNF and (b) SiCN/BP composites, respectively. 196
Figure 7-8 FTIR comparison SiCN/BN, SiCN/BNF, and SiCN/BP composites. 197
Figure 7-9 Thermogravimetric analysis plots comparing 'neat' SiCN/BN and SiCN/BN/rGO composite paper electrode (in flowing air). 198
Figure 7-10 1st and 2nd cycle voltage profile and differential capacity curve (a,b) BN/rGO and (c,d) BP/rGO anode. 200
Figure 7-11 1st and 2nd cycle voltage profile and differential capacity curve (a,b) SiCN/BNF/rGO, (c,d) SiCN/BP/rGO and (e,f) SiCN/rGO anode. 201
Figure 7-12 1st and 2nd cycle (a) voltage profile and (b) differential capacity curve of SiCN/BN/rGO. (c) Charge capacity of SiCN/BN/rGO with BN/rGO and SiCN/rGO for comparison. Cells were cycled asymmetrically at increasing rates for every five cycles. (d) Charge capacity when symmetrically at 1600 mA g-1 for 1000 cycles and return to 100 mA g-1. Charge capacity of SiCN/BN was more than twice than the capacity of SiCN. 202
Figure 7-13 Charge capacity of SiCN-BNF/rGO, SiCN/BP/rGO and BP/rGO electrodes: (a) asymmetrically cycled at different rates for every 5 cycles and (b) consecutively cycled symmetrically at 1600 mA g-1 (w.r.t. total weight of the electrode) for 1000 cycles. 203
Figure 7-14 GITT Data: (a) Charge and discharge cycles with 15 min of current pulse at 100 mAh.g-1 followed by 8 h of relaxation. (b) Calculated diffusion coefficient based on the relaxation steps at the corresponding voltages. 204
Figure 7-15 Voltage discharge/charge profile of three different SiCN-BN/rGO electrodes. Capacity is w.r.t. total electrode weight. 207

List of Tables

Table 2.1 $MoS_2$and MoS_2 composite synthesis methods, morphology and electrochemical performance 30
Table 2.2 Summary of the experimental results of the electrochemical cycling of PDC and their nanocomposites. 33
Table 4.1 Elemental composition obtained by EDX analysis of cross-section of 60MoS_2 paper (obtained for Figure 4.6). 88
Table 4.2 Comparison of properties of rGO, 20MoS_2, 40MoS_2 and 60MoS_2 free standing paper 97
Table 4.3Elemental composition obtained by EDX analysis of top surface of 60MoS_2 paper after electrochemical cycling (obtained from Figure 4.14). 101
Table 4.4 Mechanical properties of free-standing paper with 40 % and 60 % MoS_2 in the composite. 103
Table 5.1 60SiOC paper battery testing results 129
Table 5.2 Summary of experimental results of various free-standing graphene hybrid papers . 135
Table 5.3 Summary of the electrical conductivity test data. 137
Table 5.4 Summary of the Raman data for various electrode specimen both pre and post cycling. 139
Table 6.1 Summary of the electrochemical data and comparison with literature on other exfoliated-MoS_2 based electrodes 174
Table 7.1 Summary of electrochemical cycling data for various electrodes used in this study and comparison with data from literature. NOTE: All electrodes in the present study were prepared with approximately 20 wt % rGO. Capacity values are with respect to total electrode weight. 206

Acknowledgements

I would like to thank my Advisor, Dr. Gurpreet Singh for his useful suggestions and comments that helped me improve the quality of my work. I am grateful for his mentorship and inspiration. In addition, I would also like to acknowledge the Mechanical and Nuclear Engineering Department at Kansas State University and NSF Award: grant no. 1454151 and grant no. 1335862 for financial support. I would also like to thank my PhD thesis committee members Dr. Mark Hollingsworth, Dr. Kevin Lease, Dr. John Schlup and Dr. Keith Hohn for reading my thesis and providing useful suggestions.

I would like to express my gratitude to the following people for providing training on/access to various characterization instruments: Dr. Daniel Boyle, Dr. Leila Maurmann, Dr. Dewey Barich (KU), Dr. Charles Ye (KU), Dr. Jerry Hunter (Virginia Tech), Dr. John Desper, Dr. Kenneth Klabunde, Dr. Stefan Bassmann and Dr. Hongwang Wang.

I am extremely thankful to my colleagues Dr. Romil Bhandavat, Nasim Rahmani and Uriel Barerra assistance with various experiments.

Dedication

I dedicate this to my parents for their unconditional love and a constant source of encouragement and inspiration in all my academic endeavors.

Chapter 1 - Introduction

1.1 Motivation

"Oil and gas dominate our lives, and their decline will change the world in radical and unpredictable ways," says a retired English petroleum geologist named Colin Campbell. He also said that oil production in easy to extract oil fields would start to decline by the end of this decade. In light of these facts, there is an urgent need to find an alternative to our oil dependent transportation system. Figure 1.1 gives a perspective of percentage of renewable energy production by source. Moreover, effects of uncontrolled burning of fossil fuel have caused alarming changes in CO_2 levels which is resulting in climate change. These compounding reasons have forced the research into renewable and green energy source into overdrive.

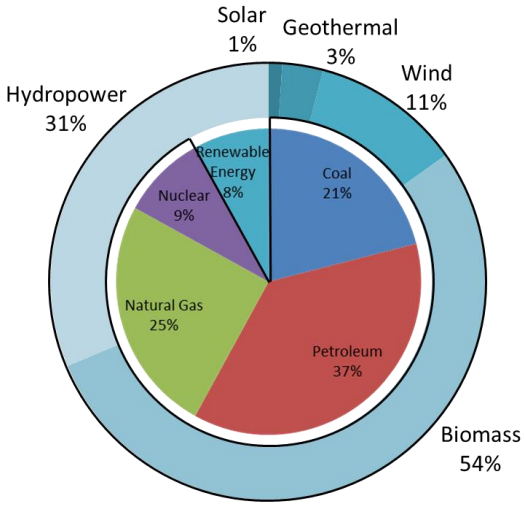

Figure 1-1 Total world energy consumption by source (2013). (Data obtained with permission from "Renewable 2014: Global Status Report" ISBN 978-3-9815934-2-6)

In the last few years, production of green energy from renewable sources has been accomplished by leaps and bounds. As shown in Figure 1.2, green energy production has increased over 300% in the last decade. Also, the quality of energy harvested from wind, solar,

geo-thermal and other renewable energy sources have contributed to more widespread use and building an energy sustainable economy.

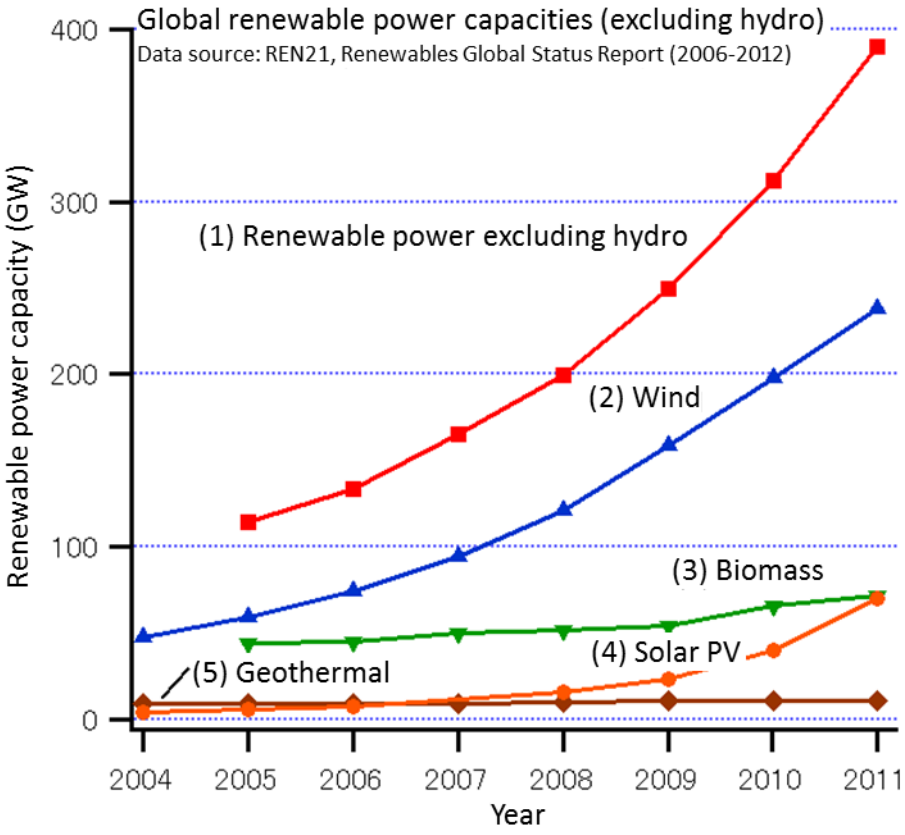

Figure 1-2 Global renewable power capacities(excluding hydro). (Reproduced with permission from REN21, Renewables Global Status Report, 2006-2012)

In its present form this energy generation approach seems promising for adequately supplying the energy needs for industries and domestic power grids of the future. But the expertise to transfer this energy into our transportation system has been limited by rechargeable battery technology. Lithium-ion batteries have shown promise as a suitable storage device for automobiles because of its 1) low reduction potential allowing it to have the highest possible cell potential and 2) one of the smallest ionic radii of any single charged ion, resulting in highest

gravimetric and volumetric capacity and energy density when compared to other chemistries like lead acid, nickel cadmium, nickel metal hydride, etc. Lithium-metal based batteries have been around since the early 1970s when Li-S batteries were aggressively pursued.[1,2] But failure to address dendrite formation in the lithium metal cathodes and sulfur shuttling in the anode caused the Li-metal battery to fail.[3] In the 1990s, further development came in the form of Li-ion batteries, in which Li is maintained as Li-ion during charging and discharging.[4,5] In a lithium ion battery the anode was made of graphite, and the cathode was a layered transition metal oxide. These materials made it possible to reversibly store Li-ions repeatedly, thus prolonging the cycle life.[6-8] This solved the dendrite issue and increased cyclability. This process was termed the rocking chair mechanism. This revolutionized the Li-ion battery technology, which enabled the commercialization of rechargeable, high energy density batteries that are conquering the market, emerged due to the introduction of graphite as anode material instead of Li metal, and the use of lithiated transition metal oxide cathode materials: $LiMO_2$ as the source of Li in the cell. Although these batteries were designed for portable electronic devices, they are more aggressively studied for use in next-generation electric cars, grid-level storage and defense applications. Despite its advantages over other batteries in terms of capacity and energy density, these batteries lack power density. Thus, there is a great commercial interest in improving the electrode material so these batteries could provide high energy and power densities simultaneously over a long cycle range.

Getting a truly grid-level storage system with Li- ion batteries comes with the risk of fire and explosion, which is intensified by the use of flammable electrolytes. To overcome this, Li-ion batteries come with an extensive battery management system to monitor the battery during cycling and prevent catastrophic failures. On the other hand sodium- ion batteries, with low

specific energy and advanced electrolyte combine to yield essentially no risk of fire or explosion. This not only makes the battery system safer on a power grid scale but also reduces the cost by removing most expensive battery management systems in the battery. Furthermore, it also has to be noted that the abundance of Li on the earth's crust is only 0.0017% when compared to Na which is 2.3%.[9] Finally, sodium is much cheaper than lithium, which doesn't hurt either. Recently, research into materials for Na-ion batteries has escalated since the demand for electric vehicles has increased. However, many challenges remain before SIBs (sodium ion batteries) can become commercially competitive with LIBs (lithium ion batteries). For instance, Na ions are about 55% larger in radius than Li ions, which make it difficult to find a suitable host material to allow reversible and rapid ion insertion and extraction.[10]

Among the academic community, the search for alternative anode materials is focused on 2D layered materials or van der Waals sheets like graphene, molybdenum disulfide (MoS_2), tungsten disulfide (WS_2) and phosphorene because of their similarities to graphite (commonly used anode material in Li-ion batteries).[11-13] Reducing the size of the bulk material to single layer sheets introduces new and more interesting properties like higher surface area, increased elasticity , enhanced pore size among others. Due to this, these materials can be used in a number of applications like optoelectronics, sensors, biological engineering, filtration, light weight/strong composite materials, photovoltaic, medicine, quantum dots, thermal management and energy storage. But synthesizing large quantities of pristine material suitable to be used as an anode has yet to be achieved.

This Ph.D. thesis addresses major challenges in material synthesis like bulk quantity production and interfacing with Li-active materials, and it further describes the mechanism of Li and Na storage in layered van der Waals materials like graphene, WS_2 and MoS_2. Although

development of cathode material is also important to complete realization of high power batteries, the focus of this thesis is on the anode electrode.

1.2 Overview of Dissertation

Chapter 2 introduces the mechanism of Li ion and Na ion batteries and includes an extensive literature review of anode and cathode materials. It also provides an introduction to graphene, MoS_2 and PDCs including their structure and properties and their application in batteries.

Chapter 3 details the synthesis and physical and chemical characterization of graphene oxide. It also includes a parametric study into the effect of temperature and reducing environment on its physical and chemical structure and their consequent effect in the Li and Na ion storage mechanism in the material.

Chapter 4 describes the electrochemical properties of MoS_2-rGO free standing paper when used as an electrode in a Na half-cell. A detailed study into the mechanism of energy storage is performed by disassembling and analyzing cycled cells using XRD and SAED.

Chapter 5 presents the introduction of high Li electrochemical capacity material like PDC-SiOC (Polymer derived SiOC ceramic) between the layers of free-standing graphene paper to make a hybrid composite material. Electrochemical performance of this hybrid is investigated with a parametric study of varying composition. A detailed study into the mechanism of energy storage is performed by studying the diffusion coefficient parameters.

In chapter 6, to improve the Li cycling stability of MoS_2, it was functionalized with polysilazane (polymeric precursor to SiCN-PDCs), which on pyrolysis forms a MoS_2-SiCN ceramic composite. A detailed study into the physical properties of these materials through scanning and transmission electron microscopy and chemical properties through EDX, Raman

spectroscopy, XRD and TGA is performed. Later, these composite materials were formed into free standing papers with addition of graphene oxide and using vacuum filtration technique. This composite showed incredible cycling stability even at very high current density.

In chapter 7, a detailed analysis of BN interfaced SiCN is presented. This unique composite had higher electrical conductivity and better Li cyclic performance than just SiCN and BN. Detailed characterization of the composite material was performed to propose a suitable molecular structure and mechanism for the observed enhancement in performance.

Chapter 8 concludes the thesis and proposes a pathway for future exploration into identifying other materials for anode electrodes in metal ion batteries. It also explores the possibility of using these layered materials in other metal ion based batteries such as Mg-ion or Ca-ion batteries.

1.3. Reference

1. Tarascon, J. M.; Armand, M., Issues and challenges facing rechargeable lithium batteries.*Nature* **2001,** *414* (6861), 359-367.

2. Whittingham, M. S., Electrical Energy-Storage and Intercalation Chemistry.*Science* **1976,** *192* (4244), 1126-1127.

3. Broussely, M.; Biensan, P.; Simon, B., Lithium insertion into host materials: the key to success for Li ion batteries. *Electrochimica Acta* **1999,** *45* (1-2), 3-22.

4. Murphy, D. W.; Disalvo, F. J.; Carides, J. N.; Waszczak, J. V., Topochemical Reactions of Rutile Related Structures With Lithium. *Materials Research Bulletin* **1978,** *13* (12), 1395-1402.

5. Lazzari, M.; Scrosati, B., Cyclable Lithium Organic Electrolyte Cell Based On 2 Intercalation Electrodes. *Journal of the Electrochemical Society* **1980,** *127* (3), 773-774.

6. Mohri, M.; Yanagisawa, N.; Tajima, Y.; Tanaka, H.; Mitate, T.; Nakajima, S.; Yoshida, M.; Yoshimoto, Y.; Suzuki, T.; Wada, H., Rechargeable Lithium Battery Based On Pyrolytic Carbon As A Negative Electrode. *Journal of Power Sources* **1989,** *26* (3-4), 545-551.

7. Mizushima, K.; Jones, P. C.; Wiseman, P. J.; Goodenough, J. B., LIXCOO2 "(Oless-Thanxless-Than-Or-Equal-To1) - A New Cathode Material For Batteries of High-Energy Density.*Materials Research Bulletin* **1980,** *15* (6), 783-789.

8. Nagaura, T.; Towaza, K. "Lithium ion rechargeable battery," *Prog. Batt. Solar Cells* **1990**, 9, 209.

9. Tarascon, J.-M., Is Lithium the New Gold? *Nature Chemistry* **2010,** *2* (6), 510-510.

10. Ellis, B. L.; Nazar, L. F., Sodium and sodium-ion energy storage batteries. *Current Opinion in Solid State & Materials Science* **2012,** *16* (4), 168-177.

Chapter 2 - Background and Literature Review

2.1 Lithium Ion Battery Concepts

Rechargeable lithium battery works by reversibly cycle Li ions, by intercalation and deintercalation between two layered compounds. In order to ensure battery stability, the reaction in the cathode is limited to:

Equation 2.1

$$\mathbf{LiCoO_2 \rightarrow \frac{1}{2}Li^+ + \frac{1}{2}e^- + Li_{0.5}CoO_2}$$

The upper voltage is limited to 4.2 V (vs Li/Li^+), which limits the theoretical capacity of the cathode to around 140 mAh/g, which is mainly, only the first-order phase reaction between $LiCoO_2$ and $Li_{0.5}CoO_2$.[1]

As represented in Figure 2.1, the uniqueness of this battery is that the source of the shuttling ion (Li^+) is the cathode material, which is a layered material rather than pure Li as in Li-metal batteries. This ensures increased safety and prolonged shelf life. Once the cell is assembled, the first reaction is always charging during which oxidation and delithiation of $LiCoO_2$ and corresponding reduction and lithiation of graphite occurs. Graphite intercalates reversibly to form LiC_6 as the final product as in the following reaction:

Equation 2.2

$$\mathbf{C_6 + Li^+ + e^- \rightarrow LiC_6}$$

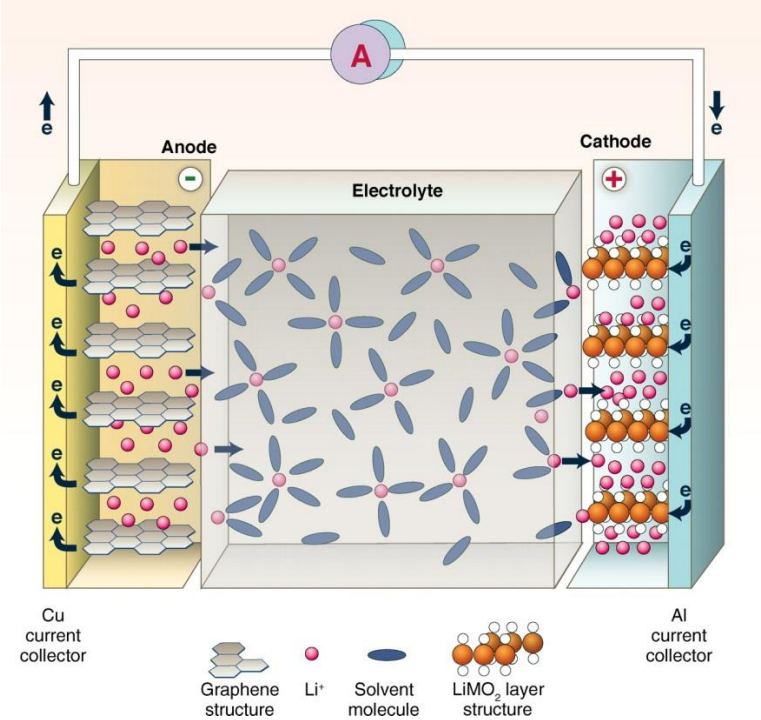

Figure 2-1 Schematic representation of discharging processes in a commonly used Li-ion battery in which graphite is used as an anode and LiCoO2 is used as the cathode. (Reproduced with permission from Sciencemag: Dunn, B. *et al.* Science, 2011, 18(334), 928)

During the process of Li intercalation in graphite, the first order phase transition reaction occurs in stages such as LiC_{24}, LiC_{27} and LiC_{12}.[2] During this process Li salts in the electrolyte reacts to form a passivation layer consuming Li which leads to irreversible charge. This layer provides a stable condition for formation of Li_xC_6 stage during the course of Li insertion into graphite.[3] Because of this loss during the first charge cycle, all Li-ion battery cathode materials are designed to be in excess to provide the necessary Li- ions to form the passivation layer of graphite surface. The passive thin film on the surface blocks further electron transport once it reaches a certain thickness but allow Li-ion transport, thus behaving as a solid electrolyte interphase (SEI) between the electrode and the solution (Figure 2.2.).[4,5] This layer clearly separates the fully lithiated graphite and the Li-ion in the electrolyte and thus enables their

apparent stability in any Li salt solutions in a non-aqueous polar aprotic solvents. The anodic stability of the electrolyte in non-aqueous polar aprotic solvents is very important because the limiting factor with respect to voltage, specific capacity and energy in a Li-ion battery is the cathode material, whose reversibility depends on the anodic stability of the electrolyte solution.

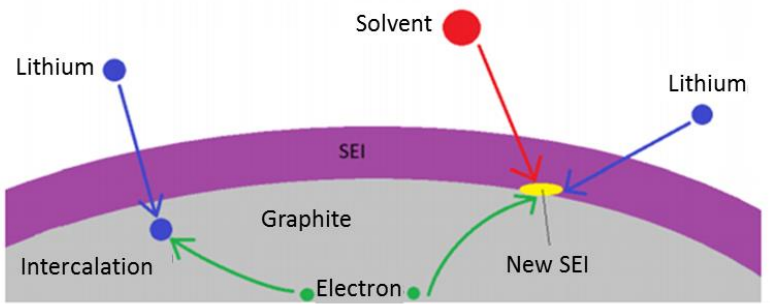

Figure 2-2 SEI layer formation on anode surface inhibits dissolution of electrolyte.

2.2 Components of a Li-ion Battery

2.2.1. Electrolyte

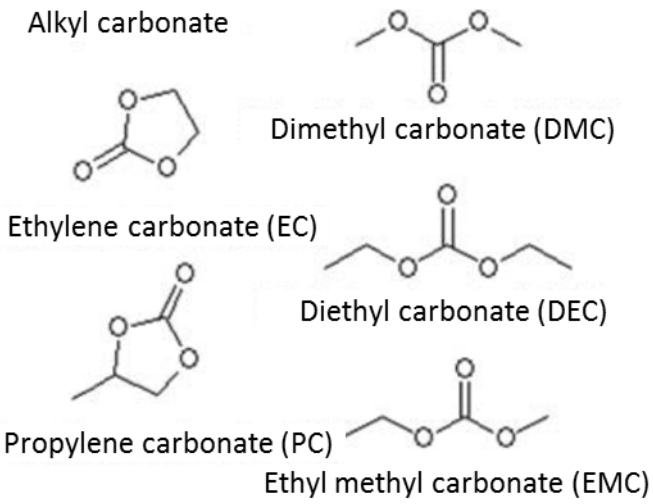

Figure 2-3 Chemical structures of all the alkyl carbonates used in Li-ion batteries

The standard electrolyte used widely in Li-ion batteries was formulated several decades earlier.[6] It consists of a Li salt such as lithium hexafluorophosphate ($LiPF_6$) dissolved in binary solvent mixtures like ethylene carbonate (EC) and dimethyl carbonate (DMC) or ethyl methyl carbonate (EMC) or diethyl carbonate (DEC).[6,7] Figure 2.3 illustrates the chemical structural formulae of all the alkyl carbonates used in Li-ion batteries.

Among these carbonate solvent mixtures, EC-DMC with $LiPF_6$ is the most preferred electrolyte for the following reasons: (a) Carbonate solvents are aprotic, polar and have a high dielectric constant, which enables $LiPF_6$ to dissolve readily even at concentrations greater than 1M. (b) EC has relatively high melting point (36.4 °C), but combined with low viscous DMC forms a liquid solution with high ionic conductivity up to -15 °C. (c) The anodic stability of EC is the highest among other carbonates because it decomposes reductively on graphite surface at around 0.8V vs Li/Li^+. This is due to the centrally located carbon having an oxidation state of 4 and relatively low number of C-H bonds, which can be considered as electron-donating. (d) It demonstrates reasonable metastability up to 5V vs Li/Li^+ by forming a passivation layer on aluminum (cathode current collector) even at elevated temperatures (60 °C).[8] In addition to these electrolytes contains additives that contribute to improve the cycle life and performance by inhibiting corrosion, removing oxide layer on electrode surface, directing SEI formation, increasing separator wettability and protecting against overcharge.[9]

2.2.2. Electrode Material

The chief measure of a battery for automotive applications is how much energy it can store and how fast it can deliver that energy and get charged up. In order to increase the energy storage capacity, various strategies have been used like: (a) Dimension reduction: Enables faster ion and electron transport, increases surface reactivity and has better mechanical stability during

expansion and contraction occurring in the course of battery cycling. (b) Conductive composite: Improves nanoscale electrical conductivity and mechanical support. (c) Surface functionalization: Improves C-rate performance and has better chemical and thermal stability. (d) Morphology controlled synthesis: Ability to tailor the electrode material to suit specific demands. (e) Coating and encapsulation: Improves the interaction between a highly reactive electrode and electrolyte and enhances conductivity.[10-15] Electrodes in general can be classified into three main categories as shown in Figure 2.4 depending on its mechanism of Li-ion storage: (a) insertion, (b) alloying and (c) conversion.

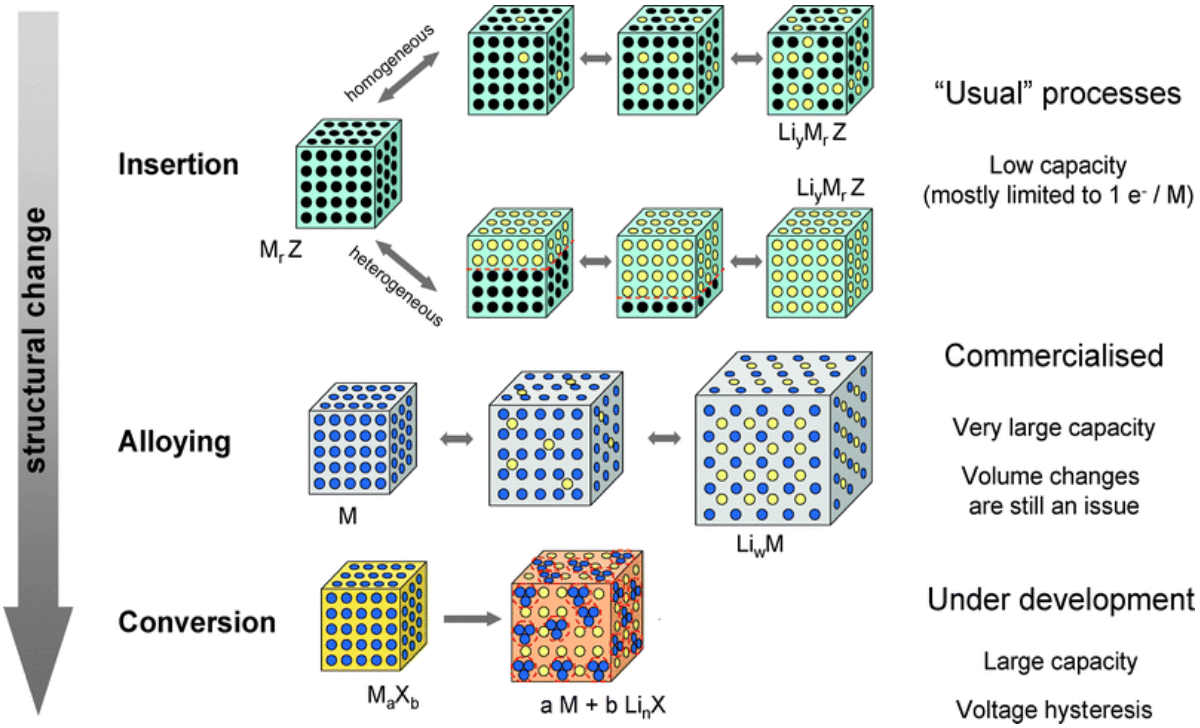

Figure 2-4 Schematic representation of the different mode of Li-ion storage mechanism observed in electrode materials for Li-ion batteries. Black circles: voids in crystal structure, blue circles: metal, yellow circles: lithium. (Reproduced with permission from The Royal Society of Chemistry: Palacin, R., Chem. Soc. Rev. 2009, 38, 2565-2575)

Cathode Materials

Insertion refers to topotactic reversible intercalation of guest atoms or ions into empty interstitial spaces present in the host material.[16-18] First generation Li-ion battery electrodes were based on this mechanism. The structure of $LiCoO_2$ (LCO) positive electrode material can be described as a cubic close packed array of oxide ions with Co(III) and lithium ions occupying the voids between alternative sheets. Although Li extraction from the layered structure is favored, in some cases it is homogeneous, in which case it forms a solid solution but in other cases it is heterogeneous.[19] This difference is shown in the Figure 2.4. The reversibility of some of these processes reduces at high voltages (above 4.3 V). Thus only 0.5 lithium ions per formula unit can be reinserted which gives a useful capacity of only 150 mAh/g. More recently, many other alternative cathode insertion materials have been studied. These are primarily composed of metal calcogenides, transition metal oxides and polyanion compounds. These can further be categorized into layered, spinel, olivine and tavorite.

Figure 2.5 shows the approximate range of average discharge potentials and specific capacities of some of the most common intercalation type cathodes. LCO has the lowest thermal stability among cathodes.[20-22] It experiences thermal runaway past ~200 °C due to an exothermic reaction between released oxygen and organic material.[23] $LiNiO_2$ (LNO) has structure similar to $LiCoO_2$ and has a theoretical capacity of 275 mAh/g. Low cost and high energy density are the driving forces for this system. But Ni in LNO has the tendency to fill the interstitial sites during delithiation and thus reducing the reversible capacity.[24] Moreover, it suffers from thermal runaway like LCO. This brings us to the next material, $LiNi_{0.8}Co_{0.15}Al_{0.05}O_2$ (NCA). It is being used in Panasonic batteries for Tesla EVs. It has high discharge capacity (~200 mAh/g) and long shelf-life. However, it suffers from high capacity fading at elevated temperatures above 40 °C due to SEI growth and micro-crack growth.[25,26]

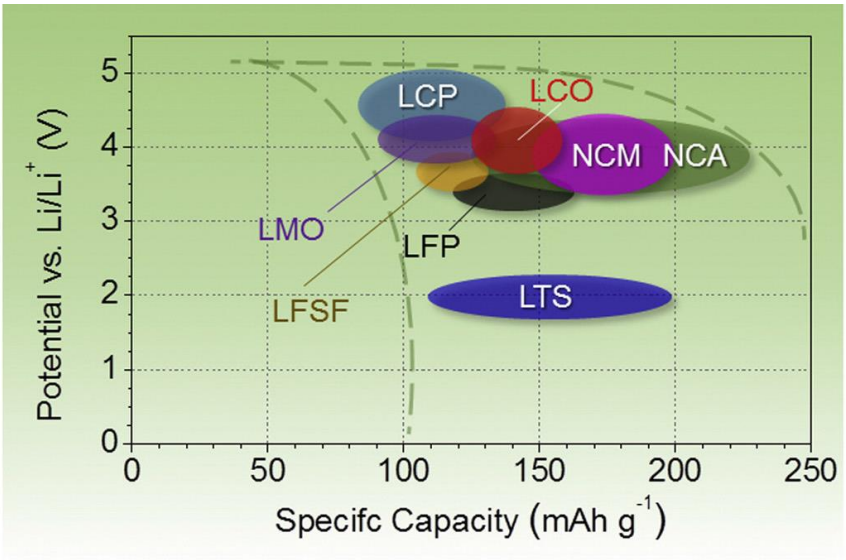

Figure 2-5 Approximate range of average discharge potentials and specific capacities of some of the most common intercalation type cathodes. (Reproduced with permission from Elsevier: Nitta, N., Mater. Today, 2014, 1)

$LiMnO_2$ (LMO) was the more desired cathode because it is much cheaper and less toxic when compared to Co and Ni. But as it is LMO suffers from a tendency to change structure from layered to spinel during Li extraction and leaches out of LMO during cycling.[27,28] This effect led to continuous research into cathode formulations and resulted in the study of $Li(Ni_{0.5}Mn_{0.5})O_2$ (NMO) cathodes. NMO is more attractive because it is similar in capacity to LCO but at a much cheaper cost. Also addition of Ni enables more Li to be extracted to achieve more capacity.[29] Adding Co into the mixture enhances structural stability.[30] $LiNi_xCo_yMn_zO_2$ (NMC) has similar or slightly higher achievable specific capacity than LCO and similar operating voltage while having lower cost since Co content is reduced. With recent effort towards improvement in microstructure like formation of microporous NMC, has improved the reversible capacity to 235 mAh/g even at 50 °C.[31] Several other cathode materials were also studied like lithium iron

phosphate (LFP), lithium titanium sulfide (LTS) and nickel cobalt aluminum oxide (NCA). For more detailed information, we recommend these review publications.[32,33]

Insertion Anode Materials

The most commonly used anode material is graphite, which also works in insertion of Li-ion between the interstitial spaces between graphene layers.[34-40] It has the most suited properties of mechanical stability, electrical conductivity, low cost, abundant availability, low delithiation potential vs Li, low relative volume change and high diffusivity. Even though it has higher gravimetric capacity (372 mAh/g) it lacks in volumetric capacity (330-400 mAh/cm^3) when compared to commercial cathode materials. Graphitic carbon undergoes 10% uniaxial strain during Li insertion along the edge planes which damages the SEI and reduces cycle life.[39-41] To overcome this issue, these electrodes are coated with amorphous carbon on the surface to protect the vulnerable edges from electrolyte and achieve high columbic efficiency.[42,43] Alternatively hard carbon has shown to possess smaller graphene particles with disordered layer which results in nano-voids and defects.[34,44-46] These properties allow them to store more Li and be less susceptible to exfoliation. But with increased interstitial spacing the volumetric capacity further reduces.

Lithium titanium oxide ($Li_4Ti_5O_{12}$/LTO) is another anode material which intercalates/deintercalates Li-ions similar to graphite. It has superior thermal stability, higher rate capability, relatively higher volumetric capacity and high cycle life.[49] It lacks in reduced cell voltage, higher cost of Ti and lower capacity (170 mAh/g and 600 mAh/cm^3). It is termed as a "zero strain" material because during lithiation/ delithiation phase change occurs. This extremely low strain of only 0.2% resulted in LTO's high rate, cyclic stability and stable SEI formation.[50-52] SEI is also restricted due to the high operating voltage of LTO (>1 V) since equilibrium voltage

is higher at ~1.55 V vs Li/Li^+. In combination with high power cathodes like NMC or LMO, the high rate capability of LTO can satisfy the needs of an electric vehicle while lasting for tens of thousands of cycles. Unfortunately, side reactions on the surface of LTO cannot be reduced. These reactions result in high gas evolution due to reaction with organic electrolyte which could be deadly in case of pouch failure.[53-55]

Alloying Anode Materials

Alloying in anodes refers to elements which electrochemically alloy and form compound phases with Li. Gravimetric and volumetric capacities are extremely high when compared to standard anode. But as illustrated in Figure 2.6 enormous volume expansion will cause the electrode to lose contact with conductive agent and can destroy the SEI layer resulting in continuous electrolyte decomposition, loss of reversible Li and increased impedance.[56-58] To avoid these issues certain strategies are employed like: (a) alloying materials are generally synthesized as a matrix with carbon material like graphene or carbon nanotubes (CNTs), (b) reduced particle size and electrolyte additives.[59-65] Even then, achieving high volumetric capacity, long cycle life and high mass loading has not been possible.

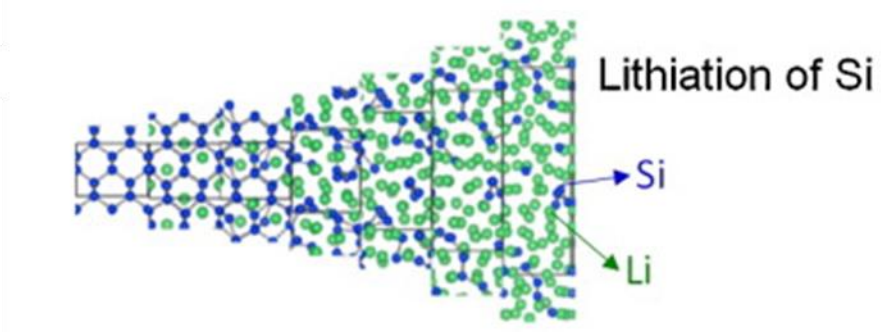

Figure 2-6 Schematic representation of volume expansion that occurs during alloying of Si.[66] (Reproduced with permission from Elsevier: Nitta, N., Mater. Today, 2014, 1)

Of all the alloying anode materials Si has been the most promising because of its relatively low average delithiation potential, extremely high gravimetric (>2000 mAh/g) and volumetric capacity, abundance, low cost, chemical stability and non-toxicity. Other alloying materials that have been studied so far are Zn, Cd, Pb, Al, Sn, P and Sb. Sn and Al suffer from fracturing even at small particle sizes. Cd, Pb, P and Sb have high capacity, and well performing electrodes have been developed by ball-milling, but these materials are highly toxic and have relatively high delithiation potentials.[67-73]

Conversion Anode Material

Recently, there is growing interest in electrochemical reaction of lithium transition metal dichalcogenides because of their unique conversion reaction mechanism which is as follows:

Equation 2.3

$$\mathbf{M_aX_b + (b.\ n)Li \leftrightarrow aM + bLi_nX}$$

where M is transition metal, X anion and n is formal oxidation state of X.

Conversion reactions have been studied since 1970s.[74,75] During 1990s it was believed that the conversion reactions were not attractive because of the easy and simplicity of intercalation reaction anodes. But once the capacity of transition metal compounds were proved to be three times that of graphite, these phase reactions were considered as promising alternatives in rechargeable Li-ion batteries. Reversibility comes from the formation of metal non domains at the end of complete lithiation. These nano domains as shown by schematic in Figure 2.7 have high surface reactivity that they can decompose lithium binary compounds (Li_nX) in which they are embedded when a reverse polarization is applied. The success of conversion reaction mechanism lies with nano-domain metallic particles which is maintained even after many charge/discharge cycles. The actual potential at which these reactions occur depends on the

transition metal and the anionic species. This gives a level of variability to the requirement of specific applications.

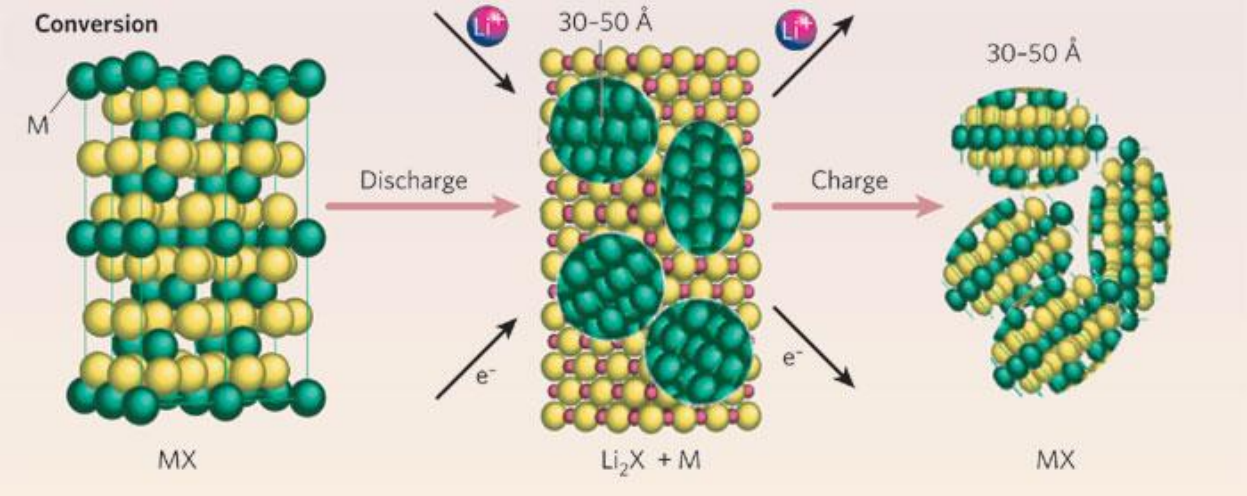

Figure 2-7 Schematic representation of conversion reaction mechanism during ion insertion/extraction in MoS_2. (Reproduced with permission from Nature: Armand, M., *et al.*, Nature, 2008, 451, 652-657)

2.3. Sodium Ion Battery Concepts

Na batteries were being studied in tandem with Li batteries early in 1980's. But the success of Li batteries overshadowed the research on Na batteries. But recently academic interests into Na systems have gained interest since availability of Li has been proven to be insufficient for future energy needs. In the periodic table, Na lies next to Li and thus has similar properties. As shown in Figure 2.8a, the fundamental principles of both Li-ion batteries and Na-ion batteries are similar: the potential difference between the two electrodes (anode and cathode) enables the Na-ion to shuttle between them during charge/discharge cycles.

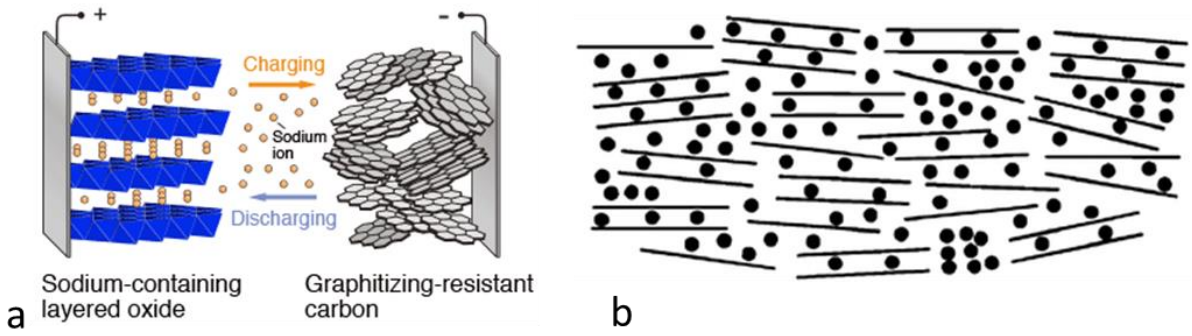

Figure 2-8 (a) Schematic representation of a typical Na-ion battery. (b) House of cards model proposed by Dunn and co-workers on sodium intercalation in hard carbon. (Reproduced with permission from Royal Society of Chemistry: Palomares, V., *et al* Energy Environmental Sci., 2012, 3, 5884-5901)

2.4. Components of aNa-ion Battery

2.4.1. Cathode

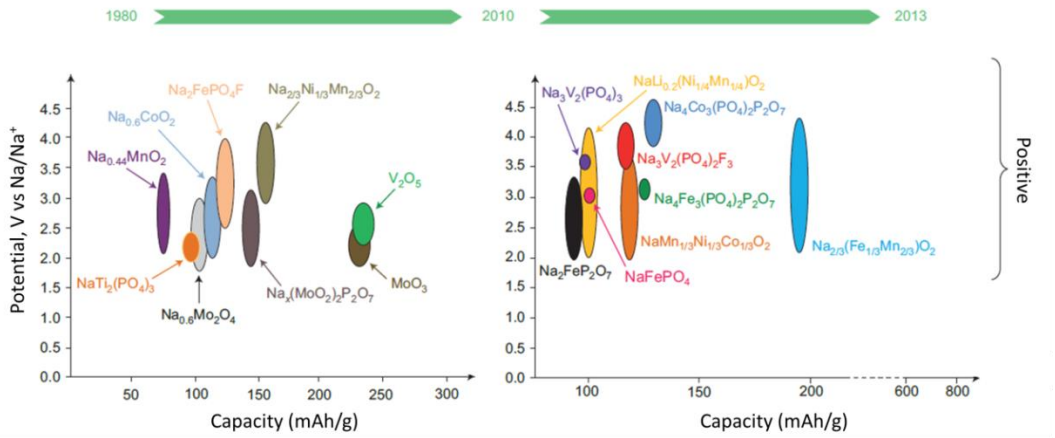

Figure 2-9 Voltage range and gravimetric capacities of various materials studied as cathode for Na-ion battery. (Reproduced with permission from Nature: Larcher, D. *et al*. Nat. Chem., 2015, 7, 19-29)

More research in Na-ion batteries has been concentrated on improving the cathode material for Na-ion batteries. Initial computational studies have showed that the electrode potential is on average ~0.4 V lower than their Li counterparts. This is a major issue since lower positive electrode potential means the cell voltage would be lower, which results in lower energy density.

As can be seen from Figure 2.9 and Figure 2.10, the study of layered transition metal oxide with intercalated Na-ions has been extensively investigated as a cathode electrode. Initial studies were based on phase transition of various Na_xCoO_2 structures, that occur during Na-ion cycling.[76] This demonstrated its feasibility as a suitable electrode. Of these phases P2-$Na_{0.7}CoO_2$ showed the highest energy density of ~260 Wh/kg) and was found to operate between $0.45 < x < 0.9$ V. [77-79]Almost all Na analogs of Li cathode materials have been studied. Recent interest has been focused on polyanion materials. $NaFePO_4F$ has been the most promising, with the capacity of ~110 mAh/g at 6.2 mA/g.[80-82] But cyclability has been an issue because it was claimed that there is vast difference in electrical conductivity and volume change between sodiated and desodiated phases coupled with high activation energy.

2.4.2. Anode

Graphite is most commonly used anode in Li batteries. But first principle calculations showed that it is harder to form intercalation compounds with Na than with other alkali materials. Thus it is imperative to identify another suitable material for Na-ion batteries. Since graphite has been excluded, other carbonation materials like graphite fibers, glucose and hard carbon have been studied. Initial studies shown that carbon fiber and crushed graphite have a very low capacity of only 83 mAh/g (NaC_{26}).[83]

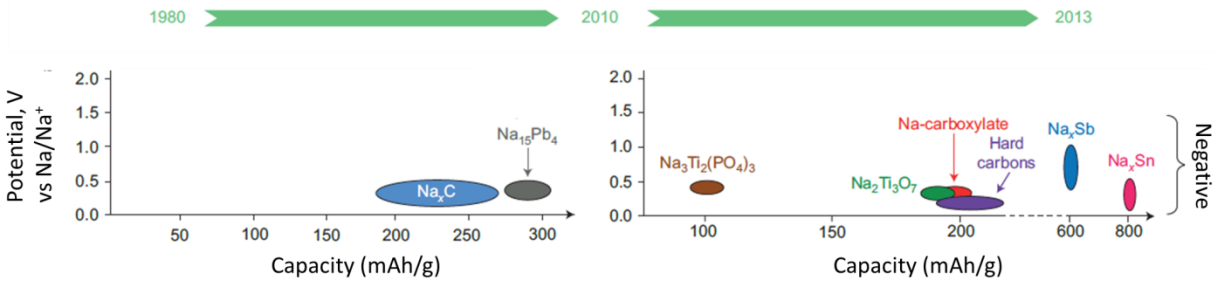

Figure 2-10 Voltage range and gravimetric capacities of various materials studied as anode for Na-ion battery. (Reproduced with permission from Nature: Larcher, D. *et al*. Nat. Chem., 2015, 7, 19-29)

In the past few years, advances have been made towards obtaining high capacity from carbon based materials. Pyrolyzed glucose showed reversible capacity of 300 mAh/g while carbon microspheres showed 285 mAh/g.[84,85] Templated carbon showed even higher performance at 130 mAh/g at relatively high current density of 75 mA/g. at current densities of 744 and 1869 mA/g it still maintained a reversible capacity of 100 mA/g.[86] This improvement was attributed to the interconnected pore structure which reduced the diffusion length and the carbon micro structure which enhanced electrical conductivity. Alloying mechanism in Na-ion batteries occurs in a similar mechanism to Li as follows:

Equation 2.4

$$\mathbf{M + \mathit{n}Na^{+} + \mathit{n}e^{-} \leftrightarrow Na_{\mathit{n}}M}$$

Sb_2O_4 showed the highest reversible capacity of 896 mAh/g.[87] But these electrodes suffer from large volume change during charge/discharge cycles and since Na-ions are 55 times larger than Li-ions, the volume change in the electrode plays a more significant role in battery design than in Li-ion batteries. Conversion reaction compounds like $NiCo_2O_4$, FeS_2 and Ni_3S_2 have been

investigated as negative electrode for Na-ion batteries.[88-92] Of these only $NiCo_2O_4$ showed a reversible capacity of 200 mAh/g.

2.5. Graphene Synthesis and Application as Battery Electrode Material

Graphene is the wonder material whose properties have been studied extensively for many applications since its first isolation in 2004. Graphene is a carbon monolayer arranged in a honeycomb structure lattice. Even though graphene was synthesized for decades, it was widely believed that graphene cannot be in its free state because of its high surface area. But in 2004 Novoselov and co-workers were able to transfer monolayered graphene onto a Si substrate.[93] Since then intense research on graphene properties has yielded numerous applications like semiconductors, batteries, LEDs, photovoltaic cells, electronic devices, and others.

Different methods of graphene synthesis are explained in Figure 2.11. Graphene synthesized using epitaxial growth on SiC or metal surface[93,94] and mechanical exfoliation[94,95] techniques are very expensive due to the ultrahigh vacuum requirement for epitaxial growth, and the overall the yield is also very low. So these methods were used only to study properties of graphene through fundamental research and in high end applications like touch screen displays and transistors. But these methods delivered defect free high quality graphene. Similarly, chemical vapor deposition techniques[95] (used widely in industry) using hydrocarbons as a precursor have limitations like high cost, low yield and relatively low purity. To obtain high yield, graphene has to be synthesized using liquid phase exfoliation[95,96] or reduction from graphene oxide.[97,98] Liquid phase exfoliation involves sonication of graphite in a solvent till it overcomes the weak van der Waals attraction between individual sheets and separates them. Usually a functionalizing agent is involved so it mildly creates a charge on graphene surface thus keep them apart even after sonication is stopped. But this process does not guarantee exfoliation

of all graphite to graphene. Nonetheless, due to its high yield and low cost there is high interest in developing this process to get high quality sheets.

2.5.1. Synthesis

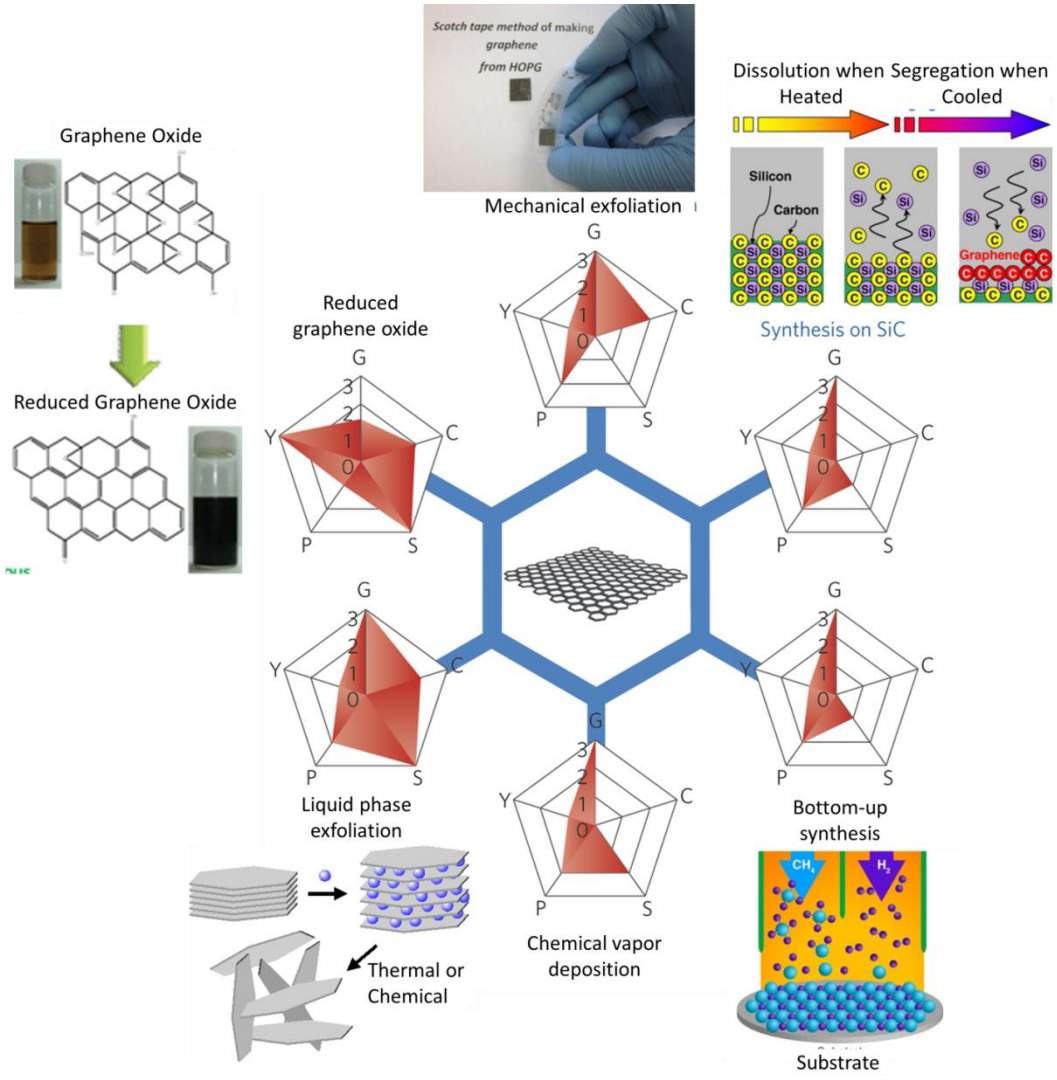

Figure 2-11 Different procedures for synthesis of graphene like mechanical exfoliation, liquid phase exfoliation, bottom-up synthesis, epitaxial growth on SiC, epitaxaial growth on metal substrates and reduction of graphene oxide. Each method is evaluated in terms of graphene quality (G), cost aspect (C)-low value corresponds to cost of production,

scalability (S), purity (P) and yield (Y). (Reproduced with permission from Nature: Raccichini, R. *et al.*, Nat. Mater. 2014, 14, 271-279)

Most widely used exfoliation technique is oxidizing graphite using high power oxidizing agents and then reducing it back to graphene.[97,98] Graphite is completely separated to individual sheets during oxidation although there is a heavy compromise on the quality of graphene sheets as the oxidizing agent creates irreversible defects in the sheet surface. In order to reduce graphene oxide (GO) chemical, thermal and electrochemical processes are widely used (Figure 2.12).

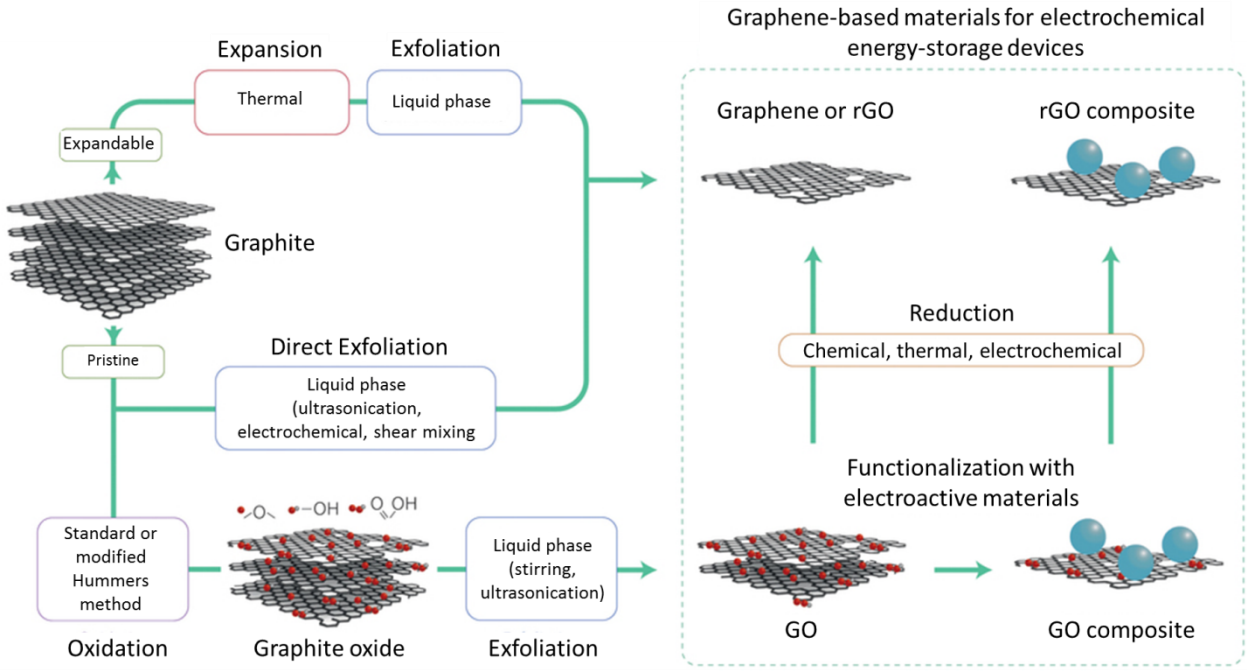

Figure 2-12 Schematic showing the most common pathways for producing reduced graphene oxide based electrode materials. (Reproduced with permission from Nature: Raccichini, R. *et al*., Nat. Mater. 2014, 14, 271-279)

2.5.2. Graphene as Battery Electrode

Recently, graphene has been widely studied as an alternative electrode material for Li-ion batteries. Graphite (commonly used anode in Li-ion battery) has a theoretical capacity of 372 mAh/g. This capacity was calculated based on intercalation mechanism between the stacked layers. It was suggested by Dahn *et. al.* that graphene monolayer can store two times as many Li-ions as graphite by storing Li on both sides of the sheets resulting in a Li_2C_6 stoichiometry that provides a specific capacity of 744 mAh/g.[99,100] The mechanism of Li storage in graphene is based on adsorption both on its internal surfaces and in the nanopores that are present between the randomly arranged graphene sheets. Li storage in graphene is different because it provides electronically and geometrically non-equivalent sites.[101] Thus, production method of both the graphene material and electrode strongly influences the capacity of graphene based anodes.

In reality, due to high surface area, high defect density and porous structure, SEI formation consumes a lot of lithium during the first insertion cycle which results in incredibly high capacity value of >2000 mAh/g.[102] During extraction cycle, the capacity is delivered at a higher potential of 1-3 V vs Li/Li^+.[103] This large hysteresis results in poor energy efficiency. In addition to low first cycle efficiency and large hysteresis, electrochemical cycling of reduced graphene oxide progressively reduces graphene which leads to restacking and subsequent reduction of storage capacity. High quality graphene sheets are therefore essential to realize the actual potential of graphene in batteries.

Graphene based composite anodes have been developed to utilize the electrical and mechanical properties of graphene (Figure 2.13). These composites are prepared by growing or functionalizing electroactive nanostructures on graphene surface. These prevent agglomeration of graphene as well. Graphene, to which the nanoparticle is attached, now acts as a porous/open support structure which allows easy diffusion of Li-ions and buffers volume change and electrically conductive network. Several materials such as TiO_2 (insertion mechanism) and Fe_2O_3 or Co_3O_4 (conversion mechanism) have been studied.[103,104]

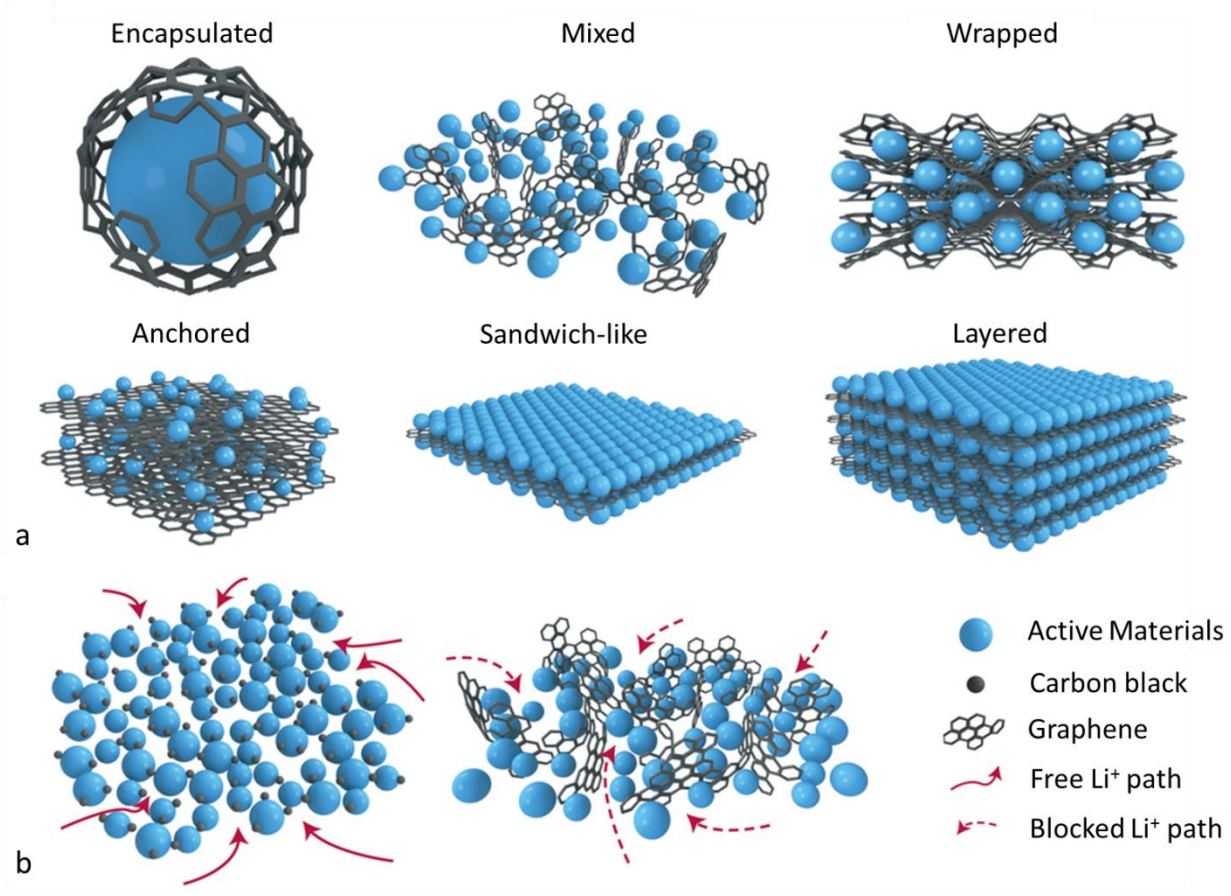

Figure 2-13 Schematic shows the various applications in which graphene is used composite electrode materials. (Reproduced with permission from Nature: Raccichini, R. *et al*., Nat. Mater. 2014, 14, 271-279)

Graphene oxide with increased interlayer spacing and higher surface area has shown promising electrochemical behavior, good cycle life and better rate capability as a Na ion battery electrode. Graphene exhibited different Na-ion capacity depending on the temperature of synthesis (as interlayer spacing changes with varying temperature) even though the Coulomb efficiency for the first cycle still remains poor. Similar to Li-ion batteries graphene-based composites have also been widely studied for Na-ion battery applications.[122-126]

2.6. Molybdenum disulfide (MoS_2) Synthesis and Application as Battery Electrode Material

Single layer 2D TMDs have gained more interest because if their relatively higher surface reactivity and ability to be separated to individual sheets by simple processes unlike graphene which is inert and can be separated only by strong surface functional groups. TMDs generalized formula is MX_2, where M is a transition metal like Tl, Zr, Hf, V, Nb, Ta, Mo, W, Tc and Re and X is a chalcogenide like Se, Se and Te. Of these, group 6 transition metals (Mo, W) have been widely studied in varied applications as an analog to graphene.[105] MoS_2 and WS_2 are semiconductors intrinsically.[106,107] Exfoliation of these materials leads to additional properties like increased surface area, elasticity, increased pore size, etc.. MoS_2 has gained notoriety in the academic community because of its unique interaction with lithium by conversion reaction mechanism. Due to this 1 mole of MoS_2 leads to 4 moles of Li^+ storage resulting in a capacity of 670 mAh/g. Figure 2.14 shows the basic dimensional properties of MoS_2.

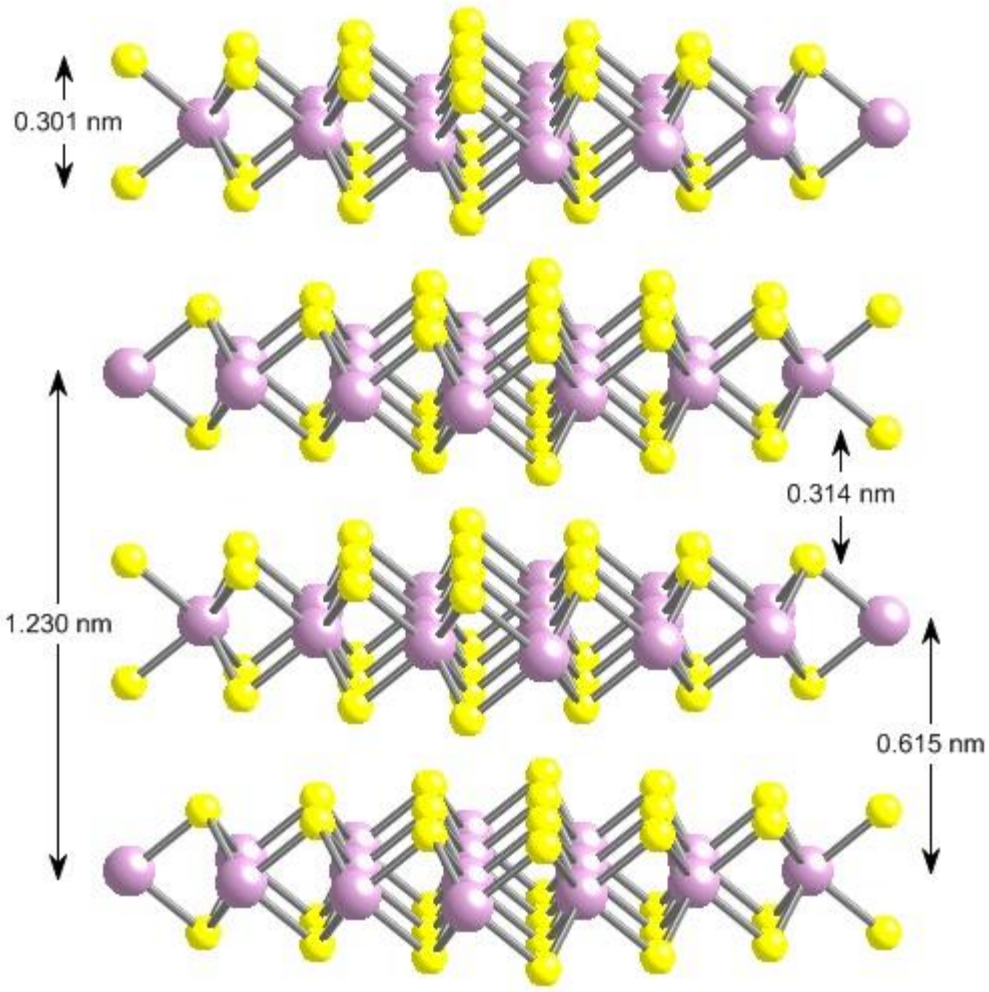

Figure 2-14 Schematic representation of MoS_2 structure. The atoms are bonded by covalent bonds within the layer and van der Waals force between the layers themselves.

2.6.1 Synthesis

Synthesis of individual sheets can be achieved by using similar techniques as that of graphene like scotch® tape method[108], liquid phase exfoliation[109] and electrochemical exfoliation[110]. But CVD synthesis of MoS_2 is slightly different from that of graphene. There are several approaches to synthesis using CVD. A two-step thermolysis process is used in which the first step involves dip coating an inert substrate in ammonia thiomolybdate [$(NH_4)_2MoS_2$] and converting to MoS_2 by annealing at 500 °C. MoS_2 sheets are formed by the following

decomposition reaction $(NH_4)_2MoS_2 + H_2 \rightarrow 2NH_3 + 2H_2S + MoS_2$. In the second step, to improve the crystallinity (or MoS_2 domain size) MoS_2 thin sheets are annealed at 1000 °C in sulfur vapor.[111] Another technique is based on sulfurization of Mo metal thin films. MoS_2 nucleation occurs near chemisorbed sulfur species and then the film is formed by the diffusion of sulfur, which is affected by pressure and temperature.[112] Alternative method involves gas phase reaction of MoO_3 with S powders with the reaction mechanism likely to be $MoO_3 + x/2S \rightarrow MoO_{3-x} + x/2SO_2$ and $MoO_{3-x} + (7-x)2S \rightarrow MoS_2 + (3-x)/2SO_2$. However, full coverage of the substrate is a challenge with this method.[113] Along with these techniques MoS_2 can also be prepared by solvothermal and hydrothermal synthesis techniques. Although these techniques results in high volume of carbon to be present with TMDs embedded in the matrix. Due to this drawback, the most attractive method for MoS_2 exfoliation has been liquid phase exfoliation using sonication technique with a mild solvent.

2.6.2. Application as Battery Electrode

Layered transition metal sulfides have shown to exhibit higher cyclability among all TMDs because of its ability to exfoliate easily during first lithiation. This derives from the weak inter layer attractions between the two facing sulfur layers. Because of this ease of exfoliation it can accommodate Li in a two-step process thus restricting volume expansion to only 103 %. Mo/WS_2 store Li by conversion reaction mechanism as follows:

Equation 2.5

$$\mathbf{MoS_2 + Li^+ + e^- \leftrightarrow Li_2S + Mo}$$

Numerous reports on MoS_2 as anode material for Li ion batteries have been published since 1980 (when it was first introduced as an anode material). Owing to various synthesis

methods employed to develop MoS_2, the morphology and particle size varies significantly. These changes have influenced its electrochemical performance.

Table 2.1 $MoS_2$and MoS_2 composite synthesis methods, morphology and electrochemical performance

Compound and Morphology	Synthesis method	Cycling stability [a]
MoS_2 nanoflowers[114]	Ionic liquid assisted hydrothermal method	439/150/0.1 C
MoS_2 nanoflakes[115]	Rheological phase reaction	840/20/0.04 C
MoS_2 nanoflakes[116]	Hydrothermal method	706/40/0.05 C
Restacked MoS_2[117]	Lithium assisted exfoliation	750/50/0.05 C
MoS_2 nanoplates[118]	Solvothermal method of $Mo(CO)_6$ and S	907/50/1.062 C
MoS_2 dispersed in carbon[119,120]	Hydrothermal method	912/100/0.1 C
Coaxial MoS_2/CNT[121]	Solution phase route	400/50/0.1 C

[a] (Capacity/# of cycles/C-rate)

As seen in Table 2.1, electrochemical property of MoS_2 has been studied thoroughly and many of the drawbacks have been addressed with hierarchical morphology, carbon impergnation and nano-sized particles. Nevertheless, some new challenges have emerged that hinder the introduction of TMD nanosheets for practical applications. These challenges include: (a) high costs due to complex procedures that limit production in large quantities (gram levels or higher), (b) capacity degradation for thick electrodes or the low volumetric capacity of nanostructured/ porous electrode design, (c) low thermodynamic and chemical stability in moisture and degradation reaction with the battery electrolyte at low discharge potentials. Efforts to cost-effectively produce large quantities of TMDs flakes via chemical exfoliation are promising; therefore, a matter of intense research. Furthermore, electrochemical study of MoS_2 in Na-ion battery system has only been intensely perused since early 2014.

2.7 Polymer Derived Ceramics (PDCs)

Polymer derived ceramics as the name suggests is a class of solid ceramic obtained from liquid polymeric precursor. Since it is derived from a liquid polymer, by altering the processing condition and composition of the initial polymeric precursor, final ceramic with desired electrical, thermal, mechanical and electrochemical property can be synthesized. The discussion in this work is limited to polysilazane and polysiloxane precursors, which results in the formation of SiCN and SiOC PDCs, respectively. The process of forming a solid ceramic from a liquid polymer is actually a two-step process. In the first step the liquid polymeric precursor is cross-linked by heating it to ~400 °C in an inert medium. Cross-linking results in increased bonding between the elements of the precursor leading to highly interconnected backbone (Si-N, Si-C, Si-O, etc.), reducing the volatility of the crosslinked product and increasing the ceramic yield. Cross-linking vinyl or silyl functional groups are intentionally added to the polymer precursor for effective cross-linking. Followed by crosslinking, pyrolysis is carried out at 800-1400 °C under inert conditions. During pyrolysis, thermal induced decomposition of cross-linked polymer releases oligomer, hydrocarbons and other volatile compounds and consolidates to amorphous ceramic. More hydrogen is retained at lower processing temperatures (~800 °C). Annealing (beyond 1400°C) results in nucleation and growth of nano-sized crystalline phases in the ceramic. Meanwhile, depending on the polymer chemical structure and composition, precipitation of free sp2 bonded carbon occurs during the polymer to ceramic conversion.

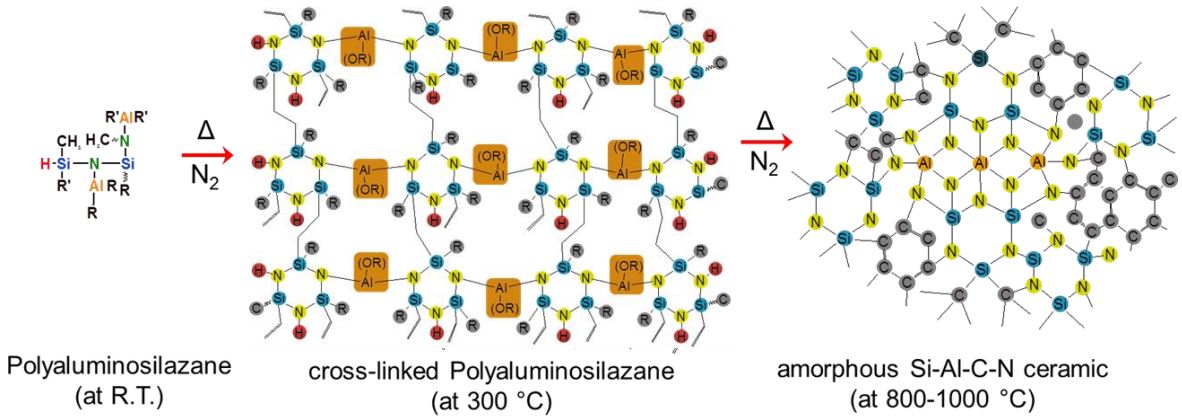

Figure 2-15 Schematic representation of molecular structure of different phases in step wise conversion of liquid polymer to solid ceramic.

Silicon-based amorphous PDC anodes have demonstrated promising results. Recent studies show that PDCs can store lithium reversibly in the voltage range of 0 to 3 V with electrochemical capacities as high as 900 mAh/g with Coulombic efficiencies exceeding 99%.[127] Other advantages include, high thermodynamic stability, open amorphous structure and processing flexibility. While major concerns include their first cycle loss (27 to 50 % depending upon the chemical composition) and voltage hysteresis (0.8 to 1.2 V). It is believed that these issues can be addressed by altering the chemical structure of the starting polymer (and hence the final ceramic), increasing surface area (by inducing porosity, surface etching) or by addition of electrically conducting nano-fillers with favorable chemical composition. Much of the work involving PDC anodes have been performed on polysilazane derived SiCN and polysiloxane derived SiOC systems. The ease of availability and well established processing methods for these PDCs are the main reasons for their popularity. Table 2.2 shows few electrochemical results of PDCs and their composite.

Table 2.2 Summary of the experimental results of the electrochemical cycling of PDC and their nanocomposites.

Compound and Morphology	First reversible capacity (mAh/g)	First cycle loss (%)	Reversible capacity after n cycles
SiOC-800 °C[127]	906	33	700 (60)
SiOC-1000 °C[127]	958	23	650 (60)
SiCN-1000 °C[128]	456	40	171 (30)
SiOC/GNS[129]	357	65	
SiCN/graphite[130]	474	35	440 (50)
SiCN:G[131]	312	24	

2.8. References

1. Whittingham, M. S., Lithium Batteries and Cathode Materials. *Chemical Reviews* **2004,** *104* (10), 4271-4301.

2. Kamali, A. R.; Fray, D. J., Review on Carbon and Silicon Based Materials as Anode Materials for Lithium Ion Batteries. *Journal of New Materials for Electrochemical Systems* **2010,** *13* (2), 147-160.

3. Verma, P.; Maire, P.; Novak, P., A Review of the Features and Analyses of the Solid Electrolyte Interphase in Li-Ion Batteries. *Electrochimica Acta* **2010,** *55* (22), 6332-6341.

4. 57 P. B. Balbuena and Y. Wang, Lithium-Ion Batteries: Solid- Electrolyte Interphase, Imperial College Press, 2004.

5. Xu, K., Nonaqueous Liquid Electrolytes for Lithium-Based Rechargeable Batteries. *Chemical Reviews* **2004,** *104*(10), 4303-4417.

6. Guyomard, D.; Tarascon, J. M., LI Metal-Free Rechargeable $LiMn_2O_4$/Carbon Cells - Their Understanding and Optimization. *Journal of the Electrochemical Society* **1992,** *139* (4), 937-948.

7. Tarascon, J. M.; McKinnon, W. R.; Coowar, F.; Bowmer, T. N.; Amatucci, G.; Guyomard, D., Synthesis Conditions and Oxygen Stoichiometry Effects on Li Insertion Into the Spinel $LiMn_2O_4$. *Journal of the Electrochemical Society* **1994,** *141* (6), 1421-1431.

8. Markovsky, B.; Amalraj, F.; Gottlieb, H. E.; Gofer, Y.; Martha, S. K.; Aurbach, D., On the Electrochemical Behavior of Aluminum Electrodes in Nonaqueous Electrolyte Solutions of Lithium Salts. *Journal of the Electrochemical Society* **2010,** *157* (4), A423-A429.

9. Aurbach, D.; Talyosef, Y.; Markovsky, B.; Markevich, E.; Zinigrad, E.; Asraf, L.; Gnanaraj, J. S.; Kim, H. J., Design of Electrolyte Solutions for Li and Li-ion Batteries: A Review. *Electrochimica Acta* **2004,** *50* (2-3), 247-254.

10. Zhou, G.; Li, F.; Cheng, H.-M., Progress in Flexible Lithium Batteries and Future Prospects. *Energy & Environmental Science* **2014,** *7* (4), 1307-1338.

11. Bloom, I.; Jones, S. A.; Battaglia, V. S.; Henriksen, G. L.; Christophersen, J. P.; Wright, R. B.; Ho, C. D.; Belt, J. R.; Motloch, C. G., Effect of Cathode Composition on Capacity Fade,

Impedance Rise and Power Fade in High-Power, Lithium-Ion Cells. *Journal of Power Sources* **2003,** *124* (2), 538-550.

12. Hu, Y.; Sun, X., Flexible Rechargeable Lithium Ion Batteries: Advances and Challenges in Materials and Process Technologies. *Journal of Materials Chemistry A* **2014,** *2* (28), 10712-10738.

13. Wang, X.; Lu, X.; Liu, B.; Chen, D.; Tong, Y.; Shen, G., Flexible Energy-Storage Devices: Design Consideration and Recent Progress. *Advanced Materials* **2014,** *26* (28), 4763-4782.

14. Xie, K.; Wei, B., Materials and Structures for Stretchable Energy Storage and Conversion Devices. *Advanced Materials* **2014,** *26* (22), 3592-3617.

15. Tarascon, J. M., Key challenges in future Li-battery research. Philosophical Transactions of the Royal Society a-Mathematical Physical and Engineering Sciences **2010,** 368 (1923), 3227-3241.

16. B. Scrosati, in Frontiers of Electrochemistry, Volume 3: Electrochemistry of Novel Materials, ed. J. Lipkowski and P. N. Ross, Wiley-VCH, New York, 1994, ch. 3, pp. 111.

17. M. Armand, in Materials for Advanced Batteries, ed. D. W. Murphy, J. Broadhead and B. C. H. Steele, NATO Conference Series VI: Materials Science, Plenum Press, New York, 1979, vol. 2, pp. 145.

18. Hagenmuller, P., Intercalation Chemistry and Chemical Bonding. *Journal of Power Sources* **2000,** *90* (1), 9-12.

19. Reimers, J. N.; Dahn, J. R., Electrochemical And Insitu X-Ray-Diffraction Studies of Lithium Intercalation in LIXCOO2. *Journal of the Electrochemical Society* **1992,** *139* (8), 2091-2097.

20. Mizushima, K.; Jones, P. C.; Wiseman, P. J.; Goodenough, J. B., Li_XCOO_2-A New Cathode Material for Batteries of High-Energy Density. *Materials Research Bulletin* **1980,** *15* (6), 783-789.

21. R. Yazami, et al. New Trends in Intercalation Compounds for Energy Storage and Conversion: Proceedings of the International Symposium, The Electrochemical Society, vol. 2003, 2003, p. 317.

22. Du Pasquier, A.; Plitz, I.; Menocal, S.; Amatucci, G., A Comparative Study of Li-Ion Battery, Supercapacitor and Nonaqueous Asymmetric Hybrid Devices for Automotive Applications. *Journal of Power Sources* **2003,** *115* (1), 171-178.

23. Dahn, J. R.; Fuller, E. W.; Obrovac, M.; Vonsacken, U., Thermal-Stability of LIXCOO2, LIXNIO2 and LAMBDA-MNO2 and Consequences For The Safety Of Li-Ion Cells. *Solid State Ionics* **1994,** *69* (3-4), 265-270.

24. Rougier, A.; Gravereau, P.; Delmas, C., Optimization of the Composition of the Li1-zNi1+zO2 Electrode Materials: Structural, Magnetic, and Electrochemical Studies. *Journal of the Electrochemical Society* **1996,** *143*(4), 1168-1175.

25. B. Sergio, P. Stefania, Effect Of Cathode Composition on Capacity Fade, Impedance Rise and Power Fade in High-Power, Lithium-Ion Cells. *Journal of Power Sources* **2003,** *124* (2), 538-550.

26. Itou, Y.; Ukyo, Y., Performance of LiNiCoO2 Materials for Advanced Lithium-Ion Batteries. *Journal of Power Sources* **2005,** *146* (1-2), 39-44.

27. Gu, M.; Li, Y.; Li, X.; Hu, S.; Zhang, X.; Xu, W.; Thevuthasan, S.; Baer, D. R.; Zhang, J.-G.; Liu, J.; Wang, C., In Situ TEM Study of Lithiation Behavior of Silicon Nanoparticles Attached to and Embedded in a Carbon Matrix.*Acs Nano* **2012,** *6* (9), 8439-8447.

28. M. Gu, et al. ACS Nano 7 (1) (2012) 760.

29. Rossen, E.; Jones, C. D. W.; Dahn, J. R., Structure and Electrochemistry of $Li_XMnYNi1-YO_2$. *Solid State Ionics* **1992,** *57* (3-4), 311-318.

30. Yabuuchi, N.; Ohzuku, T., Novel Lithium Insertion Material of LiCo1/3Ni1/3Mn1/3O2 for Advanced Lithium-Ion Batteries. *Journal of Power Sources* **2003,** *119*, 171-174.

31. Shaju, K. M.; Bruce, P. G., Macroporous Li(Ni1/3Co1/3Mn1/3)O-2: A High-Power and High-Energy Cathode for Rechargeable Lithium Batteries. *Advanced Materials* **2006,** *18* (17), 2330.

32. Masquelier, C.; Croguennec, L., Polyanionic (Phosphates, Silicates, Sulfates) Frameworks as Electrode Materials for Rechargeable Li (or Na) Batteries. *Chemical Reviews* **2013,** *113* (8), 6552-6591.

33. B. Sergio, P. Stefania, Nanotechnology for Sustainable Energy, vol. 1140, American Chemical Society, (2013), p. 67.

34. Kaskhedikar, N. A.; Maier, J., Lithium Storage ion Carbon Nanostructures. *Advanced Materials* **2009,** *21* (25-26), 2664-2680.

35. [193] M.E. Spahr, in: M. Yoshio, et al. (Eds.), Lithium-Ion Batteries: Science and Technologies, Springer, 2009, pp. 117.

36. Levi, M. D.; Aurbach, D., Diffusion Coefficients Of Lithium Ions During Intercalation into Graphite Derived from the Simultaneous Measurements and Modeling of Electrochemical Impedance and Potentiostatic Intermittent Titration Characteristics Of Thin Graphite Electrodes. *Journal of Physical Chemistry B* **1997,** *101* (23), 4641-4647.

37. Markevich, E.; Levi, M. D.; Aurbach, D., Comparison Between Potentiostatic and Galvanostatic Intermittent Titration Techniques for Determination of Chemical Diffusion Coefficients in Ion-Insertion Electrodes. *Journal of Electroanalytical Chemistry* **2005,** *580* (2), 231-237.

38. Persson, K.; Sethuraman, V. A.; Hardwick, L. J.; Hinuma, Y.; Meng, Y. S.; van der Ven, A.; Srinivasan, V.; Kostecki, R.; Ceder, G., Lithium Diffusion in Graphitic Carbon. *Journal of Physical Chemistry Letters* **2010,** *1* (8), 1176-1180.

39. Billaud, D.; McRae, E.; Herold, A., Synthesis and Electrical-Resistivity of Lithium-Pyrographite Intercalation Compounds (Stage-I, Stage-II And Stage-III). *Materials Research Bulletin* **1979,** *14* (7), 857-864.

40. Qi, Y.; Guo, H.; Hector, L. G., Jr.; Timmons, A., Threefold Increase in the Young's Modulus of Graphite Negative Electrode during Lithium Intercalation. *Journal of the Electrochemical Society* **2010,** *157* (5), A558-A566.

41. Bar-Tow, D.; Peled, E.; Burstein, L., A Study of Highly Oriented Pyrolytic Graphite as A Model For The Graphite Anode In Li-Ion Batteries. *Journal of the Electrochemical Society* **1999,** *146* (3), 824-832.

42. Nozaki, H.; Nagaoka, K.; Hoshi, K.; Ohta, N.; Inagaki, M., Carbon-Coated Graphite for Anode of Lithium Ion Rechargeable Batteries: Carbon Coating Conditions And Precursors. *Journal of Power Sources* **2009,** *194* (1), 486-493.

43. Carbon Powders for Lithium Battery Systems, Timcal Graphite & Carbon, Switzerland, 2005.

44. Winter, M.; Besenhard, J. O.; Spahr, M. E.; Novak, P., Insertion Electrode Materials for Rechargeable Lithium Batteries. *Advanced Materials* **1998,** *10* (10), 725-763.

45. Mukherjee, R.; Thomas, A. V.; Datta, D.; Singh, E.; Li, J.; Eksik, O.; Shenoy, V. B.; Koratkar, N., Defect-Induced Plating of Lithium Metal Within Porous Graphene Networks. *Nature Communications* **2014,** *5*.

46. Dahn, J. R.; Zheng, T.; Liu, Y. H.; Xue, J. S., Mechanisms for Lithium Insertion in Carbonaceous Materials. *Science* **1995,** *270* (5236), 590-593.

47. Yamada, H.; Urata, C.; Higashitamori, S.; Aoyama, Y.; Yamauchi, Y.; Kuroda, K., Critical Roles of Cationic Surfactants in the Preparation of Colloidal Mesostructured Silica Nanoparticles: Control of Mesostructure, Particle Size, and Dispersion. *Acs Applied Materials & Interfaces* **2014,** *6* (5), 3491-3500.

48. Teshima, K.; Inagaki, H.; Tanaka, S.; Yubuta, K.; Hozumi, M.; Kohama, K.; Shishido, T.; Oishi, S., Growth of Well-Developed Li4Ti5O12 Crystals by the Cooling of a Sodium Chloride Flux. *Crystal Growth & Design* **2011,** *11*(10), 4401-4405.

49. D. Doughty, E.P. Rother, Electrochem. Soc. Interface 21 (2) (2012) 35.

50. Scharner, S.; Weppner, W.; Schmid-Beurmann, P., Evidence of Two-Phase Formation Upon Lithium Insertion into the $Li_{1.33}Ti_{1.67}O_4$ Spinel. *Journal of the Electrochemical Society* **1999,** *146* (3), 857-861.

51. Wagemaker, M.; Simon, D. R.; Kelder, E. M.; Schoonman, J.; Ringpfeil, C.; Haake, U.; Luetzenkirchen-Hecht, D.; Frahm, R.; Mulder, F. M., A Kinetic Two-Phase and Equilibrium Solid Solution in Spinel $Li_{4+x}Ti_5O_{12}$. *Advanced Materials* **2006,** *18* (23), 3169-+.

52. Colin, J.-F.; Godbole, V.; Novak, P., In Situ Neutron Diffraction Study Of Li Insertion in Li4Ti5O12.*Electrochemistry Communications* **2010,** *12* (6), 804-807.

53. He, Y.-B.; Li, B.; Liu, M.; Zhang, C.; Lv, W.; Yang, C.; Li, J.; Du, H.; Zhang, B.; Yang, Q.-H.; Kim, J.-K.; Kang, F., Gassing in $Li_4Ti_5O_{12}$-Based Batteries and its Remedy. *Scientific Reports* **2012,** *2*.

54. He, Y.-B.; Liu, M.; Huang, Z.-D.; Zhang, B.; Yu, Y.; Li, B.; Kang, F.; Kim, J.-K., Effect of Solid Electrolyte Interface (SEI) Film on Cyclic Performance Of $Li_4Ti_5O_{12}$ Anodes for Li Ion Batteries. *Journal of Power Sources* **2013,***239*, 269-276.

55. Song, M.-S.; Kim, R.-H.; Baek, S.-W.; Lee, K.-S.; Park, K.; Benayad, A., Is Li4Ti5O12 A Solid-Electrolyte-Interphase-Free Electrode Material in Li-Ion Batteries? Reactivity Between the $Li_4Ti_5O_{12}$ Electrode and Electrolyte. *Journal of Materials Chemistry A* **2014,** *2* (3), 631-636.

56. Wang, J.; Chen-Wiegart, Y.-c. K.; Wang, J., In Situ Three-Dimensional Synchrotron X-Ray Nanotomography of the (De) Lithiation Processes in Tin Anodes**. *Angewandte Chemie-International Edition* **2014,** *53* (17), 4460-4464.

57. Chan, C. K.; Peng, H.; Liu, G.; McIlwrath, K.; Zhang, X. F.; Huggins, R. A.; Cui, Y., High-Performance Lithium Battery Anodes Using Silicon Nanowires. *Nature Nanotechnology* **2008,** *3* (1), 31-35.

58. Oumellal, Y.; Delpuech, N.; Mazouzi, D.; Dupre, N.; Gaubicher, J.; Moreau, P.; Soudan, P.; Lestriez, B.; Guyomard, D., The failure mechanism of nano-sized Si-based negative electrodes for lithium ion batteries. *Journal of Materials Chemistry* **2011,** *21* (17), 6201-6208.

59. Magasinski, A.; Dixon, P.; Hertzberg, B.; Kvit, A.; Ayala, J.; Yushin, G., High-performance lithium-ion anodes using a hierarchical bottom-up approach. *Nature Materials* **2010,** *9* (4), 353-358.

60. Hertzberg, B.; Alexeev, A.; Yushin, G., Deformations in Si-Li Anodes Upon Electrochemical Alloying in Nano-Confined Space. *Journal of the American Chemical Society* **2010,** *132* (25), 8548-+.

61. Wang, B.; Li, X.; Zhang, X.; Luo, B.; Zhang, Y.; Zhi, L., Contact-Engineered and Void-Involved Silicon/Carbon Nanohybrids as Lithium-Ion-Battery Anodes. *Advanced Materials* **2013,** *25* (26), 3560-3565.

62. Liu, N.; Wu, H.; McDowell, M. T.; Yao, Y.; Wang, C.; Cui, Y., A Yolk-Shell Design for Stabilized and Scalable Li-Ion Battery Alloy Anodes. *Nano Letters* **2012,** *12* (6), 3315-3321.

63. Chen, S.; Gordin, M. L.; Yi, R.; Howlett, G.; Sohn, H.; Wang, D., Silicon Core-Hollow Carbon Shell Nanocomposites with Tunable Buffer Voids for High Capacity Anodes of Lithium-Ion Batteries. *Physical Chemistry Chemical Physics* **2012,** *14* (37), 12741-12745.

64. Park, Y.; Choi, N.-S.; Park, S.; Woo, S. H.; Sim, S.; Jang, B. Y.; Oh, S. M.; Park, S.; Cho, J.; Lee, K. T., Si-Encapsulating Hollow Carbon Electrodes via Electroless Etching for Lithium-Ion Batteries. *Advanced Energy Materials* **2013,** *3* (2), 206-212.

65. Tao, H.; Fan, L.-Z.; Song, W.-L.; Wu, M.; He, X.; Qu, X., Hollow Core-Shell Structured Si/C Nanocomposites as High-Performance Anode Materials for Lithium-Ion Batteries. *Nanoscale* **2014,** *6* (6), 3138-3142.

66. Chan, M. K. Y.; Wolverton, C.; Greeley, J. P., First Principles Simulations of the Electrochemical Lithiation and Delithiation of Faceted Crystalline Silicon. *Journal of the American Chemical Society* **2012,** *134* (35), 14362-14374.

67. Xu, L.; Kim, C.; Shukla, A. K.; Dong, A.; Mattox, T. M.; Milliron, D. J.; Cabana, J., Monodisperse Sn Nanocrystals as a Platform for the Study of Mechanical Damage during Electrochemical Reactions with Li. *Nano Letters* **2013,** *13* (4), 1800-1805.

68. Liu, X. H.; Huang, S.; Picraux, S. T.; Li, J.; Zhu, T.; Huang, J. Y., Reversible Nanopore Formation in Ge Nanowires during Lithiation-Delithiation Cycling: An In Situ Transmission Electron Microscopy Study. *Nano Letters***2011,** *11* (9), 3991-3997.

69. Liang, W.; Yang, H.; Fan, F.; Liu, Y.; Liu, X. H.; Huang, J. Y.; Zhu, T.; Zhang, S., Tough Germanium Nanoparticles under Electrochemical Cycling. *Acs Nano* **2013,** *7* (4), 3427-3433.

70. Okamoto, H., Ga-Li (gallium-lithium). *Journal of Phase Equilibria and Diffusion* **2006,** *27* (2), 200-200.

71. Liu, Y.; Hudak, N. S.; Huber, D. L.; Limmer, S. J.; Sullivan, J. P.; Huang, J. Y., In Situ Transmission Electron Microscopy Observation of Pulverization of Aluminum Nanowires and Evolution of the Thin Surface Al_2O_3 Layers during Lithiation-Delithiation Cycles. *Nano Letters* **2011,** *11* (10), 4188-4194.

72. Qian, J.; Qiao, D.; Ai, X.; Cao, Y.; Yang, H., Reversible 3-Li Storage Reactions of Amorphous Phosphorus as High Capacity and Cycling-Stable Anodes for Li-ion Batteries. *Chemical Communications* **2012,** *48* (71), 8931-8933.

73. Darwiche, A.; Marino, C.; Sougrati, M. T.; Fraisse, B.; Stievano, L.; Monconduit, L., Better Cycling Performances of Bulk Sb in Na-Ion Batteries Compared to Li-Ion Systems: An Unexpected Electrochemical Mechanism. *Journal of the American Chemical Society* **2012,** *134* (51), 20805-20811.

74. Whittingham, M. S., Chemistry of Intercalation Compounds - Metal Guests in Chalcogenide Hosts. *Progress in Solid State Chemistry* **1978,** *12* (1), 41-99.

75. Benavente, E.; Santa Ana, M. A.; Mendizabal, F.; Gonzalez, G., Intercalation chemistry of molybdenum disulfide. *Coordination Chemistry Reviews* **2002,** *224* (1-2), 87-109.

76. Delmas, C.; Braconnier, J. J.; Fouassier, C.; Hagenmuller, P., Electrochemical Intercalation Of Sodium In NAXCOO2 Bronzes. *Solid State Ionics* **1981,** *3-4* (AUG), 165-169.

77. Berthelot, R.; Carlier, D.; Delmas, C., Electrochemical investigation of the P2-NaxCoO2 phase diagram. *Nature Materials* **2011,** *10* (1), 74-U3.

78. Bhide, A.; Hariharan, K., Physicochemical properties of NaxCoO2 as a cathode for solid state sodium battery.*Solid State Ionics* **2011,** *192* (1), 360-363.

79. Shu, G. J.; Chou, F. C., Sodium-ion diffusion and ordering in single-crystal P2-Na(x)CoO(2). *Physical Review B***2008,** *78* (5).

80. Barpanda, P.; Chotard, J.-N.; Recham, N.; Delacourt, C.; Ati, M.; Dupont, L.; Armand, M.; Tarascon, J.-M., Structural, Transport, and Electrochemical Investigation of Novel AMSO(4)F (A = Na, Li; M = Fe, Co, Ni, Mn) Metal Fluorosulphates Prepared Using Low Temperature Synthesis Routes. *Inorganic Chemistry* **2010,** *49* (16), 7401-7413.

81. Ellis, B. L.; Makahnouk, W. R. M.; Rowan-Weetaluktuk, W. N.; Ryan, D. H.; Nazar, L. F., Crystal Structure and Electrochemical Properties of A(2)MPO(4)F Fluorophosphates (A = Na, Li; M = Fe, Mn, Co, Ni). *Chemistry of Materials* **2010,** *22* (3), 1059-1070.

82. Tripathi, R.; Ramesh, T. N.; Ellis, B. L.; Nazar, L. F., Scalable Synthesis of Tavorite LiFeSO4F and NaFeSO4F Cathode Materials. *Angewandte Chemie-International Edition* **2010,** *49* (46), 8738-8742.

83. Lu, Z. H.; Dahn, J. R., Understanding the anomalous capacity of Li/Li NixLi(1/3-2x/3)Mn(2/3-x/3 O-2 Cells Using In Situ X-Ray Diffraction and Electrochemical Studies. *Journal of the Electrochemical Society* **2002,** *149* (7), A815-A822.

84. Alcantara, R.; Lavela, P.; Ortiz, G. F.; Tirado, J. L., Carbon Microspheres Obtained From Resorcinol-Formaldehyde as High-Capacity Electrodes for Sodium-Ion Batteries. *Electrochemical and Solid State Letters* **2005,** *8* (4), A222-A225.

85. Stevens, D. A.; Dahn, J. R., High Capacity Anode Materials for Rechargeable Sodium-Ion Batteries. *Journal of the Electrochemical Society* **2000,** *147* (4), 1271-1273.

86. Wenzel, S.; Hara, T.; Janek, J.; Adelhelm, P., Room-Temperature Sodium-Ion Batteries: Improving the Rate Capability of Carbon Anode Materials By Templating Strategies. *Energy & Environmental Science* **2011,** *4* (9), 3342-3345.

87. David, L.; Bhandavat, R.; Singh, G., MoS_2/Graphene Composite Paper for Sodium-Ion Battery Electrodes. *Acs Nano* **2014,** *8* (2), 1759-1770.

88. Chadwick, A. V.; Savin, S. L. P.; Fiddy, S.; Alcantara, R.; Fernandez Lisbona, D.; Lavela, P.; Ortiz, G. F.; Tirado, J. L., Formation and Oxidation Of Nanosized Metal Particles by

Electrochemical Reaction of Li and Na with $NiCo_2O_4$: X-ray Absorption Spectroscopic Study. *Journal of Physical Chemistry C* **2007,** *111* (12), 4636-4642.

89. Kim, T. B.; Choi, J. W.; Ryu, H. S.; Cho, G. B.; Kim, K. W.; Ahn, J. H.; Cho, K. K.; Ahn, H. J., Electrochemical Properties of Sodium/Pyrite Battery at Room Temperature. *Journal of Power Sources* **2007,** *174* (2), 1275-1278.

90. Kim, J.-S.; Cho, G.-B.; Kim, K.-W.; Ahn, J.-H.; Wang, G.; Ahn, H.-J., The Addition of Iron to Ni_3S_2 Electrode For Sodium Secondary Battery. *Current Applied Physics* **2011,** *11* (1), S215-S218.

91. Liu, X.; Kang, S.; Kim, J.; Ahn, H.; Lim, S.; Ahn, I., A Study of Ni_3S_2 Synthesized by Mechanical Alloying for Na/Ni3S2 cell. *Rare Metals* **2011,** *30*, 5-10.

92. Kim, J.-S.; Ahn, H.-J.; Ryu, H.-S.; Kim, D.-J.; Cho, G.-B.; Kim, K.-W.; Nam, T.-H.; Ahn, J. H., The Discharge Properties of Na/Ni3S2 Cell at Ambient Temperature. *Journal of Power Sources* **2008,** *178* (2), 852-856.

93. Novoselov, K. S.; Geim, A. K.; Morozov, S. V.; Jiang, D.; Zhang, Y.; Dubonos, S. V.; Grigorieva, I. V.; Firsov, A. A., Electric Field Effect in Atomically Thin Carbon Films. *Science* **2004,** *306* (5696), 666-669.

94. 10. Warner, J. H., Schäffel, F., Bachmatiuk, A. & Rümmeli, M. H. Graphene: Fundamentals and Emergent Applications Ch. 4 (Elsevier, 2013).

95. Novoselov, K. S.; Fal'ko, V. I.; Colombo, L.; Gellert, P. R.; Schwab, M. G.; Kim, K., A Roadmap for Graphene. *Nature* **2012,** *490* (7419), 192-200.

96. Cai, M.; Thorpe, D.; Adamson, D. H.; Schniepp, H. C., Methods of Graphite Exfoliation. *Journal of Materials Chemistry* **2012,** *22* (48), 24992-25002.

97. 17. Hummers, W. S. Jr & Offeman, R. E. Preparation of Graphitic Oxide. J. Am. Chem. Soc. 80, 1339 (1957).

98. Kovtyukhova, N. I.; Ollivier, P. J.; Martin, B. R.; Mallouk, T. E.; Chizhik, S. A.; Buzaneva, E. V.; Gorchinskiy, A. D., Layer-By-Layer Assembly Of Ultrathin Composite Films From Micron-Sized Graphite Oxide Sheets And Polycations. *Chemistry of Materials* **1999,** *11* (3), 771-778.

99. Dahn, J. R.; Zheng, T.; Liu, Y. H.; Xue, J. S., Mechanisms For Lithium Insertion In Carbonaceous Materials. *Science* **1995,** *270* (5236), 590-593.

100. Liu, Y. H.; Xue, J. S.; Zheng, T.; Dahn, J. R., Mechanism of Lithium Insertion in Hard Carbons Prepared by Pyrolysis of Epoxy Resins. *Carbon* **1996,** *34* (2), 193-200.

101. Winter, M.; Besenhard, J. O.; Spahr, M. E.; Novak, P., Insertion Electrode Materials for Rechargeable Lithium Batteries. *Advanced Materials* **1998,** *10* (10), 725-763.

102. Vargas C, O. A.; Caballero, A.; Morales, J., Can the Performance of Graphene Nanosheets for Lithium Storage in Li-Ion Batteries Be Predicted? *Nanoscale* **2012,** *4* (6), 2083-2092.

103. Wu, Z.-S.; Zhou, G.; Yin, L.-C.; Ren, W.; Li, F.; Cheng, H.-M., Graphene/Metal Oxide Composite Electrode Materials for Energy Storage. *Nano Energy* **2012,** *1* (1), 107-131.

104. Xu, C.; Xu, B.; Gu, Y.; Xiong, Z.; Sun, J.; Zhao, X. S., Graphene-Based Electrodes for Electrochemical Energy Storage. *Energy & Environmental Science* **2013,** *6* (5), 1388-1414.

105. Chhowalla, M.; Shin, H. S.; Eda, G.; Li, L.-J.; Loh, K. P.; Zhang, H., The Chemistry of Two-Dimensional Layered Transition Metal Dichalcogenide Nanosheets. *Nature Chemistry* **2013,** *5* (4), 263-275.

106. Mak, K. F.; Lee, C.; Hone, J.; Shan, J.; Heinz, T. F., Atomically Thin MoS_2: A New Direct-Gap Semiconductor. *Physical Review Letters* **2010,** *105* (13).

107. Splendiani, A.; Sun, L.; Zhang, Y.; Li, T.; Kim, J.; Chim, C.-Y.; Galli, G.; Wang, F., Emerging Photoluminescence in Monolayer MoS_2. *Nano Letters* **2010,** *10* (4), 1271-1275.

108. Zeng, Z.; Sun, T.; Zhu, J.; Huang, X.; Yin, Z.; Lu, G.; Fan, Z.; Yan, Q.; Hng, H. H.; Zhang, H., An Effective Method for the Fabrication of Few-Layer-Thick Inorganic Nanosheets. *Angewandte Chemie-International Edition***2012,** *51* (36), 9052-9056.

109. Hernandez, Y.; Nicolosi, V.; Lotya, M.; Blighe, F. M.; Sun, Z.; De, S.; McGovern, I. T.; Holland, B.; Byrne, M.; Gun'ko, Y. K.; Boland, J. J.; Niraj, P.; Duesberg, G.; Krishnamurthy, S.; Goodhue, R.; Hutchison, J.; Scardaci, V.; Ferrari, A. C.; Coleman, J. N., High-Yield Production of Graphene by Liquid-Phase Exfoliation of Graphite. *Nature Nanotechnology* **2008,** *3* (9), 563-568.

110. Joensen, P.; Frindt, R. F.; Morrison, S. R., Single-Layer MoS_2. *Materials Research Bulletin* **1986,** *21* (4), 457-461.

111. Liu, K.-K.; Zhang, W.; Lee, Y.-H.; Lin, Y.-C.; Chang, M.-T.; Su, C.; Chang, C.-S.; Li, H.; Shi, Y.; Zhang, H.; Lai, C.-S.; Li, L.-J., Growth of Large-Area and Highly Crystalline MoS_2 Thin Layers on Insulating Substrates. *Nano Letters* **2012,** *12* (3), 1538-1544.

112. Zhan, Y.; Liu, Z.; Najmaei, S.; Ajayan, P. M.; Lou, J., Large-Area Vapor-Phase Growth and Characterization of MoS_2 Atomic Layers on a SiO2 Substrate. *Small* **2012,** *8* (7), 966-971.

113. Lee, Y.-H.; Zhang, X.-Q.; Zhang, W.; Chang, M.-T.; Lin, C.-T.; Chang, K.-D.; Yu, Y.-C.; Wang, J. T.-W.; Chang, C.-S.; Li, L.-J.; Lin, T.-W., Synthesis of Large-Area MoS_2 Atomic Layers with Chemical Vapor Deposition.*Advanced Materials* **2012,** *24* (17), 2320-2325.

114. Li, H.; Li, W.; Ma, L.; Chen, W.; Wang, J., Electrochemical Lithiation/Delithiation Performances of 3D Flowerlike MoS_2 Powders Prepared by Ionic Liquid Assisted Hydrothermal Route. *Journal of Alloys and Compounds* **2009,** *471*(1-2), 442-447.

115. Feng, C.; Ma, J.; Li, H.; Zeng, R.; Guo, Z.; Liu, H., Synthesis of Molybdenum Disulfide (MoS_2) for Lithium Ion Battery Applications. *Materials Research Bulletin* **2009,** *44* (9), 1811-1815.

116. Wang, S.; Li, G.; Du, G.; Jiang, X.; Feng, C.; Guo, Z.; Kim, S.-J., Hydrothermal Synthesis of Molybdenum Disulfide for Lithium Ion Battery Applications. *Chinese Journal of Chemical Engineering* **2010,** *18* (6), 910-913.

117. Du, G.; Guo, Z.; Wang, S.; Zeng, R.; Chen, Z.; Liu, H., Superior Stability and High Capacity of Restacked Molybdenum Disulfide as Anode Material for Lithium Ion Batteries. *Chemical Communications* **2010,** *46* (7), 1106-1108.

118. Hwang, H.; Kim, H.; Cho, J., MoS_2 Nanoplates Consisting of Disordered Graphene-like Layers for High Rate Lithium Battery Anode Materials. *Nano Letters* **2011,** *11* (11), 4826-4830.

119. Li, H.; Ma, L.; Chen, W.-x.; Wang, J.-m., Synthesis of MoS_2/C Nanocomposites by Hydrothermal Route Used as Li-Ion Intercalation Electrode Materials. *Materials Letters* **2009,** *63* (15), 1363-1365.

120. Chang, K.; Chen, W.; Ma, L.; Li, H.; Li, H.; Huang, F.; Xu, Z.; Zhang, Q.; Lee, J.-Y., Graphene-like MoS_2/Amorphous Carbon Composites With High Capacity and Excellent Stability as Anode Materials for Lithium Ion Batteries. *Journal of Materials Chemistry* **2011,** *21* (17), 6251-6257.

121. Wang, Q.; Li, J., Facilitated Lithium Storage in MoS_2 Overlayers Supported on Coaxial Carbon Nanotubes. *Journal of Physical Chemistry C* **2007,** *111* (4), 1675-1682.

122. Yu, D. Y. W.; Prikhodchenko, P. V.; Mason, C. W.; Batabyal, S. K.; Gun, J.; Sladkevich, S.; Medvedev, A. G.; Lev, O., High-Capacity Antimony Sulphide Nanoparticle-Decorated Graphene Composite as Anode for Sodium-Ion Batteries. *Nature Communications* **2013,** *4*.

123. Prikhodchenko, P. V.; Yu, D. Y. W.; Batabyal, S. K.; Uvarov, V.; Gun, J.; Sladkevich, S.; Mikhaylov, A. A.; Medvedev, A. G.; Lev, O., Nanocrystalline Tin Disulfide Coating of Reduced Graphene Oxide Produced by the Peroxostannate Deposition Route For Sodium Ion Battery Anodes. *Journal of Materials Chemistry A* **2014,** *2* (22), 8431-8437.

124. Nithya, C.; Gopukumar, S., rGO/Nano Sb Composite: A High Performance Anode Material for Na+ Ion Batteries and Evidence for the Formation of Nanoribbons From the Nano rGO Sheet During Galvanostatic Cycling. *Journal of Materials Chemistry A* **2014,** *2* (27), 10516-10525.

125. Qin, W.; Yu, W.; Zi, W.; Liu, X.; Yuan, T.; Yang, D.; Wang, S.; Tu, G.; Zhang, J.; Liu, F. S.; Li, C., High Efficiency Organic/A-Si Hybrid Tandem Solar Cells with Complementary Light Absorption. *Journal of Materials Chemistry A* **2014,** *2* (37), 15303-15307.

126. Qu, B.; Ma, C.; Ji, G.; Xu, C.; Xu, J.; Meng, Y. S.; Wang, T.; Lee, J. Y., Layered SnS2-Reduced Graphene Oxide Composite - A High-Capacity, High-Rate, and Long-Cycle Life Sodium-Ion Battery Anode Material. *Advanced Materials* **2014,** *26* (23), 3854-3859.

127. Xing, W.B. Wilson, A.M. Eguchi, KZank, G. Dahn, J.R. "Pyrolyzed Polysiloxanes for use as Anode Materials in Lithium-Ion Batteries." *Journal of Electrochemical Society,* **1997**, *144*, 2410-2416.

128. Fukui, H. Ohsuka, H. Hino, T. Kanamura, K. "Polysilane/Acenaphthylene Blends Toward Si-O-C Composite Anodes for Rechargeable Lithium-Ion Batteries." *Journal of Electrochemical Society*, **2011,** *158*, A550-A555.

129. Feng, Y. "Electrochemical Properties of Heat-Treated Polymer-Derived SiCN Anode for Lithium Ion Batteries." *Electrochimica Acta,* **2010,** *55*, 5860-5866.

130. Kim, T. Mo, Y.H. Nahm, K.S. Oh, S.M. "Carbon nanotubes (CNTs) as a Buffer Layer In Silicon/CNTs Composite Electrodes for Lithium Secondary Batteries." *Journal of Power Sources,* **2006,** *162*, 1275-1281.

131. Landi, B.J. Dileo, R.A. Schauerman, C.M. Cress, C.D. Ganter, M.J. Raffaelle, R.P. "Multi-Walled Carbon Nanotube Paper Anodes for Lithium Ion Batteries." *Journal of Nanoscience and Nanotechnology*, **2009**, *9*, 3406-3410.

Chapter 3 - Reduced Graphene Oxide Paper Electrode[1]

3.1. Abstract

We study long-term electrochemical sodium and lithium cycling, and tensile testing behavior of thermally reduced graphene oxide (rGO) paper electrodes. We find strong dependence of annealing temperature and gas environment on the electrical conductivity, electrochemical capacity, and rate capability of the electrodes. The effect, however, was opposing for the two cell types. Lithium charge capacity increased with increasing annealing temperatures reaching a stable value of ~325 $mAh.g_{anode}^{-1}$ (~100 $mAh.cm^{-3}_{anode}$ at ~48 $\mu A.cm^{-2}$ with respect to total volume of the electrode) for specimen annealed at 900 °C. While a sharp decline in Na charge capacity was noted for rGO annealed above 500 °C. Maximum sodium charge capacity of ~140 $mAh.g^{-1}_{anode}$ at 100 $mA.g^{-1}_{anode}$ (~98 $mAh.cm_{anode}^{-3}$ at ~70 $\mu A.cm^{-2}$) was realized for specimen reduced at 500 °C. These values are the highest reported for GO paper electrodes. More important, annealing of GO in NH_3 environment resulted in a complete shutdown of its Na-ion cyclability showing near zero charge capacity. On the contrary, NH_3 annealing only improved the electrode's Li-ion cycling efficiency and rate capability. This behavior is attributed to the increased level of ordering in graphene sheets and decreased interlayer spacing with increasing annealing temperatures in Ar or reduction at moderate temperatures in NH_3 atmosphere. Further, uni-axial tensile tests and videography highlighted the superior elasticity and high strain to failure of crumpled paper electrodes. The present work provides new insights toward the optimization and design of Li and other larger metal-ion battery

[1] Reprinted with permission from (L. David, and G. Singh, "Reduced Graphene Oxide Paper Electrode: Opposing Effect of Thermal Annealing on Li and Na Cyclability" Journal Physical Chemistry C, **118**, 49, 28401 - 28408). Copyright (2015) American Chemical Society.

electrodes where graphene is utilized as an active material, conductive agent or a flexible mechanical support.

3.2. Introduction

Increasing demand for small size, lightweight, high capacity, and safer electrical energy storage system has pushed researchers into exploring new electrode materials and rechargeable batteries. Along with Advanced Li-ion batteries (a-LIB), Li-sulfur (Li-S) and Na-ion batteries (NIB) are at the forefront.[1-7] However, for practical applications, traditional Li-ion battery technology (developed in 1990s) continues to dominate primarily because of its high operating potential, long shelf life, and relatively simple design. [8, 9] Research into newer battery systems has been mainly motivated by two major shortcomings in traditional LIB; one is the limited electrochemical capacity of the graphite negative electrode, which has already reached its theoretical gravimetric capacity of approximately 372 $mAh.g^{-1}$ and is therefore unable to meet future energy needs. And second is the high cost and limited availability of Li in earth's crust, which may not be able to satisfy increased demand in the years to come. [10, 11] Sodium-based batteries have been proposed as an alternative to LIBs since Na resources are practically inexhaustible and the chemistry is largely similar which may allow easy transition to a Na-based system, at least for stationary storage applications.

Consequently, new electrode materials that can offer high gravimetric capacity at high C-rates for longer durations (for example, more than 1000 cycles) with cycling efficiency comparable to graphite are under investigation. [12-17] One of which is reduced graphene oxide (or rGO); structural defects on rGO's surface lead to enhanced Li adsorption, resulting in much higher gravimetric capacity than traditional graphite anode. [18-41] In addition, rGO can be conveniently prepared in the form of a flexible and electrically conducting paper there-by

opening-up opportunities for making batteries/supercapacitors that can power rolling-up and wearable electronics. [42-49] Yet, research on sodiation mechanisms in GO and other graphene-derivatives have largely been non-existent, primarily because traditional graphite, which is a precursor for GO, is not amenable to insertion by sodium ions. [50] Then again, it is believed that rGO with its large number of surface defects, increased interlayer spacings, and high surface area may exhibit high Na capacity through mechanisms other than the classical staged intercalation of Li/graphite system. There have already been reports where rGO was utilized as conducting agent or an elastic support to improve Na-ion cyclability of NIB anodes. [51, 52]

Along these lines, we study the sodiation/desodiation and lithiation/delithiation mechanisms in rGO paper electrodes as function of interlayer spacing and/ or defect density modulated by varying the GO annealing temperature and gas environment. Further, the effect of annealing temperature on fracture strength and strain to failure of the crumpled paper electrode is also evaluated. Two main observations are as follows: (i) Li charge capacity of the electrode increased with increasing thermal reduction temperature, reaching first cycle charge capacity of 364 $mAh.g^{-1}_{anode}$ (total electrode weight) at 900 °C, which is one of the highest reported for paper electrodes prepare by similar techniques. (ii) Na charge capacity was near zero (~13 $mAh.g^{-1}_{anode}$) for GO annealed at 900°C in Ar and 500 °C in NH_3. While the highest stable Na capacity (~140 $mAh.g^{-1}_{anode}$) was realized for specimen annealed at 500 °C in Ar.

To the best of our knowledge the long-term electrochemical behavior of 'neat' graphene oxide paper electrodes reduced at varying temperatures, as NIB anode has not been reported so far. Unlike other rGO-based multi-component electrodes on copper foils, specimen here were prepared without any external-conducting agents (such as carbon black), insulating polymeric binders (such as PVDF or PVA), or the copper current collector substrates.[19, 20, 25, 34, 37] The

electrodes were therefore self-supporting and capture the 'true' performance of graphene/Li and graphene/Na cells without any parasitic or side reactions. Such paper-based electrodes are in demand because of their high flexibility (even higher than conventional metal foils), lightweight (due to elimination of Li or Na inactive phases), and high surface area etc.[36-44]

3.3. Experimental Section

3.3.1. Materials and Instrumentation

Sodium nitrate (99.2%), potassium permanganate (99.4%), sulfuric acid (96.4%), hydrogen peroxide (31.3% solution in water), hydrochloric acid (30% solution in water), methanol (99.9%) were purchased from Fisher Scientific. All materials were used as received without further purification.

Scanning electron microscopy (SEM) of the synthesized material was carried out on a Carl Zeiss EVO MA10 system with incident voltage of 5 kV - 30 kV. TEM images were digitally acquired by use of a Phillips CM100 operated at 100 kV. Material characterization was made using an X-ray diffractometer (XRD) operating at room temperature with nickel-filtered Cu Kα radiation (λ = 1.5418 Å). Raman spectra were measured using a LabRAM ARMIS Raman spectrometer using 633 nm laser excitation (laser power of 17 mW) as the light source. Electrical conductivity measurements were carried out by use of a four-point probe setup and Keithley 2636A (Cleveland, OH) dual channel sourcemeter in the Ohmic region. The surface chemical composition was studied by X-ray photoelectron spectroscopy (XPS, PHI Quantera SXM) using monochromatic Al Kα X-radiation. Static uniaxial in-plane tensile tests were conducted in a simple test setup. The sample strip is secured on one end by a computer-controlled movable stage (M-111.2DG from PI), while the other end is fixed to a 1 N load cell (ULC-1N Interface), which in turn is fixed to an immovable stage. All tensile tests were conducted in controlled strain

rate mode with a strain rate of 0.2% min^{-1}. The samples were cut with a razor into rectangular strips of approximately 5 x 15 mm^2 for testing without further modification. Electrochemical cycling of the assembled cells was carried out using multichannel battery test equipment (Arbin-BT2000, Austin, TX) at atmospheric conditions.

3.3.2. Preparation of graphene oxide

Modified Hummer's method was used to make graphene oxide.[53, 54] Concentrated H_2SO_4 (130 mL) was added to a mixture of graphite flakes (3 g) and $NaNO_3$ (1.5 g). The mixture was cooled down using an ice bath. $KMnO_4$ was added slowly to this mixture. The mixture was stirred for 12 h at 50 °C. Then it was quenched with water (400 mL) with 30% H_2O_2 (3 mL) while in an ice bath such that the temperature does not go beyond 20°C. The remaining material was then washed in succession with 200 mL of water twice, 200 mL of 30% HCl and 200 mL of ethanol. The material remaining after these extended washes was filtered through a paper filter. The filtrate was dried overnight to obtain dry graphene oxide (GO).

3.3.3. Preparation of free-standing paper

10 mL colloidal suspension of GO in 1:1 (v/v) water was made by sonication for 10 minutes. The suspension was filtered through a 10 μm polycarbonate membrane under vaccum. Filtrate in the form of free-standing paper was carefully separated from the filter membrane and dried. This dry paper then underwent reduction by heat treatment in a tube furnace at various temperatures ranging from 300 to 900 °C under high purity Ar or NH_3 for 2 h. The thermal reduction process results in conversion of GO to rGO. The reduced paper was then punched into small circles and used as working electrode for LIB and NIB half-cells. The loading was approxmately 0.75 $mg.cm^{-2}$.

3.3.4. Coin Cell Assembly

Half-cell batteries were made by punching 14.3 mm diameter out of the paper for use as working electrode. A few drops of electrolyte solution of 1 M $LiPF_6$ (Alfa Aesar) dissolved in (1:1 v/v) dimethyl carbonate: ethylene carbonate (ionic conductivity 10.7 $mS.cm^{-1}$) was used. A glass separator (19 mm diameter), soaked in electrolyte was placed between the working electrode and pure lithium metal (14.3 mm diameter), which acted as a counter electrode. Washer, spring and a top casing were placed on top to complete the assembly before crimping. The whole procedure was carried out in an Ar-filled glovebox.

Electrochemical performance of the assembled coin cells was tested using a multichannel BT2000 Arbin test unit sweeping between 2.5 V - 10 mV vs Li/Li^+ (or Na/Na^+) using following cycle schedule: (a) Asymmteric mode: Li (or Na) was inserted at 100 $mA.g^{-1}_{anode}$ (w.r.t. total electrode weight), while the extraction was performed at increasing current densities of 100, 200, 400, 800, 1600, and 2400 mAg^{-1}_{anode} for 5 cycles each, and returning back to 100 $mA.g^{-1}_{anode}$ for the next 10 cycles. (b) Symmetric mode: Later, all the cells were subjected to symmetric cycling at a current density of 1600 $mA.g^{-1}_{anode}$ for up to 1000 cycles, returning back to 100 $mA.g^{-1}_{anode}$ for the last 50 cycles. 500rGO was further tested in NIB cell using symmetric cycling at 20, 30, 40, 50, 80, 100, 200 and 20 mA g^{-1}_{anode} for every 2 cycles followed a constant 100 mA g^{-1}_{anode} for 1000 cycles.

3.4. Results And Discussion

3.4.1 Chemical and Structural Analysis

Chemical characterization GO (prepared by Hummer's method[53]) thermally annealed at various temperatures is presented in Figure 3.1.

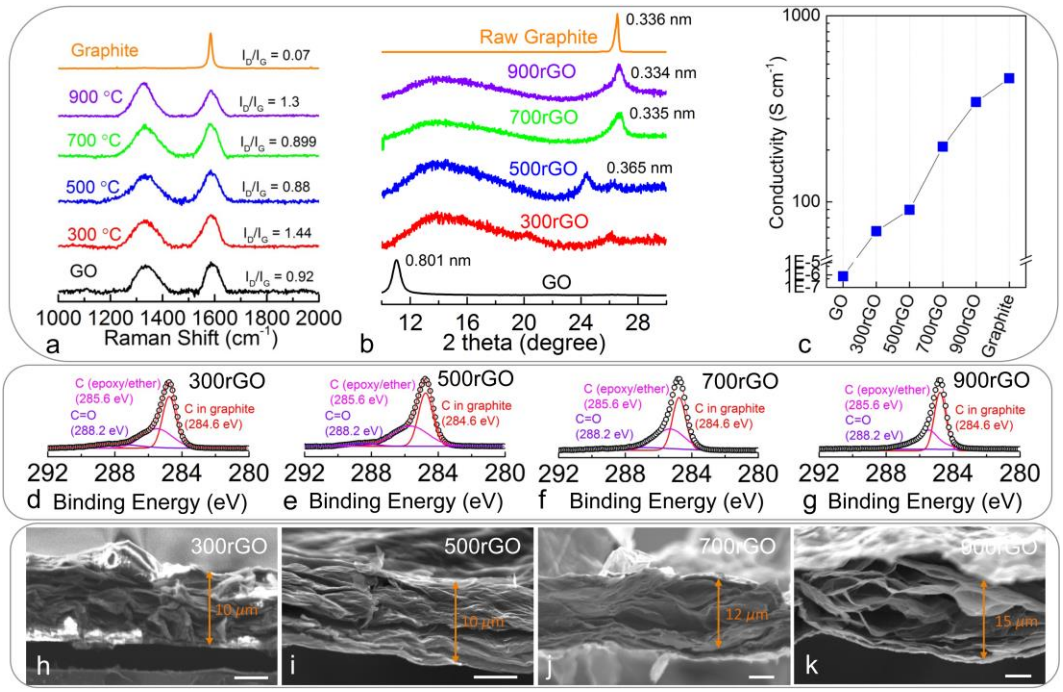

Figure 3-1 Material characterization. (a) Raman, (b) XRD, and (c) Electrical conductivity data of free-standing rGO papers. Data for GO paper and graphite powder is included for comparison purposes. High-resolution XPS of C1s peak corresponding to (d) 300rGO, (e) 500rGO, (f) 700rGO and (g) 900rGO. SEM cross-sectional images of (h) 300rGO, (i) 500rGO, (j) 700rGO and (k) 900rGO show the morphology of the paper. Average paper thickness was observed to be ~ (10 - 15) µm. Scale bar is 5 µm.

Successful oxidation of graphite to GO, and subsequent reduction to rGO was confirmed by Raman, X-ray diffraction (XRD) and XPS techniques. The Raman spectrum in Figure 3.1a showed the typical G-peak along with the emergence of D-peak in GO and rGO papers. No appreciable change was observed in the peak position as a function of annealing temperature. Subsequent characterization involved XRD (Figure 3.1b) which showed significant increase in interlayer spacing between graphite with its characteristic peak at 26.55 ° 2θ (d-spacing ~3.4 Å) and GO at 11 ° 2θ (d-spacing~8.01 Å) owing to the heavy functionalization. [54, 55] Due to removal

of O-groups during thermal reduction, the interlayer spacing of rGO shifted closer and closer to that of graphite. [56-58] Peak broadening was also observed, which suggests large distribution of graphene interlayer spaces in the paper. Further characterization involved measurement of the electrical conductivity (Figure 3.1c) by use of a four-point technique. For the 300rGO specimen, the conductivity was considerably higher than GO paper, almost 8 orders of magnitude higher. The conductivity of the papers annealed at higher temperatures gradually approached that of graphite powder with 900rGO paper showing approximately 344 $S.cm^{-1}$. Further chemical analysis of thermally reduced GO was conducted by XPS of the C 1s peak, which is shown in Figure 3.1(d-g). The intensity of the C=O peak decreased while concurrently graphitic carbon and epoxy/ether carbon peak became narrower with increasing annealing temperature. [55, 59, 60] Synonymously, the percentage of oxygen (O 1s) decreased from 15.41 atom % - 10.71 atom % as the annealing temperature was raised from 300 °C - 900 °C. The scanning electron microscopy (SEM) cross-sectional images of the free-standing papers (Figure 3.1(h-k)) showed more open and disordered structure as a result of annealing at elevated temperatures. This is attributed to the structural changes that occur as more and more O-groups are removed leaving behind a defective graphitic plane. This increased unevenness of individual graphene sheets made the papers look fluffier with thickness increasing from 10 μm for 300rGO to 15 μm for 900rGO.

3.4.2. Initial Electrochemical Analysis

Once the morphology and composition of the rGO papers was established, their electrochemical charge/discharge characteristics were studied as working electrode in Li and Na-ion half-cells.

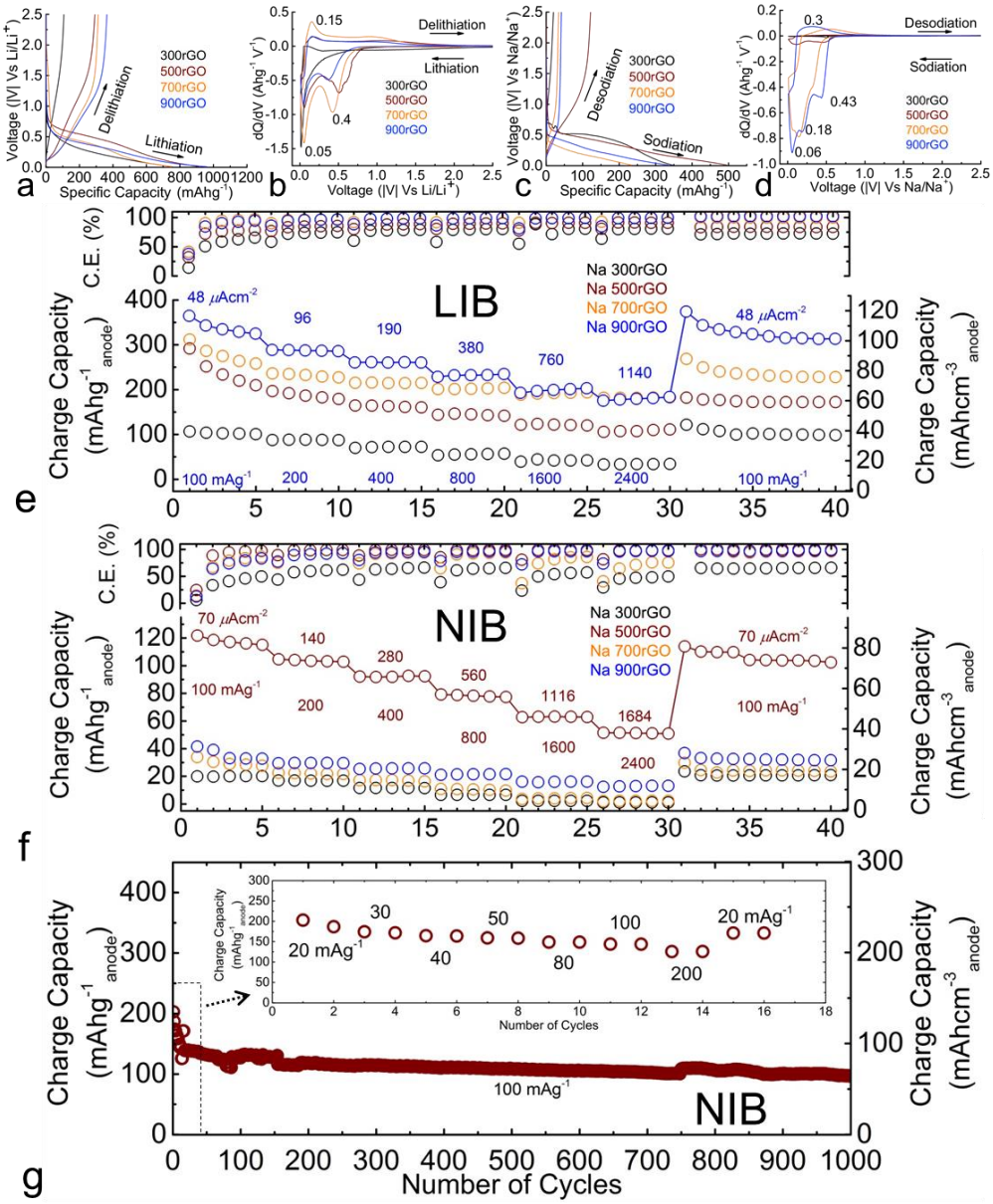

Figure 3-2 Electrochemical characterization. Comparison of first cycle charge/discharge and differential capacity curves of 300rGO, 500rGO, 700rGO and 900rGO papers cycled in (a, b) Li-ion and (c, d) Na-ion battery half-cell at 100 mA g-1anode. (e) Li charge capacity and corresponding columbic efficiency of various rGO electrodes asymmetrically cycled at varying current densities. (f) Na charge capacity and corresponding columbic efficiency of various rGO anodes asymmetrically cycled at varying current densities. (g) Na

charge capacity data for long-term symmetric cycling of 500rGO anode when cycled initially at lower current densities (see inset). Current densities and capacities are normalized w.r.t. total electrode weight and total electrode volume.

Figure 3.2(a and b) shows the voltage charge/discharge profile and corresponding differential capacity curves of the electrodes tested in Li half-cell. When cycled at 100 mA g^{-1}_{anode} for the first five cycles, 900rGO had the highest charge capacity of 364 mAh g^{-1}_{anode} followed by 700rGO, 500rGO and 300rGO at 312, 292 and 104 mAh g^{-1}_{anode}, respectively. These values are higher than previously reported graphene paper electrodes prepared under similar conditions.[42, 44, 46, 61] From the differential capacity curve it is observed that all electrodes had a major cathodic peak at 50 mV and a anodic peak at ~200 mV, which are attributed to Li-ion insertion and extraction in the graphitic structure, respectively. Another cathodic peak, which is characteristic to solid electrolyte interface (SEI) formation, was observed at 550 mV for 300rGO. This peak gradually shifted to 350 mV for the 900rGO specimen. This is because annealing at higher temperatures causes individual graphene layers to get closer and perhaps more ordered in a structure similar to that of graphite (see XRD data), which has been known to form SEI in LIBs at lower discharge potentials.[62]

Na half-cell voltage discharge profiles were substantially different than LIB. As shown in Figure 3.2c, when cycled at a current density of 100 mA g^{-1}_{anode} against Na/Na^{+}, 500rGO had the highest charge capacity of 122 mAh g^{-1}_{anode}. Surprisingly, all other cells had much lower charge capacity at 20, 34 and 41 mAh g^{-1}_{anode} for 300rGO, 700rGO, and 900rGO electrodes, respectively. Differential capacity curve (Figure 3.2d) showed two cathodic (insertion) peaks at ~120 and 500 mV and one anodic (extraction) peak ~100 mV.

3.4.3. Long-Term Electrochemical Analysis

In case of LIB half-cell (Figure 3.2e), 900rGO maintained a charge capacity of 324 mA g^{-1}_{anode} (90% capacity retention) while 700 and 500rGO retained approximately 83 and 72 % of their initial charge capacities, respectively. With increasing current density of 2.4 A g^{-1}_{anode}, the charge capacity of 900rGO dropped down to the same level as 700rGO at 180 mAh g^{-1}_{anode}. However, the cell reverted back to higher capacity once it was cycled back to a current density of 100 mA g^{-1}_{anode}. Later, the electrodes were subjected to symmetric cycling at a current density of 1.6 A g^{-1}_{anode} (Figure 3.3a). Under these conditions, the 900rGO was the best performing cell with a stable charge capacity of 72 mAh g^{-1}_{anode}. Which reverted to its original first cycle charge capacity of 327 mAh g^{-1}_{anode} when cycled back at 100 mA g^{-1}_{anode}. On the other hand, the 300rGO electrode had practically no charge capacity at 1.6 A g^{-1}_{anode} and the cell had fickle performance at 100 mA g^{-1}_{anode}, indicating that the anode structural integrity was compromised.

Rate capability data for Na half-cell is presented in Figure 3.2f. 500rGO had the best performance with a charge capacity of ~115 mAh g^{-1}_{anode} (95% of first cycle capacity) after 5 cycles. The cell remained fairly stable with a charge capacity of 52 mAh g^{-1}_{anode} even at extremely high current density of 2.4 A g^{-1}_{anode}. And when cycled back at 100 mA g^{-1}_{anode}, it recovered to a stable charge capacity at ~110 mA g^{-1}_{anode}, which is 98% of its initial capacity. 500rGO had a relatively high charge capacity even when cycled symmetrically at 1.6 A g^{-1}_{anode} (Figure 3.3b). Impressively, when the cell was reverted to cycling at 100 mA g^{-1}_{anode}, the charge capacity recovered to its initial value and the cell performance was stable thereafter for another 50 cycles.

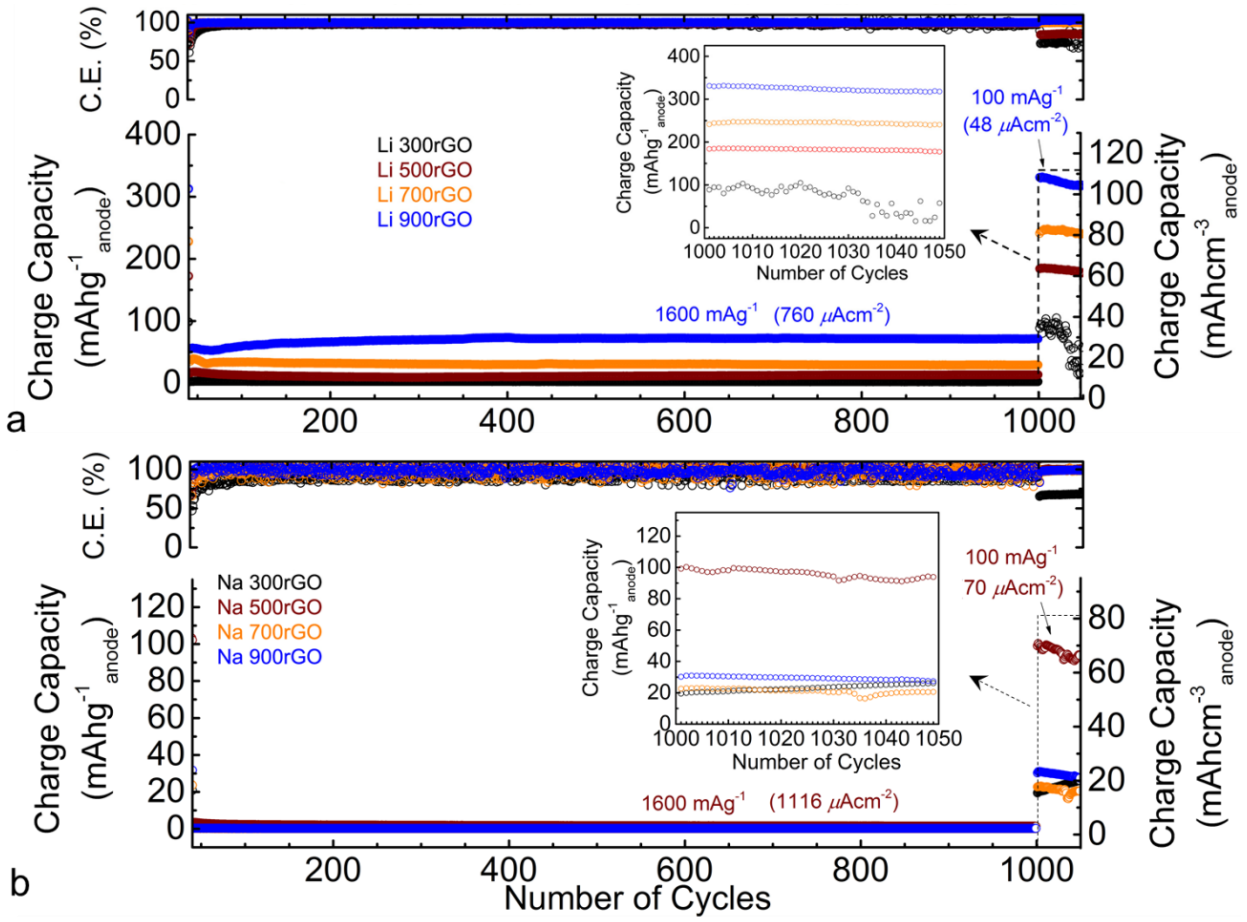

Figure 3-3 Long-term electrochemical cycling data for various rGO electrodes (a) LIB and (b) NIB. All the anodes were cycled at 1600 mA g-1 anode for 1000 cycles.

In an another experiment (see inset in Figure 3.2g), the 500rGO anode was initially cycled at even lower current density (20, 30, 40, 50, 80, 100, 200 and 20 mA g^{-1}_{anode} for every 2 cycles, followed by 100 mA g^{-1}_{anode} for 1000 cycles). This cell performed incredibly well demonstrating ~200 mAh g^{-1}_{anode} charge capacity at 20 mA g^{-1}_{anode} and remained largely stable for up to 1000 cycles at 100 mA g^{-1}_{anode}. We believe that initial cycling at low current density provided an opportunity for stable SEI formation leading to stable and higher charge capacity with extended cycling at 100 mA g^{-1}_{anode}. This electrode showed better rate capability than recently reported rGO electrode (on copper foil) (Figure 3.4).[19]

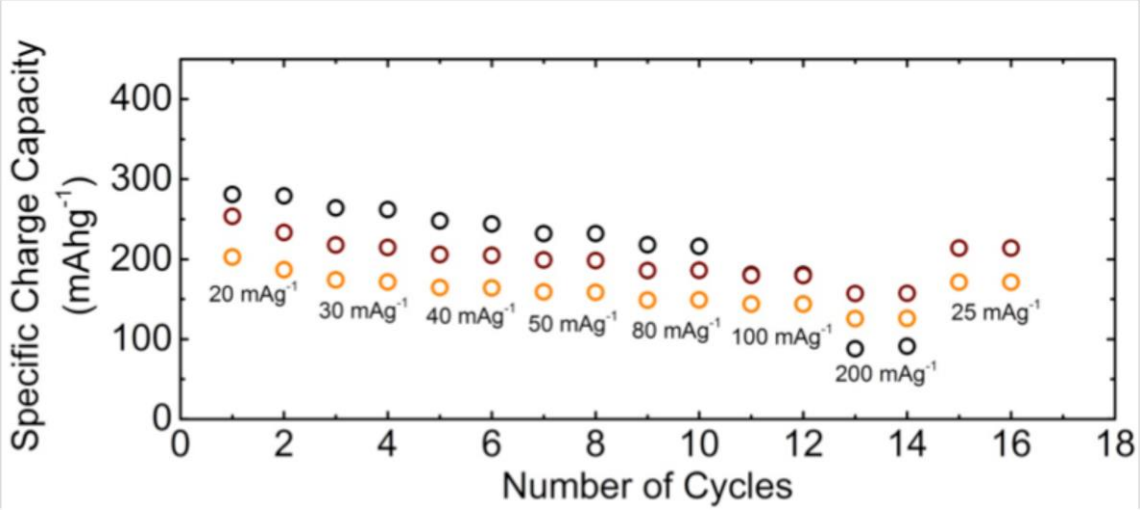

Figure 3-4 Comparison of NIB electrochemical cycling data for 500rGO paper (shown by brown color) with expanded graphite anode (on copper foil) from the literature (Black: capacity with respect to active weight and Yellow: capacity normalized with respect to the film weight, data reproduced from Wen et al.[19]).

Based on the performance of all electrodes cycled in Li half-cell, the increase in charge or reversible capacity with increasing thermal reduction temperature is attributed to: (a) observed decrease in percentage of oxygen functional groups present in GO and increased degree of crystallization of rGO as shown in Figure 3.5 and (b) resulting improvement in electrical conductivity of the composite paper (Figure 3.1c). However, for electrodes cycled in Na half-cell, the charge capacity decreased with increasing annealing temperature for specimens reduced at 700 and 900 °C. This could again be attributed to that fact that Na insertion capacity of ordered graphite is negligible.[63] A slight decrease in Coulombic efficiency was also observed for these specimens. While the higher charge capacity of 500rGO over 300rGO electrode is attributed to its improved conductivity and less defective structure that allowed faster and efficient Na-ion extraction from the expanded graphene layers.

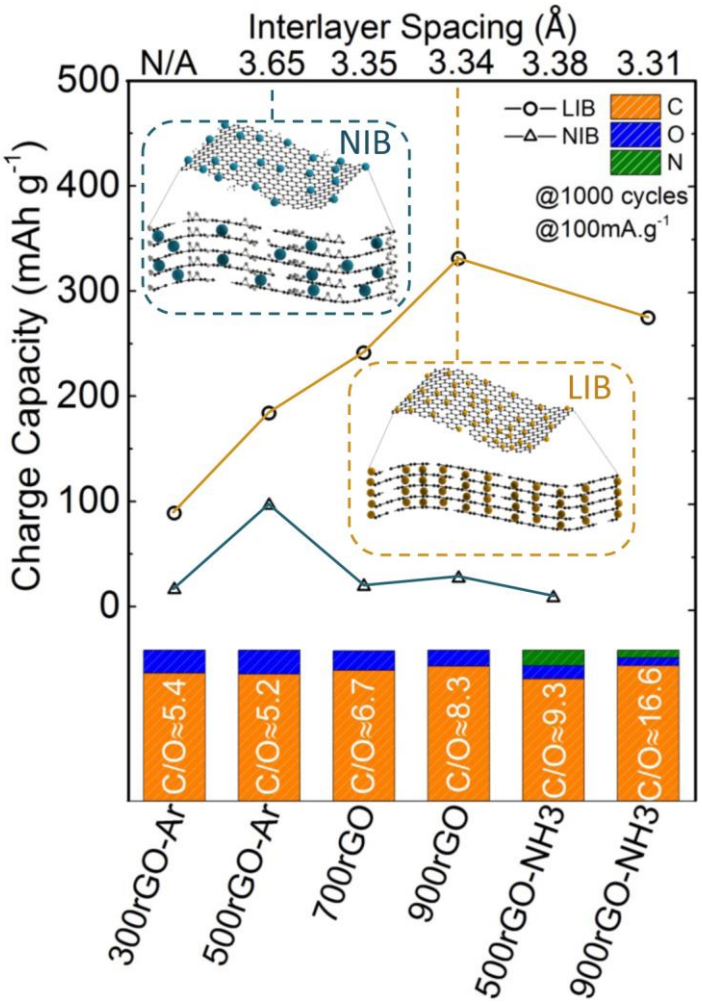

Figure 3-5 Comparison of 1000th cycle charge capacity data for Li and Na half-cells presented as a function of electrode annealing temperature and C/O ratio.

In order to further substantiate these observations we decided to anneal the specimen in ammonia (NH_3) atmosphere, rather than Ar. Reduction of GO in NH_3 have been known to simultaneously reduce GO to rGO, bring more order to its structure [64, 65], and improve electrical conductivity due to N-doping.[65, 66] Only the best performing electrodes i.e., 900 rGO (Li) and 500 rGO (Na) were selected for these experiments. The XRD plot showing improved order of graphene in rGO, electrical conductivity data showing improvement due to N-doping, and cycling data are presented in Figures 3.6a, 3.6b, and 3.7, respectively. Here again we make two

very important observations: (a) Li charge capacity for 900 rGO/NH_3 did not improve. However, its Li rate capability was astoundingly high, the electrode delivered a straight-line performance (~200 $mAh.g^{-1}_{anode}$ at 2400 $mA.g^{-1}_{anode}$), and (b) Na charge capacity for 500 rGO/NH_3 was a complete shut-down (~13 $mAh.g^{-1}_{anode}$). These observations further show that high Na-ion charge capacity can only be realized in moderately disordered or expanded rGO sheets while electrical conductivity only affects the rate capability of the paper electrode.

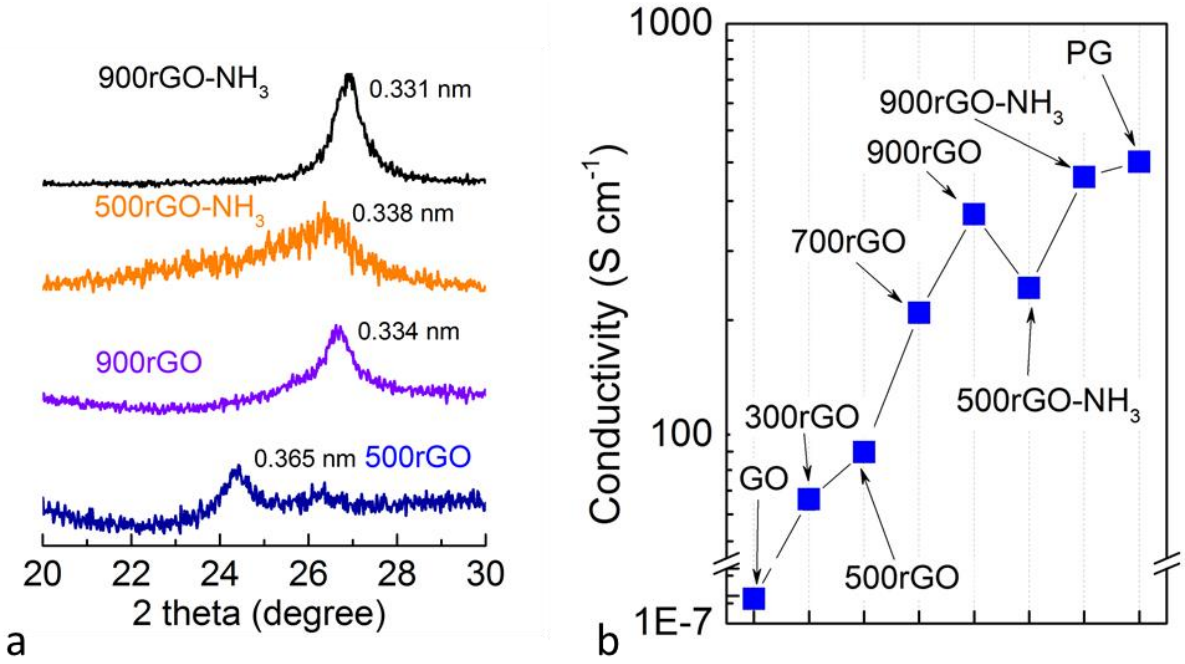

Figure 3-6 (a) XRD data comparing ammonia reduced GO with argon reduced GO for annealing time of 2 h. Decreased interlayer spacing in NH3 over Ar reduction is clearly seen. (b) Four-point electrical conductivity of various rGO specimens prepared in this study. Ammonia-reduced specimens have higher electrical conductivity than argon-reduced specimens.

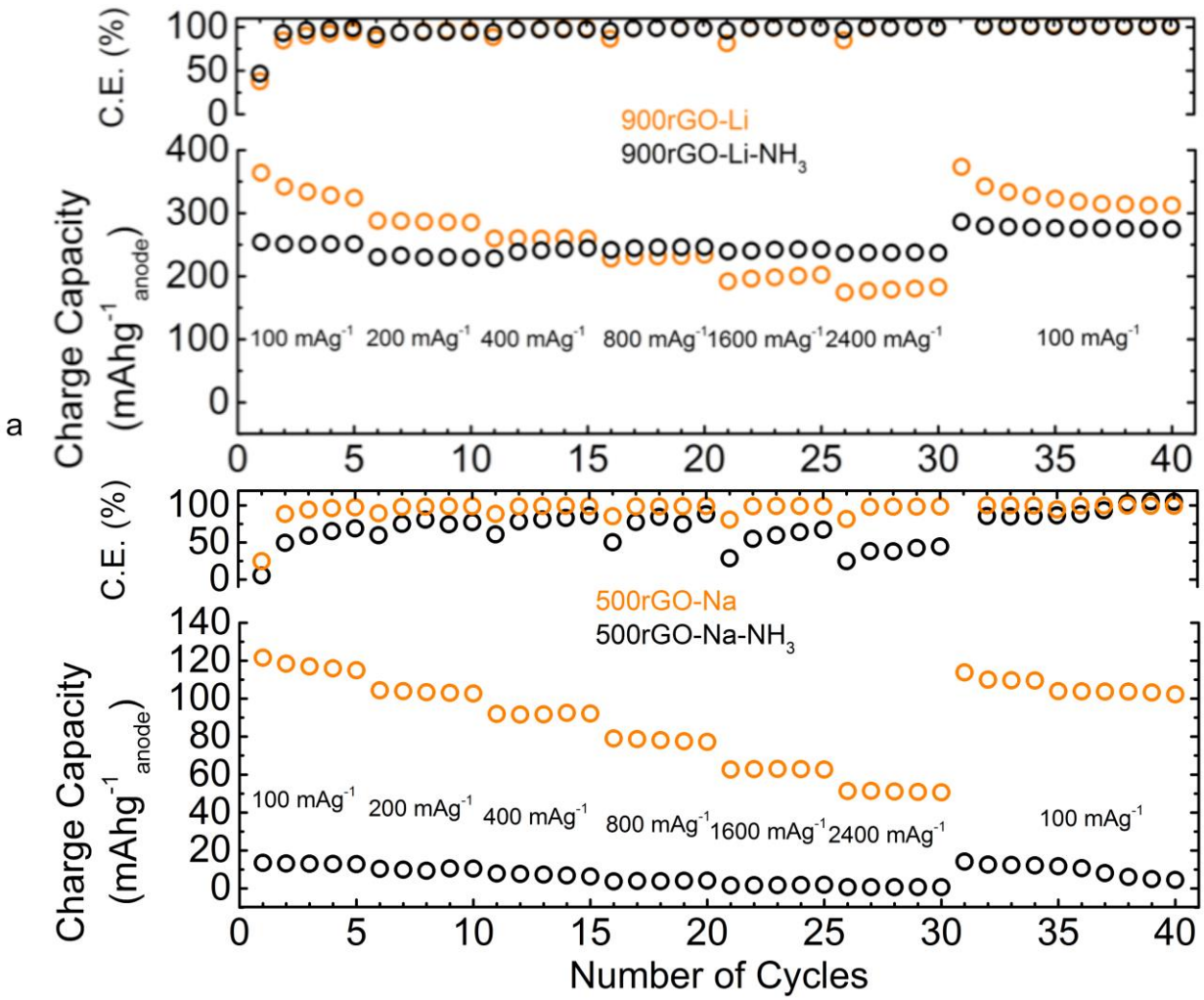

Figure 3-7 Figure 3.8 Electrochemical cycling data (Rate capability test) for (a) LIB and (b) NIB rGO half-cells: argon-annealed rGO compared with corresponding ammonia-annealed electrodes.

3.4.4. Post-Electrochemical Analysis

Later, the cells were disassembled in lithiated or sodiated state to study the electrode's morphology and chemical structure.

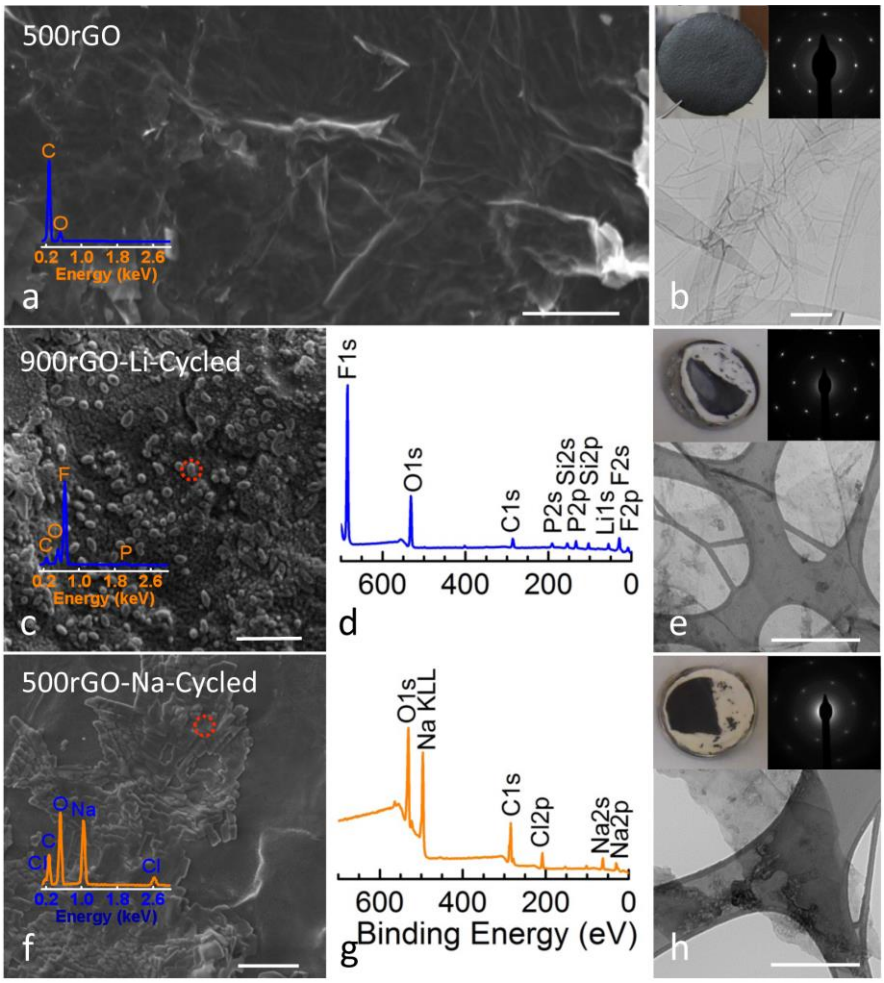

Figure 3-8 Post Electrochemical cycling data. (a) SEM and (b) TEM image of GO reduced at 500 °C. (c) SEM image, (d) XPS and (e) TEM image of dissembled 900rGO electrode from LIB. (f) SEM image, (g) XPS and (h) only half the paper electrode is shown, the other half was dispersed in EC/DMC solution for preparing TEM specimens). Cells were dissembled after 1050 cycles. The scale bar in (a,c,f) is 5 µm and (b,e,h) is 500 nm.

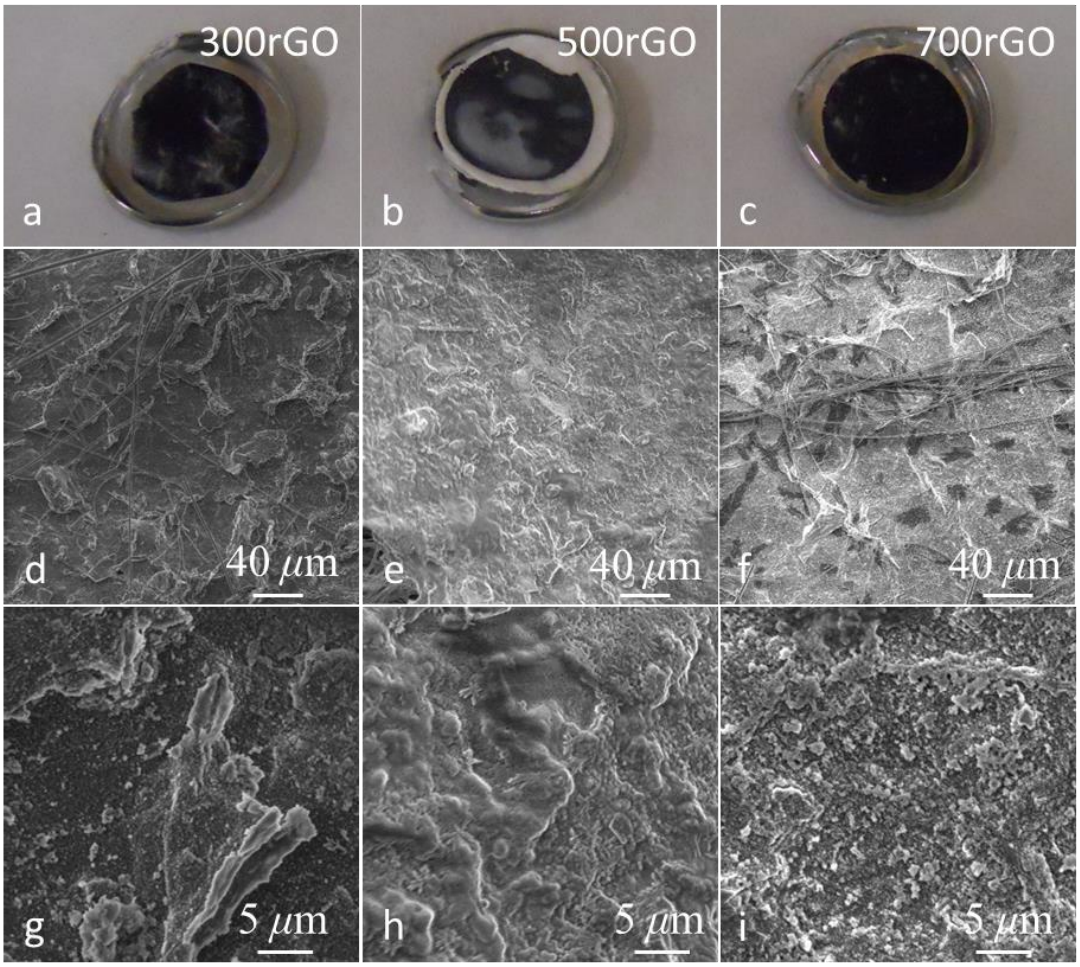

Figure 3-9Post Electrochemical cycling data for LIB electrodes. Digital camera image of (a) 300rGO, (b) 500rGO and (c) 700rGO free-standing anodes after cycling in a Li half-cell. (d through i) are the corresponding SEM images. Cells were dissembled in their lithiated state after 1050 cycles.

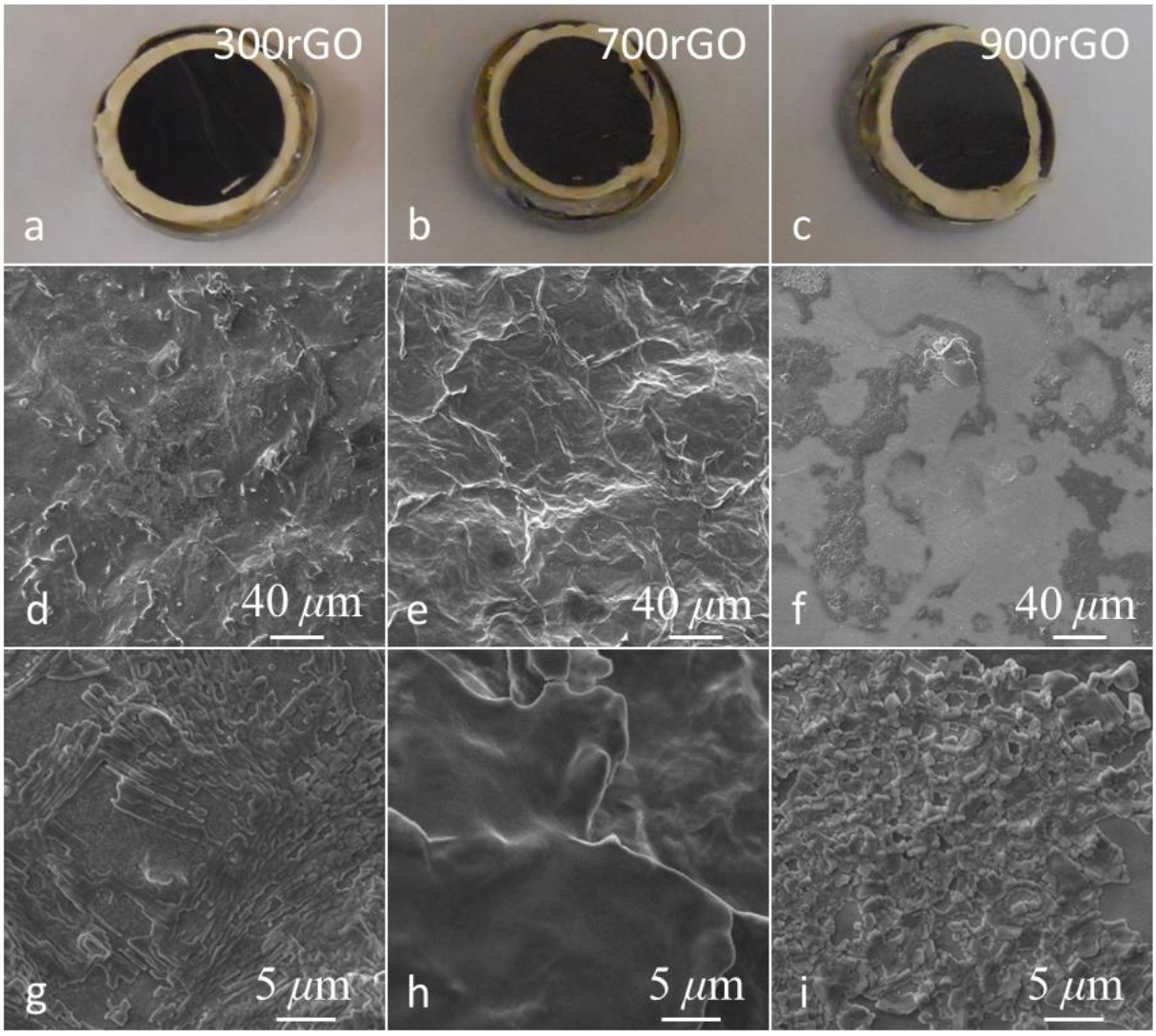

Figure 3-10 Post Electrochemical cycling data for NIB electrodes. Digital camera image of (a) 300rGO, (b) 700rGO and (c) 900rGO free-standing anodes after cycling in a Na half-cell. (d through i), are the corresponding SEM images. Cells were dissembled in their sodiated state after 1050 cycles.

Post-cycling analysis of best performing electrodes (i.e., 900rGO-Li and 500rGO-Na) is presented in Figure 3.8 (a through h). Data for other electrodes is included in Figures 3.9 and 3.10. Remarkably, all electrode specimens looked intact with no visible large or micro surface cracks. Further, a stable SEI layer formation and the presence of glass fiber separator residue

could be observed. A comparison of high-resolution SEM (Figure 3.8 a, c, f) and TEM (Figure 3.8 b, e, h) images of cycled electrodes highlighted some very distinct differences. In case of Li cycled electrode, the SEI had formed in the shape of circular balls but for Na cycled electrodes, layering with pine tree like features and nano-flower like features were observed similar to recently reported Na/MoO_3 electrodes.[67] Further analysis was conducted using EDX and XPS techniques. EDX spectra in Figure 3.8 (c) show that the structures observed in cycled 900rGO-Li were largely composed of C (8.04 atom %), O (11.04 atom %), F (78.47 atom %) and P (2.45 atom %). While SEI film in 500rGO-Na (Figure 3.8f) was composed of C (31.4 atom %), O (38.3 atom %), Na (19.52 atom %) and Cl (10.78 atom %). XPS survey spectra in Figure 3.8 (d, g) further corroborated these observations.

3.4.5. Mechanical Characterization

Lastly, since elevated temperature annealing has been known to affect the mechanical properties of GO papers, we performed static tensile testing of papers to ascertain their fracture strength and strain to failure (see methods). Engineering stress-strain plots derived from load displacement curves and digital images at various stages of specimen loading are presented in Figure 3.11 (a through c). Both the fracture strength and corresponding strain to failure decreased for specimens prepared at increasing annealing temperatures. The papers annealed at 700 and 900 were considerably more brittle than those annealed at 500 °C. The fracture strength was observed to be almost an order of magnitude lower than those reported for rGO papers prepared by chemical reduction at room temperatures.[68-70] Whereas the failure strain in our experiments was observed to almost 2 to 3 times higher than highly ordered well-packed rGO paper prepared at room or slightly higher temperatures. The decrease in strength for specimens annealed at higher temperatures is attributed to the structural damage and introduction of vacancies and other

topological defects in the platelets resulting from the release of gaseous components under high pressures.[70]

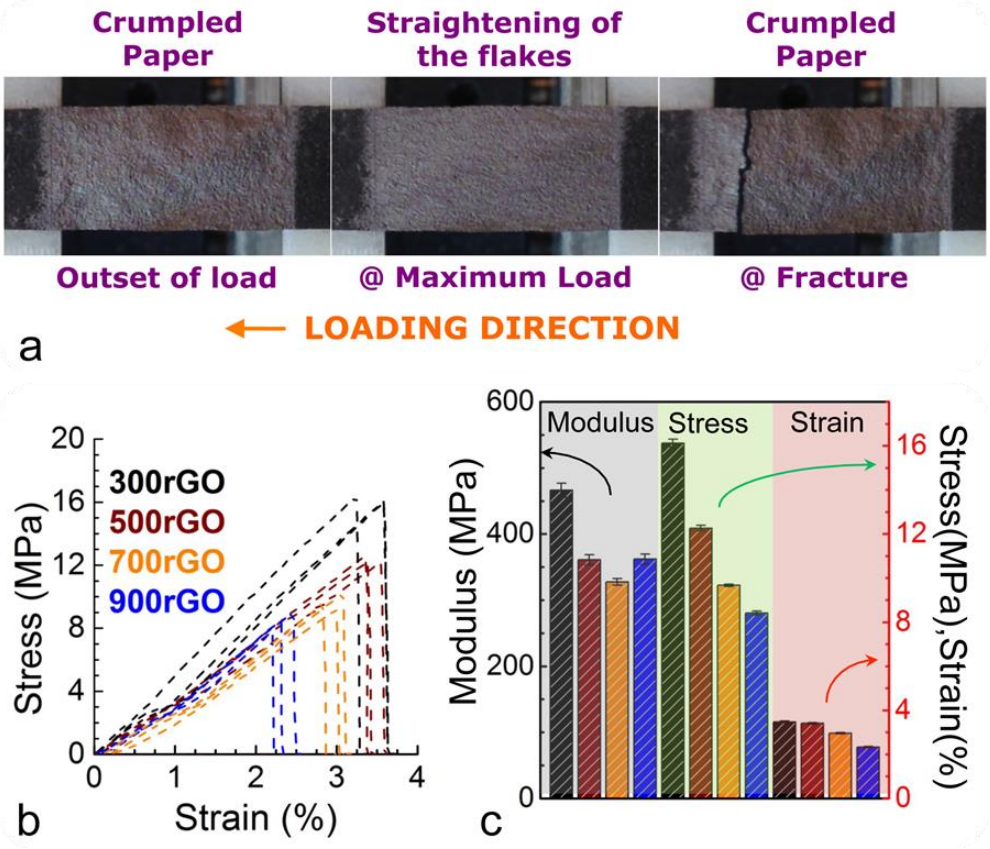

Figure 3-11 Mechanical testing data. (a) Digital camera images at various stages of the loading. (b) Engineering stress-strain plots of 300rGO, 500rGO, 700rGO and 900rGO papers, and (c) bar chart representing the calculated mean of their modulus, failure stress, and failure strain. This behavior is better captured in the media file (see Supporting Information Media File for 700rGO specimen as it fractures with a bang).

The high strain to failure (as high as 3%), observed in all specimens is most likely due to the highly crumpled structure of the paper that allowed considerable straightening and unfolding of the platelets upon application of the tensile load (Figure 3.11a).

3.5. Conclusion

In conclusion, an opposing effect of thermal annealing and reduction atmosphere was observed on the electrochemical Na and Li cycling of reduced graphene oxide paper electrodes. Li charge capacity increased with increasing thermal reduction temperature of the GO, reaching a maximum stable value of ~325 $mAh.g^{-1}_{anode}$ (~100 $mAh.cm^{-3}_{anode}$ w.r.t. total volume of the electrode at a current density of ~48 $\mu A.cm^{-2}$) at 900 °C. The Na charge capacity was highest for specimen annealed at 500 °C in Ar, reaching 140 $mAh.g_{anode}^{-1}$ (~98 $mAh.cm^{-3}_{anode}$ at ~70 $\mu A.cm^{-2}$) and equaling the volumetric capacity of the Li-ion rGO anode. Negligible Na charge capacity was noted for specimens annealed in NH_3 and 900 °C in Ar. These observations are a direct result of the changing nature of ordering in graphene layers in the paper electrodes i.e., increasing order and decreased interlayer spacing caused complete shutdown of sodium's cyclability in the electrode. Our results show that thermal annealing is an important tool in tailoring of electrochemical metal-ion storage and mechanical properties of chemically modified graphenes. Further, the potential of rGO in nanostructured electrodes for Li-ion and other larger metal-ion battery electrodes is highlighted.

3.6. Acknowledgements

Some portion of this research is based on work supported by the National Science Foundation-Chemical, Bioengineering, Environmental, and Transport Systems Division (CBET) under grant no. 1335862 to G. Singh. We thank Professors Scott Bunch (Boston University) and Vivek Shenoy (U. Penn) for useful discussions related to graphene. G. Singh thanks Professor Yury Gogotsi (Drexel University) for reading the manuscript and providing valuable insights. Thanks are also due to Professor Prashant Kamat (University of Notre Dame) for his comments.

3.7. References

1. Dunn, B.; Kamath, H.; Tarascon, J. M. Electrical Energy Storage for the Grid: A Battery of Choices. Science 2011, 334, 928-935.

2. Dahn, J. R.; Zheng, T.; Liu, Y. H.; Xue, J. S. Mechanisms for Lithium Insertion in Carbonaceous Materials. Science 1995, 270, 590-593.

3. David, L.; Bhandavat, R.; Singh, G. MoS_2/Graphene Composite Paper for Sodium-Ion Battery Electrodes. ACS Nano 2014, 8, 1759-1770.

4. Simon, P.; Gogotsi, Y.; Dunn, B. Where do Batteries End and Supercapacitors Begin? Science 2014, 343, 1210–1211.

5. Farbod, B.; Cui, K.; Kalisvaart, W. P.; Kupsta, M.; Zahiri, B.; Kohandehghan, A.; Memarzadeh, E.; Li, Z.; Luber, E. J.; Mitlin, D. Anodes for Sodium Ion Batteries Based on Tin-Germanium-Antimony Alloys ACS Nano 2014, 8, 4415–4429.

6. Bhandavat, R.; David, L.; Singh, G. Synthesis of Surface-Functionalized WS_2 Nanosheets and Performance as Li-Ion Battery Anodes. J. Phys. Chem. Lett. 2012, 3, 1523-1530.

7. Bhandavat, R.; Singh, G. Stable and Efficient Li-Ion Battery Anodes Prepared from Polymer-Derived Silicon Oxycarbide-Carbon Nanotube Shell/Core Composites. J. Phys. Chem. C 2013, 117, 11899-11905.

8. Armand, M.; Tarascon, J. M. Building Better Batteries. Nature 2008, 451, 652-657.

9. Tarascon, J. M.; Armand, M. Issues and Challenges Facing Rechargeable Lithium Batteries. Nature 2001, 414, 359-367.

10. Kim, S. W.; Seo, D. H.; Ma, X.; Ceder, G.; Kang, K. Electrode Materials for Rechargeable Sodium-Ion Batteries: Potential Alternatives to Current Lithium-Ion Batteries. Adv. Energy Mater. 2012, 2, 710-721.

11. Cao, Y.; Xiao, L.; Wang, W.; Choi, D.; Nie, Z.; Yu, J.; Saraf, L. V.; Yang, Z.; Liu, J. Reversible Sodium Ion Insertion in Single Crystalline Manganese Oxide Nanowires with Long Cycle Life. Adv. Mater. 2011, 23, 3155.

12. Cui, L.-F.; Hu, L.; Choi, J. W.; Cui, Y. Light-Weight Free-Standing Carbon Nanotube-Silicon Films for Anodes of Lithium Ion Batteries. ACS Nano 2010,4, 3671-3678.

13. Luo, J.; Zhao, X.; Wu, J.; Jang, H. D.; Kung, H. H.; Huang, J. Crumpled Graphene-Encapsulated Si Nanoparticles for Lithium Ion Battery Anodes. J. Phys. Chem. Lett. 2012, 3, 1824-1829.

14. Cui, L.-F.; Yang, Y.; Hsu, C. M.; Cui, Y. Carbon-Silicon Core-Shell Nanowires as High Capacity Electrode for Lithium Ion Batteries. Nano Lett. 2009, 9, 3370-3374.

15. Hwang, T. H.; Lee, Y. M.; Kong, B.-S.; Seo, J.-S.; Choi, J. W. Electrospun Core-Shell Fibers for Robust Silicon Nanoparticle-Based Lithium Ion Battery Anodes. Nano Lett. 2012, 12, 802-807.

16. Magasinski, A.; Dixon, P.; Hertzberg, B.; Kvit, A.; Ayala, J.; Yushin, G. High-Performance Lithium-Ion Anodes Using a Hierarchical Bottom-Up Approach. Nat. Mater. 2010, 9, 353-358.

17. Hertzberg, B.; Alexeev, A.; Yushin, G. Deformations in Si-Li Anodes upon Electrochemical Alloying in Nano-Confined Space. J. Am. Chem. Soc. 2010, 132, 8548.

18. Wan, L.; Ren, Z.; Wang, H.; Wang, G.; Tong, X.; Gao, S.; Bai, J. Graphene Nanosheets Based on Controlled Exfoliation Process for Enhanced Lithium Storage in Lithium-Ion Battery. Diamond Relat. Mater. 2011, 20, 756-761.

19. Wen, Y.; He, K.; Zhu, Y.; Han, F.; Xu, Y.; Matsuda, I.; Ishii, Y.; Cumings, J.; Wang, C. Expanded Graphite as Superior Anode for Sodium-Ion Batteries. Nat. Commun. 2014, 5.

20. Wu, Z.-S.; Ren, W.; Xu, L.; Li, F.; Cheng, H.-M. Doped Graphene Sheets As Anode Materials with Superhigh Rate and Large Capacity for Lithium Ion Batteries. ACS Nano 2011, 5, 5463-5471.

21. Balbuena, P.; Wang, Y. Lithium-ion Batteries: Solid-Electrolyte Interphase. Imperial College Press: London, UK, 2004.

22. Divincenzo, D. P.; Mele, E. J. Cohesion and Structure in Stage-1 Graphite-Intercalation Compounds. Phys. Rev. B 1985, 32, 2538-2553.

23. Maiti, A. Application of Carbon Nanotubes as Electromechanical Sensors - Results from First-Principles Simulations. Phys. Status Solidi B-Basic Res. 2001, 226, 87-93.

24. Yoo, E.; Kim, J.; Hosono, E.; Zhou, H. S.; Kudo, T.; Honma, I. Large Reversible Li Storage of Graphene Nanosheet Families for Use in Rechargeable Lithium Ion Batteries. Nano Lett. 2008, 8, 2277-2282.

25. Wang, Y-X.; Chou, S-L.; Liu, H-K.; Dou, S-X. Reduced Graphene Oxide with Superior Cycling Stability and Rate Capability for Sodium Storage. Carbon, 2013, 57, 202-208.

26. Zhou, L.-J.; Hou, Z. F.; Wu, L.-M. First-Principles Study of Lithium Adsorption and Diffusion on Graphene with Point Defects. J. Phys. Chem. C 2012, 116, 21780-21787.

27. Liu, Y.; Artyukhov, V. I.; Liu, M.; Harutyunyan, A. R.; Yakobson, B. I. Feasibility of Lithium Storage on Graphene and Its Derivatives. J. Phys. Chem. Lett. 2013, 4, 1737-1742.

28. Park, M.; Zhang, X.; Chung, M.; Less, G. B.; Sastry, A. M. A Review of Conduction Phenomena in Li-Ion Batteries. J. Power Sources 2010,195, 7904-7929.

29. Park, C.-M.; Kim, J.-H.; Kim, H.; Sohn, H.-J. Li-Alloy Based Anode Materials for Li Secondary Batteries. Chem. Soc. Rev. 2010, 39, 3115-3141.

30. Xu, K. Electrolytes and Interphasial Chemistry in Li Ion Devices. Energies 2010, 3, 135-154.

31. Goodenough, J. B.; Kim, Y. Challenges for Rechargeable Li Batteries. Chem. Mater. 2010, 22, 587-603.

32. Landi, B. J.; Ganter, M. J.; Cress, C. D.; DiLeo, R. A.; Raffaelle, R. P. Carbon Nanotubes for Lithium Ion Batteries. Energy Environ. Sci. 2009, 2, 638-654.

33. Manthiram, A.; Murugan, A. V.; Sarkar, A.; Muraliganth, T. Nanostructured Electrode Materials for Electrochemical Energy Storage and Conversion. Energy Environ. Sci. 2008, 1, 621-638.

34. Wang, G.; Shen, X.; Yao, J.; Park, J. Graphene Nanosheets for Enhanced Lithium Storage in Lithium Ion Batteries. Carbon 2009, 47, 2049-2053.

35. Vinayan, B. P.; Nagar, R.; Raman, V.; Rajalakshmi, N.; Dhathathreyan, K. S.; Ramaprabhu, S. Synthesis of Graphene-Multiwalled Carbon Nanotubes Hybrid Nanostructure by Strengthened Electrostatic Interaction and Its Lithium Ion Battery Application. J. Mater. Chem. 2012, 22, 9949-9956.

36. Zhang, J.; Cao, H.; Tang, X.; Fan, W.; Peng, G.; Qu, M. Graphite/Graphene Oxide Composite as High Capacity and Binder-Free Anode Material for Lithium Ion Batteries. J. Power Sources 2013, 241, 619-626.

37. Lian, P.; Zhu, X.; Liang, S.; Li, Z.; Yang, W.; Wang, H. Large Reversible Capacity of High Quality Graphene Sheets as an Anode Material for Lithium-Ion Batteries. Electrochim. Acta 2010, 55, 3909-3914.

38. Wang, J.-Z.; Zhong, C.; Chou, S.-L.; Liu, H.-K. Flexible Free-Standing Graphene-Silicon Composite Film for Lithium-Ion Batteries. Electrochem. Comm. 2010, 12, 1467-1470.

39. Lee, J. K.; Smith, K. B.; Hayner, C. M.; Kung, H. H. Silicon Nanoparticles-Graphene Paper Composites for Li Ion Battery Anodes. Chem. Comm. 2010, 46, 2025-2027.

40. Datta, D.; Li, J.; Shenoy, V. B. Defective Graphene as a High-Capacity Anode Material for Na- and Ca-Ion Batteries. ACS Appl. Mater. Interfaces 2014, 6, 1788-1795.

41. Qian, J.; Chen, Y.; Wu, L.; Cao, Y.; Ai, X.; Yang, H. High Capacity Na-Storage and Superior Cyclability Of Nanocomposite Sb/C Anode for Na-Ion Batteries. Chem. Comm. 2012, 48, 7070-7072.

42. Abouimrane, A.; Compton, O. C.; Amine, K.; Nguyen, S. T. Non-Annealed Graphene Paper as a Binder-Free Anode for Lithium-Ion Batteries. J. Phys. Chem. C 2010, 114, 12800-12804.

43. Bi, H.; Chen, J.; Zhao, W.; Sun, S.; Tang, Y.; Lin, T.; Huang, F.; Zhou, X.; Xie, X.; Jiang, M. Highly Conductive, Free-Standing and Flexible Graphene Papers for Energy Conversion and Storage Devices. RSC Adv. 2013, 3, 8454-8460.

44. Hu, Y.; Li, X.; Geng, D.; Cai, M.; Li, R.; Sun, X. Influence of Paper Thickness on the Electrochemical Performances of Graphene Papers as an Anode for Lithium Ion Batteries. Electrochim. Acta 2013, 91, 227-233.

45. Liu, F.; Song, S.; Xue, D.; Zhang, H. Folded Structured Graphene Paper for High Performance Electrode Materials. Adv. Mater. 2012, 24, 1089-1094.

46. Liu, S.; Chen, K.; Fu, Y.; Yu, S.; Bao, Z. Reduced Graphene Oxide Paper by Supercritical Ethanol Treatment and its Electrochemical Properties. Appl. Sur. Sci. 2012, 258, 5299-5303.

47. Park, H. H.; Choi, Y.; Kim, B.; Yun, Y. S.; Jin, H. J. Free-Standing Nitrogen-Doped Reduced Graphene Oxide Anode for Lithium-Ion Batteries. J. Nanosci. Nanotech. 2013, 13, 7950-7954.

48. Zhao, X.; Hayner, C. M.; Kung, M. C.; Kung, H. H. Flexible Holey Graphene Paper Electrodes with Enhanced Rate Capability for Energy Storage Applications. ACS Nano 2011, 5, 8739-8749.

49. Zhong, C.; Wang, J. Z.; Wexler, D.; Liu, H. K. Microwave Autoclave Synthesized Multi-Layer Graphene/Single-Walled Carbon Nanotube Composites for Free-Standing Lithium-Ion Battery Anodes. Carbon 2014, 66, 637-645.

50. Stevens, D. A.; Dahn, J. R. The Mechanisms of Lithium and Sodium Insertion in Carbon Materials. J. Electrochem. Soc. 2001, 148, A803-A811

51. Wang, Y. X.; Lim, Y. G.; Park, M. S.; Chou, S. L.; Kim, J. H.; Liu, H. K.; Dou, S. X.; Kim, Y. J. Ultrafine SnO2 Nanoparticle Loading Onto Reduced Graphene Oxide as Anodes for Sodium-Ion Batteries With Superior Rate and Cycling Performances. J. Mater. Chem. A 2014, 2, 529-534.

52. Yu, D. Y. W.; Prikhodchenko, P. V.; Mason, C. W.; Batabyal, S. K.; Gun, J.; Sladkevich, S.; Medvedev, A. G.; Lev, O. High-Capacity Antimony Sulphide Nanoparticle-Decorated Graphene Composite as Anode for Sodium-Ion Batteries. Nat. Comm. 2013, 4, 7.

53. Hummers, W. S.; Offeman, R. E. Preparation of Graphitic Oxide. J. Am. Chem. Soc. 1958, 80, 1339-1339.

54. Marcano, D. C.; Kosynkin, D. V.; Berlin, J. M.; Sinitskii, A.; Sun, Z.; Slesarev, A.; Alemany, L. B.; Lu, W.; Tour, J. M. Improved Synthesis of Graphene Oxide. ACS Nano 2010, 4, 4806-4814.

55. Stankovich, S.; Dikin, D. A.; Piner, R. D.; Kohlhaas, K. A.; Kleinhammes, A.; Jia, Y.; Wu, Y.; Nguyen, S. T.; Ruoff, R. S. Synthesis of Graphene-Based Nanosheets Via Chemical Reduction of Exfoliated Graphite Oxide. Carbon 2007,45, 1558-1565.

56. Schniepp, H. C.; Li, J. L.; McAllister, M. J.; Sai, H.; Herrera-Alonso, M.; Adamson, D. H.; Prud'homme, R. K.; Car, R.; Saville, D. A.; Aksay, I. A. Functionalized Single Graphene Sheets Derived From Splitting Graphite Oxide. J. Phys. Chem. B 2006, 110, 8535-8539.

57. Li, Z. Q.; Lu, C. J.; Xia, Z. P.; Zhou, Y.; Luo, Z. X-ray Diffraction Patterns of Graphite and Turbostratic Carbon. Carbon 2007, 45, 1686-1695.

58. McAllister, M. J.; Li, J.-L.; Adamson, D. H.; Schniepp, H. C.; Abdala, A. A.; Liu, J.; Herrera-Alonso, M.; Milius, D. L.; Car, R.; Prud'homme, R. K.; Aksay, I. A. Single Sheet Functionalized Graphene by Oxidation and Thermal Expansion of Graphite. Chem. Mater. 2007, 19, 4396-4404.

59. Briggs, D.; Beamson, G. High Resolution XPS of Organic Polymers. The Scienta ESCA300 Database. John Wiley and Sons: New York, 1992.

60. Stankovich, S.; Piner, R. D.; Chen, X. Q.; Wu, N. Q.; Nguyen, S. T.; Ruoff, R. S. Stable Aqueous Dispersions of Graphitic Nanoplatelets via the Reduction of Exfoliated Graphite Oxide in the Presence of Poly(Sodium 4-Styrenesulfonate). J. Mater. Chem. 2006, 16, 155-158.

61. Wang, C.; Li, D.; Too, C. O.; Wallance, G. G. Electrochemical Properties of Graphene Paper Electrodes Used in Lithium Batteries. Chem. Mater., 2009, 21, 2604–2606

62. Doron, A. Review of Selected Electrode-Solution Interactions Which Determine the Performance of Li and Li Ion Batteries. J. Power Sources 2000, 89, 206-218.

63. Ge, P.; Fouletier, M. Electrochemical Intercalation of Sodium in Graphite. Solid State Ionics 1988; 28–30, 1172–1175.

64. Li, X.; Wang, H.; Robinson, J. T.; Sanchez, H.; Diankov, G.; Dai, H. Simultaneous Nitrogen Doping and Reduction of Graphene Oxide. J. Am. Chem. Soc. 2009, 131, 15939–15944

65. Hu, J.; Yang, P.; Lieber, C. M. Nitrogen-driven sp(3) to sp(2) Transformation in Carbon Nitride Materials. Phys. Rev. B 1998, 57, 3185-3188

66. Wu, Z-S.; Ren, C.; Xu, L.; Li, F.; Cheng, H-M. Doped Graphene Sheets As Anode Materials with Superhigh Rate and Large Capacity for Lithium Ion Batteries. ACS Nano, 2011, 5, 5463–5471

67. Hariharan, S.; Saravanan, K.; Balaya, P. alpha-MoO3: A High Performance Anode Material for Sodium-Ion Batteries. Electrochem. Comm. 2013, 31, 5-9

68. Chen, H.; Mueller, M. B.; Gilmore, K. J.; Wallace, G. G.; Li, D. Mechanically Strong, Electrically Conductive, and Biocompatible Graphene Paper. Adv. Mater. 2008, 20, 3557.

69. Compton, O. C.; Dikin, D. A.; Putz, K. W.; Brinson, L. C.; Nguyen, S. T. Electrically Conductive "Alkylated" Graphene Paper via Chemical Reduction of Amine-Functionalized Graphene Oxide Paper. Adv. Mater. 2010, 22, 892– 896.

70. Compton, O. C.; Nguyen, S. T. Graphene Oxide, Highly Reduced Graphene Oxide, and Graphene: Versatile Building Blocks for Carbon-Based Materials. Small 2010, 6, 711– 723.

Chapter 4 - Large Area MoS_2/graphene Composite Paper Based Electrode for Room Temperature Na-ion Batteries[2]

4.1. Abstract

We study the synthesis, electrochemical and mechanical performance of large area layered freestanding papers composed of acid functionalized few layer molybdenum disulfide (MoS_2) and reduced graphene oxide (rGO) flakes for use as a self-standing flexible electrode in sodium ion batteries. Synthesis was achieved through vacuum filtration of homogenous dispersions consisting of varying wt. % of exfoliated MoS_2 flakes in GO in DI water, followed by thermal reduction. The electrochemical behavior of the composite paper (at a loading of 4 mg/cm^2) was evaluated as counter electrode against pure Na foil in a half-cell configuration. The papers showed good Na cycling ability with charge capacity of approx. 225 $mAh.g^{-1}$ with respect to total weight of the electrode and coulombic efficiency reaching 99%. In addition, uniaxial tensile testing of the composite papers showed fracture strength as much as 3 to 6 MPa with high average strain to failure strain reaching 1.8 %.

[2] Reprinted with permission from (L. David, R. Bhandavat and G. Singh, "MoS_2/graphene Composite Paper for Sodium-ion Battery" ACS Nano **8**, 2, 1759 - 1770). Copyright (2015) American Chemical Society.

4.2. Introduction

Lithium ion batteries (LIBs) have been extensively studied for energy-storage applications like portable electronic devices and electric vehicles[1-3]. However, concerns over the cost, safety and availability of Li reserves[4] for large-scale applications involving renewable energy integration and the electrical grid have to be answered. In this regard, sodium ion batteries (SIBs) have drawn increasing attention because in contrast to lithium[5-9], sodium resources are practically inexhaustible and evenly distributed around the world while the ion insertion chemistry is largely identical to that of lithium. Also, from electrochemical point of view, sodium has a very negative redox potential (-2.71 V, vs. SHE) and a small electrochemical equivalent (0.86 gAh^{-1}), which make it the most advantageous element for battery applications after lithium. However, many challenges remain before SIBs can become commercially competitive with LIBs. For instance, Na ions are about 55% larger in radius than Li-ions, which makes it difficult to find a suitable host material to allow reversible and rapid ion insertion and extraction[10]. Despite many encouraging works in the past decades, only high-temperature Na/S and $Na/NiCl_2$ (ZEBRA battery) systems have been commercially developed for electric vehicles and MWh scale electric storage[11]. A major obstacle hindering the broad market penetration of these Na batteries is the stability and endurance of the battery components at the high operating temperatures of >300 °C [11]. If a practical room temperature Na-ion rocking chair battery (Na-ion battery) can be achieved, it would bring about a great improvement in the safety and operational simplicity with respect to conventional high temperature Na batteries and current Li-ion batteries.

To this end, researchers have proposed a number of high-capacity sodium host materials (negative electrode) involving either carbon or group IVA and VA elements that form intermetallic compounds with Na[12-16]. The alloying compounds demonstrate high first cycle Na-

storage capacities, such as $Na_{15}Sn_4$ (847 $mAhg^{-1}$), $Na_{15}Pb_4$ (485 $mAhg^{-1}$), Na_3Sb (600 $mAhg^{-1}$) and Na_3P (2560 $mAhg^{-1}$), respectively. However, this comes at the cost of very high volume change upon Na-insertion (as much as 500 % in some cases), resulting in formation of internal cracks, loss of electrical contact, and eventual failure of the electrode (particularly for thick electrodes)[17]. Although, novel nanostructured designs that can accommodate large volumetric strains are currently being explored[18-21]. For carbon-based electrode materials, much of the emphasis has been on hard carbons due to large interlayer spacing and disordered structure [22-29]. For example, hard carbon prepared from pyrolyzed glucose, carbon black, and carbon microspheres have been shown to exhibit initial reversible capacities of 300 $mAhg^{-1}$, 200 $mAhg^{-1}$, and 285 $mAhg^{-1}$, respectively in a Na-ion cell [18-20]. More recently, another hard carbon material that could deliver a reversible capacity of more than 200 $mAhg^{-1}$ over 100 cycles has been reported [22]. However, these studies were conducted on traditional anode architecture (prepared through slurry coating of active material on metallic current collector foil and the capacities reported were with respect to the active material only), either at low cycling current rates or at elevated temperatures. Overall, new electrode design and concepts based on chemistry other than ion-intercalation and alloying must also be explored to realize improved performance in Na-ion batteries under normal operating conditions.

Studies on Li-ion batteries have shown that 2-D layered nanomaterials such as graphene and transition metal dichalcogenides (TMDCs such MoS_2, WS_2) are promising materials for efficient storage and release of Li-ions[27-42]. However, when compared with graphite, the electrochemical lithiation in TMDCs is distinct as majority of the lithium is stored by means of a conversion reaction in which Li-ion reacts with the TMDC forming Li_2S and transition metal phases as the reaction products. Moreover, this type of a conversion reaction can allow transfer

of 2 to 6 electrons per transition metal compared to single electron in the case of intercalation reaction (lithium/carbon system)[1, 40]. Although layered graphite has been ruled out for sodium-based systems (as Na ions do not tend to form staged intercalation compounds with graphite) [43-46], a graphene based free-standing paper based electrode can provide a porous and flexible support structure for a TMDC to undergo a reversible conversion reaction with Na-ions. It can also act an efficient electronic current collector, thereby eliminating the need for metallic substrate (generally a 10 μm thick foil at 10 mg.cm^{-2}) [47, 48], electrically conducting additives and polymeric binders that amount to a total of approx. 10 % of the cell weight [45] in traditional negative electrodes[49-54]. Herein, we provide the first report of (a) synthesis of large area composite papers from acid functionalized MoS_2 and reduced graphene oxide flakes, (b) improved capacity and high efficiency reversible Na storage in the self-standing flexible MoS_2/graphene electrodes at room temperatures, and (c) mechanical characterization that highlight the high strain to failure these composite papers.

4.3. Materials and Instrumentation

4.3.1. Instrumentation

ζ potential surface measurements were carried out on a ZetaPlus Zeta Potential Analyzer (Brookhaven's Inst. Corp.). The effect of ionic concentration on the potential measured is minimized by using a low concentration of basic (0.01 M NaOH) solution for controlling the pH. Scanning electron microscopy (SEM) of the synthesized material was carried out on a Carl Zeiss EVO MA10 system with incident voltage of 5 KV to 30 KV. TEM images were digitally acquired by use of a Phillips CM100 operated at 100 KV. Material characterization was made using X-ray diffractometer (XRD) operating at room temperature, with nickel-filtered CuKα radiation (λ=1.5418 Å). Thermogravimetric analysis (TGA) was performed using Shimadzu 50

TGA (limited to 800 °C). Samples weighing, ~2.5 mg, were heated in a platinum pan at a rate of 10 °C/min in air flowing at 20 mL/min. Raman spectra were measured using a LabRAM ARMIS Raman spectrometer using 633 nm laser excitation (laser power of 17 mW) as the light source. The surface chemical composition was studied by X-ray photoelectron spectroscopy (XPS, PHI Quantera SXM) using monochromatic Al Kα X-radiation. Static uniaxial in-plane tensile tests were conducted in a simple test setup.. The sample strip is secured on one end by a computer controlled movable stage (M-111.2DG from PI®) with 0.02 % maximum error, while the other end it fixed to a 1N load cell (ULC-1N Interface®) with 0.05 % maximum error, which in turn is fixed to an immovable stage. All tensile tests were conducted in controlled strain rate mode with a strain rate of 0.2 %/min. The samples were cut with a razor into rectangular strips of approximately 5 x 15 mm^2 for testing without further modification. Electrical conductivity measurements were carried out by use of a four-point probe setup and Keithley 2636A (Cleveland, OH) dual channel sourcemeter in the ohmic region. Electrochemical cycling of the assembled cells was carried out using multichannel Battery Test Equipment (Arbin-BT2000, Austin, TX) at atmospheric conditions.

The ζ potential measured at varying solution pH with the same MoS_2 concentration can provide an understanding of the pH-dependent MoS_2 sheet stability in the solution. Hence, a separate solution of 1 mg/mL MoS_2 in superacid (top portion) was used for ζ potential measurements.

Accordingly, the total potential energy (V_T) at the surface interaction of two adjacent MoS_2 sheets is the difference in repulsive potential energy ($V_{DLVO} \approx 4A\varepsilon_r\varepsilon_o\kappa\zeta^2 e^{-\kappa D}$) and attractive van der Waals energy ($V_{vdW} \approx A\pi\rho^2 C/\ 2D^4$). V_{DLVO} for MoS_2 surfaces is determined using the measured ζ potential, surfactant concentration, and distance between two separated sheets, and

V_{vdW} is calculated using atomic density and surface energy. The total potential energy is then given by

Equation 4.1

$$V_T \approx V_{DLVO} - V_{vdW}$$

Substituting the expressions on the above equation we get the overall potential energy of two parallel, two-dimentional sheets as,

Equation 4.2

$$V_T \approx 4A\varepsilon_r\varepsilon_o\kappa\zeta^2 e^{-\kappa D} - A\pi\rho^2 C/\ 2D^4$$

where A is the area of MoS_2 sheet, ρ is the number of atoms per unit area, ε_r and ε_0 are the relative permittivity of water (80.1 at 20 °C) and the absolute permittivity (8.85×10^{-12} F/ m), respectively, ζ is the experimentally measured surface potential (36.3 mV), D is the distance of sheet separation, $\rho^2 C$ is the estimated surface energy per unit area[43] (approximately 2.06×10^{-38} J/m^2), and κ is the double-layer thickness given as

Equation 4.2

$$\kappa = 1/[\varepsilon_r\varepsilon_0 kT/2e^2 n_0]^{0.5}$$

($n_0 = 9.05 \times 10^{23}$ is the number of surfactant molecules per unit volume of solution; $e = 1.6 \times 10^{-19}$ C).

4.3.2. Preparation graphene oxide

Sodium nitrate (99.2%), potassium permanganate (99.4%), sulfuric acid (96.4 %), hydrogen peroxide (31.3 % solution in water), hydrochloric acid (30 % solution in water), methanol (99.9 %) were purchased from Fisher Scientific. All materials were used as received without further purification. Modified Hummer's method was used to make graphene oxide[55]. Concentrated H_2SO_4 (130 mL) was added to a mixture of graphite flakes (3 g) and $NaNO_3$ (1.5

g). The mixture was cooled down using an ice bath. KMnO4 was added slowly to this mixture. The mixture was stirred for 12 hours at 50 °C. Then it was quenched with water (400 mL) with 30 % H_2O_2 (3 mL) while in an ice bath such that the temperature does not go beyond 20 °C. The remaining material was then washed in succession with 200 mL of water twice, 200 mL of 30 % HCl and 200 mL of ethanol. The material remaining after these extended washes is coagulated with 200 mL of ether and filtered through a paper filter. The filtrate is dried overnight to obtain dry graphene oxide (GO).

4.3.3. Preparation of exfoliated or acid treated MoS_2 flakes

MoS_2 powder (2 mg/mL, 99 %, Sigma Aldrich) was sonicated for 30 min in concentrated chlorosulfonic acid (superacid, 99%, Sigma Aldrich), and the non-exfoliated sheets were allowed to settle. Please note that the superacid was very slowly added to the MoS_2 powder in an argon-filled glovebox (dew point −50 °C). The solution was then carefully quenched in 1.0 L of distilled water (done with extreme caution in a glovebox). Additional dilution with DI water was done to reduce the solution acidity. The solution was then dried in a conventional oven to obtain dry superacid treated MoS_2 (MoS_2-SA).

4.3.4. Preparation of reduced graphene oxide and MoS_2 composite paper

15 mg GO and varying wt. % of MoS_2 (prepared from the procedure state above) were mixed together in 1:1 (v/v) water and isopropanol solution. The mixture was then sonicated for 60 min (Branson Sonifier S-450A, 400 W). The composite suspension was then filtered by vacuum filtration process through a 47 mm diameter 10 μm pore sized filter membrane (HPLC grade, Millipore). MoS_2/GO composite paper thus obtained was dried in an oven at 70 °C overnight and subsequently reduced at 500 °C for 2h and 900 °C for 5 minutes in argon atmosphere. The samples were labeled as rGO, 20MoS_2, 40MoS_2 and 60MoS_2 for pristine rGO

paper and rGO with 20, 40 and 60 % of MoS_2 in the total weight of the paper, respectively. The $60MoS_2$-raw paper was synthesized with as-obtained MoS_2 and GO, following the process stated above. Later, the large-area paper with $60MoS_2$ composition (approx. 6.25" diameter, cut into rectangular strip shown in Figure 4.3b) was prepared following similar procedure by use of a Büchner funnel with a polypropylene filter paper (Celgard®).

4.3.5. Coin Cell/Battery assembly

For electrochemical testing, 2032 half coin cells were made by punching 14.3 mm diameter out of the composite paper for use as working electrode. 1M $NaClO_4$ (Alfa Aesar) in (1:1 v/v) dimethyl carbonate:ethylene carbonate (ionic conductivity 10.7 mS cm^{-1}) served as the electrolyte. A 25 μm thick (19 mm diameter) glass separator soaked in electrolyte was placed between the working electrode and pure Na metal (14.3 mm diameter, 75 μm thick) counter electrode. Washer, spring and a top casing were placed on top to complete the assembly before crimping. The assembled cells were tested using multichannel BT2000 Arbin test unit sweeping between 2.25 V to 10 mV v/s Na/Na^+. C-rate performance of the best performing electrode material ($60MoS_2$) was tested in the voltage range from 2.25 V to 0.1 V vs Na/Na^+ using the following cycle schedule: Na^+ was inserted at 100 mAg^{-1} while the extraction was performed at current densities of 50, 100, 25, 150, 200 and 25 mAg^{-1} for 5 cycles consecutively.

4.4. Results and Discussions

4.4.1. Material Synthesis

Layered "as-obtained" MoS_2 was exfoliated by mechanical sonication in chlorosulfonic acid followed by quenching in DI water (see methods section). A digital image of the acid treated MoS_2 dispersion immediately after quenching in DI water is shown in Figure 4.1a. From SEM observations, the particle size for MoS_2-raw was observed to be approx. 20 to 40 μm

(Figure 4.1b) while that of MoS_2-SA was less than 1 μm (Figure 4.1c). Shown in Figure 4.2 are high-resolution TEM image of exfoliated MoS_2 sheets. All the sheets were observed to be only few layers thick with flack size ranging from 100 nm to 1 μm. From literature, we can correlate the reason for exfoliation of MoS_2 to electrostatic repulsion forces caused by protonation of MoS_2 surfaces [56]. Using DLVO theory, ζ potential measurements can quantify this surface charge on MoS_2 sheet and hence help in establishing the dispersion stability. For ζ potential measurements, the pH was varied by adding 0.01 M NaOH solution and since the contribution from dissociated OH^- ions in the measured potential is minimal, it was neglected in the analysis. The lower pH range was limited to protect the instrument electrode. The surface potential showed a range varying from −35 mV at pH of 4 to −60 mV at pH of 10, shown as an insert in Figure 4.1d. As higher surface potential (negative) implies more stable suspensions, based on the obtained results, higher pH suggests a larger exposed MoS_2 sheet surface. This dependence of surface potential on pH is similar to that observed for exfoliated (surface-functionalized) graphene sheets by Coleman's group[57]. Further, we used their model of graphene stabilization mechanism for explaining the superacid−MoS_2 interaction mechanism [58]. Figure 4.1d is the plot for total interaction energy per unit area of the sheet (V_T/A).

Further analysis involved Raman spectroscopy and X-ray diffraction before and after acid treatment. Raman spectrum (Figure 4.1e) obtained by use of 633 nm wavelength laser showed typical E^1_{2g}, A_{1g}, 2LA(M) and A_{1g}+LA(M) peaks at 380, 407, 460 and 641 cm^{-1}, respectively. The in-plane E^1_{2g} peak results from opposite vibration of two S atoms with respect to the Mo atom while the A_{1g} peak is associated with the out-of-plane vibration of only S atoms in opposite directions.[59] The intensity of A_{1g} peak arises from the resonance Raman (RR) scattering, because the incident laser is in resonance with the direct bandgap (~1.96 eV) at the K point. The

asymmetric 2LA(M) peak is associated with second-order zone- edge phonon (LA(M)) and a first order optical phonon peak (A_{2u}).[60-63] These results along with electron microscopy results suggests that the structure is relatively undistorted MoS_2 [64-65].

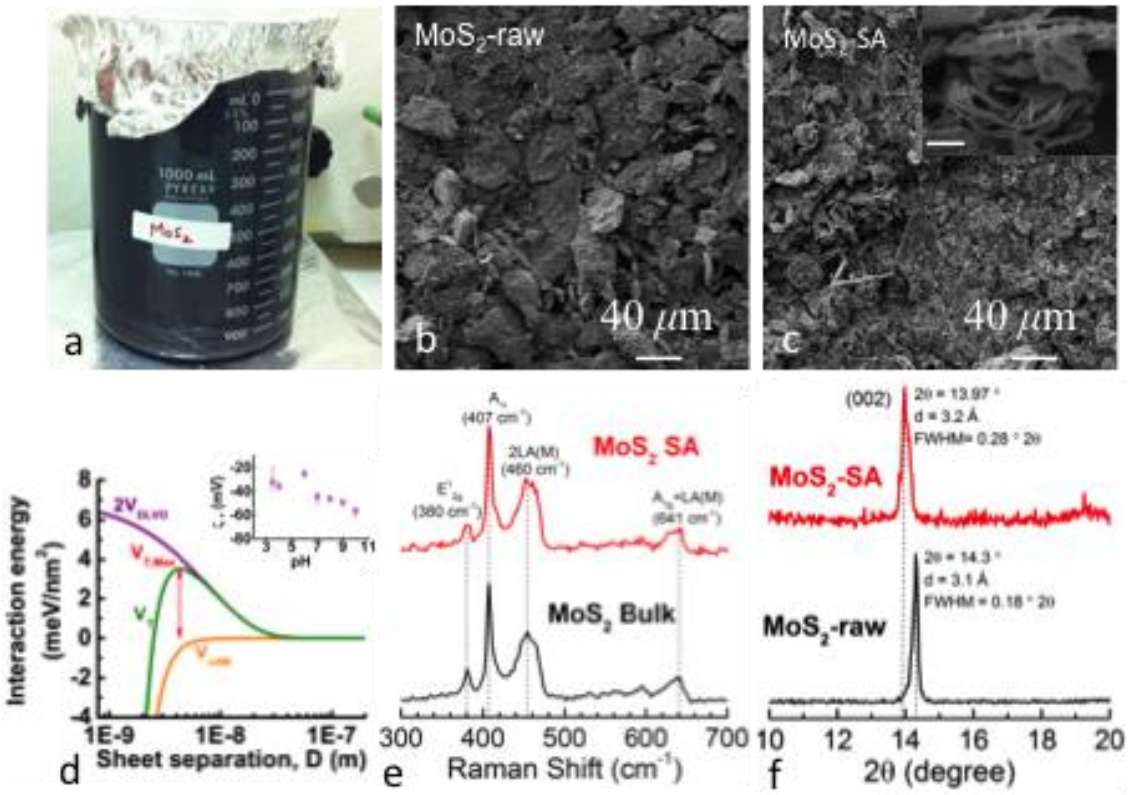

Figure 4-1 (a) Photographic image showing a litre of MoS_2 dispersed in DI water using superacid as stabilizer. The concentration of the dispersion is ~2 mg/mL. SEM images showing the structure and size distribution of MoS_2 (b) before and (c) after exfoliated with superacid. Average particle size was ~20 to 40 and less than 20 µm for MoS_2-raw and MoS_2-SA, respectively. The scale bar in the inset is 2 µm (d) Calculated total interaction potential energy (VT), repulsion (VDLVO), and attraction energy (VvdW) (per unit area) with increasing MoS_2 sheet separation distance (log scale) is shown. Inset: Experimentally measured zeta potential measurements, showing better dispersion stability at higher pH values. (e) Raman spectra of MoS_2 before and after exfoliation with superacid. The

similarity in the relative intensity and position of the E12g and A1g peaks suggests that the structure is undistorted MoS_2. (f) The change in intensity and FWHM of MoS_2 peak at 14° 2θ in the XRD spectra suggests that MoS_2 is exfoliated after acid treatment.

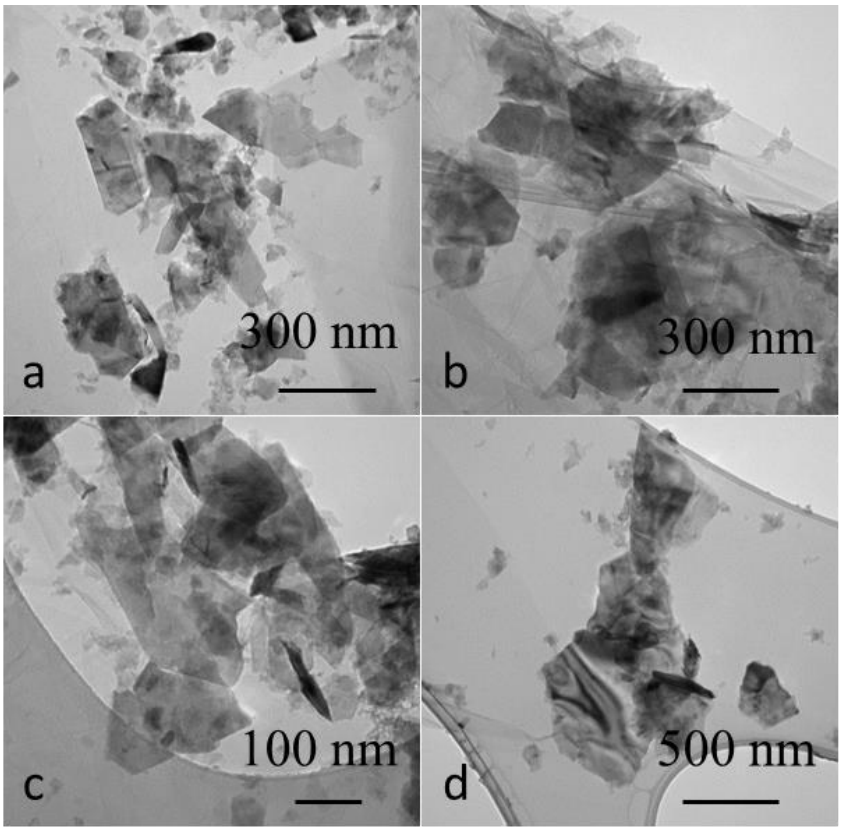

Figure 4-2 High-resolution TEM image of superacid exfoliated MoS_2 sheets.

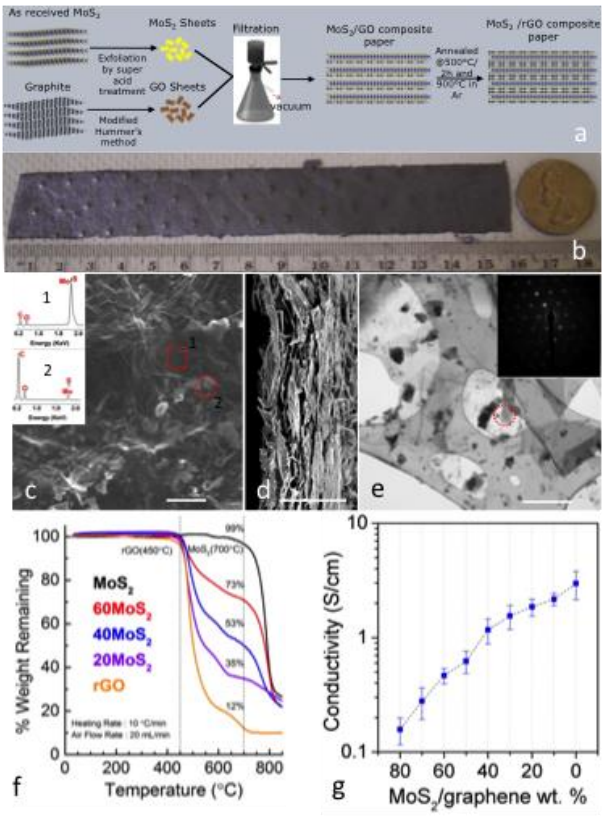

Figure 4-3 (a) Schematic representation showing synthesis of rGO/MoS_2 composite paper. (b) Digital picture showing large area composite paper prepared through vaccum filtration. (c) SEM top-view image of 60MoS_2 paper, the insert shows the EDX spectra of spots in the SEM image indicating the material to be rGO (square) and MoS_2 (circle). (d) Corresponding SEM cross-sectional images shows the morphology of the paper. Average thickness of the paper was observed to be ~20 µm. (e) TEM images and SAED patterns of 60MoS_2. The MoS_2 sheets are observed to be wraped with graphene sheets. In SAED pattern in the insert, multiple spot pattern is observed one of which is due to the polycrystallinity of restacked rGO sheets while second set of spot pattern were due to MoS_2 sheets. (g) Thermogravimetric analysis data for MoS_2-SA, MoS_2-rGO composite paper and rGO paper. (g) Graph of conductivity vs percentage of MoS_2 in free-standing paper.

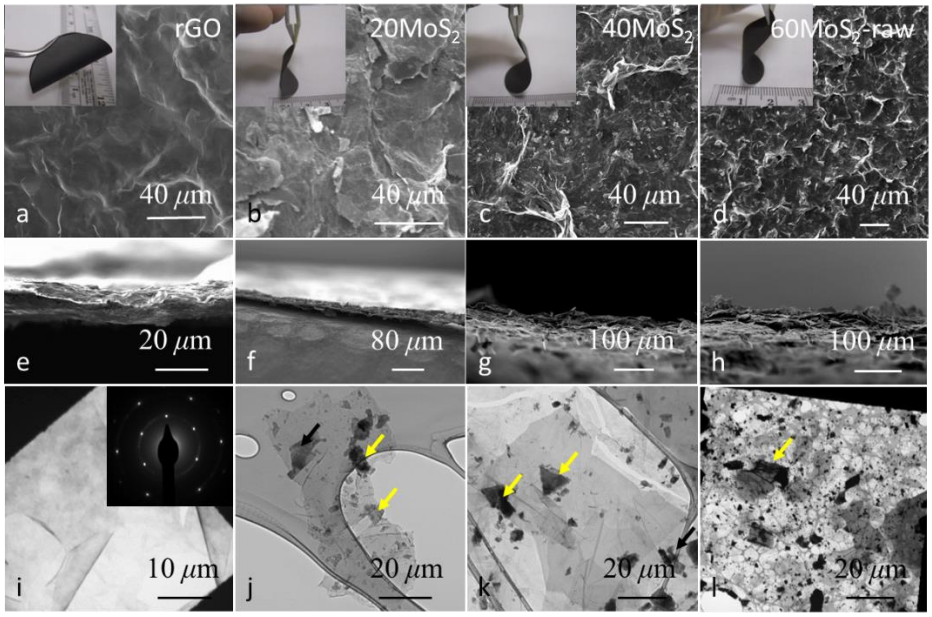

Figure 4-4 SEM images of (a) rGO and (b) $20MoS_2$, (c) $40MoS_2$ and (d) $60MoS_2$-raw paper and (e-h) their corresponding SEM cross-sectional images. The inserts in (a-c) are digital photographs demonstrating the flexibility of rGO and rGO/MoS_2 paper shown in the corresponding SEM image. TEM images and SAED patterns (insert) of (i) rGO and (j-l) rGO/MoS_2 composite corresponding to the SEM images above.

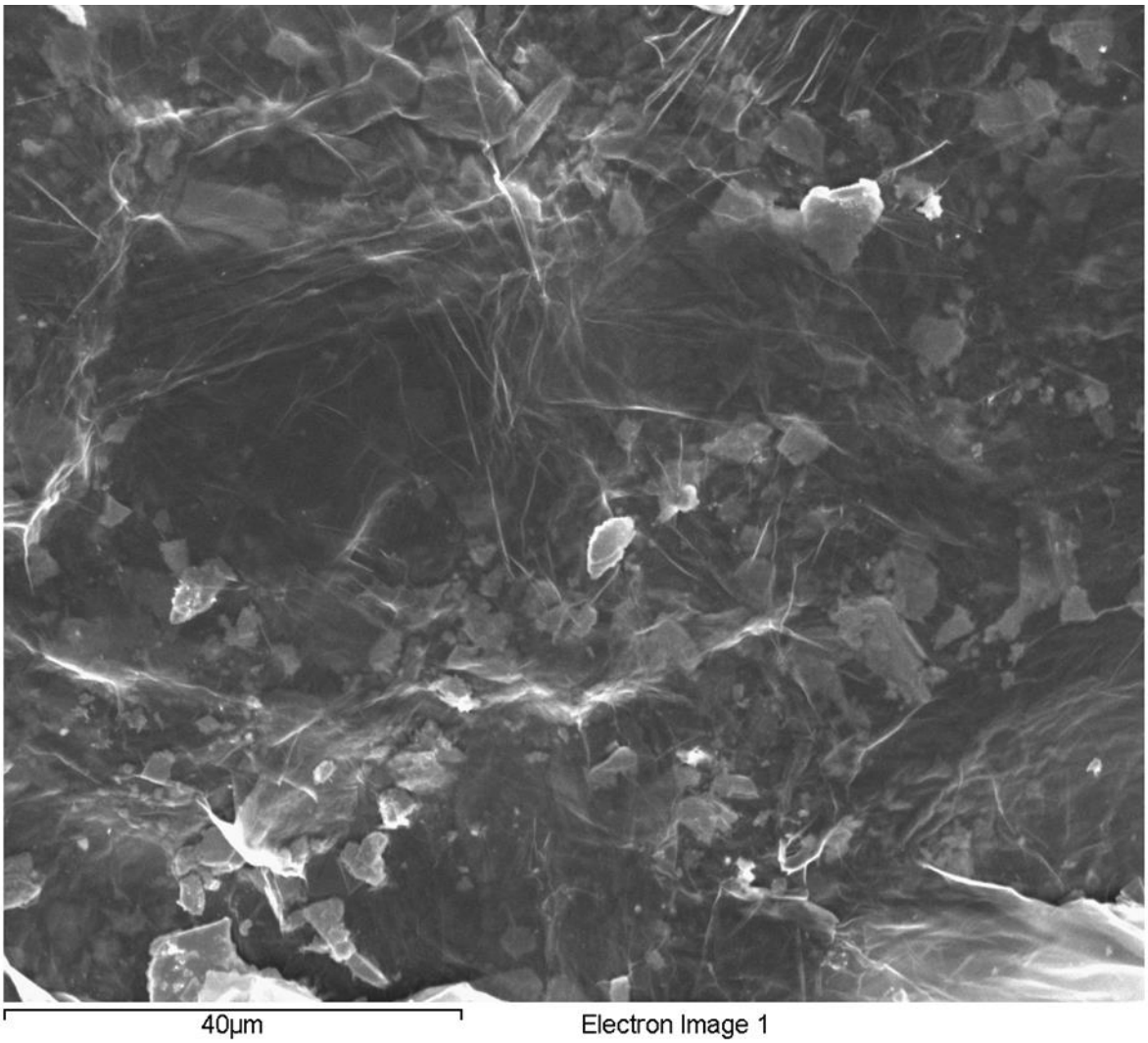

Figure 4-5 High resolution SEM image of 60MoS_2 composite paper which shows flakes of exfoliated MoS_2 sheets overlaped with rGO sheets.

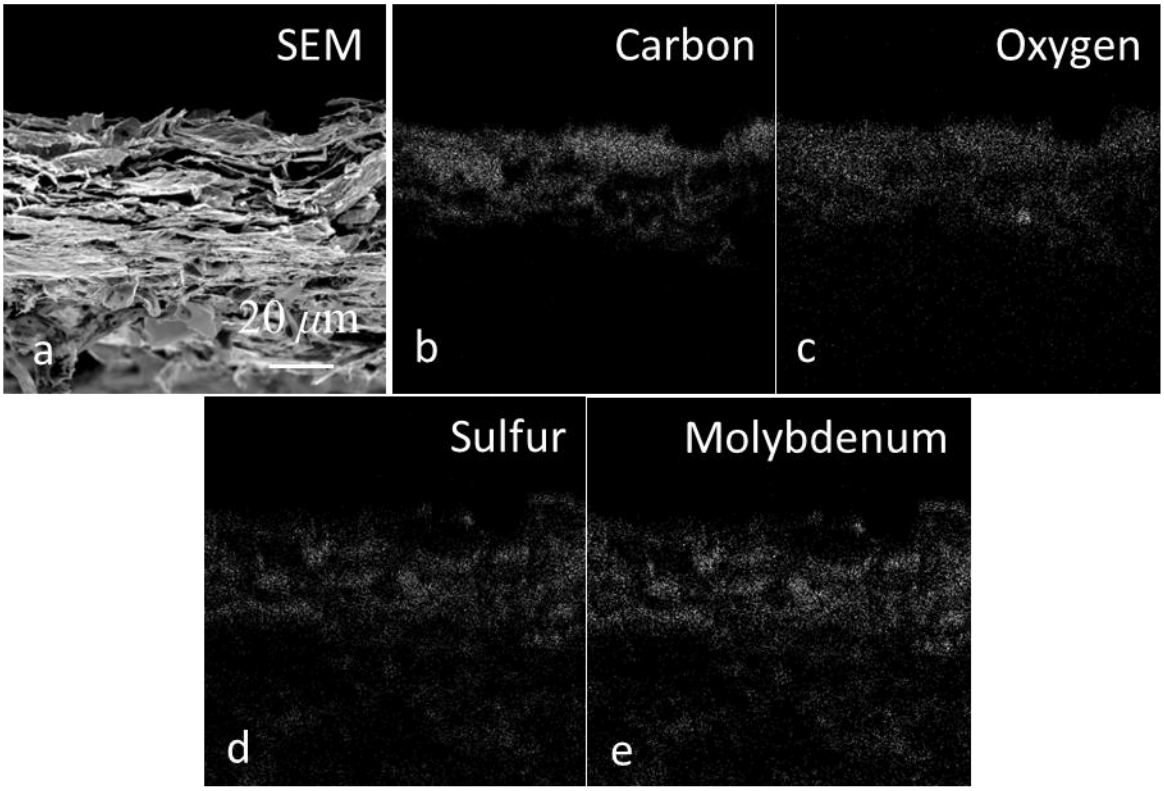

Figure 4-6 (a) SEM cross-sectional inmage of 60MoS_2 and EDX map of (b) carbon, (c) oxygen, (d) sulfur and (e) molybdenum.

Table 4.1 Elemental composition obtained by EDX analysis of cross-section of 60MoS_2 paper (obtained for Figure 4.6).

Element	Weight percentage (%)	Atomic percentage (%)
Carbon	53.46	79.78
Oxygen	6.96	7.79
Molybdenum	26.07	4.87
Sulfur	13.51	7.55

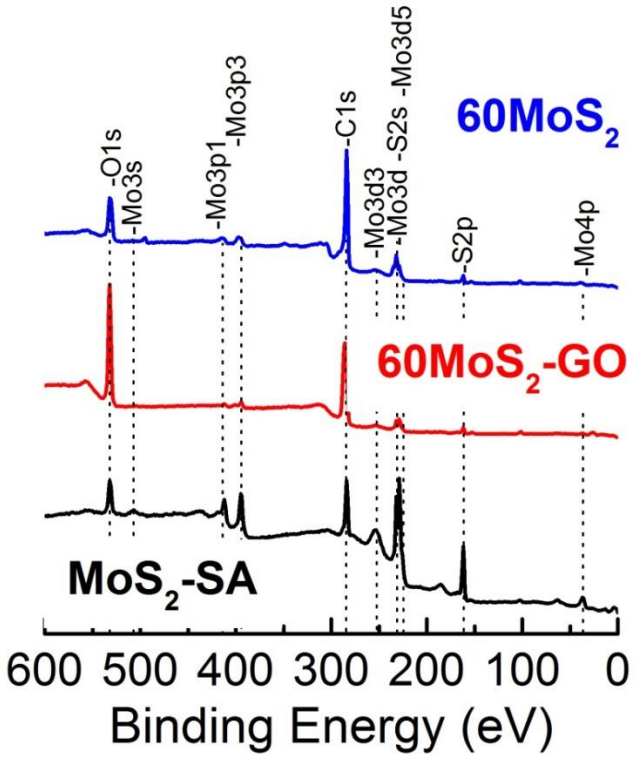

Figure 4-7 X-ray photoelectron spectroscopy plot of as-synthesized MoS_2-SA and 60MoS_2 free-standing paper before and after heat treatment.

Further, X-ray diffraction analysis (XRD) of MoS_2-raw and MoS_2-SA in Figure 4.1f showed distinct peak at 14.3 ° and 13.97 ° 2θ with FWHM of 0.18 ° and 0.28 ° 2θ, respectively. The change in peak position between MoS_2-raw and MoS_2-SA is attributed to increase in 'd' spacing due to exfoliation of MoS_2 sheets. Using Scherrer equation L = Kλ/ [66]

Later, the MoS_2/rGO papers were prepared by vacuum filtration of graphene oxide (GO) and molybdenum disulfide (MoS_2) sheets dispersed in water:isoproponal (1:1) solution, which is shown with the help of a schematic in Figure 4.3a. SEM image in Figure 4.3c,d and Figure 4.4 (a through h) shows the top-view and corresponding cross-section of 60MoS_2, rGO, 20MoS_2, 40MoS_2 and 60MoS_2-raw free-standing papers, respectively. The papers were approx. 10 to 20 μm thick (depending upon the weight percentage of MoS_2 in GO) with a relatively homogeneous

composition. The interleaved structure observed in the cross-sectional images is preferred by larger Na-ions for easy insertion and extraction at higher current densities or C-rates. The digital photograph in insert of Figure 4.4 (a through d) confirms the outstanding structural flexibility of rGO and MoS_2/graphene composite papers that were approx. 2" in diameter while a large area $60MoS_2$ composite paper (approx. 6" x 1") is shown in Figure 4.3b for comparison (also see High resolution SEM image in Figure 4.5 and methods section for synthesis details). Further analysis involved SEM-X-ray energy dispersive spectroscopy, shown in insert in Figure 4.3c. The EDX spectra from spot 1(square) showed peaks at 0.27 KeV and 0.52 KeV, which correspond to carbon (85.43 at %) and oxygen (10.41 at %) Kα energy, respectively. The low oxygen content indicate that rGO was highly reduced and pristine. In addition to carbon and oxygen, two small peaks at 2.29 KeV and 2.3 KeV corresponding to molybdenum Lα (1.39 at. %) and sulfur Kα (2.78 at. %) energy, respectively were also observed. At spot 2, peaks corresponding to Mo (26.13 at. %) and S (46.48 at. %) were prominent when compared to that of carbon (24.39 at. %), which unambiguously confirm the presence of MoS_2 sheets in the composite. Transmission electron microscopy (TEM) images are shown in Figure 4.3e and Figure 4.4 (i through l). It is clear that the rGO sheets were layered with few layers of MoS_2 forming a very good electron conductive layer and also a support structure for free-standing paper. The insert in Figure 4.3e is the selected area electron diffraction (SAED) pattern that indicates multiple spot pattern, one of which is due to the polycrystallinity of restacked rGO sheets while second set of spot pattern were due to MoS_2 sheets. The hexagonal spot pattern (insert of Supplementary Figure 4.4i) indicate that the graphitic AB stacking was preserved in the lattice after thermal reduction. To further observe the distribution of MoS_2 in the composite, EDX elemental mapping was performed on the cross-section of $60MoS_2$ specimen (Figure 4.6).

A slightly higher percentage of elemental carbon (graphene) was observed on one end of the paper, which is somewhat typical in a high inclusion content (in this case MoS_2 in graphene) matrix. Supplementary Table S1 summarizes the percentage of each element detected in the corresponding EDX map. Further evidence showing presence of MoS_2 in rGO was achieved through X-ray photoelectron spectroscopy (XPS) (Figure 4.7) that compares powered MoS_2 -SA with $60MoS_2$ paper before and after reduction. MoS_2 peaks that were present in the starting material were also present in the free-standing paper. Notable change was observed in the intensity of oxygen (O1s) and carbon (C1s) peaks for $60MoS_2$ specimen (before and after reduction) due to addition of GO. Further, the exact amount of MoS_2 in the final composite paper (after reduction) was inferred by carrying out thermogravimetric analysis (TGA) in flowing air. As can be seen in Figure 4.3f, rGO and MoS_2 had oxidation events at approx. 450 and 700 °C, respectively. From the TGA data it was observed that thermally reduced $60MoS_2$, $40MoS_2$ and 20 MoS_2 papers had 73, 53 and 35 wt. % of MoS_2 in rGO.

Later, the effect of change in electrical conductivity by change in filler concentration in nanocomposite was studied by use of a four-point measurement technique, which is presented in Figure 4.3g. The increase in conductivity with increasing percentage of rGO is the composite was not linear. This type of behavior is typical when electrically insulating filler (MoS_2) is added to a relatively conducting matrix (rGO) because significant increase in conductivity can only occur after the first conducting path through the sample is formed. [67-68]

4.4.2. Electrochemical Performance

Figure 4.10 shows the voltage charge/discharge and differential capacity curves for rGO and rGO/ MoS_2 with varying MoS_2 content. Figure 4.8a shows the voltage profiles of rGO for 1st and 2nd cycle. The first cycle discharge and charge capacities were 784 $mAhg^{-1}$ and 86 $mAhg^{-1}$.

The differential capacity profiles in Figure 4.8b showed a primary reduction peak at 200 mV, a secondary reduction peak at 610 mV and a weak oxidation peak at 0.9 V. The peak at 200 mV, which is present in all subsequent cycles, is associated with intercalation of rGO, while the peak at 610 mV suggests formation of solid electrolyte interphase (SEI) layer, which exists only in the first cycle. Figure 4.8d shows the differential capacity curves of 1^{st} and 2^{nd} cycle of 20MoS_2 free-standing anode. In the first cycle there are three reduction peaks at around 150 mV that are attributed to MoS_2 /rGO intercalation. Peaks at 580 mV and 0.8 V are attributed to SEI formation in rGO and MoS_2, respectively as these peaks were present only during the first cycle. Only one subtle anodic peak at 1.35 V was observed. As the percentage of MoS_2 increased from 40 % (Figure 4.8f) and 60 % (Figure 4.10b), the domination of Na intercalation in MoS_2 over rGO increased which was evidently seen with increase in the intensity of the reduction peak at around 0.8 V and 0.9 V in the first cycle (peak at 580 mV observed in rGO electrode was relatively absent). In the case of 60MoS_2-raw (Figure 4.8h) electrode, similar peaks to that of 60MoS_2 were observed.

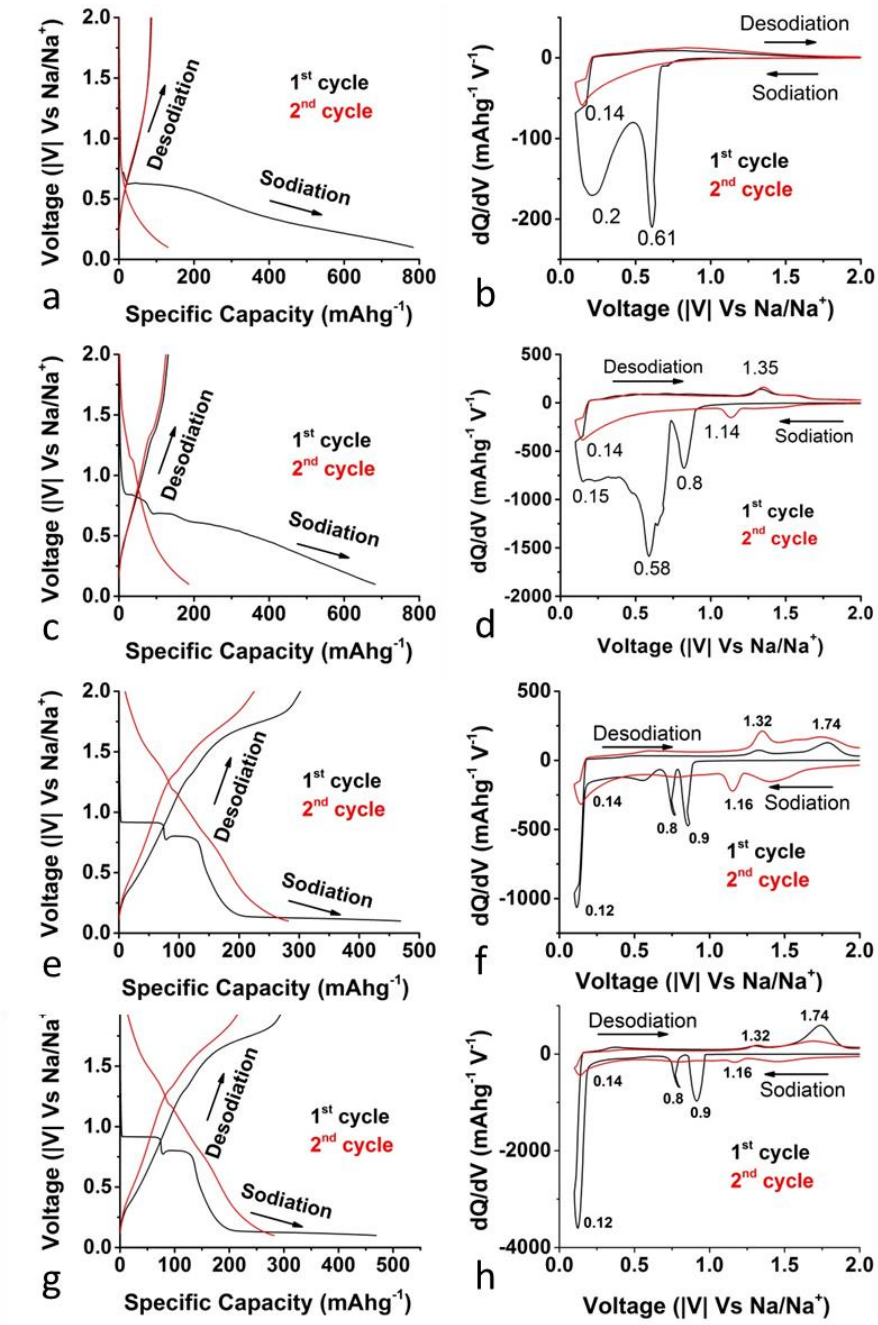

Figure 4-8 First and second cycle voltage profile of MoS_2/rGO composite (a) rGO, (c) 20MoS_2, (e) 40MoS_2 and (g) 60MoS_2-raw along with corresponding (b, d, f, h) differential capacity curves.

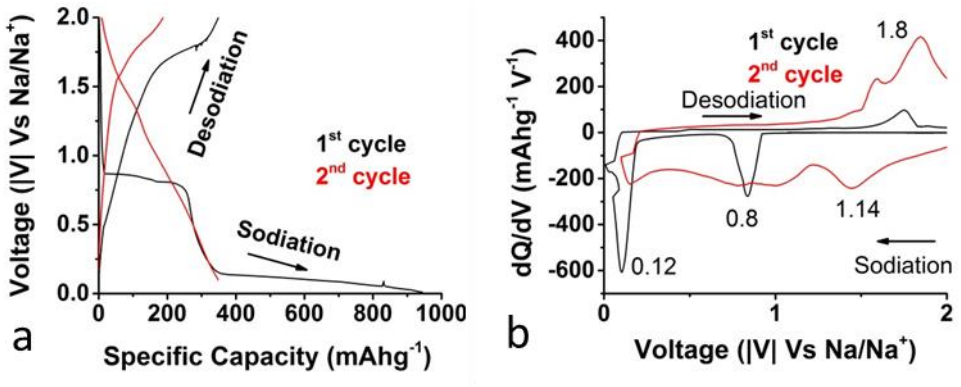

Figure 4-9(a) First and second cycle voltage profile of 90MoS_2 composite paper (b)along with its differential capacity curves.

Figure 4.8c shows the charge capacities and columbic efficiency of rGO, 20MoS_2, 40MoS_2, 60MoS_2 and 60MoS_2 -raw anodes cycled at a constant current density of 25 mAg^{-1}. For rGO we observed that the 1st cycle charge capacity was ~81.5 $mAhg^{-1}$ which was stable at ~70.5 $mAhg^{-1}$ in the 20th cycle The high irreversible first cycle capacity results from electrochemical reaction contributing to SEI layer formation. In the case of rGO/ MoS_2 composite, the first cycle charge capacity increased with increasing percentage of MoS_2 in the composite i.e., 20MoS_2, 40MoS_2, and 60MoS_2 showed 139 $mAhg^{-1}$, 263 $mAhg^{-1}$, and 338 $mAhg^{-1}$, respectively. After initial drop in the capacity, rGO/ MoS_2 composite electrode remained constant at 123, 172 and 218 $mAhg^{-1}$ for 20MoS_2, 40MoS_2 and 60MoS_2 respectively. 60MoS_2 anode was the best performing with 83 % capacity retention and approx. 98 % average efficiency. While MoS_2-raw electrode showed a first cycle charge capacity of 233 $mAhg^{-1}$ that reduced to below ~100 $mAhg^{-1}$ after 20 cycles. Later, rGO/MoS_2 composite paper with 80 % MoS_2 was also tested (see Figure 4.9). The first cycle discharge and charge capacities were 943 and 347 $mAhg^{-1}$. Even though the capacity was higher than 60MoS_2 the anode started to show random spikes in signs of mechanical degradation after second cycle.

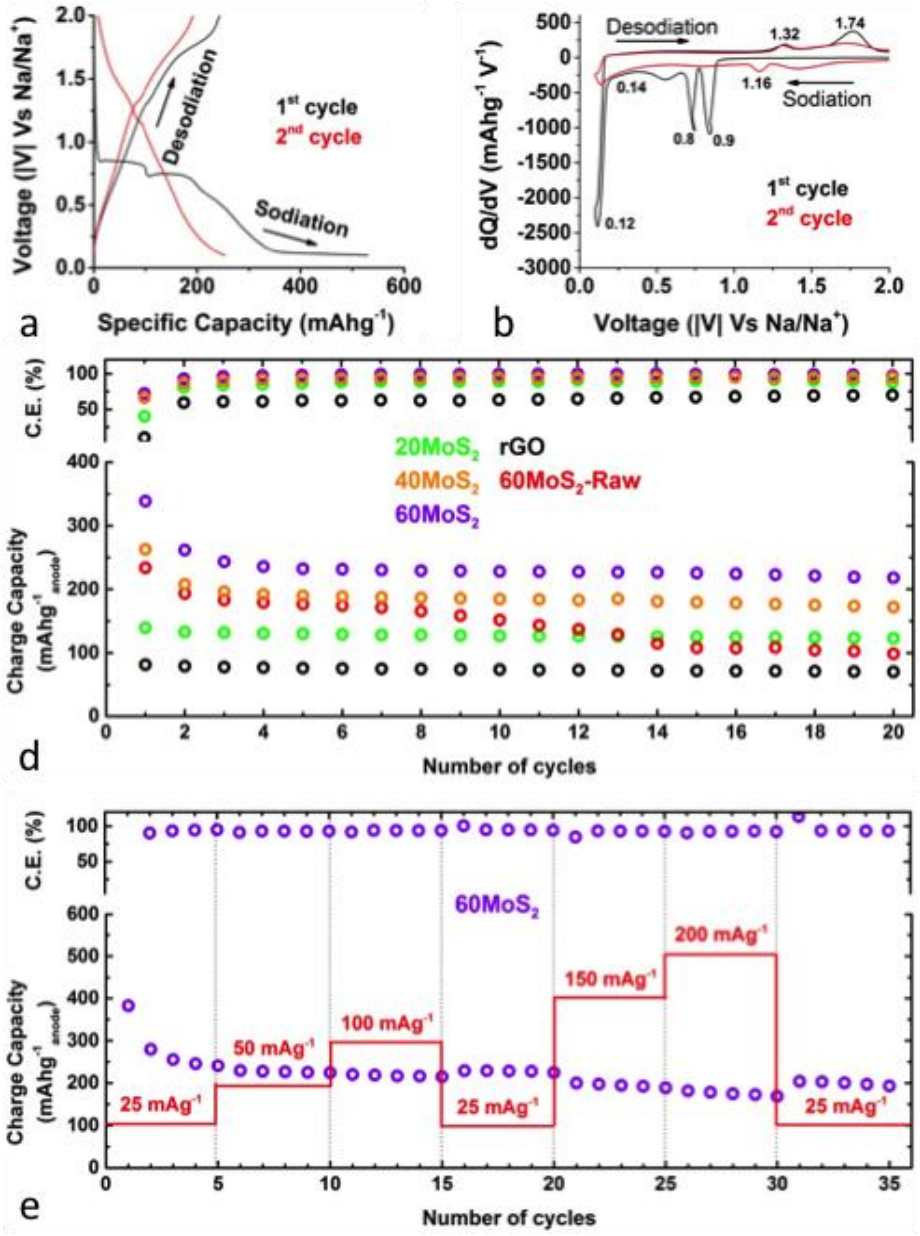

Figure 4-10 (a) Voltage profile of $60MoS_2$ free-standing anode along with its corresponding (b) differential capacity curves for the first two cycles. (b) Sodium charge capacity of all the anodes symmetrically cycled at a constant current density of 25 mAg-1 along with their cyclic efficiencies. (e) Sodium charge capacity and corresponding columbic efficiency of $60MoS_2$ anode asymmetrically cycled at varying current densities.

In case of MoS_2-raw electrode, it is possible that the formation of SEI with successive cycles (and un-exfoliated nature of the flakes), may have hindered the diffusion of Na into the bulk of the specimen, resulting in capacity fading on consecutive cycling. While for acid treated MoS_2-SA electrode the more open and interleaved structure enabled it to utilize the entire bulk of the material in the electrode resulting in exceptional cyclic stability. Presence of conducting graphene sheets further provided the necessary platform on which volume or morphology changes due to conversion reaction could occur without any breakdown in the electrical contact.

Later, the rate capability tests were performed on the best performing electrode specimen i.e., $60MoS_2$ and the C-rate data specimen is shown in Figure 4.10d. This new cell stabilized to a charge capacity of 240 $mAhg^{-1}$ at a current density of 25 mAg^{-1} (with respect to total weight of the electrode) after initial 5 cycles. The charge capacity remained stable (214 $mAhg^{-1}$, 90 % retention) even at current densities as high 100 mAg^{-1}. The anode regained most of its charge capacity (230 $mAhg^{-1}$, 96% retention) when the current density was brought back to 25 mAg^{-1} after 15 cycles. On further increasing the current density to 200 mAg^{-1}, 72% (173 $mAhg^{-1}$) of the initial stable capacity was retained. And again when the current density was brought back to initial 25 mAg^{-1}, the electrode recovered 87 % of its capacity and remained stable for another 5 cycles. It is remarkable that even at 200 mAg^{-1}, the electrode had a stable charge/discharge cycles with no abnormalities, which suggests the improved mechanical stability of this interleaved architecture.

Table 4.2 Comparison of properties of rGO, 20MoS_2, 40MoS_2 and 60MoS_2 free standing paper

Specimen	Thickness, µm	Conductivity, S/cm	Loading, g/cm^2	1st cycle charge capacity, mAh/g	1st cycle efficiency, %	Charge capacity at 20th cycle, mAh/g	Efficiency at 20th cycle, %
rGO	5	2.97	0	81.5	10.2	70.5	70
20MoS_2	10	1.86	0.90258	139	40.2	123	88.2
40MoS_2	15	1.17	2.40688	263	66.4	171.8	95
60MoS_2	20	0.47	5.41548	338	72.2	218.2	98

Further, to check the integrity of the electrode specimen, the cells were disassembled and the electrode recovered for further characterization. Figure 4.11 shows the digital photographs (a-e), low resolution (f-j) and high-resolution (k-o) SEM images of the dissembled cells after 20 cycles. No evidence of surface cracks, volume change or physical imperfections could be observed in the SEM image, suggesting high mechanical/structural strength of the MoS_2 /rGO composite paper. In all cases, the evidence of formation of a thin layer covering the electrode surface, possibly the SEI layer could be observed. The contamination in the specimen, indicated by the arrows, is from the residue of glass separator fibers. Also, these anodes may have been exposed to air during the transfer process resulting in oxidation of Na species, which appeared as bright spots in the images (due to its non-conducting nature). Figure 4.12 shows the images obtained by EDX mapping of the electrode surface. Table S2 shows the at. wt % of various elements detected during the EDX mapping. A high percentage of sodium (19.46 at. %) was

observed on the electrode surface, which is generally attributed to formation of SEI layer during the electrochemical cycling process. Even higher percentage of surface oxygen (41.46 at. %) was observed, which may have come from oxidation of intercalated sodium metal.

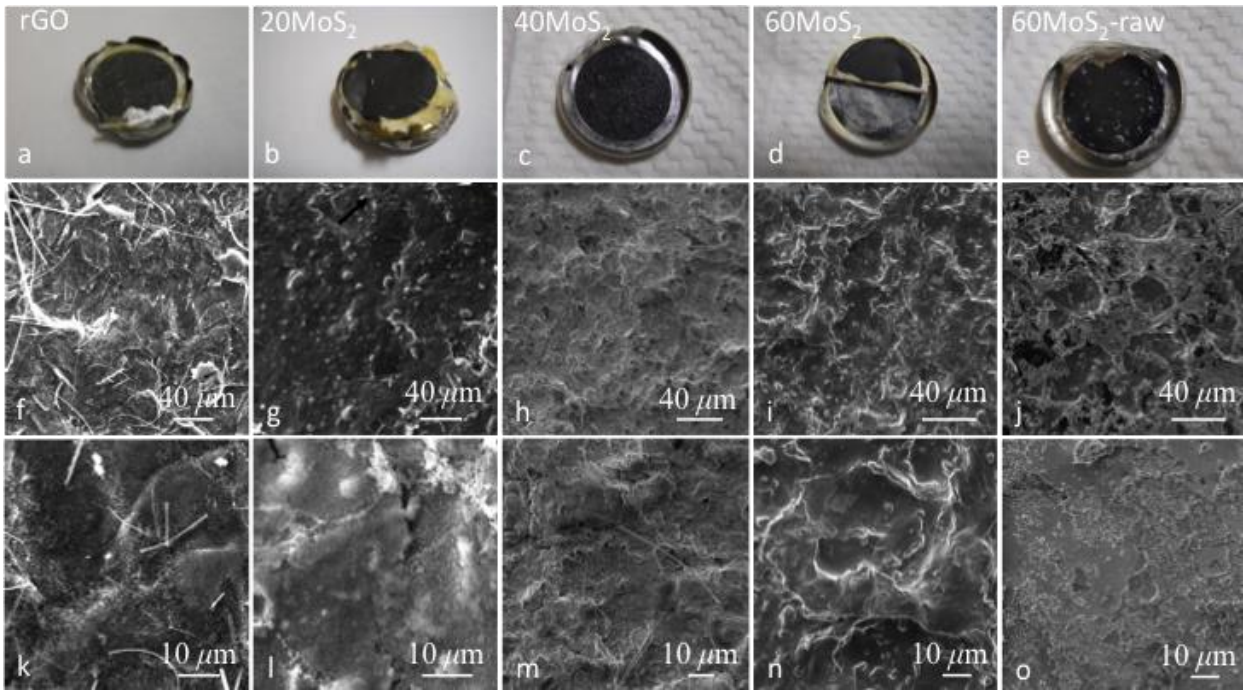

Figure 4-11 Post cycle analysis of the cycled anodes: (a through e) Digital camera images of rGO, 20MoS_2, 40MoS_2, 60MoS_2 and 60MoS_2-raw composite anodes. (f through j): Low magnification SEM images, and (k through o): High magnification SEM images of the dissembled anodes.

Based on the voltage profiles and differential capacity plots, we predict the mechanism of Na-ion's reaction with MoS_2-graphene composite to be a combination of intercalation and conversion type reaction that is generally observed in Li/TMDC systems[40] and previously demonstrated in Na/Ni_3S_2 cathodes as well.[69] Figure 4.13 shows the schematic that illustrates the predicted reaction mechanism in 2.0 to 0.1 V range. Based on a recent study early this year[70], Step 1 is seen as a combination of Na intercalation reaction into the ordered MoS_2 (~0.9 V) and

later into the disordered Na_xMoS_2 layers (~0.8 V). While step 2 represents the conversion reaction resulting in breakdown of MoS_2 in to Mo and Na_2S (since the voltage plateau at ~0.12 V was not observed in rGO electrode, Figure 4.14). Nonetheless, more detailed in-situ spectroscopy studies[71, 72] are needed to elucidate the exact reaction mechanism, particularly in the lower voltage range. This could be the focus of future research.

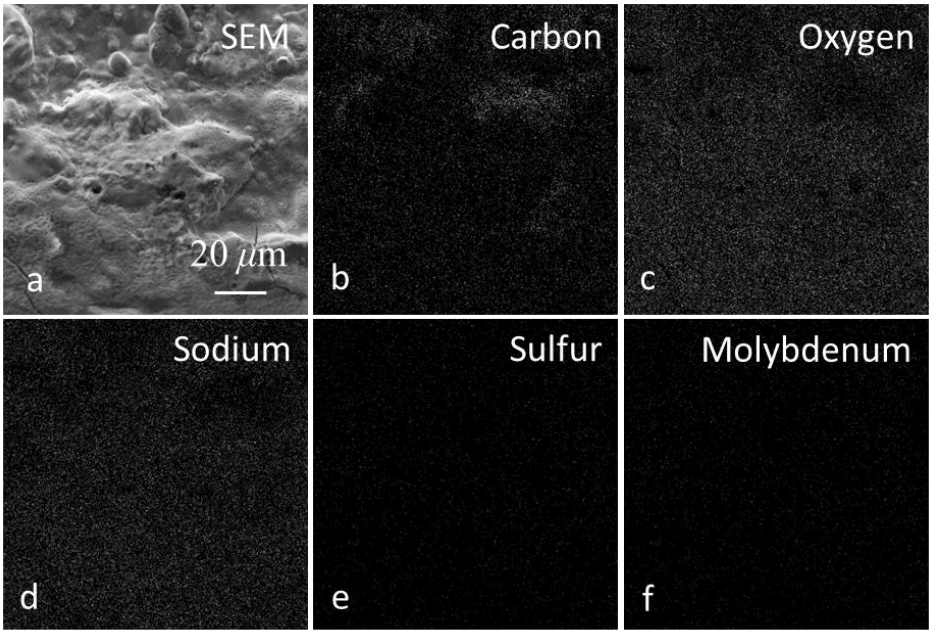

Figure 4-12 (a) SEM cross-sectional inmage of 60MoS_2 and EDX map of (b) carbon, (c) oxygen, (d) sodium, (e) sulfur and (f) molybdenum.

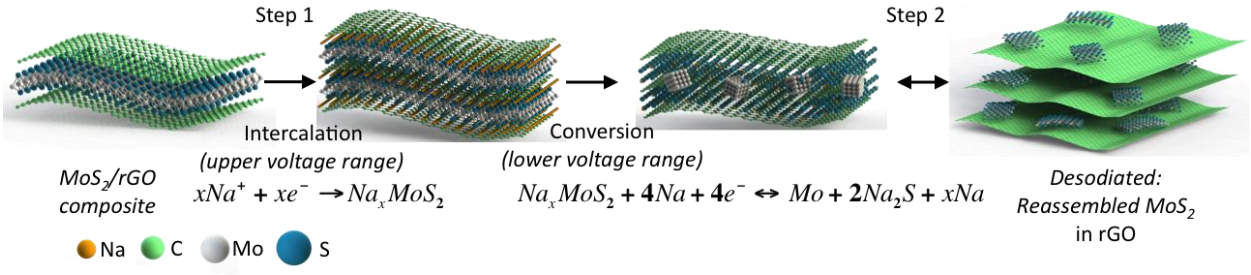

Figure 4-13 Schematic representation showing the predicted mechanism for Na insertion and extraction into the MoS_2/rGO free-standing composite paper electrode. rGO provides

the mechanical/ structural stability and high electrical conductivity network to the TMDC undergoing insertion and conversion reactions with Na-ions.

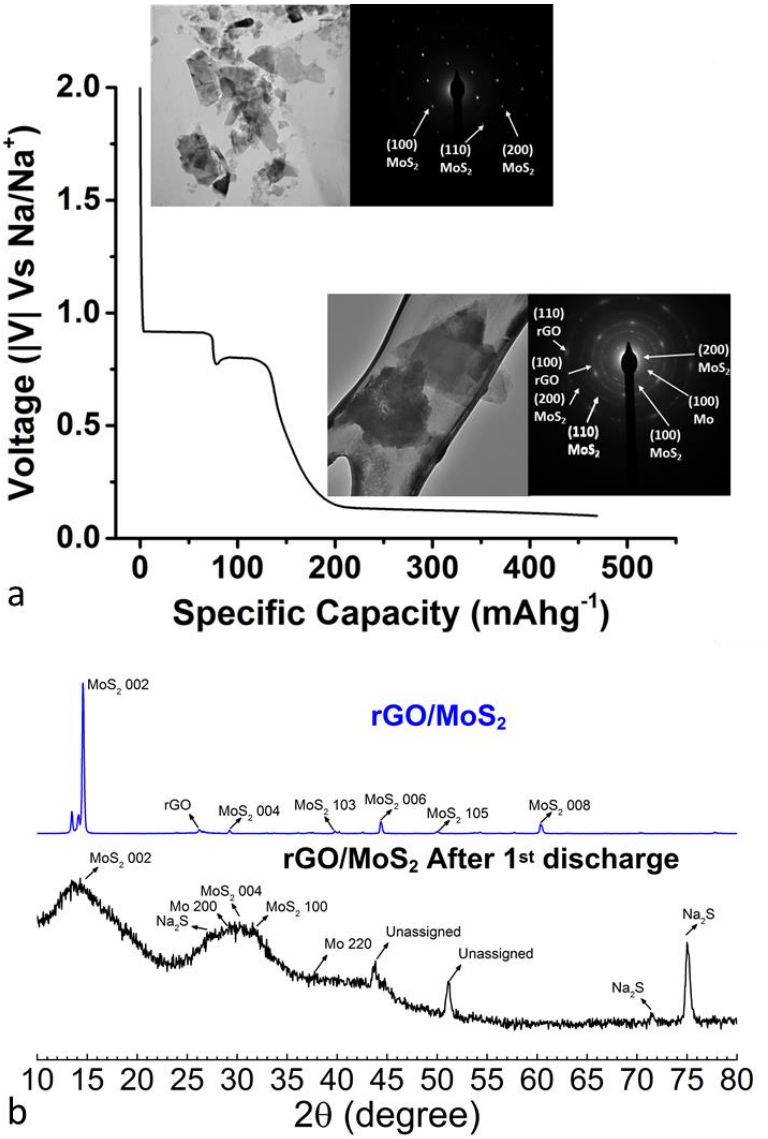

Figure 4-14 Post cycling TEM with SAED pattern and (b) XRD pattern of rGO/MoS_2 before and end of discharge cycle.

Table 4.3Elemental composition obtained by EDX analysis of top surface of 60MoS_2 paper after electrochemical cycling (obtained from Figure 4.14).

Element	Weight percentage (%)	Atomic percentage (%)
Carbon	11.83	24.06
Oxygen	27.43	41.87
Molybdenum	34.91	8.89
Sulfur	7.52	5.73
Sodium	18.31	19.46

Further, the rGO, 40MoS_2 and 60MoS_2 papers were subjected to static tensile tests to ascertain the fracture strength and strain to failure (see methods). Figure 4.15a shows the setup that was used to perform the uniaxial tensile tests. As can be seen, the specimen strip is secured on one end by a computer controlled movable stage, while the other end is fixed to a load cell, which in turn is fixed to an immovable stage. Engineering stress-strain plots are shown in Figure 4.15b. 40MoS_2 showed higher fracture strength and modulus (~7 MPa, ~400 MPa) than 60MoS_2 (~2 MPa, ~100 MPa) composite paper. On comparison, rGO had fracture strength and modulus of approx. 12 MPa and 886 MPa, respectively. The strain to failure was higher in case of 60MoS_2 specimen reaching values in excess of approx. 2 %. A total of five specimens were tested for 40MoS_2 and 60MoS_2 paper each that are shown in the photographic image in Figure 4.15c and d, respectively. Data is summarized in Table 6.4. Figure 4.15e and f are the corresponding SEM images of the fractured edge for 40MoS_2 and 60MoS_2, respectively. The edge was observed to be more regular and smooth for 60MoS_2 than for 40MoS_2. The tensile

strength of rGO paper is comparable to those reported by Nyugen's group involving in-situ reduced GO papers[73].

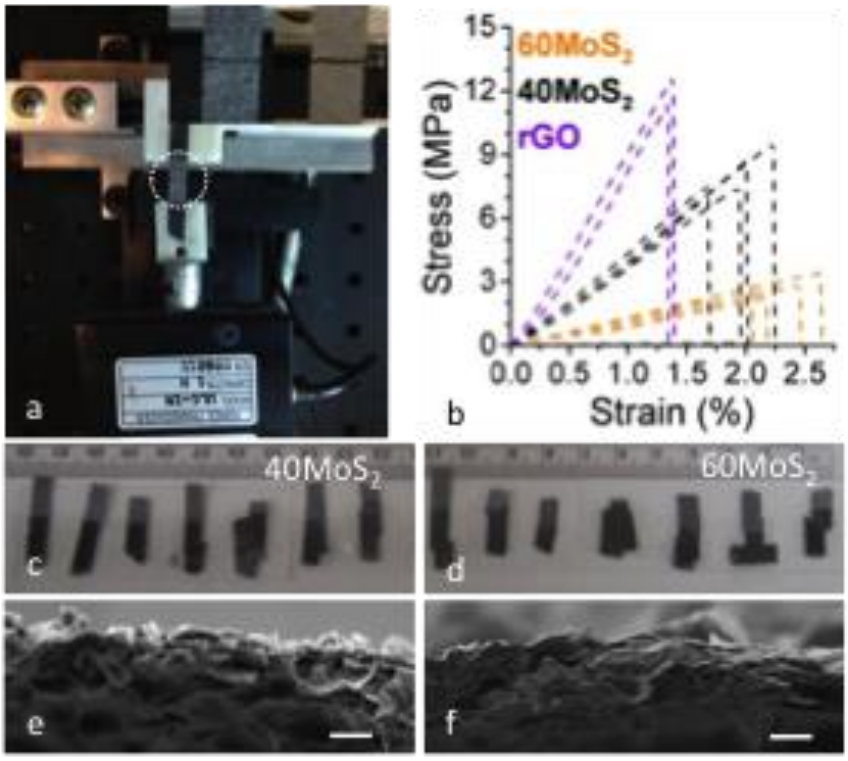

Figure 4-15 Tensile test setup with sample after fracture from loading. (b) Stress-strain plot for rGO, $40MoS_2$ and $60MoS_2$ freestanding papers. Photographic image of (c) $40MoS_2$ and (d) $60MoS_2$ paper tested in this study. (e, and f) are the corresponding SEM cross-sectional images showing the fractured surface. The scale bar is 20 µm.

Table 4.4 Mechanical properties of free-standing paper with 40 % and 60 % MoS_2 in the composite.

Specimen	Young's Modulus (MPa)	Ultimate Tensile Strength (MPa)	Failure Strain (%)
rGO	897.86±89.7	12.57±0.6	1.4±0.02
	874.62±87.4	11.37±0.6	1.3±0.02
$40MoS_2$	427.03±42.7	9.48±0.5	2.22±0.04
	434.5±43.4	8.69±0.4	2±0.04
	386.01±38.6	7.45±0.4	1.93±0.04
	450±45	7.56±0.4	1.68±0.03
	424.8±42.4	6.06±0.3	1.43±0.03
$60MoS_2$	130.8±13	3.44±0.2	2.63±0.05
	115.92±11.5	2.84±0.1	2.45±0.05
	102.76±10.3	2.23±0.1	2.17±0.04
	131.22±13.1	2.69±0.1	2.05±0.04
	125.85±12.6	2.13±0.1	1.69±0.03

These values are however, much lower than GO papers but this is hardly surprising considering that our papers were annealed at high temperatures (500 °C and 900 °C) and the mechanical strength of GO generally decreases with increasing annealing temperatures caused release of oxygen groups that disturbs the mechanical integrity of the paper resulting in a highly crumpled structure[74]. The large variation in strain to failure for the composite specimen could be due to variation in the homogeneity of the specimens (large size of the paper and higher loading 4 $mg.cm^{-2}$) or due to the process in which both layered materials (graphene and MoS_2) are interlayered. Subsequently, combined with observations in SEM images, $60MoS_2$ had a larger variation in failure strain as the more slippery MoS_2 sheets can slide better than crumpled rGO sheets.

4.5. Conclusion

We have demonstrated synthesis of a composite layered paper consisting of acid exfoliated MoS_2 nanoflakes in an rGO matrix. Mechanical tests involving static uniaxial tension reveal good mechanical strength (approx. 2 MPa fracture strength) and high failure strain (approx. 1.8 %) in these materials. Further, the composite paper was directly utilized as counter electrode in Na^+ battery half-cell and its performance was evaluated as a potential anode for use in a Na^+ battery full cell. These tests revealed high first cycle electrochemical capacity of 338 $mAhg^{-1}$ with respect to total weight of the electrode with excellent cycleability of Na^+ at room temperature. This study provides the first experimental evidence of reversible electrochemical storage of Na in layered self-standing MoS_2 composite electrode at room temperatures and is expected to open new avenues for use of large area free-standing binder-free flexible electrodes for Na-ion battery applications.

4.6. Acknowledgements

Lamuel David would like to thank Erin Black for assistance with specimen preparation. Thanks are also due to Professor Kevin Lease (Kansas State University) for access to his lab for mechanical testing.

4.7. References

1. Armand, M.; Tarascon, J. M.; Building better batteries. *Nature*, 2008, *451* (7179), 652-657.

2. Manthiram, A.; Fu, Y.; Su, Y. S., In Charge of the World: Electrochemical Energy Storage. *The Journal of Physical Chemistry Letters* 2013, *4* (8), 1295-1297

3. Saravanan, K.; Mason, C. W.; Rudola, A.; Wong, K. H.; Balaya, P., The First Report on Excellent Cycling Stability and Superior Rate Capability of $Na_3V_2(PO_4)_3$ for Sodium Ion Batteries. *Advanced Energy Materials* 2013, *3*(4), 444-450.

4. Tarascon, J. M.; Is lithium the new gold? *Nat. Chem*., 2010, 2, 510.

5. Ellis. B. L.; Makahnouk. W. R. M.; Makimura. Y.; Toghill. K.; Nazar. L. F.; *Nat. Mater.*, 2007, 6, 749-753.

6. Kim, D.; Kang, S. H.; Slater, M.; Rood, S.; Vaughey, J. T.; Karan, N.; Balasubramanian, M.; Johnson, C. S., Enabling Sodium Batteries Using Lithium-Substituted Sodium Layered Transition Metal Oxide Cathodes. *Advanced Energy Materials* 2011, *1* (3), 333-336.

7. Cao, Y.; Xiao, L.; Wang, W.; Choi, D.; Nie, Z.; Yu, J.; Saraf, L. V.; Yang, Z.; Liu, J., Reversible Sodium Ion Insertion in Single Crystalline Manganese Oxide Nanowires with Long Cycle Life. *Advanced Materials* 2011, *23* (28), 3155-3160.

8. Liu, H.; Zhou, H.; Chen, L.; Tang, Z.; Yang, W., Electrochemical insertion/deinsertion of sodium on NaV_6O_{15} nanorods as cathode material of rechargeable sodium-based batteries. *Journal of Power Sources* 2011, *196* (2), 814-819.

9. Whitacre, J. F.; Tevar, A.; Sharma, S., $Na_4Mn_9O_{18}$ as a positive electrode material for an aqueous electrolyte sodium-ion energy storage device. *Electrochemistry Communications* 2010, *12* (3), 463-466.

10. Barker, J.; Saidi, M. Y.; Swoyer, J. L., A Sodium-Ion Cell Based on the Fluorophosphate Compound $NaVPO_4F$. *Electrochemical and Solid-State Letters* 2003, *6* (1), A1-A4.

11. Lu, X.; Xia, G.; Lemmon, J. P.; Yang, Z., Advanced materials for sodium-beta alumina batteries: Status, challenges and perspectives. *Journal of Power Sources* 2010, *195* (9), 2431-2442.

12. Chevrier, V. L.; Ceder, G., Challenges for Na-ion Negative Electrodes. *Journal of The Electrochemical Society* 2011, *158* (9), A1011-A1014.

13. Lin, Y. M.; Abel, P. R.; Gupta, A.; Goodenough, J. B.; Heller, A.; Mullins, C. B., Sn–Cu Nanocomposite Anodes for Rechargeable Sodium-Ion Batteries. *ACS Applied Materials & Interfaces* 2013, *5* (17), 8273–8277.

14. Darwiche, A.; Marino, C.; Sougrati, M. T.; Fraisse, B.; Stievano, L.; Monconduit, L., Better Cycling Performances of Bulk Sb in Na-Ion Batteries Compared to Li-Ion Systems: An Unexpected Electrochemical Mechanism. *Journal of the American Chemical Society* 2012, *134* (51), 20805-20811.

15. Xiao, L.; Cao, Y.; Xiao, J.; Wang, W.; Kovarik, L.; Nie, Z.; Liu, J., High capacity, reversible alloying reactions in SnSb/C nanocomposites for Na-ion battery applications. *Chemical Communications* 2012, *48* (27), 3321-3323.

16. Qian, J.; Chen, Y.; Wu, L.; Cao, Y.; Ai, X.; Yang, H., High capacity Na-storage and superior cyclability of nanocomposite Sb/C anode for Na-ion batteries. *Chemical Communications* 2012, *48* (56), 7070-7072.

17. Qian, J.; Wu, X.; Cao, Y.; Ai, X.; Yang, H., High Capacity and Rate Capability of Amorphous Phosphorus for Sodium Ion Batteries. *Angewandte Chemie International Edition* 2013, *52* (17), 4633-4636.

18. Kim, Y.; Park, Y.; Choi, A.; Choi, N.S.; Kim, J.; Lee, J.; Ryu, J. H.; Oh, S. M.; Lee, K. T., An Amorphous Red Phosphorus/Carbon Composite as a Promising Anode Material for Sodium Ion Batteries. *Advanced Materials 2013, (25)*, 3045–3049.

19. Xiong, H.; Slater, M. D.; Balasubramanian, M.; Johnson, C. S.; Rajh, T., Amorphous TiO_2 Nanotube Anode for Rechargeable Sodium Ion Batteries. *The Journal of Physical Chemistry Letters* 2011, *2* (20), 2560-2565.

20. Zhu, H.; Jia, Z.; Chen, Y.; Weadock, N.; Wan, J.; Vaaland, O.; Han, X.; Li, T.; Hu, L., Tin Anode for Sodium-Ion Batteries Using Natural Wood Fiber as a Mechanical Buffer and Electrolyte Reservoir. *Nano Letters* 2013, *13* (7), 3093-3100.

21. Zhu, Y.; Han, X.; Xu, Y.; Liu, Y.; Zheng, S.; Xu, K.; Hu, L.; Wang, C., Electrospun Sb/C Fibers for a Stable and Fast Sodium-Ion Battery Anode. *ACS Nano* 2013, *7* (7), 6378-6386.

22. Stevens, D. A.; Dahn, J. R., High Capacity Anode Materials for Rechargeable Sodium-Ion Batteries. *Journal of The Electrochemical Society* 2000, *147* (4), 1271-1273.

23. Alcántara, R.; Jiménez-Mateos, J. M.; Lavela, P.; Tirado, J. L., Carbon black: a promising electrode material for sodium-ion batteries. *Electrochemistry Communications* 2001, *3* (11), 639-642.

24. Alcántara, R.; Jiménez Mateos, J. M.; Tirado, J. L., Negative Electrodes for Lithium- and Sodium-Ion Batteries Obtained by Heat-Treatment of Petroleum Cokes below 1000°C. *Journal of The Electrochemical Society* 2002, *149* (2), A201-A205.

25. Komaba, S.; Murata, W.; Ishikawa, T.; Yabuuchi, N.; Ozeki, T.; Nakayama, T.; Ogata, A.; Gotoh, K.; Fujiwara, K., Electrochemical Na Insertion and Solid Electrolyte Interphase for Hard-Carbon Electrodes and Application to Na-Ion Batteries. *Advanced Functional Materials* 2011, *21* (20), 3859-3867.

26. Cao, Y.; Xiao, L.; Sushko, M. L.; Wang, W.; Schwenzer, B.; Xiao, J.; Nie, Z.; Saraf, L. V.; Yang, Z.; Liu, J., Sodium Ion Insertion in Hollow Carbon Nanowires for Battery Applications. *Nano Letters* 2012, *12* (7), 3783-3787.

27. Palacin, M. R., Recent advances in rechargeable battery materials: a chemist's perspective. *Chemical Society Reviews* 2009, *38* (9), 2565-2575.

28. Ponrouch, A.; Goñi, A. R.; Palacín, M. R., High capacity hard carbon anodes for sodium ion batteries in additive free electrolyte. *Electrochemistry Communications* 2013, *27* (0), 85-88.

29. Buchholz, D.; Moretti, A.; Kloepsch, R.; Nowak, S.; Siozios, V.; Winter, M.; Passerini, S., Toward Na-ion Batteries—Synthesis and Characterization of a Novel High Capacity Na Ion Intercalation Material. *Chemistry of Materials* 2012, *25* (2), 142-148.

30. Chang, K.; Geng, D.; Li, X.; Yang, J.; Tang, Y.; Cai, M.; Li, R.; Sun, X., Ultrathin MoS_2/Nitrogen-Doped Graphene Nanosheets with Highly Reversible Lithium Storage. *Advanced Energy Materials* 2013, *3* (7), 839-844.

31. Liu, H.; Su, D.; Zhou, R.; Sun, B.; Wang, G.; Qiao, S. Z., Highly Ordered Mesoporous MoS_2 with Expanded Spacing of the (002) Crystal Plane for Ultrafast Lithium Ion Storage. *Advanced Energy Materials* 2012, *2* (8), 970-975.

32. Tepavcevic, S.; Xiong, H.; Stamenkovic, V. R.; Zuo, X.; Balasubramanian, M.; Prakapenka, V. B.; Johnson, C. S.; Rajh, T., Nanostructured Bilayered Vanadium Oxide Electrodes for Rechargeable Sodium-Ion Batteries. *ACS Nano* 2011, *6* (1), 530-538.

33. Hu, Y.; Li, X.; Lushington, A.; Cai, M.; Geng, D.; Banis, M. N.; Li, R.; Sun, X., Fabrication of MoS_2-Graphene Nanocomposites by Layer-by-Layer Manipulation for High-Performance Lithium Ion Battery Anodes. *ECS Journal of Solid State Science and Technology* 2013, *2* (10), M3034-M3039.

34. Xiao, J.; Wang, X.; Yang, X. Q.; Xun, S.; Liu, G.; Koech, P. K.; Liu, J.; Lemmon, J. P., Electrochemically Induced High Capacity Displacement Reaction of PEO/MoS_2/Graphene Nanocomposites with Lithium. *Advanced Functional Materials* 2011, *21* (15), 2840-2846.

35. Zhou, X.; Wan, L. J.; Guo, Y. G., Facile synthesis of MoS_2@CMK-3 nanocomposite as an improved anode material for lithium-ion batteries. *Nanoscale* 2012, *4* (19), 5868-5871.

36. Zhou, X.; Wan, L.-J.; Guo, Y. G., Synthesis of MoS_2 nanosheet-graphene nanosheet hybrid materials for stable lithium storage. *Chemical Communications* 2013, *49* (18), 1838-1840.

37. Hwang, H.; Kim, H.; Cho, J., MoS_2 Nanoplates Consisting of Disordered Graphene-like Layers for High Rate Lithium Battery Anode Materials. *Nano Letters* 2011, *11* (11), 4826-4830.

38. Chang, K.; Chen, W., l-Cysteine-Assisted Synthesis of Layered MoS_2/Graphene Composites with Excellent Electrochemical Performances for Lithium Ion Batteries. *ACS Nano* 2011, *5* (6), 4720-4728.

39. Das, S. K.; Mallavajula, R.; Jayaprakash, N.; Archer, L. A., Self-assembled MoS_2-carbon nanostructures: influence of nanostructuring and carbon on lithium battery performance. *Journal of Materials Chemistry* 2012, *22* (26), 12988-12992.

40. Cabana, J.; Monconduit, L.; Larcher, D.; Rosa Palacin, M. Beyond Intercalation- Based Li-Ion Batteries: The State of the Art and Challenges of Electrode Materials Reacting Through Conversion Reactions. *Advanced Materials* 2010, *22*, E170-E192.

41. Ji, H.; Zhang, L.; Pettes, M. T.; Li, H.; Chen, S.; Shi, L.; Piner, R.; Ruoff, R. S., Ultrathin Graphite Foam: A Three-Dimensional Conductive Network for Battery Electrodes. *Nano Letters* 2012, *12* (5), 2446-2451.

42. Chhowalla, M. ; Shin, H. S.; Eda, G.; Li, L. J.; Loh, K. P.; Zhang, H., The chemistry of two-dimensional layered transition metal dichalcogenide nanosheets. *Nature Chemistry* 2013, *5* (4), 263-275.

43. Ge, P.; Fouletier, M., Electrochemical intercalation of sodium in graphite. *Solid State Ionics* 1988, *28–30, Part 2*(0), 1172-1175.

44. Stevens, D. A.; Dahn, J. R., The Mechanisms of Lithium and Sodium Insertion in Carbon Materials. *Journal of The Electrochemical Society* 2001, *148* (8), A803-A811.

45. Asher, R. C., A lamellar compound of sodium and graphite. *Journal of Inorganic and Nuclear Chemistry* 1959, *10* (3–4), 238-249.

46. Hwang, H.; Kim, H.; Cho, J., MoS_2 Nanoplates Consisting of Disordered Graphene-like Layers for High Rate Lithium Battery Anode Materials. *Nano Letters* 2011, *11* (11), 4826-4830.

47. Hu, L.; Choi, J. W.; Yang, Y.; Jeong, S.; La Mantia, F.; Cui, L.F.; and Cui, Y. Highly Conductive Paper for Energy-Storage Devices. *Proceedings of the National Academy of Sciences*, 2009, *106* (51), 21490-21494.

48. Cui, L. F.; Hu, L.; Choi, J. W.; and Cui, Y. Light-Weight Free-Standing Carbon Nanotube-Silicon Films for Anodes of Lithium Ion Batteries. *ACS Nano*, 2010, *4* (7), 3671-3678.

49. Wang, D.; Kou, R.; Choi, D.; Yang, Z.; Nie, Z.; Li, J.; Saraf, L. V.; Hu, D.; Zhang, J.; Graff, G. L.; Liu, J.; Pope, M. A.; Aksay, I. A., Ternary Self-Assembly of Ordered Metal Oxide−Graphene Nanocomposites for Electrochemical Energy Storage. *ACS Nano* 2010, *4* (3), 1587-1595.

50. Li, N.; Chen, Z.; Ren, W.; Li, F.; Cheng, H. M., Flexible graphene-based lithium ion batteries with ultrafast charge and discharge rates. *Proceedings of the National Academy of Sciences* 2012, *109* (43), 17360-17365.

51. Zhao, X.; Hayner, C. M.; Kung, M. C.; Kung, H. H., In-Plane Vacancy-Enabled High-Power Si–Graphene Composite Electrode for Lithium-Ion Batteries. *Advanced Energy Materials* 2011, *1* (6), 1079-1084.

52. Abouimrane, A.; Compton, O. C.; Amine, K.; Nguyen, S. T., Non-Annealed Graphene Paper as a Binder-Free Anode for Lithium-Ion Batteries. *The Journal of Physical Chemistry C* 2010, *114* (29), 12800-12804.

53. Koo, M.; Park, K. I.; Lee, S. H.; Suh, M.; Jeon, D. Y.; Choi, J. W.; Kang, K.; Lee, K. J., Bendable Inorganic Thin-Film Battery for Fully Flexible Electronic Systems. *Nano Letters* 2012, *12* (9), 4810-4816.

54. Magasinski, A.; Dixon, P.; Hertzberg, B.; Kvit, A.; Ayala, J.; Yushin, G., High-performance lithium-ion anodes using a hierarchical bottom-up approach. *Nature Materials* 2010, *9* (4), 353-358

55. Hummers, W. S.; Offeman, R. E., Preparation of Graphitic Oxide. *Journal of the American Chemical Society* 1958, *80* (6), 1339-1339.

56. Bhandavat, R.; David, L.; Singh, G., Synthesis of Surface-Functionalized WS_2 Nanosheets and Performance as Li-Ion Battery Anodes. *The Journal of Physical Chemistry Letters* 2012, *3* (11), 1523-1530.

57. Lotya, M.; Hernandez, Y.; King, P. J.; Smith, R. J.; Nicolosi, V.; Karlsson, L. S.; Blighe, F. M.; De, S.; Wang, Z.; McGovern, I. T.; Duesberg, G. S.; Coleman, J. N., Liquid Phase Production of Graphene by Exfoliation of Graphite in Surfactant/Water Solutions. *Journal of the American Chemical Society* 2009, *131* (10), 3611-3620.

58. Coleman, J. N.; Lotya, M.; O'Neill, A.; Bergin, S. D.; King, P. J.; Khan, U.; Young, K.; Gaucher, A.; De, S.; Smith, R. J.; Shvets, I. V.; Arora, S. K.; Stanton, G.; Kim, H. Y.; Lee, K.; Kim, G. T.; Duesberg, G. S.; Hallam, T.; Boland, J. J.; Wang, J. J.; Donegan, J. F.; Grunlan, J. C.; Moriarty, G.; Shmeliov, A.; Nicholls, R. J.; Perkins, J. M.; Grieveson, E. M.; Theuwissen, K.; McComb, D. W.; Nellist, P. D.; Nicolosi, V., Two-Dimensional Nanosheets Produced by Liquid Exfoliation of Layered Materials. *Science* 2011, *331* (6017), 568-571.

59. Bertrand, P. A., Surface-phonon dispersion of MoS_{2}. *Physical Review B* 1991, *44* (11), 5745-5749.

60. Chen, J. M.; Wang, C. S., Second order Raman spectrum of MoS_2. *Solid State Communications* 1974, *14* (9), 857-860.

61. Windom, B.; Sawyer, W. G.; Hahn, D., A Raman Spectroscopic Study of MoS_2 and MoO_3: Applications to Tribological Systems. *Tribology Letters* 2011, *42* (3), 301-310.

62. Stacy, A. M.; Hodul, D. T., Raman spectra of IVB and VIB transition metal disulfides using laser energies near the absorption edges. *Journal of Physics and Chemistry of Solids* 1985, *46* (4), 405-409.

63. Frey, G. L.; Tenne, R.; Matthews, M. J.; Dresselhaus, M. S.; Dresselhaus, G., Raman and resonance Raman investigation of MoS_{2} nanoparticles. *Physical Review B* 1999, *60* (4), 2883-2892.

64. Jiménez Sandoval, S.; Yang, D.; Frindt, R. F.; Irwin, J. C., Raman study and lattice dynamics of single molecular layers of MoS_{2}. *Physical Review B* 1991, *44* (8), 3955-3962.

65. Frey, G. L.; Reynolds, K. J.; Friend, R. H.; Cohen, H.; Feldman, Y., Solution-Processed Anodes from Layer-Structure Materials for High-Efficiency Polymer Light-Emitting Diodes. *Journal of the American Chemical Society* 2003, *125* (19), 5998-6007.

66. Moser, J.; Lévy, F., Growth mechanisms and near-interface structure in relation to orientation of MoS_2 sputtered thin films. *Journal of Materials Research* 1992, *7* (03), 734-740 M3 - 10.1557/JMR.1992.0734.

67. Cunningham, G.; Lotya, M.; McEvoy, N.; Duesberg, G. S.; van der Schoot, P.; Coleman, J. N., Percolation scaling in composites of exfoliated MoS_2 filled with nanotubes and graphene. *Nanoscale* 2012, *4* (20), 6260-6264.

68. D. Stauffer and A. Aharony, Introduction to Percolation Theory, Taylor & Francis, London, 1985.

69. Kim, J. S.; Ahn, H. J.; Ryu, H. S; Kim, D. J.; Cho, G. B.; Kim, K. W.; Nam, T. H.; Ahn, J. H., The discharge properties of Na/Ni_3S_2 cell at ambient temperature. *Journal of Power Sources* 2008, *178* (2), 852–856.

70. Park, J.; Kim, J.S.; Park, J.W.; Nama, T.H.; Kim, K.W.; Ahn, J.H.; Wang, G.; Ahn, H.J., Discharge mechanism of MoS_2 for sodium ion battery: Electrochemical measurements and characterization. *Electrochimica Acta* 2013, *92*, 427– 432.

71. Bhattacharyya, R.; Key, B.; Chen, H.; Best, A.S.; Hollenkamp, A.F.; Grey, C.P., In situ NMR Observation of the Formation of Metallic Lithium Microstructures in Lithium Batteries. *Nature Materials* 2010, *9*, 504-510.

72. Yamakawa, N.; Jiang, M.; Key, B.; Grey, C. P., A study of the lithium conversion mechanism of iron fluoride in a Li ion battery, by using solid state NMR, XRD and PDF analysis studies. *Journal of the American Chemical Society* 2009, *131*, 10525-10536.

73. Compton, O. C.; Dikin, D. A.; Putz, K. W.; Brinson, L. C.; Nguyen, S. T., Electrically Conductive "Alkylated" Graphene Paper Via Chemical Reduction of Amine-Functionalized Graphene Oxide Paper. *Advanced Materials* 2010, *22*, 892– 896.

74. Compton, O. C.; Nguyen, S. T., Graphene Oxide, Highly Reduced Graphene Oxide, and Graphene: Versatile Building Blocks for Carbon-Based Materials *Small* 2010, *6*, 711– 723.

Chapter 5 - Silicon Oxycarbide/Graphene Composite Paper Electrode for Long Cycle Lithium-Ion Batteries[3]

5.1. Abstract

Silicon-based Lithium-ion battery anodes are known to suffer from low cyclability because of large volume changes associated with Li-insertion and extraction; especially for thick/heavy anodes that are foremost for any practical application. Here in we report a new type of large area (approximately 6 in. x 1 in.) self-standing anode material consisting of molecular precursor-derived silicon oxycarbide (SiOC) glass particles embedded in a chemically modified crumpled graphene (rGO) matrix. The porous three-dimensional (3-D) crumpled rGO matrix served as an effective electron conductor and current collector with a stable chemical and mechanical structure, and the embedded amorphous SiOC particles actively cycled Li-ions with high efficiency. Owing to this morphology, the SiOC/rGO composite electrode (at 2 $mg.cm^{-2}$) exhibited stable charge capacity (total electrode weight) of 543 $mAh.g^{-1}$ at current densities up to 2400 $mA.g^{-1}$ with nearly 100% average cycling efficiency at room temperature. At sub-zero temperatures (-15 °C), the capacity was observed to be approximately 200 $mAh.g^{-1}$. The paper electrode showed no signs of damage even after continuous cycling for more than 1000 charge/discharge cycles. Static uni-axial tensile tests analysis revealed the difference in fracture mechanism between rGO and 60SiOC composite freestanding paper.

[3] Submitted for Publication in Nature Communications (L. David, R. Bhandavat and G. Singh, "SiOC-rGO Composite Free Standing Paper for Li-ion Battery Applications" Manuscript # NCOMMS-15-04605).

5.2. Introduction

Concentrated efforts are currently employed to discover a practical replacement for traditional Li-ion battery electrodes i.e., graphite anode and $LiCoO_2$ cathode with materials that continuously deliver high power and energy densities at high cycling efficiencies without damage. [1-5] Alloying reaction electrodes such as silicon that can deliver as much as 5 to 10 times higher discharge capacity than traditional graphite, are at the forefront of this research. High capacity electrodes, however, are prone to enormous volume changes (approx. 300%) that generally lead to structural collapse and capacity fading during successive lithiation/delithiation. [6−12] Recent work has shown that decreasing particle size or electrode nanostructuring allows the electrode to withstand high volumetric strains associated with repeated Li alloying and de-alloying. Pomegranate-inspired carbon-coated Si nanoparticles, yoke shell-structured SiC nanocomposites, and Si/C core/shell composites (prepared at low mass loading) have proven to survive several hundred cycles without damage.[9-12] Yet, electrode nanostructuring has lead to new fundamental challenges such as low volumetric capacity (low tap density), increased electrical resistance between the nanoparticles, increased manufacturing costs, and lower Coulombic efficiency due to side reactions with the electrolyte. These challenges have not been fully addressed. What's more, a particle-based electrode's long−term cyclability hinges on the inter-particle electrical connection and particle adhesion to the metallic substrate which decreases rapidly with increasing charge/discharge cycles, particularly for thick high capacity electrodes.[13]

In this context, the graphene−based multicomponent composite anodes are an attractive alternative to traditional (binder and carbon-black) designs, chiefly because of graphene's superior electronic conductivity, mechanical strength and ability to be interfaced with Li active redox components such as particles of Si, Ge, and transition metals sulfides/oxides resulting in

electrodes that are intrinsically conducting and promote faster ion diffusion. [14–41] Additional advantages include weight savings of up to 10 % of the total battery weight[6] if the electrode is prepared in the freestanding form, improved corrosion resistance (elimination of metal foil), and enhanced flexibility, particularly for bendable, implantable, and roll-up electronics.

In spite of these advantages, graphene paper-electrodes do not offer an absolute solution because of associative disadvantages: (a) potential limiting of overall battery capacity due to insufficient active mass (thickness generally limited to submicrometers), (b) expensive techniques required for synthesis of Li-redox components, and (c) more important, paper anodes generally show very high first cycle loss (50 to 60%), low cycling efficiency (95 to 98%), and poor capacity retention at high current densities (damage at high C-rates),[23–41] making graphene-paper electrodes somewhat impractical for use in an Li ion battery full-cell. Here again, very few studies have been performed to investigate the mechanical and fracture properties of composite paper-based electrodes.

Continued search for better anodes has brought attention to unique, rarely studied molecular precursor-derived Si-based glass-ceramics (such as silicon oxycarbide or SiOC) materials.[42-49] SiOC is a high temperature glass-ceramic with an open polymer-like network structure consisting of two interpenetrating amorphous phases of SiOC (Si bonded to O and C) and disordered carbon. [45] Its low weight density (~2.1 $g.cm^{-3}$) and open structure enables high charge and discharge rates with a gravimetric capacity more than twice that of commercial graphite electrode. More important, major portion of the electrochemical capacity in SiOC is due to reversible Li-adsorption in the disordered carbon phase and not the conventional alloying reaction with Si, ensuing relatively lower volumetric changes.[46,47] Regrettably, these glass-ceramics are poor conductors of electronic/ionic current and consequently the electrode

preparation involves incorporation of conducting agents and binders in order to hold the particles on a metal current collector, a method known as screen printing.[48] Such foil-based electrodes carry the dead weight of conducting agents, polymeric binders, and the metal foil that do not contribute toward the battery capacity.

As an attractive solution to screen printed electrodes, we present our results related to fabrication of a well-organized, interleaved, freestanding, large-area composite anode consisting of SiOC particles supported by crumpled reduced graphene oxide (rGO) matrix. The electrode delivers higher volumetric capacity than the most advanced pomegranate Si/carbon nanotube composite paper-electrode reported recently by Cui et al. Large micrometer size rGO sheets serve as an ideal host material to SiOC particles, providing the necessary electronic path and consistent cycling performance at high current densities along with high structural stability. Because of their unique nanodomain amorphous structure, SiOC particles offer required chemical and thermodynamic stability, and high Li intercalation capacity for the anode. Further, we demonstrate the exceptionally high strain-to-failure in paper electrodes that exceeded 2 % as measured in a uniaxial tensile test. In-depth microscopic analysis revealed that modes of failure differ significantly between composite papers and pristine rGO papers.

SiOC particles in this study were prepared by direct thermal decomposition of a commercial off-the-rack polysiloxane precursor.

5.3. Methods

5.3.1. Preparation Of Polymer-Derived SiOC Ceramic

SiOC was prepared through the polymer pyrolysis route,[44] liquid 1,3,5,7-tetramethyl-1,3,5,7-tetravinylcyclotetrasiloxane (TTCS, Gelest, PA) precursor (with 1 wt% dicumyl peroxide added as the cross-linking agent) was cross-linked at 380 °C in argon for 5 h, which resulted in a

white infusible mass. The infusible polymer was ball-milled in to fine powder and pyrolyzed at 1000 °C for 10 h in flowing argon resulting in a fine black SiOC ceramic powder.

5.3.2. Preparation of Reduced Graphene Oxide and SiOC Composite Paper

Modified Hummer's method was used to make graphene oxide (GO).[51] 20 mL colloidal suspension of GO in 1:1 (v/v) water and isopropanol was made by sonication for 10 min. Varying weight percentages of SiOC particles (with respect to GO) were added to the solution and the solution was sonicated for an additional 60 min and stirred for 6 h for homogenous mixing. The composite suspension was then filtered by vacuum filtration through a 10 μm filter membrane (HPLC grade, Millipore). The GO/SiOC composite paper obtained was carefully removed from the filter paper, dried, and thermally reduced at 500 °C under argon atmosphere for 2 h. The large-area paper with 60SiOC composition (with an approximately 6.25 in. diameter, cut into rectangular strip) was similarly prepared by use of a Büchner funnel with a polypropylene filter paper (Celgard). The heat-treated paper was then punched (cut) into small circles and used as working electrode material for Li-ion battery half-cells.

5.3.3. Coin Cell/Battery Assembly

Li-ion battery coin cells were assembled in an argon-filled glove box. 1 M $LiPF_6$ (Alfa Aesar) in (1:1 v/v) dimethyl carbonate:ethylene carbonate (ionic conductivity 10.7 $mS.cm^{-1}$) was used as the electrolyte. A 25 μm thick (19 mm diameter) glass separator soaked in electrolyte was placed between the working electrode and pure Li foil (14.3 mm diameter, 75 μm thick) as the counter electrode. Washer, spring, and a top casing were placed to complete the assembly before crimping.

Electrochemical performance of the assembled coin cells was tested using a multichannel BT2000 Arbin test unit sweeping between 2.5 V to 10 mV versus Li/Li^+ that followed a cycle

schedule: (a) Asymmteric mode: Li was inserted at 100 $mA.g^{-1}$, while the extraction was performed at increasing current densities of 100, 200, 400, 800, 1600, and 2400 $mA.g^{-1}$ for 5 cycles each, and returned to 100 $mA.g^{-1}$ for the next 10 cycles. The test schedule for the 40SiOC cell differed slightly in that 20 cycles were performed at 2400 $mA.g^{-1}$, ending with 23 cycles at 100 $mA.g^{-1}$ during charge half of the cycle. (b) Symmetric mode: Later, all the cells were subjected to symmetric cycling at a current density of 1600 $mA.g^{-1}$ for up to 1000 cycles, returning to 100 $mA.g^{-1}$ for the last 10 cycles.

5.3.4. Instrumentation

Sodium nitrate (99.2%), potassium permanganate (99.4%), sulfuric acid (96.4%), hydrogen peroxide (31.3% solution in water), hydrochloric acid (30% solution in water), and methanol (99.9%) were purchased from Fisher Scientific. All materials were used as received without further purification.

Scanning electron microscopy (SEM) of the synthesized material was carried out on a Carl Zeiss EVO MA10 system with incident voltage of 5 kV to 30 kV. TEM images were digitally acquired by use of a Phillips CM100 operated at 100 kV. Material characterization was made using X-ray diffractometer (XRD) operating at room temperature, with nickel-filtered CuKα radiation (λ=1.5418 Å). Thermogravimetric analysis (TGA) was performed using Shimadzu 50 TGA (limited to 800 °C). Samples weighing, approximately 2.5 mg, were heated in a platinum pan at a rate of 10 $°C.min^{-1}$ in air flowing at 20 $mL.min^{-1}$.

Static uniaxial in-plane tensile tests were conducted in a custom-built test setup. One end of the setup was connected to a 1N load cell (ULC-1N Interface®) and the other end was clamped to a computer-controlled translation stage (M-111.2DG from PI®). The entire setup was located on a bench with self-adjusting feet. All tensile tests were conducted in controlled strain

rate mode with a strain rate of 0.2%.min^{-1}. Paper electrodes were cut (punched out) into rectangular strips of approximately 5 x 15 mm^2 for testing without any further modification. Electrical conductivity measurements were carried out by use of a four-point probe setup and Keithley 2636A (Cleveland, OH) dual channel sourcemeter in the Ohmic region. Electrochemical cycling of assembled cells was carried out using multichannel Battery Test Equipment (Arbin-BT2000, Austin, TX) at atmospheric conditions.

5.4. Results and Discussions

5.4.1. Material Synthesis and Electrode Fabrication.

Polymer-derived SiOC ceramic particles were prepared using controlled thermolysis of TTCS polymeric precursor. The polymer-to-ceramic transformation was complete at 1000 °C.[44] Detailed characterization of cross-linked polymer and resulting SiOC material is presented in Figure 5.1a through 4.1g. SEM images of SiOC particles in Figure 5.1a confirmed average particle size to be approximately 4 μm (with standard deviation of 1.8 μm). X-ray photoelectron spectroscopy (XPS) showed O1s, C1s, Si2s, Si2p and O2s peaks for both cross-linked and pyrolyzed SiOC ceramic (Figure 5.1b). Close analysis of the deconvoluted silicon band (for Si 2p photoelectrons) in SiOC revealed the emergence of peaks at 103.5 and 102.2 eV, corresponding to SiO_4 and $CSiO_3$ phases, respectively (Figure 5.1c). In addition, peaks at 534.5, 533.1 and 532.4 eV corresponding to C=O, SiO_2, and Si-O phases, respectively, were observed in O1s-oxygen band (Figure 5.1d), whereas the C1s band (Figure 5.1e) was fitted with 3 peaks at 286.5, 284.5, and 284.7 eV corresponding to C=O, C−C, and C−Si phases, respectively. Raman spectroscopy of SiOC particles, shown in Figure 5.1f, showed two distinct peaks at 1350 and 1590 cm^{-1}, which are the commonly observed D and G-peaks of graphene-like free carbon phase present in the ceramic. Similarly, Fourier Transform Infrared Spectroscopy (FTIR) analysis also

confirmed transformation of TTCS polymer to ceramic SiOC (Figure 5.1g).[44] Figure 5.1h present spectroscopic evidence of the predicted chemical structure of the cross-linked polymer and resultant ceramic (Figure 5.2), which is in agreement with previous work on polymer-derived SiOC. [45]

Microstructure of the composite paper was characterized by electron microscopy and is presented in Figure 5.1i and Figure 5.4. The SEM image of rGO paper in Figure 5.4a showed a sheet-like structure with a smooth surface.[52,53] SEM images of rGO/SiOC composite papers with 10, 40, 60 wt% of SiOC in GO are shown in Figure 5.4 (b through d) and Figure 5.1i, respectively. Well-ordered stacks of rGO were observed with SiOC particles interlayered between rGO sheets. From cross-sectional SEM image in Figure 5.1j, the average thickness of the paper was measured to be ~15 μm. Similar to SEM images, the increasing percentage of SiOC and uniform distribution was also noticed in the transmission electron microscopy (TEM) images (Figure 5.4e through h). The GO/SiOC TEM images showed large micrometer-sized thin rGO sheets along with smaller SiOC particles. The rGO sheets seem to ocassionaly fold and cover individual SiOC particles and other instances show GO being interlayered by SiOC. The hexagonal spot pattern, shown in the insert of Figure 5.4e, indicates that graphitic AB stacking was largely preserved in the lattice after thermal reduction. For the selected area electon diffraction (SAED) pattern in Figure 5.1k, the multiple spot pattern is a result of polycrystallinity of restacked rGO sheets and the faint ring pattern is attributed to amorphous SiOC material.

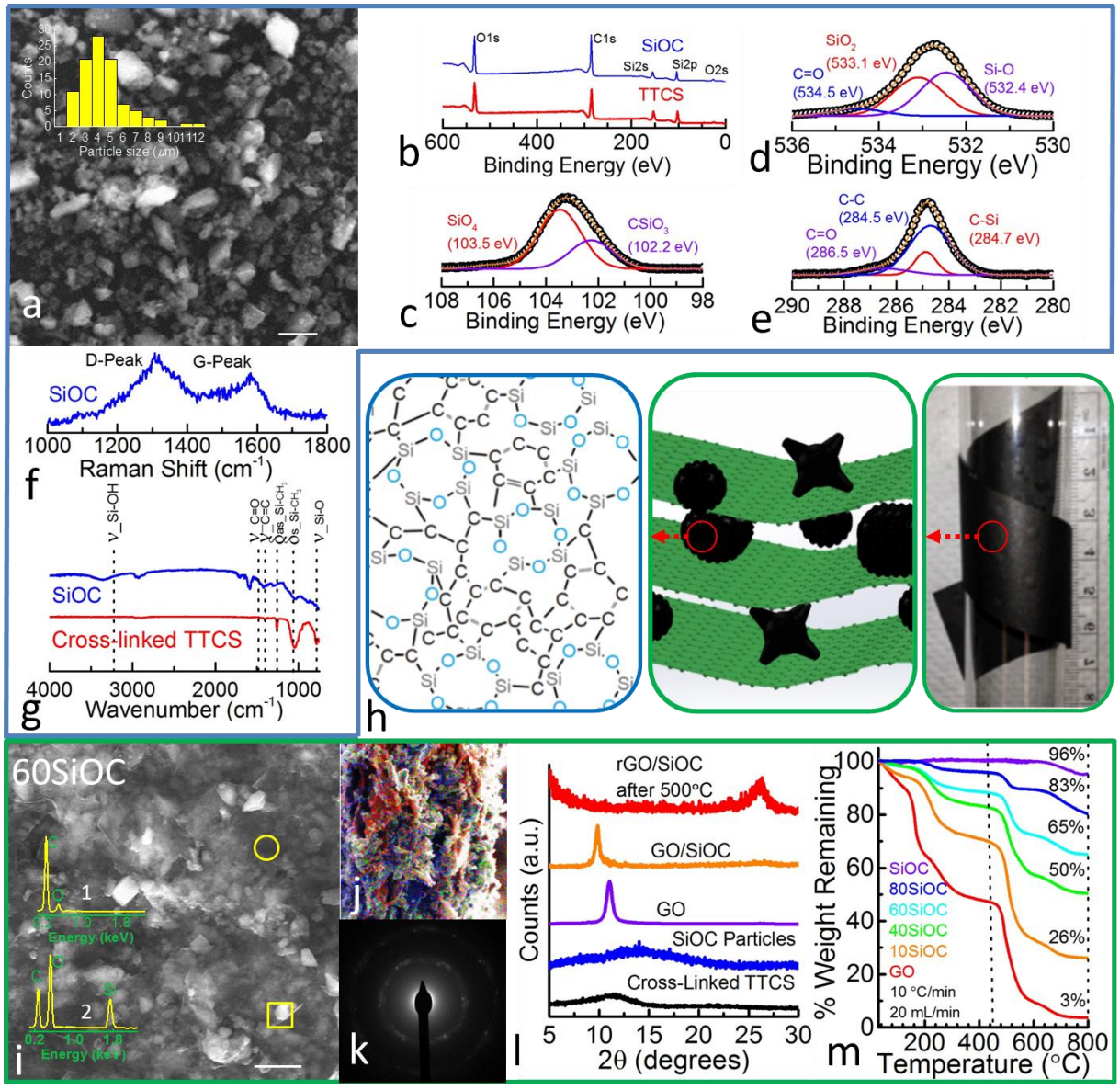

Figure 5-1 Characterization of SiOC ceramic and SiOC/rGO composite papers. (a) SEM image of SiOC particles after pyrolysis of the polymeric TTCS particles. Average SiOC particle size was approximately 4 to 5 μm. The scale bar is 10 μm. (b) X-ray photoelectron spectroscopy data for cross-linked TTCS and pyrolyzed SiOC. High resolution XPS spectrum of pyrolyzed SiOC particles in the (c) Si2p region, (d) O1s region, and (e) C1s region were consistent with the polymer-derived SiOC nanodomain model. Deconvoluted peaks indicate the various bonds between Si, C and O atoms, which is distinct to pyrolyzed

SiOC. (f) Raman spectrum of SiOC showed peaks that are characteristic of graphitic carbon (D-peak: 1350 cm−1 and G-peak: 1590 cm−1). (g) Attenuated Total Reflectance Fourier Transformation Infrared (ATR-FTIR) spectra of SiOC and cross-linked TTCS (ν: stretching vibration mode and δ: bending vibration mode). (h) Schematic illustration of proposed hybrid structure of the freestanding paper and the atomic structure of pyrolyzed SiOC particle. (i) SEM image of 60SiOC paper and (j) its corresponding cross-sectional images with EDX map in which Si, C, and O are indicated by red, blue and green, respectively. Insets in (i) are EDX spectra of spots shown in the corresponding SEM image indicating the material to be rGO (circle) and SiOC (square). The scale bar is 10 μm. (k) TEM SAED pattern showed multiple spot pattern due to polycrystallinity of restacked rGO sheets with faint ring pattern attributed to amorphous SiOC material. (l) XRD of cross-linked TTCS, SiOC particles, GO paper, GO/SiOC paper before and after (rGO/SiOC) thermal reduction. Complete reduction of GO to rGO is illustrated in the plot. (m) TGA curves of GO paper and GO/SiOC composite papers measured from 30 to 800 °C at a heating rate of 10 °C.min−1 in flowing air. The weight percentage of SiOC in the GO/SiOC composite is as indicated in the figure.

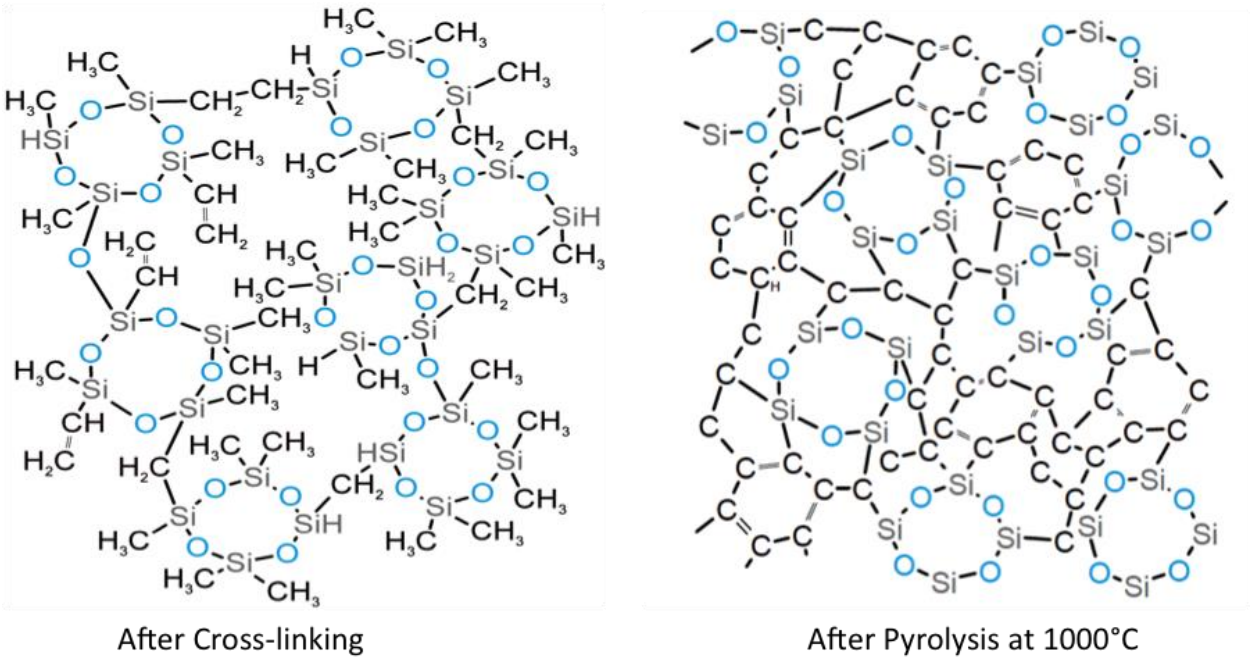

Figure 5-2 Schematic illustration showing the predicted structure of cross-linked polymeric precursor (i.e., TTCS) and polymer-derived SiOC ceramic obtained upon pyrolysis of the cross-linked polymer at 1000°C. This type of structure is plausible based on the Raman, FTIR, XRD, and XPS data presented here and earlier work on similar systems.

The rGO/SiOC composite papers were prepared following a vacuum filtration technique (see Materials section for details). Samples were labeled as rGO, 10SiOC, 40SiOC, 60SiOC, and 80SiOC for pristine rGO paper and rGO with 10, 40, 60, and 80% of SiOC in SiOC−GO paper, respectively. The schematic in Figure 5.3 describes the synthesis process.

Figure 5-3 Electrode design and fabrication. Schematic illustrating the procedure for fabrication of free-standing SiOC/graphene composite paper for use as Li-ion battery anode. The composite paper was sufficiently robust to be handled by hand and flexible enough to be rolled on to a cylinder several times without breaking.

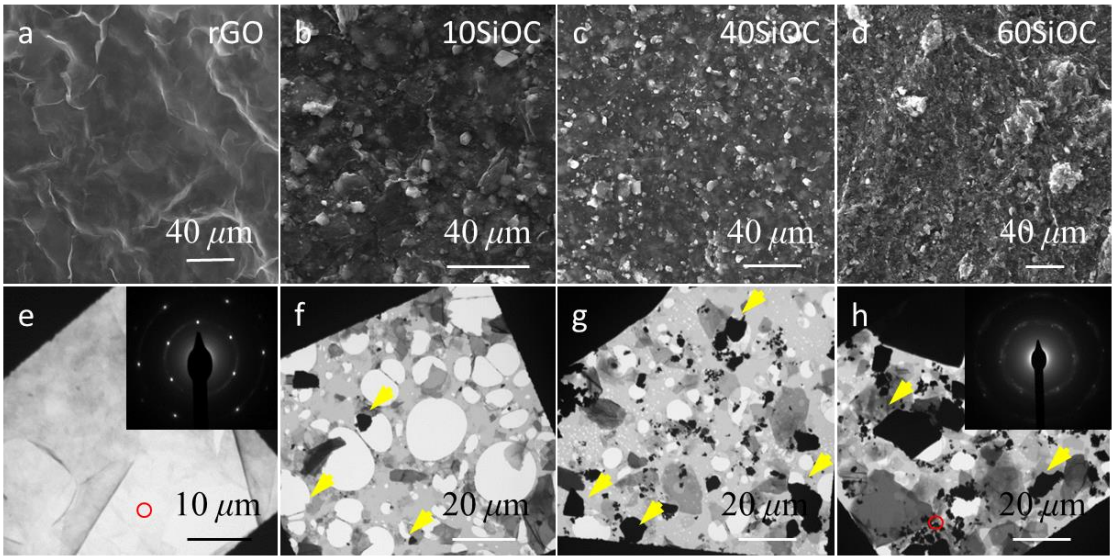

Figure 5-4 Microstructure of SiOC/rGO composite papers. SEM images of (a) rGO and (b) 10SiOC, (c) 40SiOC and (d) 60SiOC paper and (e-h) their corresponding TEM images.

These images reveal that because graphene sheets occupy larger volume in the composite, well-dispersed rGO sheets (during the layer−by−layer filtration process) could methodically arrange themselves around the SiOC particles to form strong, flexible composite paper. SEM and TEM images prove that morphology of the composite paper is planar and porous. This structure can facilitate easier and rapid diffusion of Li ions in SiOC active phases.

Further analysis involved SEM-X-ray energy dispersive spectroscopy (EDX) of the composite paper. The EDX spectra (Figure 5.1i) from Spot 1(circle) showed peaks at 0.27 keV and 0.52 keV, corresponding to carbon (90 at%) and oxygen (10 at%) Kα energy, respectively. Low oxygen content indicated that rGO was highly reduced and pristine. In addition to carbon and oxygen peaks, another peak at 1.75 keV, corresponding to Si Kα energy, was observed from Spot 2 (square). The particle had composition of 17 at% Si, 46 at% O and 37 at% C, unambiguously confirming the presence of SiOC.

The reduction of GO (non-conducting) to rGO (conducting) was confirmed by use of X−ray diffraction (XRD). As shown in Figure 1l, both GO and GO/SiOC papers, had peaks at 11.05 and 9.8°, corresponding to interlayer spacing of 8 and 12 Å, respectively. Interlayer spacing was large compared with that of graphite (with major peak (002) at 26.53°, corresponding to 3.36 Å) because of oxygen functional groups present in GO and water molecules held between the layers. After thermal annealing at 500 °C for 2h, the paper showed a broad peak at 2θ = 26° 2θ, typical of reduced GO material. [53] The broad peak observed in the spectra suggests inhomogeneous spacing between the layers. XRD spectra of cross-linked TTCS and SiOC particles were both featureless, confirming the amorphous nature of these ceramics (hallmark of these materials). Also, Raman spectrum (Id/Ig) pre and post thermal reduction was

relatively unchanged (Figure 5.5). Reduction of GO to rGO was verified by the disappearance of oxide peaks in the high resolution XPS analysis of C1s peak (Figure 5.6).

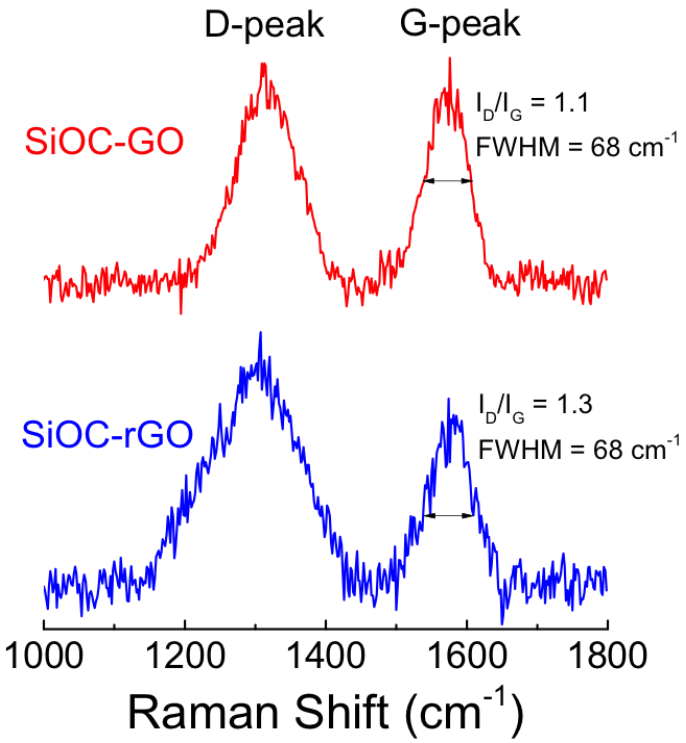

Figure 5-5 Comparison of Raman spectra of free-standing papers before and after annealing showed no distinct change in position or relative intensity of the peaks. The ID/IG ratio remained approximately the same (~1.1 to 1.3).

Thermogravimetric analysis (TGA) was performed to ascertain the mass loading of SiOC in rGO/SiOC composite papers. Figure 5.1m shows the percentage composition of filtered GO/SiOC composite paper. After heat treatment (Figure 5.7) due to GO weight loss, the ratio of SiOC material in the composite increased depending on the percentage of GO originally in the composite. SiOC content in 10SiOC, 40SiOC, 60SiOC, and 80SiOC increased from 10 to 30 %, 50 to 65 %, 65 to 78 %, and 83 to 92 %, respectively. In the traditional method of electrode preparation, active material is mixed with polymeric binder and conductive agent in an 80:10:10

ratio, followed by slurry coating on metal current collector foil. However, using this method we have made a freestanding and lightweight electrode, containing up to 72% SiOC as active material and 22% of rGO (acting as binder and conductive agent). Paper electrodes were directly utilized as the working electrodes. Electrochemical performance is presented in the following section.

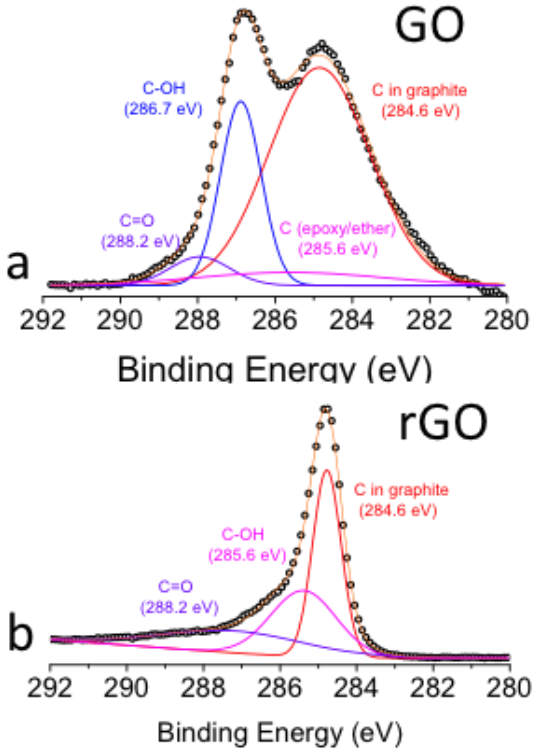

Figure 5-6 Deconvoluted XPS spectrum of (a) as-prepared graphene oxide (GO) paper and (b) reduced graphene oxide (rGO) paper in the C1s region, the C-OH peak at 286.7 eV completely disappeared upon annealing proving the reduction of graphene oxide to reduced graphe

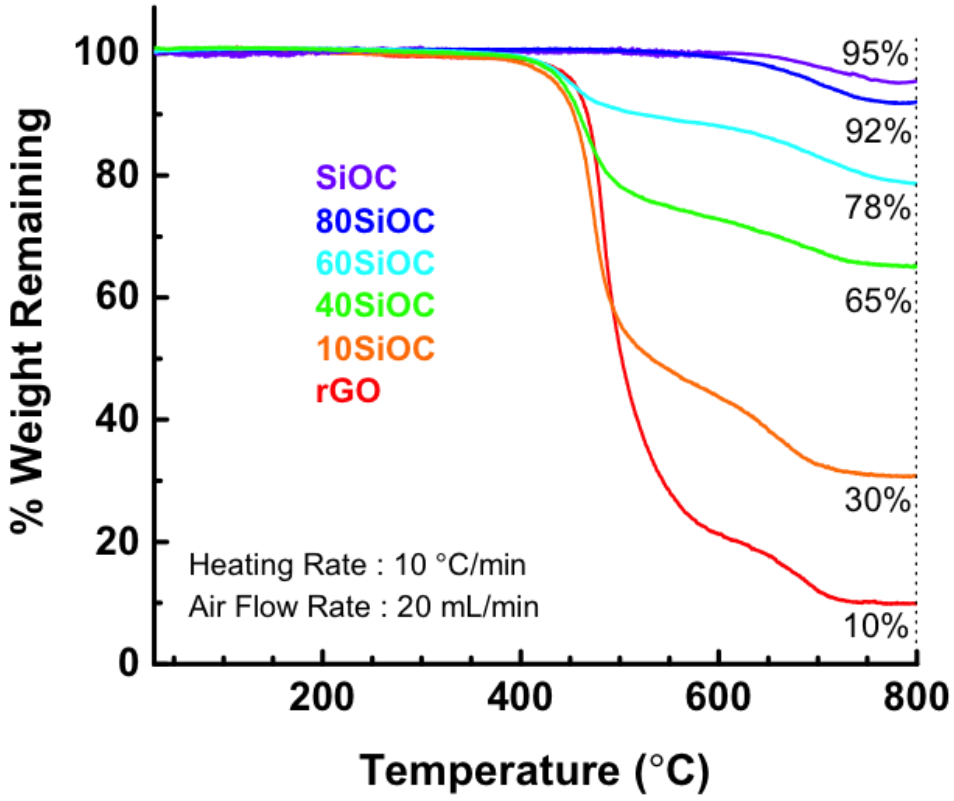

Figure 5-7 TGA curves of rGO paper and rGO/SiOC composite papers measured from 30 to 800 °C at a heating rate of 10 °C.min-1 in air. The weight percentage of SiOC in the rGO/SiOC composite was as indicated in the figure.

5.4.2. Electrochemical Performance

Figure 5.9 (a) shows charge capacities and columbic efficiency of rGO, 10SiOC, 40SiOC, 60SiOC anodes cycled at varying current densities. For rGO, the first-cycle charge capacity at 100 $mA.g^{-1}$ was ~210 $mAh.g^{-1}$, it dropped to ~200 $mAh.g^{-1}$ in the second cycle, and then the charge capacity stabilized at approximately 180 $mAh.g^{-1}$ after 5 cycles. When current density increased to 2400 $mA.g^{-1}$, charge capacity was retained at ~175 $mAh.g^{-1}$. Returning the current density back to 100 $mA.g^{-1}$ led to the return of higher capacity of 192 $mAh.g^{-1}$.

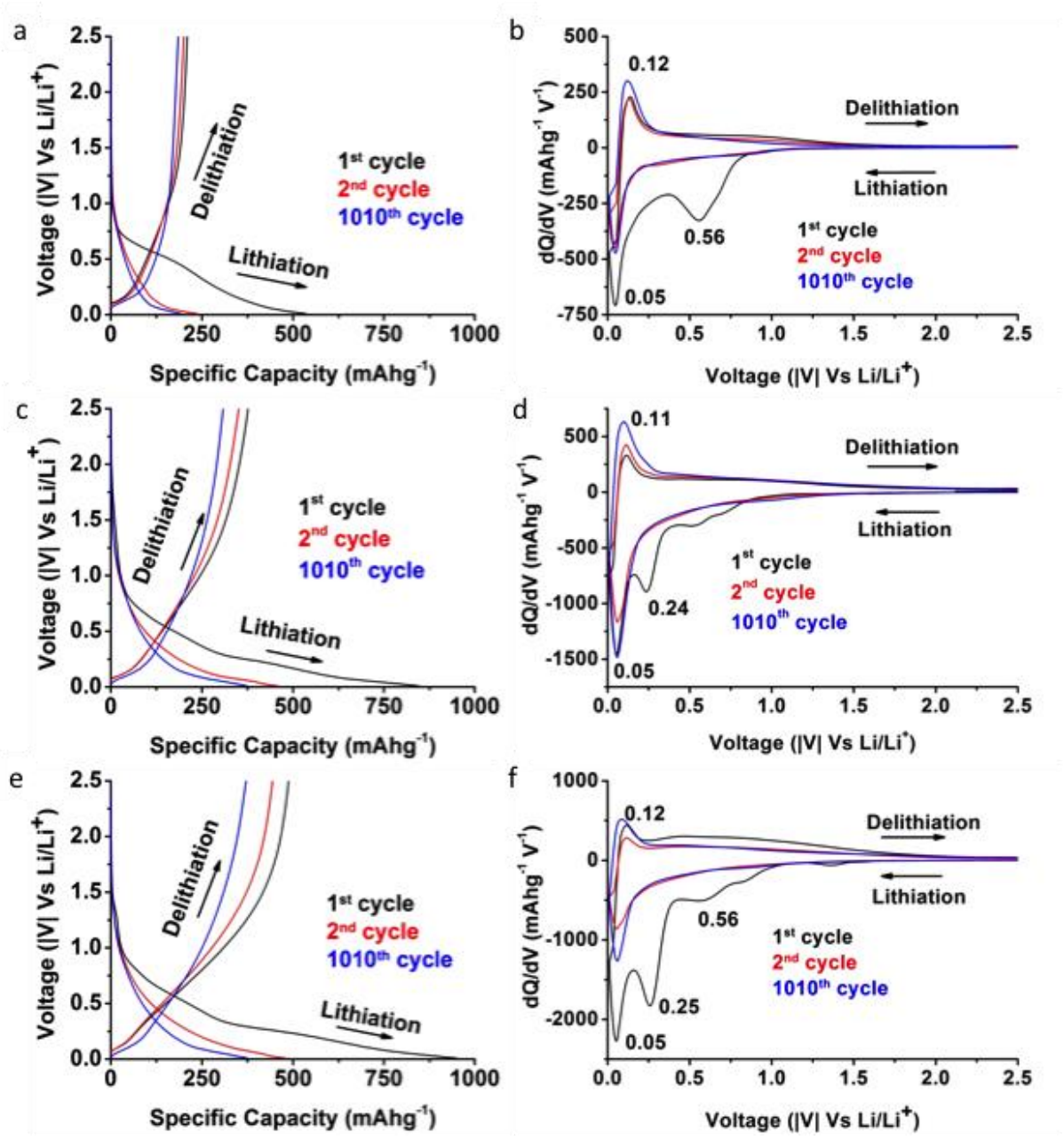

Figure 5-8 Voltage profiles along with corresponding differentiated capacity curve of (a, b) rGO, (c, d) 10SiOC, and (e, f) 40SiOC. Reduction peak at 50 mV, a secondary reduction peak at 750 mV and an oxidation peak at 133 mV are distinct to Li reaction with rGO while reduction peak at 250 mV is distinct to Li reaction with SiOC.

Table 5.1 60SiOC paper battery testing results

Cycle Number	Discharge Capacity (mAh g^{-1})	Charge Capacity (mAh g^{-1})	Efficiency (%)
1	702.18	1032.22	68.03
2	667.97	690.74	96.70
3	650.54	666.80	97.56
4	641.48	653.35	98.18
5	629.85	640.28	98.37
6	611.43	632.66	96.64
7	604.20	611.75	98.77
8	602.17	608.44	98.97
9	598.45	603.77	99.12
10	591.41	596.66	99.12

High irreversible first-cycle capacity results from electrochemical reaction contributed to solid-electrolyte interphase (SEI) layer formation. For the rGO/SiOC composite, the first-cycle charge capacity increased in correspondence to the percentage of SiOC in the electrode. For example, 10SiOC showed 376 mAh.g^{-1}, while 40SiOC and 60SiOC showed 488 mAh.g^{-1} and 702 mAh.g^{-1}, respectively. The 60SiOC had 97% of the theoretical capacity of the composite material (theoretical capacity of graphite being 372 mAh.g^{-1} and highest reported reversible capacity of SiOC being 958 mAh.g^{-1}).

Similar to rGO anode, when current density increased to 2400 mA.g^{-1}, composites 10SiOC, 40SiOC, and 60SiOC retained reversible capacity at 296, 343 and 543 mAh.g^{-1}, respectively. Capacity retention at 2400 mA.g^{-1} of 83.5% and first-cycle loss of 68% for 60SiOC is the highest reported performance for any freestanding graphene-based electrode (as compared

in Table 4.1). [38-47] When current density was lowered again to 100 mA.g^{-1}, charge capacity increased to 304 mAh.g^{-1} (80.85% retained), 418 mAh.g^{-1} (85.66% retained), and 626 mAhg^{-1} (97% retained) for 10SiOC, 40SiOC and 60SiOC, respectively. The 60SiOC electrode showed high cycling efficiency, as presented in Table 4.2.

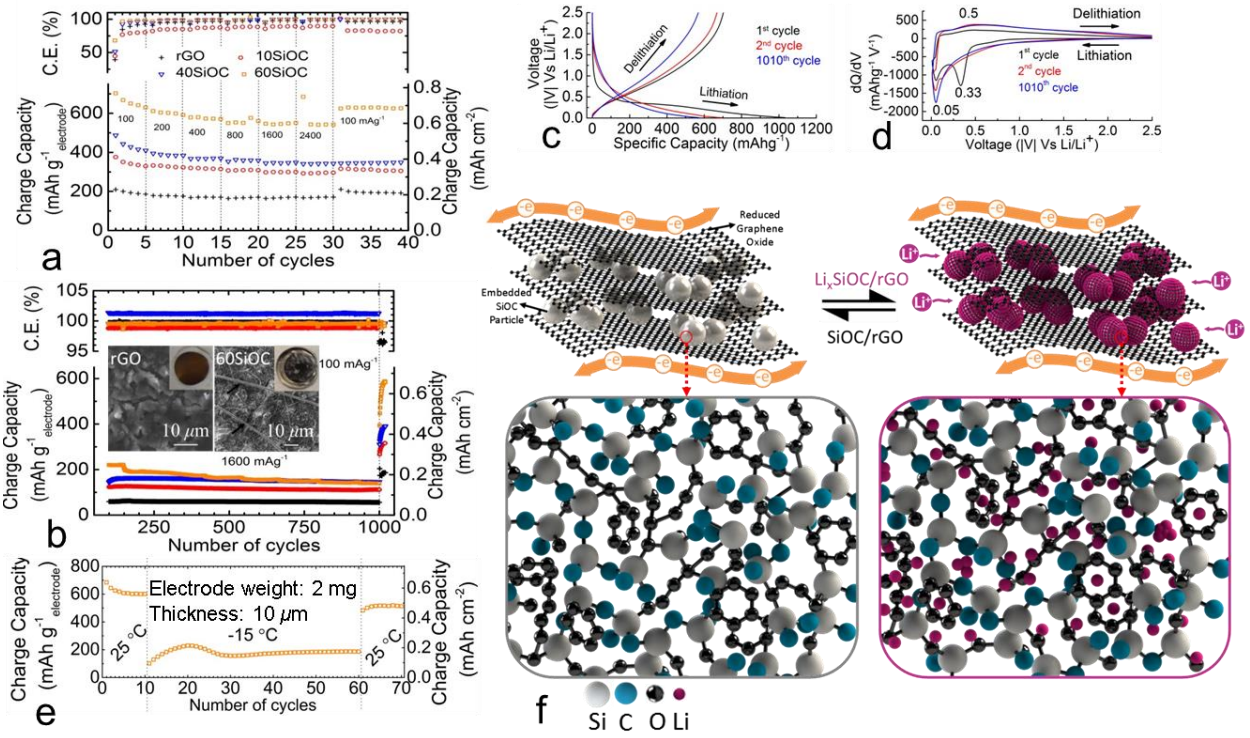

Figure 5-9 Electrochemical characteristics and proposed lithium storage mechanism. (a) Charge capacity (total electrode weight) of various paper electrodes asymmetrically cycled at increasing current densities and their cyclic efficiencies. (b) The plot shows extended cycling behavior (charge capacity versus cycle number) of anodes symmetrically cycled at 1600 mA.g−1. After 900 cycles, all anodes recovered their original capacities when they were cycled again at 100 mA.g−1. Insets show the postcycling optical and SEM images of the dissembled rGO and 60SiOC electrodes after 1020 cycles. (c) Voltage profile of 60SiOC composite and corresponding (d) differential capacity curves cycled at various current densities. (e) Schematic representing the mechanism of lithiation/delithiation in SiOC glass

particles. Majority of lithiation occurs via adsorption at disordered carbon phase uniformly distributed in the SiOC amorphous matrix. Graphene sheets serve as an efficient electron conductor and elastic support. (f) Charge capacity of 60SiOC cycled at 100 mA.g−1 at 25 °C for 10 cycles, -15 °C for 50 cycles and then back at 25 °C for 10 cycles. After cooling down to -15 °C, the cell demonstrated a stable charge capacity of ~200 mAh.g−1. The cell regained approximately 86 % of its initial capacity when returned to cycling at room temperature.

In order to test cyclic stability of the anodes, the cells were also subjected to symmetric cycling at a current density of 1600 $mA.g^{-1}$. Charge capacity for this test is shown in Figure 5.9(b). As shown in the figure, three of the four cells demonstrated virtually no capacity fading for 1000 cycles: Efficiency was approximately 100%. Charge capacity of 40SiOC anode was highest at approximately 160 $mAh.g^{-1}$ after 1000 cycles, while 60SiOC and 10SiOC papers were approximately 139 and 115 $mAh.g^{-1}$, respectively. Charge capacity of 60SiOC continued to show some decline as the cells were subjected to prolonged cycling at 1600 $mA.g^{-1}$. This decline was not observed in other composite specimens, thereby demonstrating the importance of graphene in the composite material. Composite paper capacities were much higher when compared to the capacity of pristine rGO electrode (approximately 58 $mAh.g^{-1}$). Most significantly, the cells regained original capacities of ~185, 310, 371 and 568 at 1010^{th} cycle when the current density was brought back to 100 $mA.g^{-1}$, while retaining ~100% efficiency. This shows that, even after 1020 cycles, the anode was robust and continued to function without appreciable degradation.

Figure 5.8a shows voltage profiles of rGO for the 1^{st}, 2^{nd} and 1010^{th} cycle. Differential capacity profiles in Figure 5.8b were similar to previous reports on rGO electrodes, with a

primary reduction peak at ~50 mV, a secondary reduction peak at ~750 mV, and an oxidation peak at ~133 mV.[41] The peak at 50 mV, present in all subsequent cycles, is associated with lithiation of rGO, whereas the peak at 750 mV signifies formation of a secondary electrolyte interphase (SEI), which exists only in the first cycle. Figure 5.8c and S7d show the voltage profile and differential capacity curves of 1st, 2nd and 1010th cycle of 10SiOC, respectively. The first cycle contained three reduction peaks at around ~50 mV, ~250 mV, and ~600 mV, attributed to rGO lithiation, Li_xSiOC formation, and SEI formation, respectively. [41,44,48] In contrast, only one subtle extraction peak at ~100 mV is observed, which represents rGO de-lithiation with an extended bulge at ~600 mV that represents Li_xSiOC de-lithiation. [41,48,49] As the SiOC increased to 40 (Figure 5.8e and f) and 60% (Figure 5.9 c, d), domination of SiOC lithiation increased, as proven by increased intensity of the Li_xSiOC formation peak at ~600 mV (compared to the rGO lithiation peak at 50 mV). Peak intensity of rGO de-lithiation at 100 mV diminished with respect to Li_xSiOC de-lithiation peak. In addition, the 2nd and the 1010th cycle charge/discharge and differential capacity curves of the electrodes had similar profiles, showing that no new phases formed even more than 1000 cycles at 1600 $mA.g^{-1}$.

More importantly, the efficiency of 60SiOC remained at approximately 100% throughout the cycling test. Tests were also conducted on 80SiOC anode specimen to ascertain if performance of the freestanding paper-based anodes can be improved further. These attempts, however, were not successful because anode specimens prepared at 80% loading were brittle and showed erratic behavior after only a few initial cycles. First-cycle charge capacity for 80SiOC was ~762 $mAh.g^{-1}$ (Figure 5.10a and b). The first cycle showed domination of Li_xSiOC lithiation and delithiation peaks over rGO peaks, similar to other samples that contain increasing percentages of SiOC in rGO. The 80SiOC electrode began to demonstrate random spikes in

charge capacity with increased cycle numbers, suggesting mechanical disintegration of paper electrodes (shown in Figure 5.11).

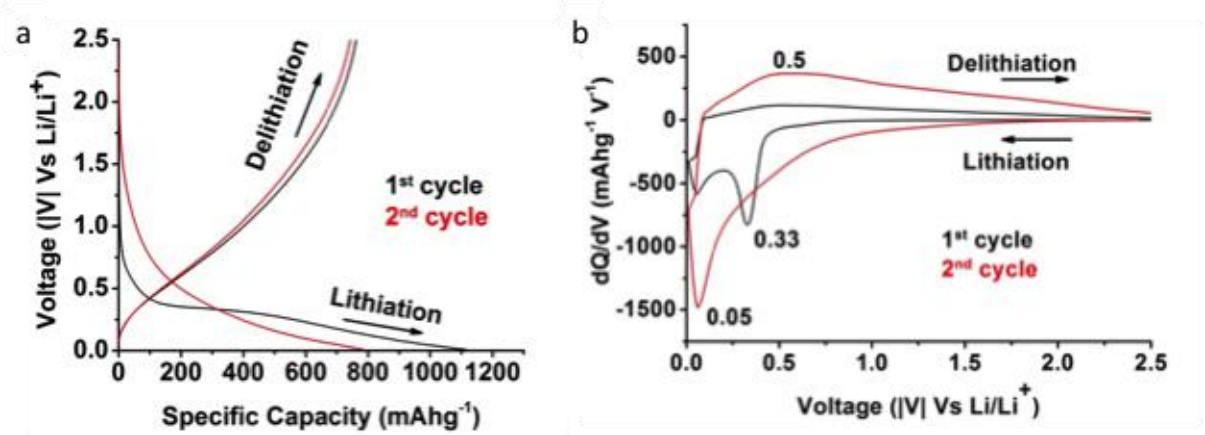

Figure 5-10 (a) Voltage profiles along with corresponding (b) differentiated capacity curve of 80SiOC cycled at various C-rates. The peaks at 0.33 and 0.05 V in the differentiated capacity curve are distinct to Li reaction with SiOC. The graphene interaction peak in virtually absent in the first cycle curve.

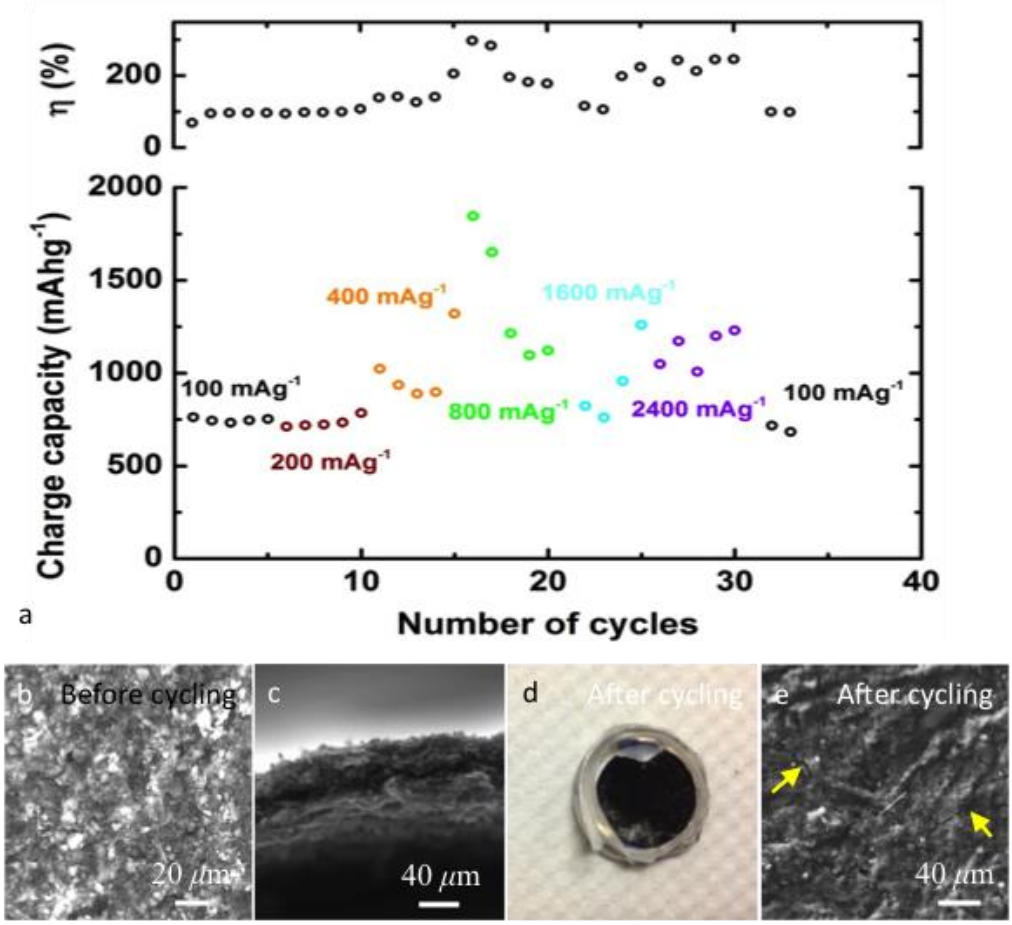

Figure 5-11 (a) Charge capacity of 80SiOC cycled at different rates along with their cyclic efficiencies. Even though the initial capacity was higher at 750 mAhg-1, the anode material began to disintegrate as the current density was progressively increased. This was expected, as there was insufficient graphene present to hold SiOC particles together and maintain electronic conducting network in the eelctrode. (b) SEM images of 80SiOC paper and (c) its corresponding cross-section view. (d) Digital picture of 80SiOC anode. (e) SEM image of 80SiOC, which was dissembled in the lithiated state after being cycled for 33 cycles. Arrows in the image indicate micro-cracks most likely due to cycling at high current density.

Table 5.2 Summary of experimental results of various free-standing graphene hybrid papers

Freestanding paper based anode material	First cycle charge capacity, mAh/g	First cycle efficiency, %	Current density, mA/g	Charge Capacity (number of cycles), mAh/g	Efficiency (number of cycles), %	Reference
60SiOC/rGO	702	68	100	626.3(40)	99.6(40)	This Work
			2400	543	100	
SiOC (bulk/traditional anode)*	1252	77	100	700(60)	~100	54
			2400	50	NA	
Graphite (bulk/traditional anode)*	298	NA	50	240(50)	NA	55
r-Graphene oxide	680	12.4	50	84(2)	80(10)	
Graphene	1050	47	50	301	NA	
rGO-Ar (Holey graphene)	819	49	50	403(10)	99.8(10)	56
			2000	178	99.8	
			10000	75	99.8	
Si/Graphene	2200	41	50	708(100)	NA	57
SiNW/Graphene	1100	NA	50	500(20)	NA	58
GeNW/Graphene	1200	NA	65.4	600(20)	NA	
SiNW/Graphene/rGO	4400	45	840	1650(50)	98	59
TiO_2/Graphene	400	65	200	157(100)	99	60
			2000	122(100)	95	
			4000	~100	NA	
MnO_2/Graphene	1300	53	100	~500(70)	NA	61
			1600	200	NA	
SnO_2/Graphene	700	28	100	438(50)	NA	62
SiO_2/Graphene/CNT	1600	52	250	635(80)	NA	63
	1000	40	1000	400(50)	NA	
SiO_2/Graphene	1250	48	250	600(10)	NA	
			1000	390	NA	
Fe_3O_4/Carbon/CNT	1148	70	156	900(10)	100	64
MWCNT	600		100	190(30)		65
Si/MWCNT	1580	~75	100	942(30)	<100	
SWCNT	1450	NA	25	187(100)	NA	66
SnO_2/SWCNT	1850	NA	25	454(100)	NA	

(Bulk material, anode prepared on copper current collector)

Van Der Pauw's four-point resistivity measurement technique[67] is a preferable technique as it helps eliminate spreading resistances and contact resistance that can be associated with the two point probe measurements. In order to find the conductivity of a material, four contacts must be applied to each edge of the surface, equal distance apart. Apply labels to each of the four points, A, B, C and D. Current is applied to A and D contacts and voltage to B and C contacts. The resistance of the material can be determined by

Equation 5-1

$$R_{AD,BC} = \frac{(V_B - V_C)}{I_{AD}} \quad \Omega$$

With the other orientation, where current is applied to contacts B and D and voltage applied to A and C, the resistance can be found by

Equation 5-2

$$R_{B,AD} = \frac{(V_A - V_C)}{I_{BD}} \quad \Omega$$

Once the two resistance measurements are complete, the resistivity can be calculated by

Equation 5-3

$$R_{A,B} = \frac{\pi t}{\ln(2)} * \frac{(R_{A,B} + R_{B,A})}{2} f_C \quad \Omega$$

where t is the sample thickness and f(=1) is a correction factor between 0 and 1 to take into account the asymmetry in the sample. The conductivity can be found out by

Equation 5-4

$$C = \frac{1}{\rho} \quad S/cm$$

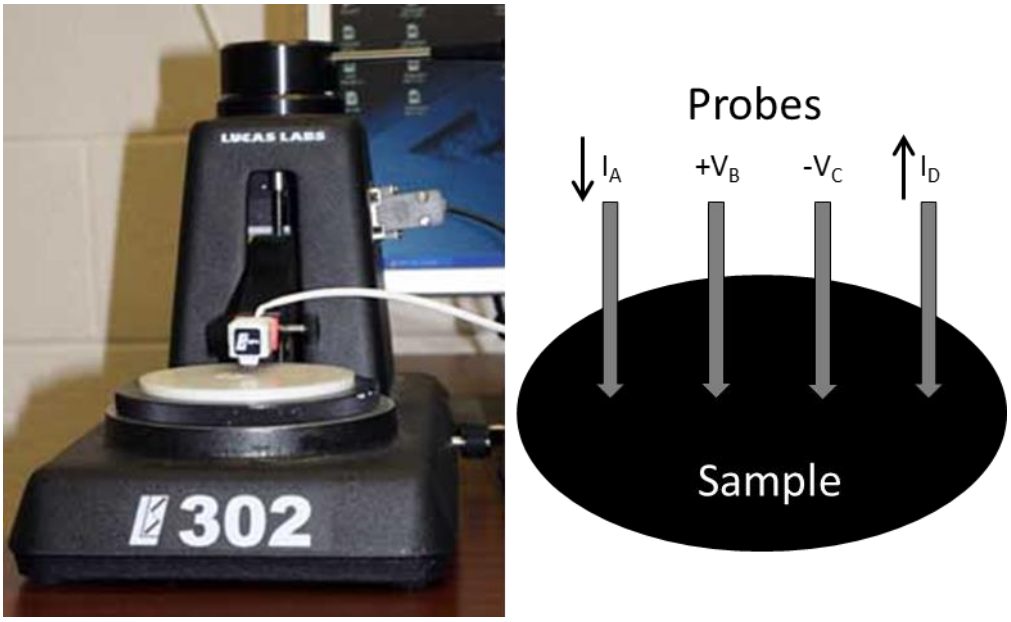

Figure 5-12 Experimental setup for the 4-point resistivity measurements.

Table 5.3 Summary of the electrical conductivity test data.

Material	Resistance, Ω	Thickness, cm	Resistivity, Ωcm	Conductivity, S/cm
rGO	40	0.0002	0.04	27.59
10SiOC	210	0.001	0.95	1.05
40SiOC	480	0.002	4.35	0.23
60SiOC	580	0.007	18.39	0.05
80SiOC	1500	0.007	47.57	0.02

Four-point electrical conductivity measurements were also performed and compared for all specimens (Figure 5.12 and Table 4.4). Conductivity values indicated that with even with approx. 80 wt% of SiOC, resistance of composite paper (580 Ω) was only marginally higher than rGO paper (480 Ω). This is an important achievement because neat SiOC is insulating and the improved electrical conductivity of the composite paper is desirable for better C−rate

characteristics. This is more evident when we compare the C−rate data for SiOC particle anode prepared on traditional copper current collectors,[49,50] where the electrochemical capacity was observed to be negligible when cycled at 1600 $mA.g^{-1}$.

Electrochemical testing at low temperature was carried out on the best performing specimen i.e., 60SiOC. The cell was placed in an air-tight container while being cycled at a constant current rate of 100 mA g^{-1} in the cooling unit (refrigerator). After cycling for 10 cycles at room temperature (25 °C), the cell was rested in the cooling unit (freezer of a household refrigerator) for 1 day to uniformly cool the cell to -15 °C before cycling it at low temperature for 50 cycles. The cell was rested at room temperature after 60^{TH} cycle for 1 day before cycling it at room temperature for another 10 cycles.

In addition to room temperature testing, the best performing specimen (i.e., 60SiOC) was subjected to electrochemical cycling at low temperature (-15 °C). Experimental details are provided in Supporting Information Section VI. When initially cycled at room temperature, the cell had a stable charge capacity of approximately 600 $mAh.g^{-1}$ that then reduced to a stable charge capacity of approximately 200 $mAh.g^{-1}$ when cycled at low temperature. The cell regained approximately 86% of its initial capacity when it returned to cycling at room temperature (Figure 5.9e).

In order to verify electrode integrity, the cells were dissembled in their lithiated state and the electrode was recovered for additional characterization. The inset in Figure 5.9b and Figure 5.13 show the digital photograph and SEM image of the dissembled anodes after 1020 cycles. Postcycling Raman spectroscopy data is presented in Figure 5.14and Table 4.5. No evidence of surface cracks, volume change, or physical imperfections were observed in the SEM images, suggesting mechanical/structural strength of rGO/SiOC composite paper. In all cases, evidence

of SEI formation due to repeated cycling of Li ions was observed. Contamination in the specimen, indicated by arrows, was a result of residue of glass separator fibers. The anodes may also have been exposed to air during the transfer process, resulting in oxidation of Li, which appeared as bright spots in the images due to non-conducting nature.

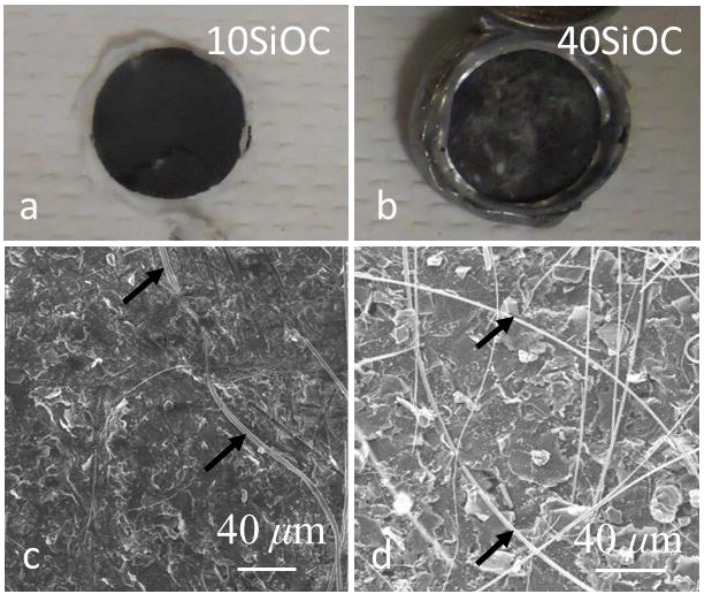

Figure 5-13 Post electrochemical surface analysis on composite electrode. Digital camera image of (a,b) rGO-SiOC composite anodes after cycling. SEM images of (c) 10SiOC and (d) 40SiOC which were obtained in the lithiated state after being cycled for 1020 cycles.

Table 5.4 Summary of the Raman data for various electrode specimen both pre and post cycling.

Pre-cycling				Post-cycling			
	I_d	I_g	I_d/I_g		I_d	I_g	I_d/I_g
60SiOC	1329.96	1571.84	0.85	60SiOC	1323.15	1583.77	0.84
40SiOC	1329.96	1576.95	0.84	40SiOC	1331.66	1597.39	0.83
10SiOC	1331.66	1576.95	0.84	10SiOC	1326.55	1575.25	0.84
rGO	1341.88	1588.88	0.84	rGO	1326.55	1590.58	0.83

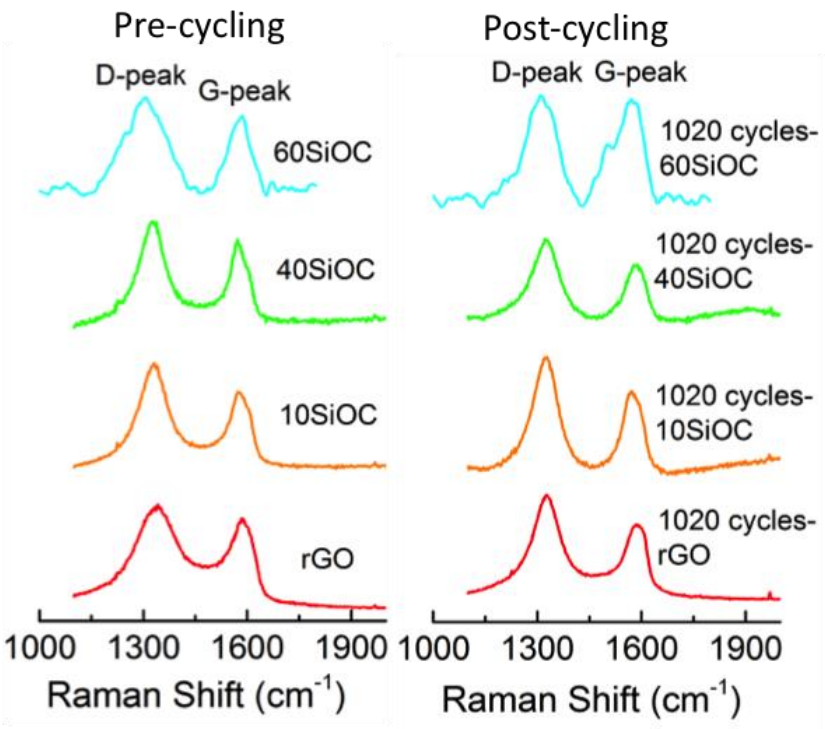

Figure 5-14 Raman data of various SiOC/rGO specimen, before and after the electrochemical testing. No considerable change in ratio of intensity was observed suggesting that the anode was largely intact even upon cycling for 1000 cycles at 1600 mA.g^{-1}.

In the galvanostatic intermittent titration technique (GITT) experiment, charge was inserted (or withdrawn) by applying a current pulse of 100 mAh.g^{-1} for 15 min, followed by 12 h of relaxation between pulses during which the change in potential with time was measured. Magnitude of voltage increased during the relaxation period in the insertion half but it decreased in the extraction half of the cycle [68,69]. The solid state lithium ion diffusion coefficients were determined using

Equation 5-5

$$D_G \approx \frac{4}{\pi\tau}\left(\frac{m_B V_M}{M_B S}\right)^2\left(\frac{\Delta E_S}{\Delta E_\tau}\right)^2$$

Where τ is pulse time (15 mins), m_B is electrode mass (3.23 mg), V_M is molar volume (5.3 cc.mol^{-1}), M_B molecular weight (12 g.mol^{-1}) and S is surface area (1.6 cm^2), ΔE_S and ΔE_T are voltage steps Figure 5.15. For this study only the best performing anode i.e., 60SiOC was used.In order to obtain the solid state Li-ion diffusion coefficient (D_{Li}), galvanostatic intermittent titration technique (GITT) was performed for 60SiOC at room and low temperature as detailed in Section VIII in the supplementary information. Acquired D_{Li} varied between ($1x10^{-7}$ to $1x10^{-9}$) $m^2.s^{-1}$ during insertion and extraction (Figure 5.15). These values are orders of magnitude higher than values reported for polymer-derived SiOC (Kasper *et al.* 10^{-13} to 10^{-15} $cm^2.s^{-1}$)[47] and SiBCN-CNT (Bhandavat *at al*. 10^{-17} to 10^{-20} $cm^2.s^{-1}$)[43] . In addition, total polarization potential and time dependent change in open-circuit voltage at various states of charge were inferred for these experiments, as shown in Figure 5.16. Density of state calculations are included in Figure 5.17. GITT performed at low temperature (-15 °C) showed D_{Li} between ($1x10^{-10}$ to $1x10^{-6}$) $m^2.s^{-1}$ during intercalation and extraction (Figure 5.18). The total polarization potential and time dependent change in open-circuit voltage at various states of charge performed at -15 °C are included in Figure 5.19.Total polarization potential was then derived from the charge/discharge curve of the titration experiment. In the charge/discharge curve that was obtained from the GITT experiment, the end point of each relaxation period was joined together to form a curve that is shown as a dotted line in Figure 5.16a. The difference in voltage at each point in the curve is the total polarization potential, which is shown in Figure 5.16b. Figure 5.16 (c, d) shows the change in voltage during the relaxation period at different states of charge (SOC). The SOC is defined as the percentage of total capacity present in the anode at that specific voltage.

Later to determine the distribution of density of states of the electrode material, voltage at specific decrement is applied till charges occupy the levels above that voltage (or the applied current becomes zero). The total charge that is inserted into the electrode (equal to the integral value of the current) at that voltage gives the density of charge that can be stored at that level. In the next step charge is stored at the next energy level and so on. In this way the density of charge stored at each voltage is determined. To determine the density of states during the extraction half cycle, voltage at specific increment is applied after full insertion of lithium in the electrode.

The cell was later subjected to testing at low temperature (-15 °C) in a similar manner. All the titration experiments results are given in Figure 5.18 and Figure 5.19.

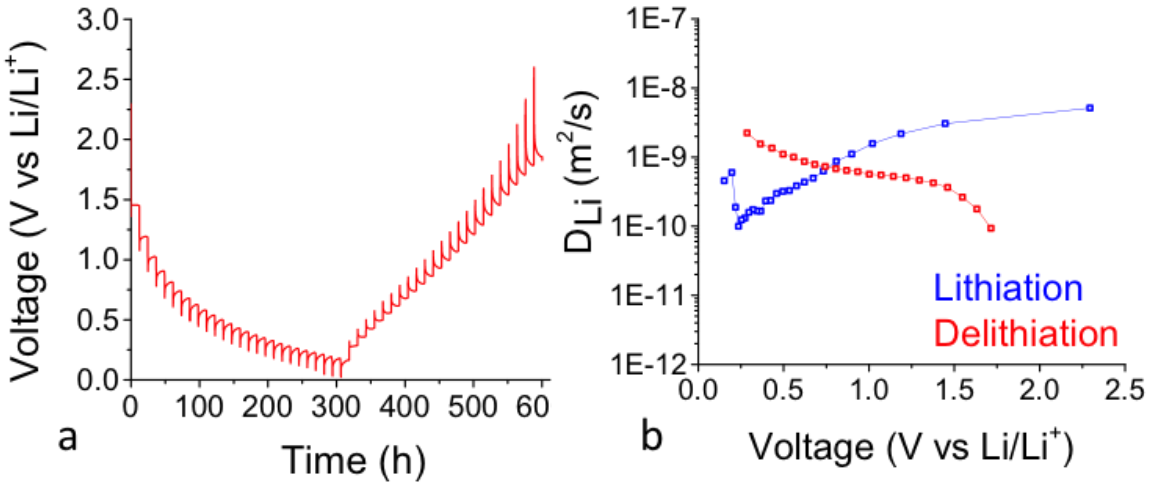

Figure 5-15 GITT Data: (a) Charge and discharge cycles with 15 min of current pulse at 100 mAh.g-1 followed by 12 h of relaxation for SiOC at room temperature (25 °C). (b) Calculated diffusion coefficient based on the relaxation steps at the corresponding voltages.

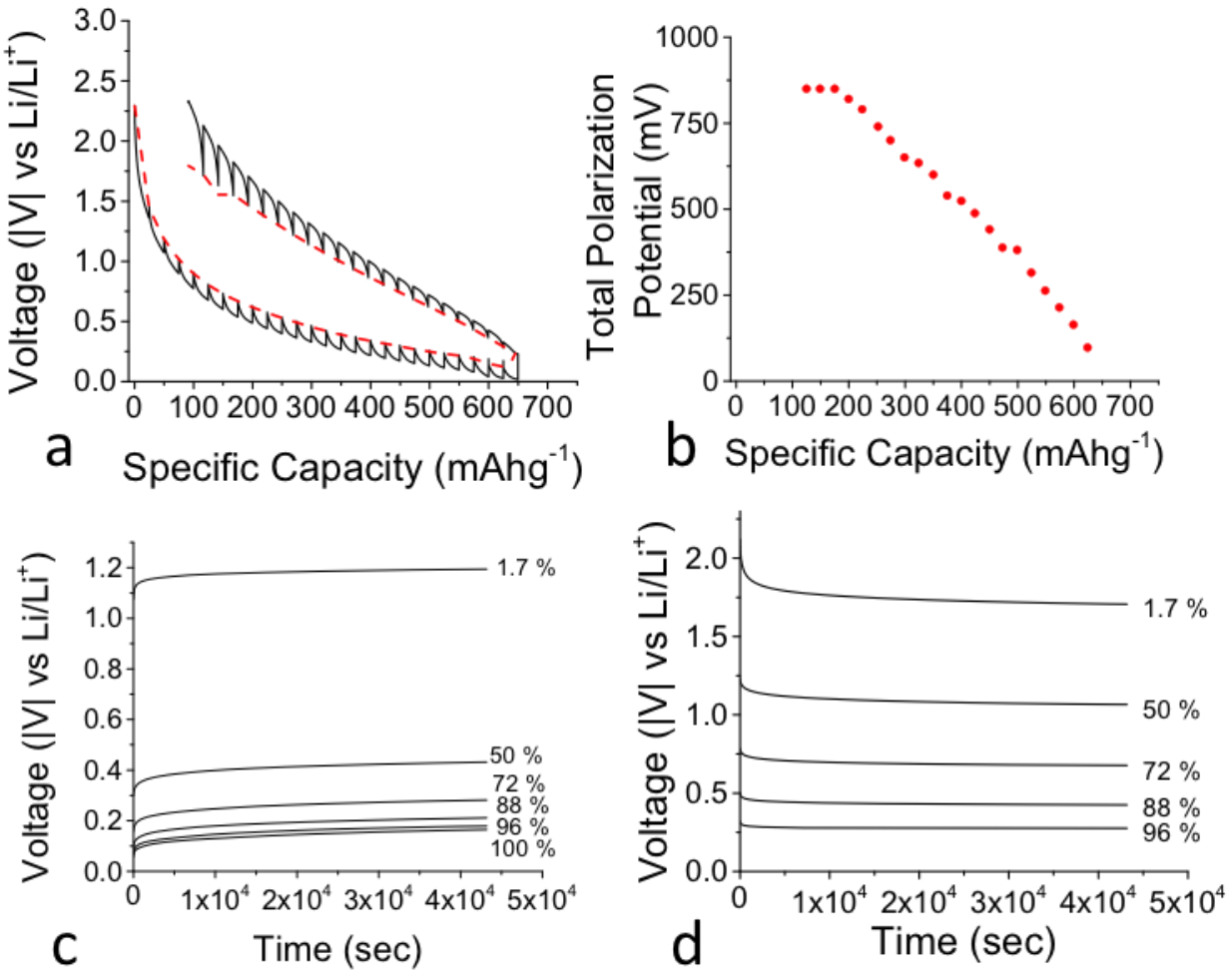

Figure 5-16 (a) Charge-discharge curve derived from titration studies. (b) Polarization potential at different states of charge. Time-dependent change in the open-circuit voltage at different states of charge (SOC) during (c) insertion and (d) extraction half cycles.

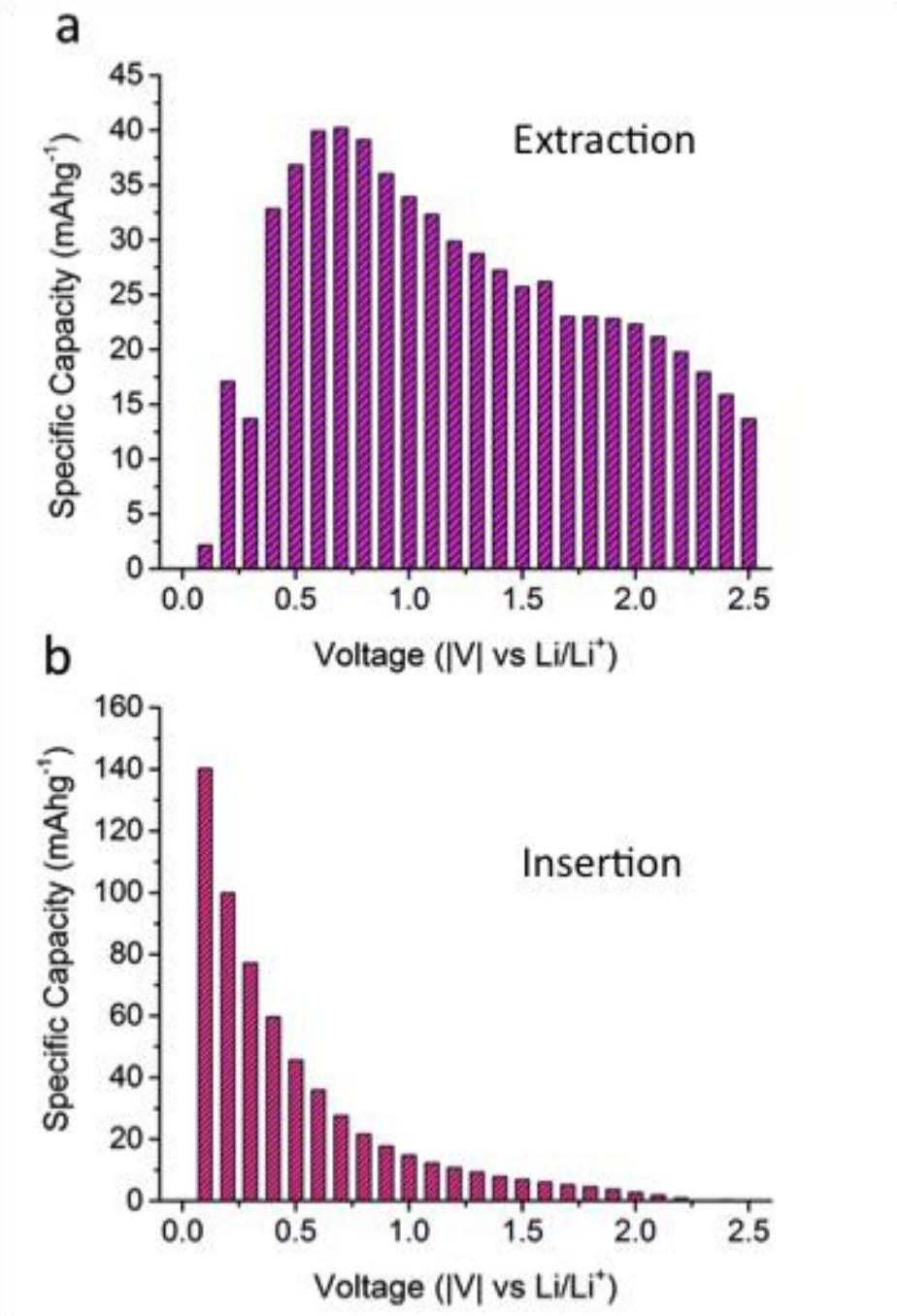

Figure 5-17 The Density of State (DOS) for (a) lithium extraction and (b) intercalation into 60SiOC electrode at room temperature.

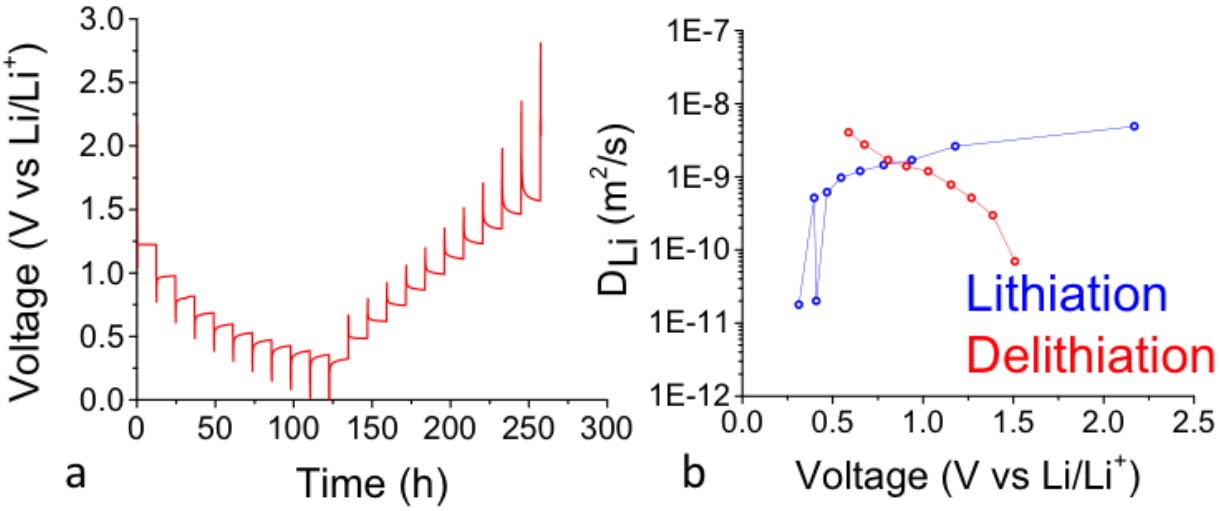

Figure 5-18 GITT Data: (a) Charge and discharge cycles with 15 min of current pulse at 100 mA.g-1 followed by 12 h of relaxation for SiOC at room temperature (-15 °C). (b) Calculated diffusion coefficient based on the relaxation steps at the corresponding voltages.

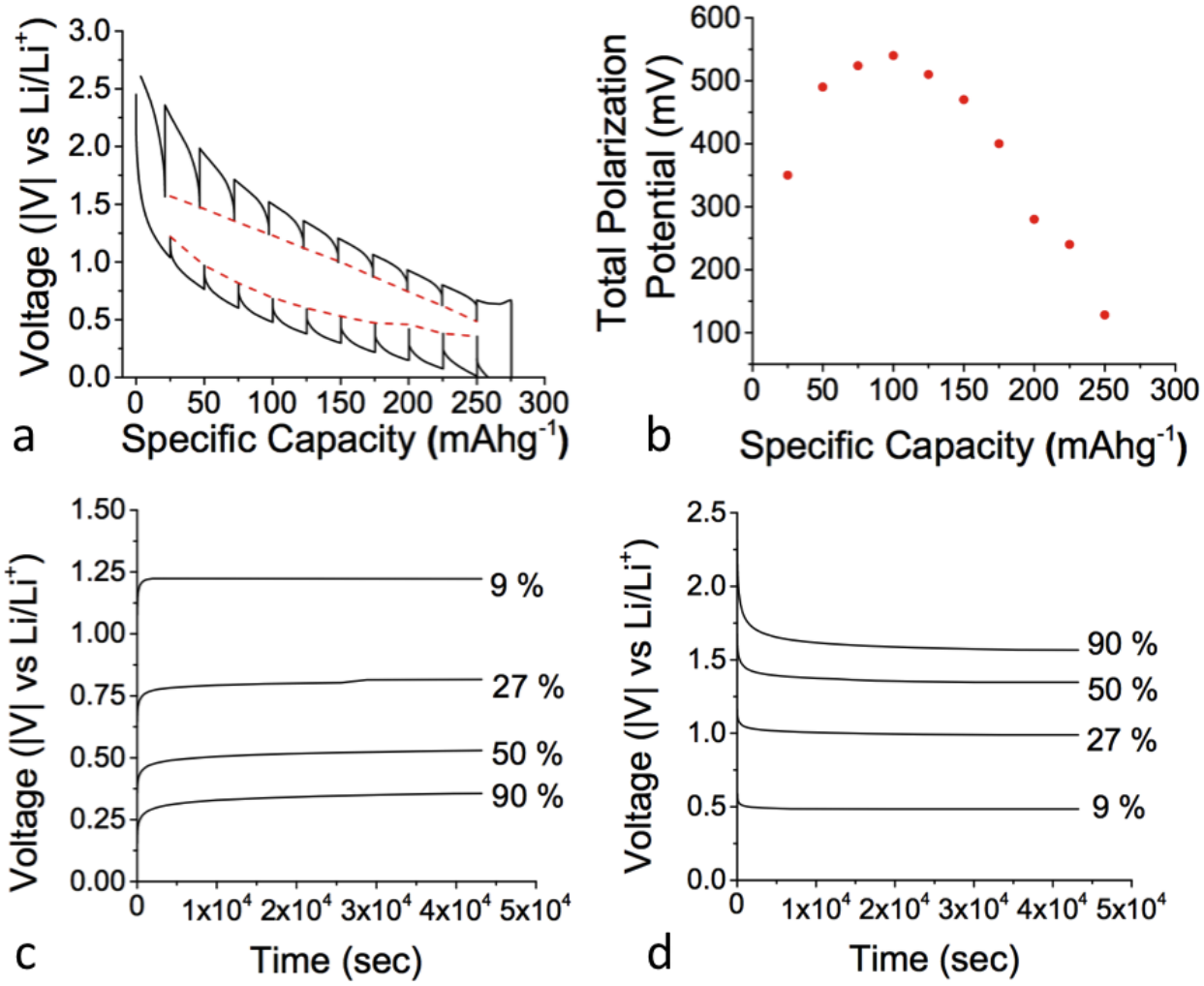

Figure 5-19 (a) Charge-discharge curve obtained during the experiment to obtain polarization potential. (b) Total polarization potential at different states of charge. Time dependent change in the open-circuit voltage at different states of charge (SOC) during (c) insertion and (d) extraction halves.

Overall, the composite paper-based electrode offered several advantages over the electrodes prepared on traditional metal foil current collectors. With its high surface area and high electrical conductivity, rGO provided a flexible, electrically conducting, and uniformly distributed architecture, allowing electrical and mechanical connection with each SiOC particle,

resulting in exceptional cycling stability at high current densities. SiOC ceramic particles acted as a reliable host for Li-ions, mainly due to SiOC's distinct amorphous structure of silica nano-domains wrapped with sp2 carbon chains, nano-voids, and silicon/carbon open bonds (see Figure 2f and supplementary Figure S1 for proposed SiOC structure), implying that the it has large number of sites in which Li-ion can be reversibly cycled with high columbic efficiency.

5.4.3. Mechanical Strength of the Composite Anode

Static uniaxial tensile tests were conducted to quantify the strength and strain-to-failure for the freestanding composite papers by use of a custom-built set-up Figure 5.20a shows a schematic of the test setup in which the load cell is attached to a digital meter, connected to a transducer electronic data sheet (TEDS) in order to transfer the data to host computer through an RS232 serial port using a program written in MATLAB. Engineering stress-strain plots and tensile modulus, derived from load-displacement curves for various paper electrodes are compared in Figure 5.20b and Figure 5.20c, respectively. The rGO sample showed tensile strength of approximately 10.7 MPa at a failure strain of 2.8%, while 60SiOC sample had tensile strength of approximately 2.7 MPa at a strain of 1.1%. Low tensile strength of the 60SiOC specimen was expected considering that it contained only approximately 20% rGO. Overall, strength and modulus for these crumpled composite papers was lower than GO and rGO papers prepared from techniques other than high temperature reduction. [39,40] However, the strain-to-failure was almost 5 to 10 times higher than a typical GO, rGO, or rGO-composite paper, suggesting that crumpled composite papers may be able to sustain larger volume changes. Surface analysis using SEM of rGO (Figure 5.20d) showed occurrence of micro features after tensile test, which we suggest, are due to rearrangement of rGO sheets under tensile load. These micro features are assumed to be due to curling of individual graphene sheets on the top surface

when they lose contact with the sheet below them. However, for 60SiOC in Figure 5.20e, ceramic particles acted as the point of fracture and caused rGO sheets to separate without stretching, as proven by SEM images that show no distinguishable changes before and after tensile test. Figure 5.21 (a through h) are cross-sectional SEM images of fractured surface. The rGO because of higher elasticity had an irregular crumpled appearance, but SiOC/rGO papers were more brittle and had sharper cross-section.

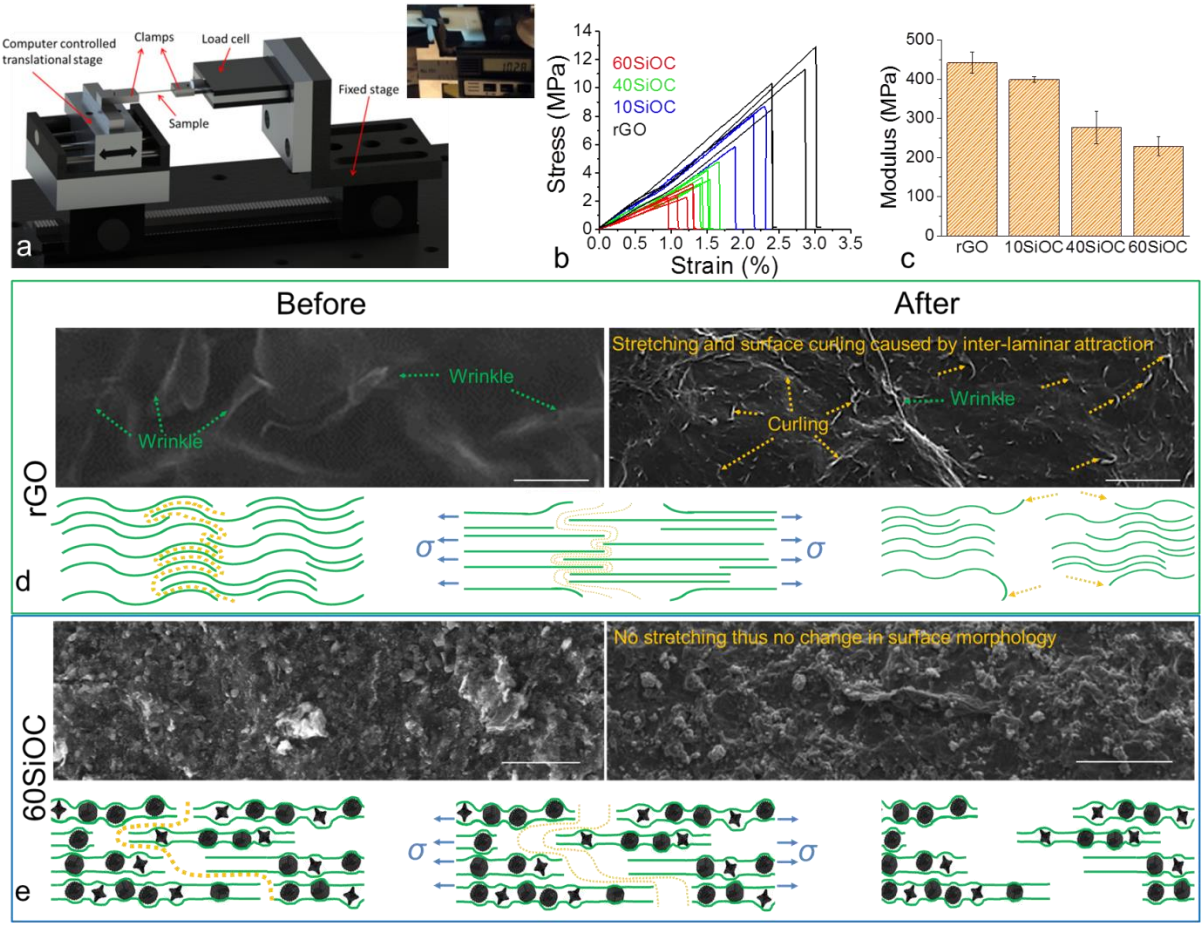

Figure 5-20 Mechanical testing data. (a) Schematic of the tensile testing setup with a photograph of rGO paper immediately after the fracture. Scale reading in the photograph indicate the change in length to be ~0.28 mm. (b) Engineering stress versus strain plots of various freestanding papers derived from load/displacement data, and (c) their

corresponding modulus values. The schematic shows the predicted mechanism of fracture for rGO and 60SiOC freestanding papers. (d) The rGO paper experienced stretching and rearrangement of graphene sheets before failure. (e) For 60SiOC paper, negligible stretching or rearrangement occurred. Fracture line follows SiOC particles embedded in rGO flakes, resulting in gradual separation/tearing of the paper. The scale bar is 20 *μ*m in all images.

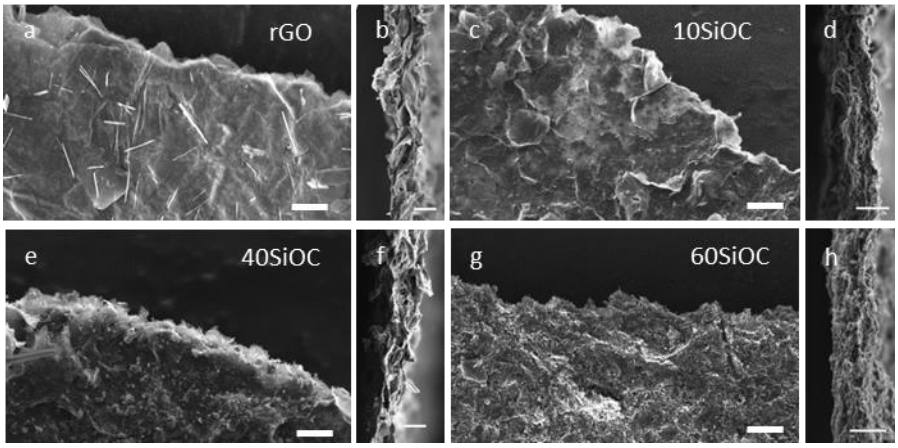

Figure 5-21 Mechanical testing data. (a-h) Cross-sectional SEM images of rGO, 10SiOC, 40SiOC and 60SiOC freestanding papers. The scale bar is 20 µm.

Mode of fracture in rGO and 60SiOC papers also differed significantly. A loud distinct sound indicated almost instantaneous fracture of the rGO specimen, accompanied by curling of both ends of the fractured paper. Fracture of 60SiOC specimen was similar to a thin plate with an edge crack, the crack propagation could be clearly observed. In addition, stress lines could be observed only in the rGO specimen, radiating from one clamp to another and indicating distribution of stress throughout the length of the specimen. These observations are explained with the help of a schematic in Figure 5.20d and Figure 5.20e. Lastly, *ex situ* Raman analysis

from the top surface of the specimens before and after tests showed no measurable changes (Figure 5.22).

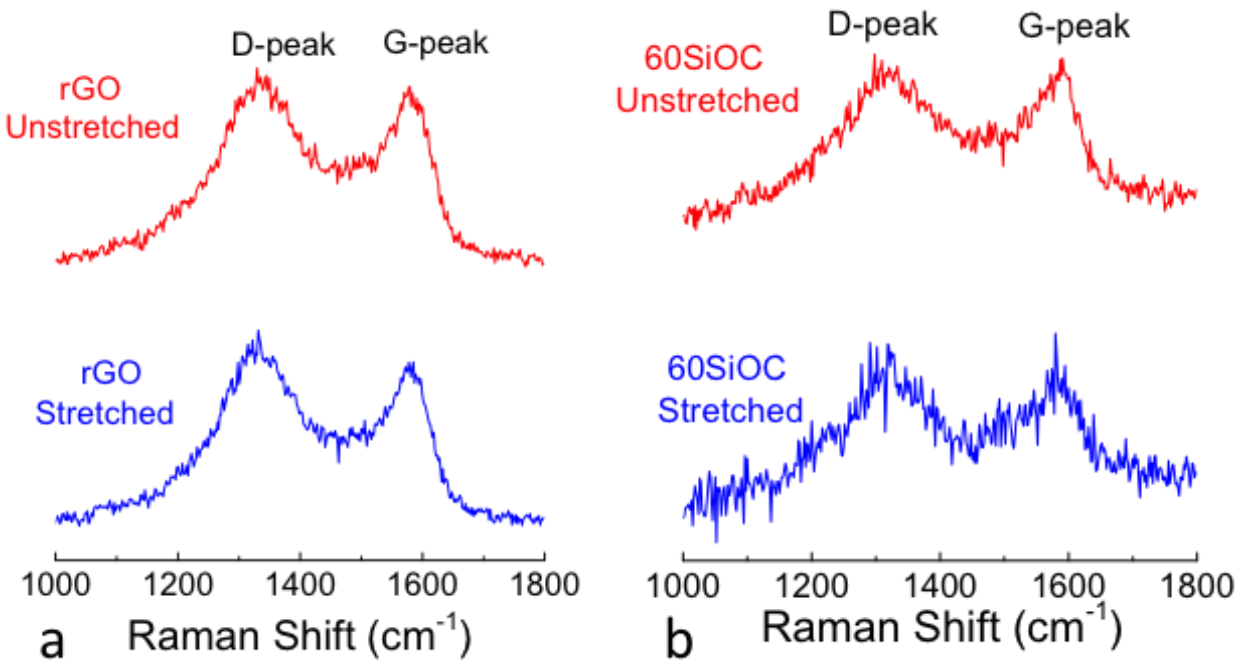

Figure 5-22 No considerable change was observed in the Raman spectrum (Id/Ig) of the composite papers pre and post tensile testing.

5.5. Conclusion

We have demonstrated synthesis of a freestanding multi-component composite paper consisting of SiOC amorphous glass-ceramic particles supported in rGO matrix as a stable and durable battery anode. The porous 3-D rGO matrix served as an effective current collector and electron conductor with a stable chemical and mechanical structure while, embedded amorphous SiOC particles actively cycled Li-ions with high efficiency. Owing to this unique morphology, the rGO/SiOC composite electrode exhibited stable charge capacity (anode) of approximately 543 $mAh.g^{-1}$ at current densities up to 2400 $mA.g^{-1}$ with ~100% efficiency. At current density of 1600 $mA.g^{-1}$ with symmetric cycling the anode exhibited stable charge capacity of

approximately 200 $mAh.g^{-1}$ after 1000 cycles again with approximately 100 % efficiency. Postcycle images of the disassembled cell revealed a completely integral electrode, thereby explaining the stable electrochemical performance. Elimination of inactive ingredients such as metal current collector, non-conducting polymeric binder, and conducting agent reduces the total electrode weight and provides the means to produce highly efficient light weight batteries.

5.6. Acknowledgements

Authors would like to thank Professor Rishi Raj (University of Colorado) for introducing us to the field of polymer-derived ceramics. Thanks are also due to Professor Kevin Lease (Kansas State University) and Nassim Rahamani for access to their lab for mechanical testing. This work is supported by the National Science Foundation grant number 1335862 and 1454151 to G. Singh.

5.7. References

1. Xiong, P. et al. Chemically Integrated Two-Dimensional Hybrid Zinc Manganate/Graphene Nanosheets with Enhanced Lithium Storage Capability. *ACS Nano* 8, 8610-8616, doi:10.1021/nn5041203 (2014).

2. Ko, M., Chae, S., Jeong, S., Oh, P. & Cho, J. Elastic a-Silicon Nanoparticle Backboned Graphene Hybrid as a Self-Compacting Anode for High-Rate Lithium Ion Batteries. *ACS Nano* 8, 8591-8599, doi:10.1021/nn503294z (2014).

3. David, L., Bhandavat, R. & Singh, G. MoS_2/Graphene Composite Paper for Sodium-Ion Battery Electrodes. *ACS Nano* 8, 1759-1770, doi:10.1021/nn406156b (2014).

4. Kamat, P. V. Graphene-Based Nanoassemblies for Energy Conversion. *Journal of Physical Chemistry Letters* 2, 242-251, doi:10.1021/jz101639v (2011).

5. Bhandavat, R., David, L. & Singh, G. Synthesis of Surface-Functionalized WS_2 Nanosheets and Performance as Li-Ion Battery Anodes. *Journal of Physical Chemistry Letters* 3, 1523-1530, doi:10.1021/jz300480w (2012).

6. Manthiram, A. Materials Challenges and Opportunities of Lithium Ion Batteries. *Journal of Physical Chemistry Letters* 2, 176-184, doi:10.1021/jz1015422 (2011).

7. Cui, L.-F., Hu, L., Choi, J. W. & Cui, Y. Light-Weight Free-Standing Carbon Nanotube-Silicon Films for Anodes of Lithium Ion Batteries. *ACS Nano* 4, 3671-3678, doi:10.1021/nn100619m (2010).

8. Luo, J. Y. *et al.* Crumpled Graphene-Encapsulated Si Nanoparticles for Lithium Ion Battery Anodes. *Journal of Physical Chemistry Letters* 3, 1824-1829, doi:10.1021/jz3006892 (2012).

9. Liu, N. et al. A pomegranate-inspired nanoscale design for large-volume-change lithium battery anodes. Nature Nanotechnology 9, 187-192, doi:10.1038/nnano.2014.6 (2014).

10. Hwang, T. H., Lee, Y. M., Kong, B. S., Seo, J. S. & Choi, J. W. Electrospun Core-Shell Fibers for Robust Silicon Nanoparticle-Based Lithium Ion Battery Anodes. *Nano Letters* 12, 802-807, doi:10.1021/nl203817r (2012).

11. Pan, L. et al. Facile Synthesis of Yolk-Shell Structured Si-C Nanocomposites as Anodes for Lithium-Ion Batteries. Chemical Communications 50, 5878-5880, doi:10.1039/C4CC01728E (2014).

12. Cui, L. F., Yang, Y., Hsu, C. M. & Cui, Y. Carbon-Silicon Core-Shell Nanowires as High Capacity Electrode for Lithium Ion Batteries. *Nano Letters* 9, 3370-3374, doi:10.1021/nl901670t (2009).

13. Hertzberg, B., Alexeev, A. & Yushin, G. Deformations in Si-Li Anodes Upon Electrochemical Alloying in Nano-Confined Space. *Journal of the American Chemical Society* 132, 8548-+, doi:10.1021/ja1031997 (2010).

14. Wang, B. *et al.* Adaptable Silicon-Carbon Nanocables Sandwiched between Reduced Graphene Oxide Sheets as Lithium Ion Battery Anodes. *Acs Nano* 7, 1437-1445, doi:10.1021/nn3052023 (2013).

15. Hu, T. *et al.* Flexible Free-Standing Graphene-TiO_2 Hybrid Paper for Use as Lithium Ion Battery Anode Materials. *Carbon* 51, 322-326, doi:10.1016/j.carbon.2012.08.059 (2013).

16. Liang, J., Zhao, Y., Guo, L. & Li, L. Flexible Free-Standing Graphene/SnO2 Nanocomposites Paper for Li-Ion Battery. *ACS Applied Materials & Interfaces* 4, 5742-5748, doi:10.1021/am301962d (2012).

17. Jia, X. *et al.* Building Robust Architectures of Carbon and Metal Oxide Nanocrystals toward High-Performance Anodes for Lithium-Ion Batteries. *ACS Nano* 6, 9911-9919, doi:10.1021/nn303478e (2012).

18. Noerochim, L., Wang, J. Z., Chou, S.-L., Wexler, D. & Liu, H.-K. Free-Standing Single-Walled Carbon Nanotube/SnO_2 Anode Paper for Flexible Lithium-Ion Batteries. *Carbon* 50, 1289-1297, doi:10.1016/j.carbon.2011.10.049 (2012).

19. Chockla, A. M. *et al.* Electrochemical Lithiation of Graphene-Supported Silicon and Germanium for Rechargeable Batteries. *The Journal of Physical Chemistry C* 116, 11917-11923, doi:10.1021/jp302344b (2012).

20. Yue, L., Zhong, H. & Zhang, L. Enhanced reversible lithium storage in a nano-Si/MWCNT free-standing paper electrode prepared by a simple filtration and post sintering process. *Electrochimica Acta* 76, 326-332, doi:10.1016/j.electacta.2012.05.038 (2012).

21. Chen, Z. *et al.* In Situ Generation of Few-Layer Graphene Coatings on SnO2-SiC Core-Shell Nanoparticles for High-Performance Lithium-Ion Storage. *Advanced Energy Materials* 2, 95-102 doi: 10.1002/aenm.201100464 (2012).

22. Ji, L. *et al.* Graphene/Si Multilayer Structure Anodes for Advanced Half and Full Lithium-Ion Cells. *Nano Energy* 1, 164-171 doi: 10.1016/j.nanoen.2011.08.003 (2012).

23. Zhang, B., Zheng, Q. B., Huang, Z. D., Oh, S. W. & Kim, J. K. SnO2-graphene-carbon nanotube mixture for anode material with improved rate capacities. *Carbon* 49, 4524-4534, doi:10.1016/j.carbon.2011.06.059 (2011).

24. Ji, L. *et al.* Fe_3O_4 Nanoparticle-Integrated Graphene Sheets for High-Performance Half and Full Lithium Ion Cells. *Physical Chemistry Chemical Physics* 13, 7170-7177 doi:10.1039/C1CP20455F (2011).

25. Yu, A. *et al.* Free-Standing Layer-By-Layer Hybrid Thin Film of Graphene-MnO2 Nanotube as Anode for Lithium Ion Batteries. *Journal of Physical Chemistry Letters* 2, 1855-1860, doi:10.1021/jz200836h (2011).

26. Xiao, J. *et al.* Electrochemically Induced High Capacity Displacement Reaction of PEO/MoS_2/Graphene Nanocomposites with Lithium. *Advanced Functional Materials* 21, 2840-2846 doi: 10.1002/adfm.201002752 (2011).

27. Lee, J. K., Smith, K. B., Hayner, C. M. & Kung, H. H. Silicon Nanoparticles-Graphene Paper Composites for Li Ion Battery Anodes. *Chemical Communications* 46, 2025-2027 doi: 10.1039/B919738A (2010).

28. Wang, H. *et al.* Mn3O4−Graphene Hybrid as a High-Capacity Anode Material for Lithium Ion Batteries. *Journal of the American Chemical Society* 132, 13978-13980, doi:10.1021/ja105296a (2010).

29. Wu, Z.-S. *et al.* Graphene Anchored with Co3O4 Nanoparticles as Anode of Lithium Ion Batteries with Enhanced Reversible Capacity and Cyclic Performance. *ACS Nano* 4, 3187-3194, doi:10.1021/nn100740x (2010).

30. Yang, S., Feng, X., Ivanovici, S. & Müllen, K. Fabrication of Graphene-Encapsulated Oxide Nanoparticles: Towards High-Performance Anode Materials for Lithium Storage. *Angewandte Chemie International Edition* 49, 8408-8411 doi: 10.1002/anie.201003485 (2010).

31. Wang, D. *et al.* Ternary Self-Assembly of Ordered Metal Oxide−Graphene Nanocomposites for Electrochemical Energy Storage.*ACS Nano* 4, 1587-1595, doi:10.1021/nn901819n (2010).

32. Wang, J. Z., Zhong, C., Chou, S.-L. & Liu, H.-K. Flexible free-standing graphene-silicon composite film for lithium-ion batteries. *Electrochemistry Communications* 12, 1467-1470, doi:10.1016/j.elecom.2010.08.008 (2010).

33. Zhou, G. et al. Graphene-Wrapped Fe3O4 Anode Material with Improved Reversible Capacity and Cyclic Stability for Lithium Ion Batteries. Chemistry of Materials 22, 5306-5313, doi:10.1021/cm101532x (2010).

34. Wang, D. *et al.* Self-Assembled TiO2–Graphene Hybrid Nanostructures for Enhanced Li-Ion Insertion. *ACS Nano* 3, 907-914, doi:10.1021/nn900150y (2009).

35. Paek, S.-M., Yoo, E. & Honma, I. Enhanced Cyclic Performance and Lithium Storage Capacity of SnO2/Graphene Nanoporous Electrodes with Three-Dimensionally Delaminated Flexible Structure. *Nano Letters* 9, 72-75, doi:10.1021/nl802484w (2008).

36. Kumar, A. *et al.* Direct Synthesis of Lithium-Intercalated Graphene for Electrochemical Energy Storage Application. *ACS Nano* 5, 4345-4349, doi:10.1021/nn201527p (2011).

37. Li, X. *et al.* Superior Cycle Stability of Nitrogen-Doped Graphene Nanosheets as Anodes for Lithium Ion Batteries. *Electrochemistry Communications* 13, 822-825 doi:10.1016/j.elecom.2011.05.012 (2011).

38. Zhao, X., Hayner, C. M., Kung, M. C. & Kung, H. H. Flexible Holey Graphene Paper Electrodes with Enhanced Rate Capability for Energy Storage Applications. *Acs Nano* 5, 8739-8749, doi:10.1021/nn202710s (2011).

39. Compton, O. C., Dikin, D. A., Putz, K. W., Brinson, L. C. & Nguyen, S. T. Electrically Conductive "Alkylated" Graphene Paper via Chemical Reduction of Amine-Functionalized Graphene Oxide Paper. *Advanced Materials* 22, 892-+, doi:10.1002/adma.200902069 (2010).

40. Compton, O. C. & Nguyen, S. T. Graphene Oxide, Highly Reduced Graphene Oxide, and Graphene: Versatile Building Blocks for Carbon-Based Materials. *Small* 6, 711-723, doi:10.1002/smll.200901934 (2010).

41. Matsuo, Y. & Sugie, Y. Preparation, Structure and Electrochemical Property of Pyrolytic Carbon From Graphite Oxide. *Carbon* 36, 301-303 doi: 10.1016/S0008-6223(98)80120-6 (1998).

42. David, L., Asok, D. & Singh, G. Synthesis and Extreme Rate Capability of Si–Al–C–N Functionalized Carbon Nanotube Spray-on Coatings as Li-Ion Battery Electrode. *ACS Applied Materials & Interfaces*, 6, 16056-16064, doi:10.1021/am5052729 (2014).

43. Bhandavat, R. & Singh, G. Improved Electrochemical Capacity of Precursor-Derived Si(B)CN-Carbon Nanotube Composite as Li-Ion Battery Anode. *Acs Applied Materials & Interfaces* 4, 5092-5097, doi:10.1021/am3015795 (2012).

44. Bhandavat, R. & Singh, G. Stable and Efficient Li-Ion Battery Anodes Prepared from Polymer-Derived Silicon Oxycarbide-Carbon Nanotube Shell/Core Composites. *Journal of Physical Chemistry C* 117, 11899-11905, doi:10.1021/jp310733b (2013).

45. Saha, A., Raj, R. & Williamson, D. L. A Model for the Nanodomains in Polymer-Derived SiCO. *Journal of the American Ceramic Society* 89, 2188-2195, doi:10.1111/j.1551-2916.2006.00920.x (2006).

46. Sanchez-Jimenez, P. E. & Raj, R. Lithium Insertion in Polymer-Derived Silicon Oxycarbide Ceramics. *Journal of the American Ceramic Society* 93, 1127-1135, doi: 10.1111/j.1551-2916.2009.03539.x (2010).

47. Kaspar, J., Graczyk-Zajac, M. & Riedel, R. Determination of the chemical diffusion coefficient of Li-ions in carbon-rich silicon oxycarbide anodes by electro-analytical methods. *Electrochimica Acta* 115, 665-670, doi:http://dx.doi.org/10.1016/j.electacta.2013.10.184 (2014).

48. Konno, H. *et al.* Si-C-O Glass-Like Compound/Exfoliated Graphite Composites for Negative Electrode of Lithium Ion Battery. *Carbon* 45, 477-483, doi:10.1016/j.carbon.2006.11.002 (2007).

49. Ahn, D. & Raj, R. Cyclic stability and C-rate performance of amorphous silicon and carbon based anodes for electrochemical storage of lithium. *Journal of Power Sources* 196, 2179-2186 (2011).

50. Graczyk-Zajac, M., Fasel, C. & Riedel, R. Polymer-derived-SiCN ceramic/graphite composite as anode material with enhanced rate capability for lithium ion batteries. *Journal of Power Sources* 196, 6412-6418, doi:10.1016/j.jpowsour.2011.03.076 (2011).

51. Marcano, D. C. *et al.* Improved Synthesis of Graphene Oxide. *ACS Nano* 4, 4806-4814, doi:10.1021/nn1006368 (2010).

52. Park, S. *et al.* Aqueous Suspension and Characterization of Chemically Modified Graphene Sheets. *Chemistry of Materials* 20, 6592-6594, doi:10.1021/cm801932u (2008).

53. Park, S. *et al.* Colloidal Suspensions of Highly Reduced Graphene Oxide in a Wide Variety of Organic Solvents. *Nano Letters* 9, 1593-1597, doi:10.1021/nl803798y (2009).

54. Ahn, D. & Raj, R. Cyclic stability and C-rate performance of amorphous silicon and carbon based anodes for electrochemical storage of lithium. Journal of Power Sources 196, 2179-2186, doi:10.1016/j.jpowsour.2010.09.086 (2011).

55. Wang, C., Li, D., Too, C. O. & Wallace, G. G. Electrochemical Properties of Graphene Paper Electrodes Used in Lithium Batteries. Chemistry of Materials 21, 2604-2606, doi:10.1021/cm900764n (2009).

56. Zhao, X., Hayner, C. M., Kung, M. C. & Kung, H. H. Flexible Holey Graphene Paper Electrodes with Enhanced Rate Capability for Energy Storage Applications. ACS Nano 5, 8739-8749, doi:10.1021/nn202710s (2011).

57. Wang, J.-Z., Zhong, C., Chou, S.-L. & Liu, H.-K. Flexible free-standing graphene-silicon composite film for lithium-ion batteries. Electrochemistry Communications 12, 1467-1470, doi:10.1016/j.elecom.2010.08.008 (2010).

58. Chockla, A. M. et al. Electrochemical Lithiation of Graphene-Supported Silicon and Germanium for Rechargeable Batteries. The Journal of Physical Chemistry C 116, 11917-11923, doi:10.1021/jp302344b (2012).

59. Wang, B. et al. Adaptable Silicon-Carbon Nanocables Sandwiched between Reduced Graphene Oxide Sheets as Lithium Ion Battery Anodes. ACS Nano 7, 1437-1445, doi:10.1021/nn3052023 (2013).

60. Hu, T. et al. Flexible free-standing graphene-TiO2 hybrid paper for use as lithium ion battery anode materials. Carbon 51, 322-326, doi:10.1016/j.carbon.2012.08.059 (2013).

61. Yu, A. et al. Free-Standing Layer-By-Layer Hybrid Thin Film of Graphene-MnO2 Nanotube as Anode for Lithium Ion Batteries. Journal of Physical Chemistry Letters 2, 1855-1860, doi:10.1021/jz200836h (2011).

62. Liang, J., Zhao, Y., Guo, L. & Li, L. Flexible Free-Standing Graphene/SnO2 Nanocomposites Paper for Li-Ion Battery. Acs Applied Materials & Interfaces 4, 5742-5748, doi:10.1021/am301962d (2012).

63. Zhang, B., Zheng, Q. B., Huang, Z. D., Oh, S. W. & Kim, J. K. SnO2-graphene-carbon nanotube mixture for anode material with improved rate capacities. Carbon 49, 4524-4534, doi:10.1016/j.carbon.2011.06.059 (2011).

64. Jia, X. et al. Building Robust Architectures of Carbon and Metal Oxide Nanocrystals toward High-Performance Anodes for Lithium-Ion Batteries. ACS Nano 6, 9911-9919, doi:10.1021/nn303478e (2012).

65. Yue, L., Zhong, H. & Zhang, L. Enhanced reversible lithium storage in a nano-Si/MWCNT free-standing paper electrode prepared by a simple filtration and post sintering process. Electrochimica Acta 76, 326-332, doi:10.1016/j.electacta.2012.05.038 (2012).

66. Noerochim, L., Wang, J.-Z., Chou, S.-L., Wexler, D. & Liu, H.-K. Free-standing single-walled carbon nanotube/SnO2 anode paper for flexible lithium-ion batteries. Carbon 50, 1289-1297, doi:10.1016/j.carbon.2011.10.049 (2012).

67. Van der Pauw, L.J., A method of measuring specific resistivity and hall effect of discs of arbitrary shape. Philips Research Reports, 13, 1, 1-9 (1958).

68. Weppner, W. & Huggins, R. A. Determination of the Kinetic Parameters of Mixed-Conducting Electrodes and Application to the System Li3Sb. Journal of the Electrochemical Society 124, 1569-1578, doi:10.1149/1.2133112 (1977).

69. Wen, C. J., Boukamp, B. A., Huggins, R. A. & Weppner, W. Thermodynamic and mass transport properties of "LiAl". Journal of the Electrochemical Society 126, 2258-2266, doi:10.1149/1.2128939 (1979).

Chapter 6 - Exfoliation of MoS_2 and Functionalization with PDC for Stable Lithium-Ion Battery Electrode[4]

6.1. Abstract

Liquid-phase exfoliated MoS_2 was functionalized with polysilazane polymer to yield ceramic SiCN-MoS_2 layered composite upon pyrolysis. Electron microscopy and spectroscopic techniques confirmed ceramization of polymer to ceramic phase on surfaces on MoS_2. Electrochemical behavior of MoS_2 and SiCN-MoS_2 on both traditional and paper-based electrode architecture was investigated in a lithium ion battery half-cell. All electrodes showed classical three-phase behavior characteristics of a conversion reaction. SiCN-MoS_2 showed stable cycling and higher reversible capacity retention than 'neat' MoS_2. The contribution of conversion reaction in MoS_2 or electrolyte decomposition in overall capacity was found to reduce in SiCN-MoS_2 electrodes, which is understood as one of the reasons for decreased first cycle loss and increased capacity retention. In addition, the freestanding paper electrode exhibited excellent C-rate performance, regaining initial charge capacity (approximately 530 $mAh.g^{-1}_{anode}$) when the current density returned to 100 $mA.g^{-1}$ (509.2 $mAh.g^{-1}_{anode}$) after cycling at 2400 $mA.g^{-1}$ (192 $mAh.g^{-1}_{anode}$).

[4] Accepted for publication (L. David, R. Bhandavat and G. Singh, "Polymer-Derived Ceramic Functionalized MoS_2 Composite Paper as a Stable Lithium-Ion Battery" Scientific Reports).

6.2. Introduction

Layered transition metal dichalcogenides (TMDs) such as molybdenum di sulfide (MoS_2) and tungsten di sulfide (WS_2) have garnered increased research interest because of applications in several emerging areas such as hydrogen storage[1], chemical catalysis[2], double-layer capacitors and rechargeable metal-ion battery electrodes[3-9]. Application as Li-ion battery anode is particularly of interest because of weak van der Waals interactions between TMD layers and unique conversion chemistry with Li that allows continuous Li-ion cycling with lower volume expansion and pulverization compared to alloying anodes such as silicon and even metal oxides.[10,11] Theoretically, conversion reaction in one mole of MoS_2 leads to four moles of stored Li+ ions resulting in a specific capacity of 670 $mAh.g^{-1}$ (approximately 1.8 times the traditional graphite anode)[12].

Reports on electrochemical performance of bulk MoS_2 began in the 1980s when TMDs were investigated as cathode material for use in Li-metal batteries.[13] However, safety issues lead to discontinuation of such batteries. Recent advances in nanotechnology, such as development of efficient liquid phase exfoliation methods,[14-20] improved understanding of the electrode/electrolyte interface, and recent success with fabrication of single layer MoS_2 transistors and membranes[21, 22] have motivated researchers to reconsider nanostructured MoS_2 as potential Li host material. However, use of MoS_2 nanosheets in rechargeable batteries and other engineering applications has been limited primarily due to (a) low thermodynamic and chemical stability in moisture[21] and (b) degradation reaction with the battery electrolyte at low discharge potentials.[17]

Highly porous MoS_2 or MoS_2/carbon electrodes prepared by hydrothermal and solvothermal techniques, gas-phase reaction of MoO_3 with H_2S or S vapor, and thermal decomposition of ammonium thiomolybdate have demonstrated performance improvements in

response to challenges presented by MoS_2 nanosheet use.[23-32] As a result, capacity values as high as ~1200 $mAh.g^{-1}$ have been achieved for such electrodes, particularly at low active weight loadings.[33] More recently, MoS_2-based hybrid nanocomposites (obtained by interfacing with carbon nanotubes or graphene) have been of interest because CNT or graphene offers high electrical conductivity[34], thereby allowing high rate capability and reversibility.[35-42] Nevertheless, some new challenges have emerged that hinder the introduction of TMD nanosheets for practical applications. These challenges include: (a) high costs due to complex procedures that limit production in large quantities, (b) capacity degradation for thick electrodes or the low volumetric capacity of nanostructured/porous electrode design, and (c) inertly high amounts of carbonaceous material in the composite which leads to uncertainty in the origins of their specific capacity. Efforts to cost-effectively produce large quantities of TMDs flakes via chemical exfoliation are promising; therefore, a matter of intense research[19,20].

Here, we report a one-step facile approach to synthesize a TMD/glass composite material. This approach could prove vital in retaining the useable (reversible) Li-ion capacity of TMD electrodes by mitigating the effect of phase-III electrolyte degradation reaction and polysulfide dissolution typically observed in these materials. The composite consists of a Si-based polymer-derived ceramic (or PDC)[43-46] chemically interfaced with the surfaces of exfoliated MoS_2. PDCs are high-temperature glasses prepared by thermal decomposition of organosilicon polymers. Monolayer thick films of PDC can be formed on a variety of substrate materials to achieve resistance to oxidation and chemical degradation without compromising the physical properties of base material; PDC/CNT and PDC/graphene are some examples.[43-48] Liquid-phase polymeric precursor allowed easy dispersion and functionalization (attainment of molecular level interfacing) of exfoliated MoS_2 flakes. Polymer molecules diffused within exfoliated sheets,[49]

forming an alternating MoS_2 and ceramic-layered morphology on pyrolysis, thereby exhibiting ideal candidate material for rechargeable battery electrodes. The composite has a tap density of ~1.5 $g.cm^{-3}$ and could be processed as either a thick film on copper foil or freestanding paper with active weight loading as high as 6 $mg.cm^{-2}$. This layered morphology may be essential for achieving long-term stable Li-cycling in Li-S and Li-ion batteries because it puts a check on the TMD/organic electrolyte degradation reaction observed at low discharge potentials.[17,50-51]

6.3. Experimental

6.3.1. Material Preparation

Acid-treated MoS_2 was prepared in a manner similar to our recent work on WS_2, described in Ref. 17 and 18. SiCN-MoS_2 composite nanosheets were prepared following the procedures shown in Figure 5.1. Approximately 30 wt. % of poly(ureamethylvinyl)silazane (commercial name: Ceraset^{TM}, Clariant) was added to acid-treated MoS_2, stirred for 24 h, and dried at 100 °C in an inert atmosphere. To allow cross-linking of the intercalated polymer, the dried polymer-MoS_2 mix was heated to 400 °C in nitrogen (held at 15 min) and then heated at 1000 °C for 1 h, resulting in thermal decomposition of the polymer into amorphous SiCN ceramic on MoS_2 surfaces. Under these processing conditions, the polymeric precursor showed a ceramic yield of approximately 70 to 75 wt. % [Figure 5.2], resulting in approximately 20 wt. % of SiCN ceramic in SiCN-MoS_2 composite.

6.3.2. Cell Assembly and Testing

Traditional electrode: These were prepared using active materials (exfoliated MoS_2 or SiCN-MoS_2 composite), acetylene black (Alfa Aesar, 99.9 %) as conducting agent and polyvinylidene fluoride (Sigma Aldrich) as a binding agent with a weight ratio of 8:1:1, respectively. Few drops of N-methyl pyrrolidone (Fisher) were added to obtain homogenously

viscous slurry. Approx. 125 μm uniformly thick coating was then prepared on copper current collector (9 μm thick) and dried in an inert medium at 80 °C for 4 h. They were then punched into circles of diameter 1.4 cm for use as working electrode in a coin cell (2032 coin cell) with Li-metal foil acting as the counter electrode. A polyethylene monolayer membrane (Celgard) soaked in 1.0 M of $LiPF_6$ in EC: DMC electrolyte (Novolyte Technologies) separated the two electrodes. The cells were assembled in a high-precision argon glove box.

Paper-based electrode: Freestanding papers were prepared in a manner similar to recent work.[52] Dispersion of SiCN-MoS_2 composite with 20 wt. % graphene oxide[53] was prepared in 1:1 water: Isopropanol solution. The dispersion was then vacuum-filtered through a 10 μm filter membrane (HPLC grade, Millipore). The paper was separated from the membrane and thermally reduced at 500 °C under argon atmosphere for 2 h. Because GO to rGO yield is approximately 50 % [Figure 6.2], the amount of rGO in the final paper was approximately 10 wt. % of the final composite. Four-point electrical conductivity of the paper was observed to be 0.11 S/cm. The heat-treated paper was then punched into small circles and directly utilized as a working electrode in the Li-ion battery half-cell.

6.3.3. Material Characterization

Scanning electron microscopy (SEM) was performed by use of Carl Zeiss EVO 10 SEM and transmission electron microscopy (TEM) was carried out on Philips CM 100 TEM (100 kV). EDX map was obtained using FEI Company Nova NanoSEM 430 with an Oxford X-Max Large Area Analytical EDS silicon drift detector (SDD) (80mm^2). Material characterization was made using an X-ray diffractometer (XRD) operating at room temperature with nickel-filtered Cu Kα radiation (λ = 1.5418 Å). Thermogravimetric analysis (TGA) was performed using Shimadzu 50 TGA (limited to 800 °C). Samples weighing, ~2.5 mg, were heated in a platinum pan at a rate of

10 °C/min in air flowing at 20 mL/min. Surface chemical composition of the powdered specimens were determined using X-ray photoelectron spectroscopy (XPS), by PHI Quantera SXM with Al Kα monochromatic X-radiation (beam size <9 μm) at 45° angle of incidence. The assembled cells were tested using Arbin BT2000 multichannel potentiostat in atmospheric conditions. The batteries were cycled from 10 mV to 3V at a constant current density of 100 $mA.g^{-1}$ during discharge and charge cycles.

6.4. Results and Discussion

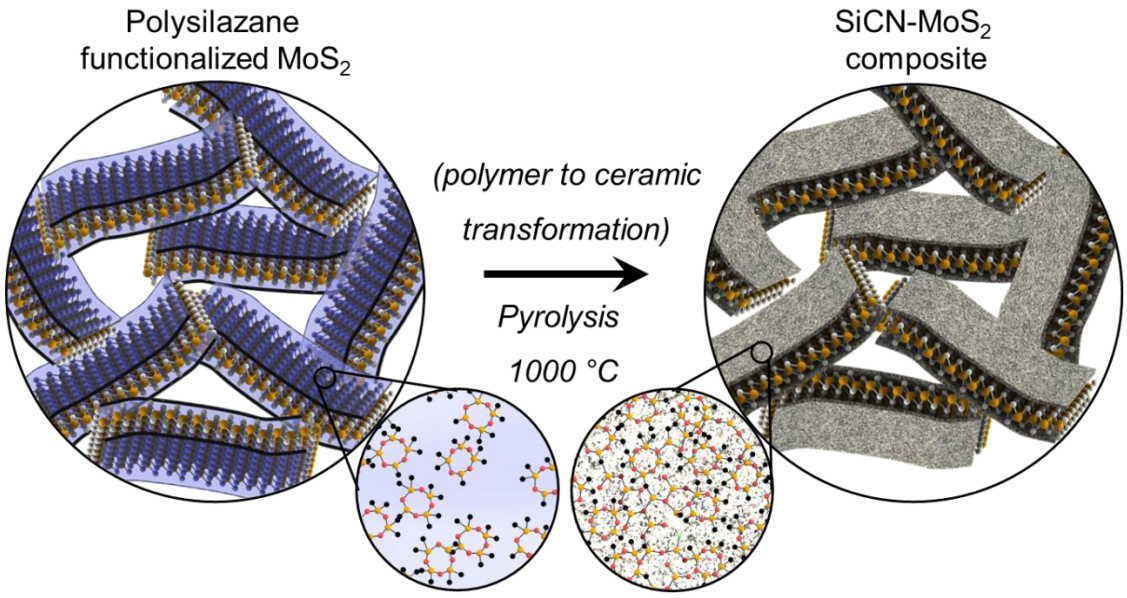

Figure 6-1 Schematic representation showing synthesis of SiCN-MoS_2 composite from in-situ pyrolysis. Liquid-phase polysilazane functionalized MoS_2 flakes undergo organic to inorganic transformation at 1000°C in flowing nitrogen leading to SiCN-MoS_2-SiCN type morphology. Sheet like morphology is retained.

Schematic representing synthesis of MoS_2-SiCN composite is presented in Figure 6.1. Electron microscopy of the acid-treated MoS_2 specimen demonstrated a large number of layered MoS_2 sheets with lateral dimensions varying between 2 μm to 5 μm (Figure 6.3(a)). SiCN functionalized MoS_2 composite also showed layered morphology, as shown in the SEM and TEM images (Figures 5.3(b-e)). The EDX map of SiCN-MoS_2 in Figure 6.3(c) (Mo-blue, Si-Green and C-red) shows an unevenly spread amorphous SiCN ceramic intercalated into MoS_2 sheets. Interlayer separation and presence of pores or gaps was evident in SiCN-MoS_2 composite. The SAED pattern in the insert of Figure 6.3(d) is similar to crystalline MoS_2 pattern, indicating the presence of intact sheets even after pyrolysis. The cross-section, top view, and EDX map of freestanding papers prepared by vacuum filtration (approximately 10 wt. % rGO) are presented in Figure 6.3f-h.

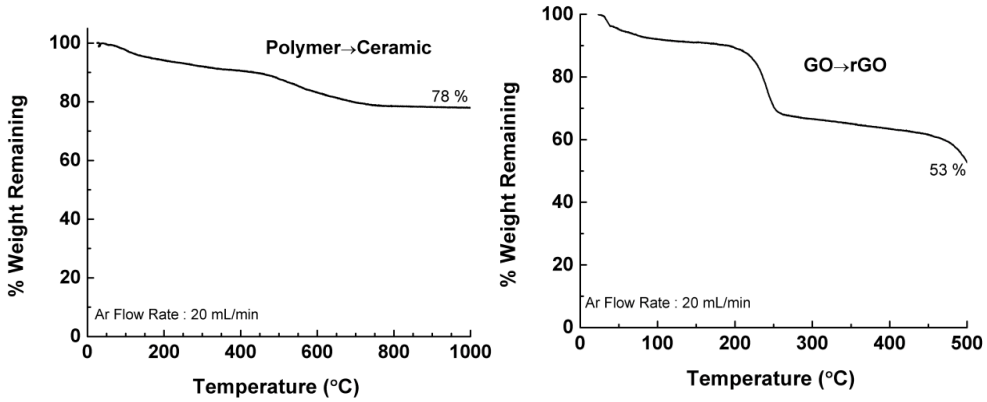

Figure 6-2 (Left) TGA data performed in flowing Ar gas for cross-linked polysilazane, shows polymer to ceramic transformation. The polymer to ceramic yield was approx. 78 %. (Right) TGA data performed in flowing Ar gas, shows thermal reduction of graphene oxide (GO) to reduced-graphene oxide (rGO). The yield was approx. 50 % when thermal reduction is performed at 500 °C.

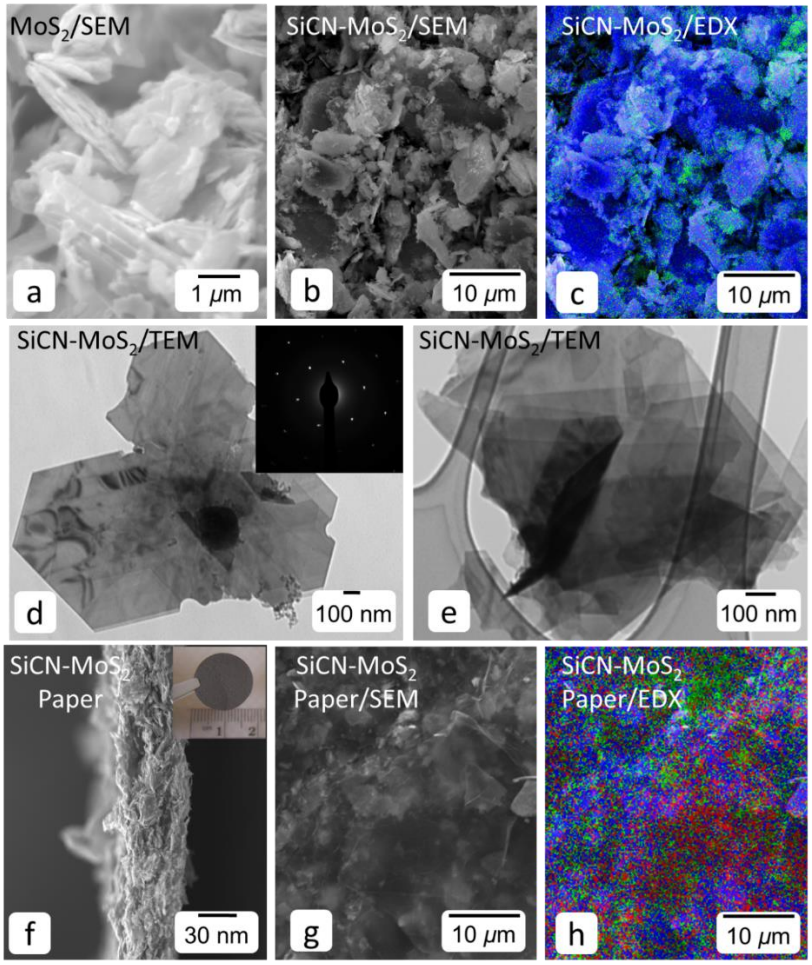

Figure 6-3 Material characterization. SEM micrograph of (a) acid-treated MoS_2 show stacked sheets with lateral dimension of 2 µm to 5 µm. (b) SEM image of SiCN/MoS_2 and (c) its corresponding EDX map show presence of Mo (blue), Si (Green) and C (red) distributed in the composite. (d,e) TEM images of SiCN/MoS_2 sheet composite show intact morphology of MoS_2 sheets after pyrolysis. The SAED pattern in the insert corresponds to crystalline MoS_2. SEM images of SiCN/MoS_2 free-standing paper (f) cross-section, (g) top view and (h) corresponding EDX map. The insert in Figure (f) is an optical photograph of SiCN/MoS_2 free-standing and flexible paper.

X-ray diffraction data for MoS_2, polymer-derived SiCN, SiCN-MoS_2 powder, and freestanding paper is presented in Figure 6.4. XPS analysis was performed on the composite material to ascertain the presence and chemical functionalization of MoS_2 by SiCN ceramic phase (Figure 6.5). High-resolution elemental Mo3d XPS spectra showed doublets at 227.8 eV and 230.9 eV. The doublets are deconvoluted into the original Mo-S state at 226.8 eV and 227.8 eV due to the Mo-Si/Mo-C bond, and the high energy 230.9 eV peak could be due to Mo-O bonds with multiple oxidation states of Mo.[54-57] A high-resolution sulfur peak emerged as a doublet at 160.7 eV and 161.9 eV due to reduced (S^{2-}) and pristine sulfur, respectively. Single and broad Si2p peak at 101.7 eV could be assigned to Si-C, Si-C/Si-N, Si-N and Si-O/Mo-Si peaks at 100.2, 101.4, 101.7 and 102.1 eV, respectively[57]. The broad oxygen peak at 531 eV could be fitted by doublets Mo-O_2 (530.2 eV and 531 eV) and more electronegative Mo-O_3 (at 531.6 eV). High-resolution C1s peak could be deconvoluted into Mo-C, Si-C and -sp^2 carbon at 282.7, 283.4 and 284.4 eV, respectively. Therefore, a possibility of chemical interaction/bond formation exists between MoS_2 sheets and SiCN ceramic, confirmed by the presence of Mo-C, Mo-Si bonds.

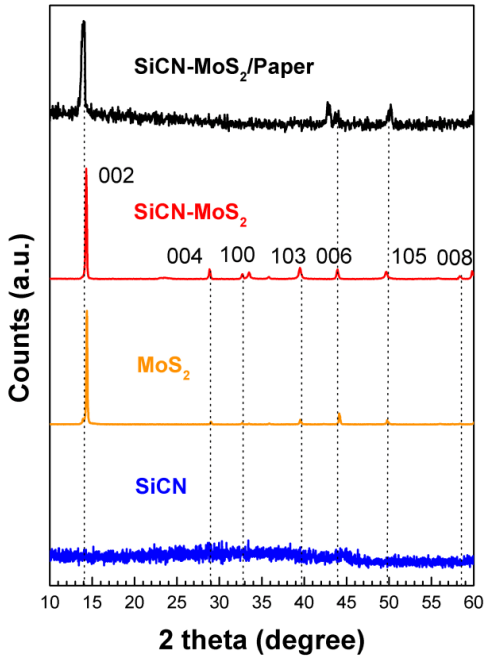

Figure 6-4 XRD diffraction data comparison for various electrode specimens prepared in this study. Polymer-derived SiCN ceramic is amorphous while crystalline peaks for MoS_2 could be clearly visualized.

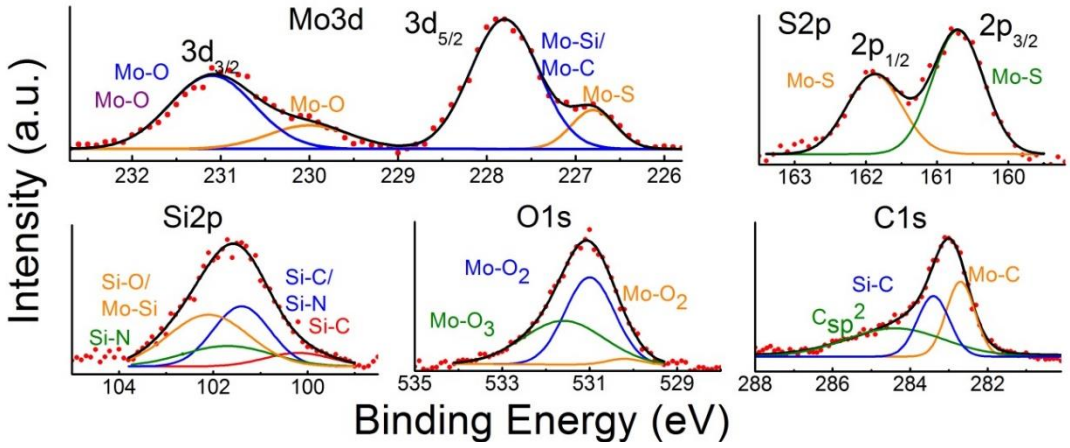

Figure 6-5 High-resolution X-ray photoelectron spectra of SiCN-MoS_2 composite nanosheets showing the characteristic MoS_2 and additional peaks that emerge as a result of chemical functionalization with SiCN ceramic.

Electrochemical performance of acid-treated MoS_2 and SiCN-MoS_2 composite electrodes was studied and compared by performing galvanostatic cycling experiments of the half-cell under constant current conditions. When cycled between 10 mV to 3 V at 100 $mA.g^{-1}$ constant current, first cycle discharge capacity of 698.9 $mAh.g^{-1}_{anode}$ (or 89.84 $mAh.g^{-1}_{electrode}$, i.e., when normalized with respect to total weight of the electrode including the current collector) and charge capacity of 476.3 $mAh.g^{-1}_{anode}$ (or 61.2 $mAh.g^{-1}_{electrode}$) were observed for the acid-treated MoS_2 specimen. Cycle hysteresis of approx. 0.5 was also observed, which is typical of a conversion type reaction. After 20 cycles, the reversible capacity decayed to 124.2 $mAh.g^{-1}_{anode}$ or 26 % of initial capacity, which was slightly lower than the theoretical capacity of 167 $mAh.g^{-1}$ for bulk MoS_2 (considering one mole of Li^+ intercalation reaction). Under cycling at similar conditions, the SiCN-MoS_2 traditional anode exhibited first cycle discharge capacity of 574.1 $mAh.g^{-1}_{anode}$ (or 126.1 $mAh.g^{-1}_{electrode}$) and reversible capacity of 457.6 $mAh.g^{-1}_{anode}$ (or 100.5 $mAh.g^{-1}_{electrode}$). During the cycling test for 20 cycles the initial reversible capacity was retained at 477 $mAh.g^{-1}_{anode}$ (or 104.7 $mAh.g^{-1}_{electrode}$). For the freestanding SiCN-MoS_2 composite paper electrode cycled under similar conditions, the first-cycle discharge capacity of 726.4 $mAh.g^{-1}_{anode}$ and reversible capacity 532.1 $mAh.g^{-1}_{anode}$ were observed. These capacities were retained after 20 cycles at 445.6 $mAh.g^{-1}_{anode}$ (73 % of initial value).

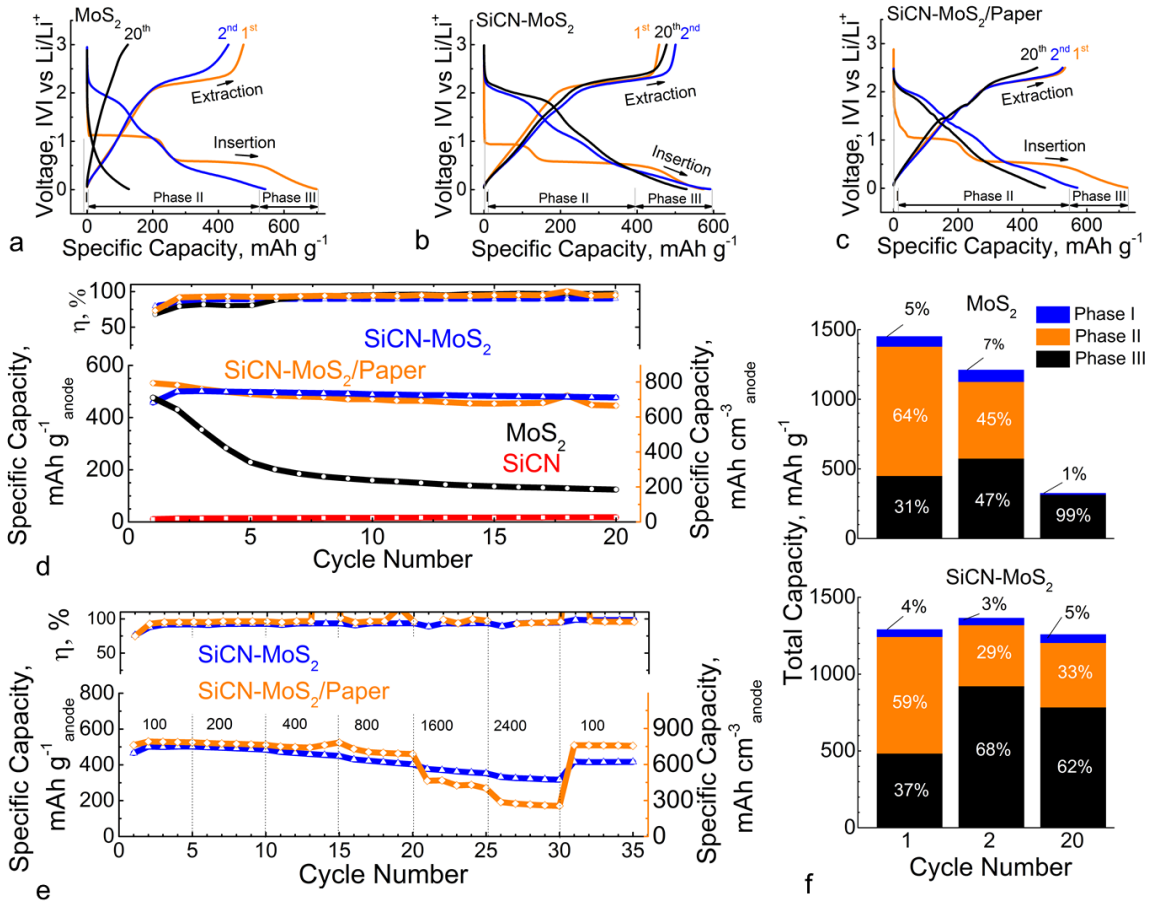

Figure 6-6 Electrochemical data. Comparison of first, second and twentieth electrochemical cycle (voltage-capacity plots) of half-cells of (a) acid-treated MoS_2 (85 mA.g-1), (b) SiCN-MoS_2 (at 116 mA.g-1) composite and (c) SiCN-MoS_2 freestanding composite paper electrodes. (d) Electrochemical cycling performance of traditional electrodes (acid-treated MoS_2, SiCN, SiCN-MoS_2 composite) and freestanding electrode (SiCN-MoS_2 paper) for initial 20 cycles. (e) C-rate cycling performance comparison of SiCN-MoS_2 composite and SiCN-MoS_2 paper. (f) Comparison of total capacity for initial (1st and 2nd) and final (20th) cycles and contribution of various reactions for (i) acid-treated MoS_2 and SiCN-MoS_2 composite sheets.

Anticipated intercalation and conversion reactions for exfoliated MoS_2 are given as:

At counter electrode,

Equation 6-1

$$Li \rightleftharpoons xLi^+ + xe^-$$

Intercalation at working electrode

Equation 6-2

$$xLi^+ + xe^- + MoS_2 \rightleftharpoons Li_xMoS_2$$

Conversion reaction at working electrode,

Equation 6-3

$$Li_xMoS_2 + 4Li^+ + 4e^- \rightleftharpoons Mo + 2Li_2S + xLi$$

Where, *x* represents the number of moles of intercalating Li-ions (or corresponding electrons) in the host material. Based on varying slope of capacity versus voltage plot, the cycling profile for these electrode materials was divided into three phases, as shown Figures 5.6(a) and 3(c). [50, 58-60] Individual contribution of each phase to overall capacity of initial and last tested cycles for MoS_2 and SiCN-MoS_2 are shown in Figure 6.6(f).

The changing voltage slope and plateaus observed in the cycled electrodes can be studied further by differentiating capacity with respect to the voltage as shown in Figure 6.7. The plateaus or steep slope observed in the cycling plot, appear as distinct peaks (labeled) in corresponding dQ/dV plots. Varying intensity of each peak indicates changing rates of Li-ion interaction within the host material, further signifying various reactions and structural phases involved. First-cycle dQ/dV for exfoliated MoS_2 showed prominent reduction peaks at approx. 1.1 V and at approx. 0.57 V, corresponding to conversion reaction whereby reduction of Li_xMoS_2 to Mo metal and Li_2S results (Equation 3).

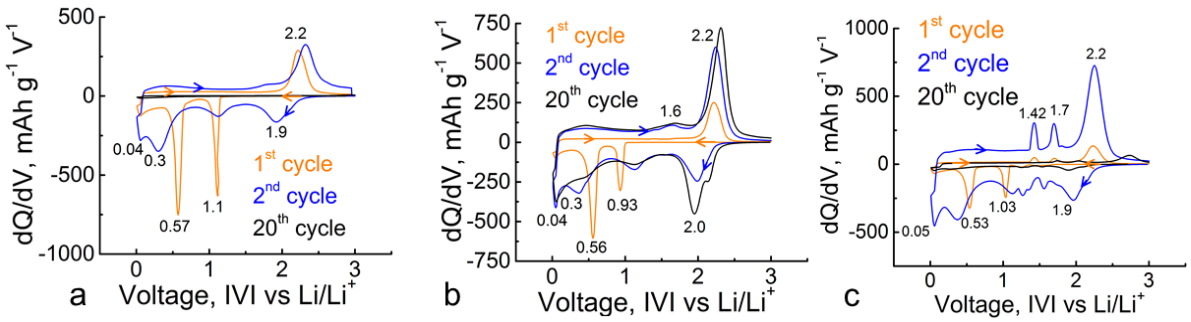

Figure 6-7 Differentiated capacity with respect to corresponding operating voltage (dQ/dV) for (a) acid-treated MoS_2, (b) SiCN-MoS_2 composite and (c) SiCN-MoS_2 free-standing composite paper.

The oxidation peak at 2.2 V is known to originate from the crystalline nature of MoS_2.[12] For the second cycle, prominent reduction peaks was observed at approx. 1.9 and 0.3 V, and an oxidation peak was observed at 2.3 V. These results are consistent with data from literature on transition metal sulfide electrodes.[9,12,17] For the first-cycle of SiCN-MoS_2 anode, a slight shift in potential of reduction peaks were observed at approx. 0.93 V, 0.56 V, 0.3 V, and 40 mV (when compared to MoS_2 first-cycle behavior). For the second cycle, major reduction peaks were observed at approx. 2 V, 1.1 V, and 0.4 V, but no change was observed in oxidation peak position. The SiCN-MoS_2 freestanding paper electrode experienced reduction and oxidation peaks similar to SiCN-MoS_2 traditional electrodes. Reduction (0.05 and 0.75 V) and oxidation (0.15V) peaks of rGO (graphene)[61] were not distinguishable from primary peaks of SiCN-MoS_2 because contribution (10% or less) of rGO to overall specific capacity was negligible.

Figure 6.6 (d) compares the charge capacity of SiCN-MoS_2 composite (traditional and paper electrodes) to acid-treated MoS_2 and SiCN ceramic electrodes cycled under similar conditions. The figure shows that SiCN-MoS_2 electrodes had approximately 26 % much higher capacity retention at 20 cycles when compared to MoS_2 . In addition, the 'neat' SiCN electrode

had negligible reversible capacity of approx. 20 $mAh.g^{-1}_{anode}$. Figure 6.6(e) shows the C-rate performance of SiCN-MoS_2 traditional and paper electrodes. First-cycle charge capacities were 465.9 $mAh.g^{-1}_{anode}$ and 530 $mAh.g^{-1}_{anode}$ for traditional and paper electrodes, respectively. When current density increased to 2400 $mA.g^{-1}$, respective charge capacities dropped to 326.4 $mAh.g^{-1}_{anode}$ and 191.9 $mAh.g^{-1}_{anode}$. However, most of the capacity was recovered when the current density was decreased to 100 $mA.g^{-1}$, reaching 414.8 $mAh.g^{-1}_{anode}$ (83 % retained) and 509.2 $mAh.g^{-1}_{anode}$ (96 % retained) for traditional and paper electrodes, respectively. After 20 electrochemical cycles, the half-cells were disassembled in delithiated state, and the electrode was recovered for further investigation of structure and chemical composition. Figures 5.8(a through c) are SEM images of the disassembled cells. The inserts are corresponding optical camera images in which the MoS_2 anode exhibited signs of microcracks, coating delamination and slight discoloration, suggesting susceptibility to volume and chemical changes during the intercalation (Phase I) and conversion (Phase II) reactions. However, SiCN-MoS_2 cycled anodes appeared to be largely intact without any change in color from the original (pre-cycled) state. SEM imaging also provided additional details regarding the effects of electrochemical cycling at the micro-scale. The cycled MoS_2 electrode showed uneven surface and mud cracks (Figure 6.8(a)), while the SiCN-MoS_2 electrodes (traditional and paper) were relatively more porous and consisted of an uninterrupted solid electrolyte interphase (S EI) film on the active material (Figures 5.8(b,c)).

Table 6.1 Summary of the electrochemical data and comparison with literature on other exfoliated-MoS_2 based electrodes

Electrode Type	Active material (mg)	First Reversible Capacity ($mAh.g^{-1}$)	ICL (%)	First Reversible Capacity ($mAh.g^{-1}_{anode}$)	Reversible Capacity in $mAh.g^{-1}_{anode}$ (20 cycles)
MoS_2 traditional	1.66	595.3	32	61.22	16
SiCN traditional	1.12	13	86.6	7.17	2
SiCN-MoS_2traditional	3.49	572.05	20.2	100.5	104.8
SiCN-MoS_2 paper electrode	6.4	623.5	27	498.8	417.8
MoS_2 exfoliated traditional (Ref.16)	N.A.	~766	32	N.A.	N.A.
MoS_2 bulk traditional (Ref.16)	N.A.	275	54	N.A.	N.A.
CNT/MoS_2 paper (Ref.20)	N.A.	375	N.A.	~375	~125
MoS_2 paper electrode (Ref.20)	N.A.	280	N.A.	~280	~225

The chemical composition of the cycled SiCN-MoS_2 composite anode was also analyzed by XPS. As shown in Figure 6.8(d) the Mo3d elemental peak evolved into three slightly overlapping peaks at 229.13 eV, 232.48 eV and 235.81 eV. Low energy peaks at 229.13 eV and 232.1 eV were attributed to Mo-S and Mo-O type bonds, respectively. Higher energy doublets at 232.48 eV and 235.81 eV could be assigned to the more electronegative Mo-O_2/MoO_3 and Mo-O_x species, respectively.[54-57] The Mo-C type bond observed in the as-synthesized composite unexpectedly did not reoccur. Both sulfur peaks shifted to higher energies of 161.06 eV and 162.02 eV, likely due to S^{2-} and polysulfide (Li-S) entities, respectively.[56,57] Broad silicon elemental peak with weak intensity could be attributed to Si-C and Si-O type bonds.

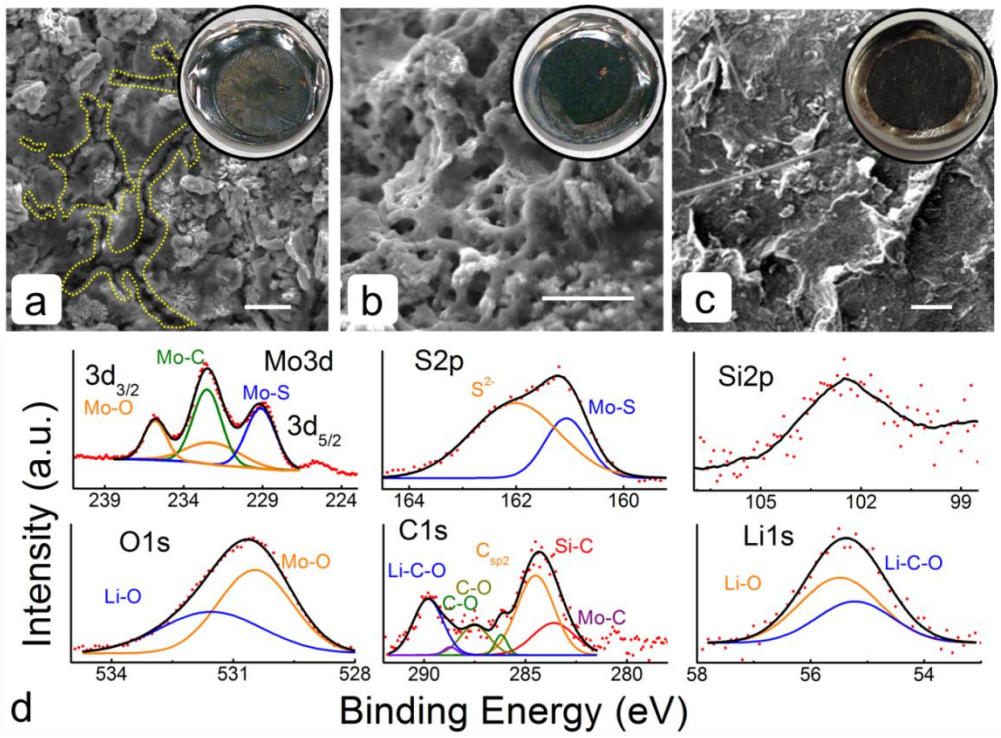

Figure 6-8 Post electrochemical analysis. SEM images of disassembled cells (a) acid-treated MoS_2, (b) SiCN-MoS_2 composite and (c) SiCN-MoS_2 paper electrodes after testing for 20 cycles. The insert shows digital images of corresponding electrode surfaces. (d) Elemental X-ray photoelectron spectra of the dissembled SiCN-MoS_2 composite electrode show Mo, S, and C phase modifications with additional Li peaks.

The shifted oxygen peak at 530.5 eV could be fitted by a peak at 530.46 eV due to Mo-O type bonds and fitted by a peak at 531.54 eV due to multiple entities of more electronegative Li_3PO_4, Li_2CO_3, Li_2O, LiOH, and Mo-O_3 compounds.[56] High-resolution C1s peak was deconvoluted into Mo-C, Si-C, C-sp^2, C-O, and Li-C-O at 282.7, 283.6, 285.5, 286.2, 287.5, and 289.8 eV, respectively. Lastly, the Li1s elemental peak at 55.4 eV was assigned to Li-C (Li_2CO_3) and Li-O (Li_2O) at 55.22 eV, and 55.48 eV, respectively.

6.4. Conclusion

Acid-treated MoS_2 was utilized to prepare polysilazane/MoS_2 composite, which upon pyrolysis in an inert environment, resulted in formation of SiCN-MoS_2 nanosheets. Electron microscopy revealed uniform distribution of SiCN-MoS_2 stacked sheets in the composite. Average sheet size was approximately 3 μm to 5 μm. XPS analysis revealed formation of Mo-C and Mo-O bonds, indicating chemical bonding of the SiCN's carbon phase with molybdenum atoms.

Electrochemical performance of the composite was studied as working electrode in LIB half-cell, revealing an increasingly stable cycling and higher capacity retention compared to 'neat' MoS_2 after 20 cycles. The contribution of conversion reaction (Phase II) and electrolyte decomposition (Phase III) to overall capacity decreased for SiCN-MoS_2 electrodes. This decrease is one of the reasons for decreased first-cycle loss and increased capacity retention for SiCN-MoS_2 composite. Additionally, the electrically conductive nature of SiCN ceramics may have resulted in faster Li-ion diffusion. Post-cycling SEM characterization of the disassembled cells also provided additional evidence for the steep capacity drop observed for case of MoS_2. The cycled MoS_2 electrode surface showed mud-cracks and delamination whereas the SiCN-MoS_2 and SiCN-MoS_2/paper electrodes showed formation of a uniform SEI layer.

6.5. References

1. Chen, J., Kuriyama, N., Yuan, H., Takeshita, H. T. & Sakai, T. Electrochemical hydrogen storage in MoS_2 nanotubes. *J. Am. Chem. Soc.* 123, 11813-11814 (2001).
2. Hu, K. H., Hu, X. G. & Sun, X. J. Morphological effect of MoS_2 nanoparticles on catalytic oxidation and vacuum lubrication. *Appl. Surf. Sci.* 256, 2517-2523 (2010).
3. Fang, X. *et al.* Lithium storage performance in ordered mesoporous MoS2 electrode material. *Micropor. Mesopor. Mat.* 151, 418-423 (2012).
4. Cheng, F., Liang, J., Tao, Z. & Chen, J. Functional materials for rechargeable batteries. *Adv. Mater.* 23, 1695-1715 (2011).
5. Etacheri, V., Marom, R., Elazari, R., Salitra, G. & Aurbach, D. Challenges in the development of advanced Li-ion batteries: A review. *Energy Environ. Sci.* 4, 3243-3262 (2011).
6. Li, H., Li, W., Ma, L., Chen, W. & Wang, J. Electrochemical lithiation/delithiation performances of 3D flowerlike MoS_2 powders prepared by ionic liquid assisted hydrothermal route. *J. Alloys Compd.* 471, 442-447 (2009).
7. Feng, C. *et al.* Synthesis of molybdenum disulfide (MoS_2) for lithium ion battery applications. *Mater. Res. Bull.* 44, 1811-1815 (2009).
8. Du, G. *et al.* Superior stability and high capacity of restacked molybdenum disulfide as anode material for lithium ion batteries. *Chem. Commun.* 46 (2010).
9. Imanishi, N., Toyoda, M., Takeda, Y. & Yamamoto, O. Study on lithium intercalation into MoS_2. *Solid State Ionics* 58, 333-338 (1992).
10. Xu, X., Wen, L., Youngsik, K. & Cho, J. Nanostructured transition metal sulfides for lithium ion batteries: Progress and challenges. *Nano Today* 9, 604–630 (2014).
11. Chan, C. K. *et al.* High-performance lithium battery anodes using silicon nanowires. *Nat. Nanotechnol.* 3, 31-35 (2008).
12. Papageorgopoulos, C. A. & Jaegermann, W. Li intercalation across and along the van-der-waals surfaces of MoS_2 (0001). *Surf. Sci.* 338, 83-93 (1995).
13. Haering, R. R., Stiles, J. A. R. & Brandt, K. Lithium molybdenum disulphide battery cathode. US Patent 4224390, 1980.
14. Chhowalla, M. *et al.* The chemistry of two-dimensional layered transition metal dichalcogenide nanosheets. *Nat. Chem.* 5, 263-275 (2013).

15. Rao, C. N. R., Matte, H. S. S. R. & Maitra, U. Graphene analogues of inorganic layered materials. *Angew. Chem. Int. Ed.* 52, 13162-13185 (2013).

16. Xiao, J. *et al.* Exfoliated MoS_2 nanocomposite as an anode material for lithium ion batteries. *Chem. Mater.* 22, 4522-4524 (2010).

17. Bhandavat, R., David, L. & Singh, G. Synthesis of surface-functionalized WS_2 nanosheets and performance as Li-ion battery anodes. *J. Phys. Chem. Lett.* 3, 1523-1530 (2012).

18. David, L., Bhandavat, R. & Singh, G. MoS_2/graphene composite paper for sodium-ion battery electrodes. *ACS Nano* 8, 1759-1770 (2014).

19. Coleman, J. N. *et al.* Two-dimensional nanosheets produced by liquid exfoliation of layered materials. *Science* 331, 568-571 (2011).

20. Smith, R. J. et al. Large-Scale Exfoliation of inorganic layered compounds in aqueous surfactant solutions. *Adv. Mater.* 23, 3944-+ (2011).

21. Radisavljevic, B., Radenovic, A., Brivio, J., Giacometti, V. & Kis, A. Single-layer MoS_2 transistors. *Nat. Nanotechnol.* 6, 147-150 (2011).

22. Brivio, J., Alexander, D. T. L. & Kis, A. Ripples and layers in ultrathin MoS_2 membranes. *Nano Lett.* 11, 5148-5153 (2011).

23. Liu, H. *et al.* Highly ordered mesoporous MoS_2 with expanded spacing of the (002) crystal plane for ultrafast lithium ion storage. *Adv. Energy Mater.* 2, 970-975 (2012).

24. Wang, S. *et al.* Hydrothermal synthesis of molybdenum disulfide for lithium ion battery applications. *Chin. J. Chem. Eng.* 18 (2010).

25. Sen, U. K. & Mitra, S. High-rate and high-energy-density lithium-ion battery anode containing 2d MoS_2 nanowall and cellulose binder. *ACS Appl. Mater. Interfaces* 5, 1240-1247 (2013).

26. Chang, K. & Chen, W. In situ synthesis of MoS_2/graphene nanosheet composites with extraordinarily high electrochemical performance for lithium ion batteries. *Chem. Commun.* 47 (2011).

27. Chang, K. & Chen, W. L-Cysteine-Assisted Synthesis of layered MoS_2/graphene composites with excellent electrochemical performances for lithium ion batteries. *ACS Nano* 5, 4720-4728 (2011).

28. Lin, Y. C. *et al.* Wafer-scale MoS_2 thin layers prepared by MoO_3 sulfurization. *Nanoscale* 4, 6637-6641 (2012).

29. Zhan, Y., Liu, Z., Najmaei, S., Ajayan, P. M. & Lou, J. Large-area vapor-phase growth and characterization of MoS_2 atomic layers on a SiO_2 substrate. *Small* 8, 966-971 (2012).

30. Shi, Y. *et al.* van der Waals epitaxy of MoS_2 layers using graphene as growth templates. *Nano Lett.* 12, 2784-2791 (2012).

31. Liu, K. K. *et al.* Growth of large-area and highly crystalline MoS_2 thin layers on insulating substrates. *Nano Lett.* 12, 1538-1544 (2012).

32. Zhou, W. *et al.* Synthesis of Few-layer MoS_2 nanosheet-coated TiO_2 nanobelt heterostructures for enhanced photocatalytic activities. *Small* 9, 140-147 (2013).

33. Chang, K. & Chen, W. In situ synthesis of MoS_2/graphene nanosheet composites with extraordinarily high electrochemical performance for lithium ion batteries. *Chem. Commun.* 47 (2011).

34. Hu, L. et al. Highly conductive paper for energy-storage devices. *PNAS* 106, 21490-21494 (2009).

35. Chen, D. *et al.* In situ nitrogenated graphene-few-layer WS_2 composites for fast and reversible Li+ storage. *Nanoscale* 5 (2013).

36. Hwang, H., Kim, H. & Cho, J. MoS_2 Nanoplates consisting of disordered graphene-like layers for high rate lithium battery anode materials. *Nano Lett.* 11, 4826-4830 (2011).

37. Shi, Y. *et al.* Self-assembly of hierarchical MoSx/CNT nanocomposites ($2<x<3$): towards high performance anode materials for lithium ion batteries. *Sci. Rep.* 3 (2013).

38. Wang, J. Z. *et al.* Development of MoS_2-CNT composite thin film from layered mos2 for lithium batteries. *Adv. Energy Mater.* 3, 798-805 (2013).

39. Wang, Z. *et al.* CTAB-assisted synthesis of single-layer MoS_2-graphene composites as anode materials of Li-ion batteries. *J. Mater. Chem. A* 1, 2202-2210 (2013).

40. Xiao, J. *et al.* Electrochemically induced high capacity displacement reaction of POE/MoS_2/graphene nanocomposites with lithium. *Adv. Funct. Mater.* 21, 2840-2846 (2011).

41. Yu, H. *et al.* Three-dimensional hierarchical architectures constructed by graphene/MoS_2 nanoflake arrays and their rapid charging/discharging properties as lithium-ion battery anodes. *Chem-Eur. J.* 19, 5818-5823 (2013).

42. Zhou, X., Wan, L. J. & Guo, Y. G. Synthesis of MoS_2 nanosheet-graphene nanosheet hybrid materials for stable lithium storage. *Chem. Commun.* 49, 1838-1840 (2013).

43. Shah, S. R. & Raj, R. Nanodevices that explore the synergies between PDCs and carbon nanotubes. *J. Eur. Ceram. Soc.* 25, 243-249 (2005).

44. Lehman, J. H. *et al.* Core-shell composite of SiCN and multiwalled carbon nanotubes from toluene dispersion. *J. Mater. Sci.* 45, 4251-4254 (2010).

45. Cai, Y. *et al.* Carbon nanotubes welded by precursor-derived silicoboron carbonitride ceramics: A TEM study. *Phys. Status Solidi a* 193, R13-R15 (2002).

46. David, L., Asok, D. & Singh, G. Synthesis and extreme rate capability of Si–Al–C–N functionalized carbon nanotube spray-on coatings as li-ion battery electrode. *ACS Appl. Mater. Interfaces* 6, 16056-16064, (2014).

47. Kroke, E. *et al.* Silazane derived ceramics and related materials. *Mat. Sci. Eng. R* 26, 97-199 (2000).

48. Ramakrishnan, P. A. *et al.* Silicoboron-carbonitride ceramics: A class of high-temperature, dopable electronic materials. *Appl. Phys. Lett.* 78, 3076-3078 (2001).

49. Divigalpitiya, W. M. R., Frindt, R. F. & Morrison, S. R. Inclusion systems of organic-molecules in restacked single-layer molybdenum-disulfide. *Science* 246, 369-371 (1989).

50. Cabana, J., Monconduit, L., Larcher, D. & Rosa Palacin, M. beyond intercalation-based li-ion batteries: the state of the art and challenges of electrode materials reacting through conversion reactions. *Adv. Mater.* 22, E170-E192 (2010).

51. Oxley, J. D., Mdleleni, M. M. & Suslick, K. S. Hydrodehalogenation with sonochemically prepared Mo_2C and W_2C. *Catal. Today* 88, 139-151 (2004).

52. David, L. & Singh, G. reduced graphene oxide paper electrode: opposing effect of thermal annealing on Li and Na cyclability. *J. Phys. Chem. C* 118, 28401-28408 (2014).

53. Hummers, W. S. & Offeman, R. E. Preparation of graphitic oxide. *J. Am. Chem. Soc.* 80, 1339-1339 (1958).

54. Levasseur, A., Vinatier, P. & Gonbeau, D. X-ray photoelectron spectroscopy: A powerful tool for a better characterization of thin film materials. *B. Mater. Sci.* 22, 607-614 (1999).

55. Baker, M. A., Gilmore, R., Lenardi, C. & Gissler, W. XPS investigation of preferential sputtering of S from MoS_2 and determination of MoSx stoichiometry from Mo and S peak positions. *Appl. Surf. Sci.* 150, 255-262 (1999).

56. Wagner, C. D., Naumkin, A. V., Kraut-Vass, A., Allison, J. W., Powell, C. J., & Rumble Jr, J. R. *NIST X-ray photoelectron spectroscopy database* 20, Version 4.1. Available at: *http://srdata.nist.gov/xps/* (Accessed 6th January 2015).

57. Benoist, L. *et al.* XPS analysis of lithium intercalation in thin-films of molybdenum oxysulfides. *Surf. Interface Anal.* 22, 206-210 (1994).

58. Julien, C., Saikh, S. I., & Nazri, G. A. Electrochemical studies of disordered MoS_2 as cathode material in lithium batteries. *Mat. Sci. Eng. B-Solid* 15, 73-77 (1992).

59. Julien, C. M. Lithium intercalated compounds - Charge transfer and related properties. *Mat. Sci. Eng. R* 40, 47-102 (2003).

60. Selwyn, L. S., Mckinnon, W. R., Vonsacken, U. & Jones, C. A. Lithium electrochemical-cells at low-voltage - decomposition of Mo and W dichalcogenides. *Solid State Ionics* 22, 337-344 (1987).

61. David, L. *et al.* Synthesis of graphene films by rapid heating and quenching at ambient pressures and their electrochemical characterization. *ACS Appl. Mater. Interfaces* 5, 546-552 (2013).

Chapter 7 - Facile Synthesis and High Rate Capability of Silicon Carbonitride/Boron Nitride Composite with a Sheet-Like Morphology[5]

7.1. Abstract

We report synthesis of a sheet-like composite composed of hexagonal boron nitride (or BN) chemically integrated with silicon carbonitride (SiCN) matrix *via* a simple pyrolysis route. The composite offers several unique features such as improved electrical conductivity, high-temperature oxidation resistance (at 1000 °C), and high electrochemical activity toward Li-ions generally not observed in SiCN or boron doped SiCN. Tested as electrode in Li-ion half-cell, SiCN/BN show charge capacity of ~517 mAh g^{-1} at 100 mA g^{-1} and 283 mAh g^{-1} at 2400 mA g^{-1} with respect to total weight of electrode. Additionally, a stable charge capacity of ~401 mAh g^{-1} at 100 mA g^{-1} is retained even after continuous operation for 1000 cycles at 1600 mA g^{-1}. Chemical characterization of the composite suggests that addition of BN to polysilazane in moderate amounts (~10 wt%) and subsequent pyrolysis resulted in an increased free-carbon content in the amorphous SiCN phase, which exceeded the percolation limit, leading to the improved electrical conductivity and Li-reversible capacity.

[5] Reprinted with permission from (L. David, S. Bernard, C. Gervais, P. Miele and G. Singh, "Facile Synthesis and High Rate Capability of Silicon Carbonitride/Boron Nitride Composite with a Sheet-like Morphology" The Journal of Physical Chemistry C **119**, 5, 2783 - 2791). Copyright (2015) American Chemical Society.

7.2. Introduction

Powering of electric vehicles or next generation wearable electronic devices that run on Li-ion battery (LIB) technology will require new electrode materials beyond the traditional graphite anode because of its poor rate capability and low charge capacity (theoretical charge capacity approximately 372 mAh g^{-1}).[1-7] Desired characteristics of next-generation LIB system include high power and energy density, improved safety, long life, and lightweight. [1-2, 8] Research has shown that silicon (Si) anodes can drastically increase the capacity of existing LIB by more than 30%. [9-11] Unfortunately, however, Si experiences huge volume changes during charge/discharge cycles and has poor electrical conductivity that generally leads to poor rate capability.[12-13] Although, nanoengineered Si-based materials (such as nanowires, nanoparticles and hollow nano-spheres) that can sustain large mechanical strains with minimal capacity degradation have shown promise in laboratory experiments, a practical and cost-effective solution is yet to be realized.[14-26]

Among other Si-based materials for LIB anodes, silicon-based polymer-derived ceramics (or PDCs) rich in carbon have shown high specific capacity even at high current densities.[27-39] These ceramics are lightweight (density ~1.8 to 2.2 $g.cm^{-3}$), chemically inert, stable at high temperatures, and readily synthesized through direct pyrolysis of single-source polymeric precursors. Two main types of PDCs, SiCO (silicon oxycarbide) and SiCN (silicon carbonitride), have gained attention because their Li discharge capacity is nearly 3 times the discharge capacity of commercial graphite anode.[28-30, 32-38] This high capacity is derived from the particular structure of PDCs, which consists of a three-dimensional network of silicon, carbon and nitrogen (or oxygen for SiCO) atoms and excess disordered carbon (or free carbon phase) that generally provides majority of active sites for reversible adsorption of lithium ions.[34] However, cycling stability and efficiency of polysilazane-derived SiCN is considerably lower than SiCO anode.

SiCN generally suffers from very high first cycle loss of Li (up to 70% in certain cases) [29, 31] and has low electrical conductivity that brings down its reversible capacity and rate capability to values similar or worse than commercial graphite after only a few initial cycles.[35-36] Research has shown that some of these weaknesses can be addressed by changing the pyrolysis conditions (such as extended heat treatment), altering the polymeric precursor type (e.g., polysilylcarbodiimide is preferred over polysilazane) or, by introducing a suitable quaternary element, such as boron or aluminum, [40-46] at molecular scale. In previous work, precursor-derived amorphous Si(B)CN ceramics showed improved electric property (up to 4 orders of magnitude higher conductivity than SiCN) and superior electrochemical performance.[46, 47] In addition, composites made of SiCN matrix with filler phases comprised of carbon nanotubes (CNTs),[48] graphite,[49] and carbon nanofiber[50] have been shown to improve electrical conductivity and resistance to mechanical cracking. However, rate capability and cycling stability of Si(B)CN and SiCN-based nanocomposite electrodes remain inferior to polymer-derived SiCO or other nanocomposite electrodes currently under investigation. One reason for this inferiority could be the presence of Si, C, N, O danglings bonds which may form Li irreversible phases resulting in high first cycle loss. For precursor-derived Si(B)CN, it could be the limited amounts of B that is ultimately retained in the pyrolyzed ceramic. Therefore, based on improved electrochemical performance of Si(B)CN ceramics compared to SiCN ceramics, we conclude that introduction of higher quantities of boron as (nano) sheets or (nano) particles in the SiCN network is a logical parallel step toward the improvement of electrochemical performance. Sheet or particle-like morphology is expected to improve overall accessibility for Li ions in the electrode during successive charge/discharge cycles.

We synthesized a SiCN/BN composite by functionalizing hexagonal boron nitride (h-BN, expressed here as BN) sheets with a commercial off-the-shelf polysilazane precursor, followed by pyrolysis at 1000 °C. We observed that preparation of SiCN/BN composite with a sheet-like morphology provided a unique opportunity to tailor the nitrogen bonds with boron and also increased free carbon content in the SiCN matrix, thereby, improving its electrical conductivity by orders of magnitude compared to boron-free SiCN ceramics. These changes in the molecular structure of the final ceramic yielded a material with excellent electrochemical stability even at high current densities. Composites made of SiCN matrix and precursor-derived BN (SiCN/BNF) and powdered boron (SiCN/BP) as filler phase were also prepared in order to extrapolate and highlight the distinctive chemistry that governs high capacity in SiCN/BN.

7.3. Materials And Instrumentation

Boron nitride (99.9%) was purchased from Sigma Aldrich. Poly (ureamethylvinyl)silazane (commercial name: Ceraset) was obtained from Clariant Corporation. All materials were used as received without further purification.

Scanning electron microscopy (SEM) of the synthesized material was carried out on a Carl Zeiss EVO MA10 system with incident voltage of 5 kV-30 kV. Transmission electron microscopy (TEM) images were digitally acquired by use of a Phillips CM100 operated at 100 kV. Surface chemical composition was studied by X-ray photoelectron spectroscopy (XPS, PHI Quantera SXM) using monochromatic Al Kα X-ray radiation. ^{11}B MAS NMR spectra were recorded at 11.7 T on a Bruker Avance500 wide-bore spectrometer operating at 160.47 MHz, using a Bruker 4 mm probe and a spinning frequency of the rotor of 12 kHz. Spectra were acquired using a spin-echo θ-□-2θ pulse sequence with θ=90° to overcome problems of probe signal. The □ delay (83 μs) was synchronized with the spinning frequency and recycle delay of

1s was used. Chemical shifts were referenced to $BF_3(OEt)_2$ (δ=0 ppm). The FTIR spectra were collected using Thermo-Nicolet Nexus 870FT-IR spectrometer. FTIR samples were prepared by mixing ~1 wt% of the finely powdered sample with FTIR grade KBr powder. Phase evolution was characterized by using Bruker powder X-ray diffractometer (Madison, WI) operating at room temperature, with CuKα radiation and nickel filter. The pyrolyzed samples were finely crushed with mortar and pestle and laid on the palette for analysis. Thermogravimetric analysis was performed using Shimadzu 50 TGA (Columbia, MD) (limited to 1000° C). Sample weighing, ~2.5 mg, was heated in a platinum pan at a rate of 10 °C min^{-1} in air flowing at 10 mL min^{-1}.

7.3.1. Preparation of SiCN/BN, SiCN/BNF, SiCN/BP

SiCN/BN: Chemical modification of Polyureasilazane (commercial name: Ceraset) was performed using commercially obtained BN (99.9%) nanosheets from Sigma Aldrich™. 1 g of BN (sonicated in propanol and dried) was mixed with 10 mL of polyureasilazane and stirred for 12 h at room temperature. Subsequently the mixture was cross-linked at 250 °C (heating rate 100 °C h^{-1}) for 180 min to obtain a white powder. The cross-linked powder was then pyrolyzed in N_2 atmospheres at 1000 °C in a tube furnace to obtain an amorphous black powder termed as SiCN/BN.

SiCN/BNF and SiCN/BP specimens: Similar procedure was followed as conducted for SiCN/BN preparation with the exception that instead of commercially obtained BN, the following boron modifiers were added to polyureasilazane: cross-linked BN polymeric precursor synthesized using procedure from literature[51-57] for synthesizing SiCN/BNF and commercially obtained boron powder from Sigma Aldrich for SiCN/BP.

7.3.2. Preparation of Paper Electrode

10 mL colloidal suspension of GO (graphene oxide) in 1:1 (v/v) water was made by sonication for 10 minutes. GO was synthesized using Hummer's method.[58] 60 wt% active material (SiCN/BN, SiCN/BNF or SiCN/BP) in 10 mL of isopropanol (ISP) was added to this solution and the solution was further sonicated for 60 min. When creation of the composite suspension was complete, it was filtered by vacuum filtration through a 10 μm filter membrane. Composite paper was carefully removed from the filter paper and dried. This dry paper then underwent reduction by heat treatment in a tube furnace at 500 °C under flowing argon gas for 2 h. The thermal reduction process resulted in conversion of GO to rGO (reduced graphene oxide) with approximately 50-60% weight loss. The thermally reduced composite papers consisted of approximately 20 wt.% rGO.

7.3.3. Coin Cell Assembly

Half-cell batteries were made by punching a 14.3 mm diameter circle from the paper for use as working electrode. A few drops of electrolyte solution of 1 M $LiPF_6$ (Alfa Aesar^{TM}) dissolved in (1:1 v/v) dimethyl carbonate: ethylene carbonate (ionic conductivity 10.7 mS cm^{-1}) was used. A 19 mm diameter glass separator soaked in electrolyte was placed between the working electrode and pure lithium metal (14.3 mm diameter), which acted as a counter electrode. Washer, spring, and a top casing were placed on top to complete the assembly before crimping. The entire procedure was conducted out in an Ar-filled glovebox.

Electrochemical performance of assembled coin cells was tested using a multichannel BT2000 Arbin^{TM} test unit sweeping 2.5 V to 10 mV versus Li/Li^+ using the following cycle schedule: (a) Asymmetric mode: Li was inserted at 0.1 A g^{-1} (with respect to total electrode weight), while the extraction was performed at increasing current densities of 100, 200, 400, 800,

1600 and 2400 mA g^{-1} for five cycles each, and returning to 100 mA g^{-1} for the subsequent 10 cycles. (b) Symmetric mode: Later, all the cells were subjected to symmetric cycling at a current density of 1600 mA g^{-1} for up to 1000 cycles, returning to 100 mA g^{-1} for the last 20 cycles.

7.4. Results and Discussions

The schematic in Figure 7.1 describes the possible reaction mechanism involved in the formation of SiCN/BN composite. We hypothesize that vigorous physical mixing of few-layer thick boron nitride (BN) sheets with liquid polysilazane results in their chemical functionalization, which, upon cross-linking at 300 °C, forms polysilazane/BN polymer composite. With additional heating in N_2 at 1000 °C, polysilazane transforms to SiCN with evolution of H_2, CH_4, and NH_3 forming an integrated SiCN/BN composite with a layered morphology.

Electron microscopy images of as-obtained BN powder and as-synthesized SiCN/BN composite are compared in Figure 7.2 and Figure 7.3. TEM and SEM images confirmed a layered and 'fluffy' structure of the as-obtained BN, while SiCN/BN composite appeared more dense and compact, although sheet-like morphology of initial BN could still be observed. The selected area electron diffraction (SAED) pattern for SiCN/BN was similar to BN, indicating that BN sheets were intact in the composite. From the SEM images, the average particle size of SiCN/BN was observed to be approximately (5 to 10) μm. As-pyrolyzed SiCN and SiCN modified with boron particles (i.e., SiCN/BP) and cross-linked polyborazylene (i.e., SiCN/BNF) appeared more irregular with tiny particles decorating big micrometer size particles, as shown in Figure 7.2(a through e) in a side-by-side comparison.

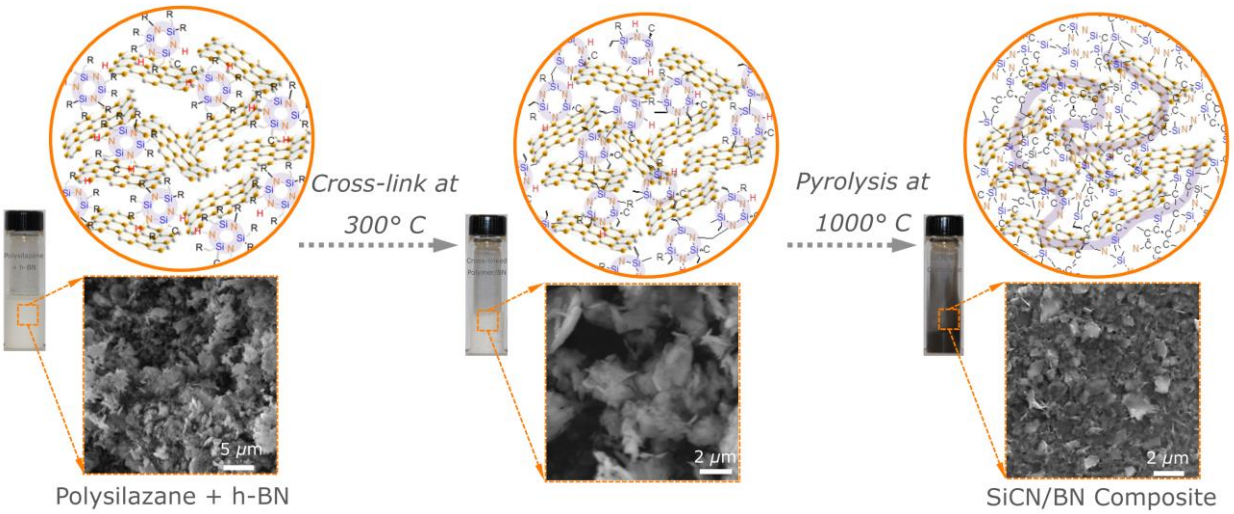

Figure 7-1 Schematic showing polymer to ceramic conversion and simultaneous incorporation of BN sheets in SiCN matrix. (L to R): polysilazane precursor uniformly wets BN sheets when they are stirred together. As the mixture is heated in flowing N2, polysilazane cross-links at approximately 300 °C to form long chains connected by BN sheets. Further pyrolysis at 1000 °C forms BN sheets embedded with SiCN ceramic matrix. Inset shows SEM images of composite at various stages of processing.

Top-view and cross-section SEM images of various paper electrodes prepared with rGO (reduced graphene oxide) as conducting support (see Methods section for electrode preparation) are presented in Figure 7.2 (f through o); the free-standing paper electrode with rGO support had a thickness of approximately 20 to 25 μm. Closer examination showed the paper to be layered with rGO platelets embedded with SiCN/BN particles which had sheet-like morphology.

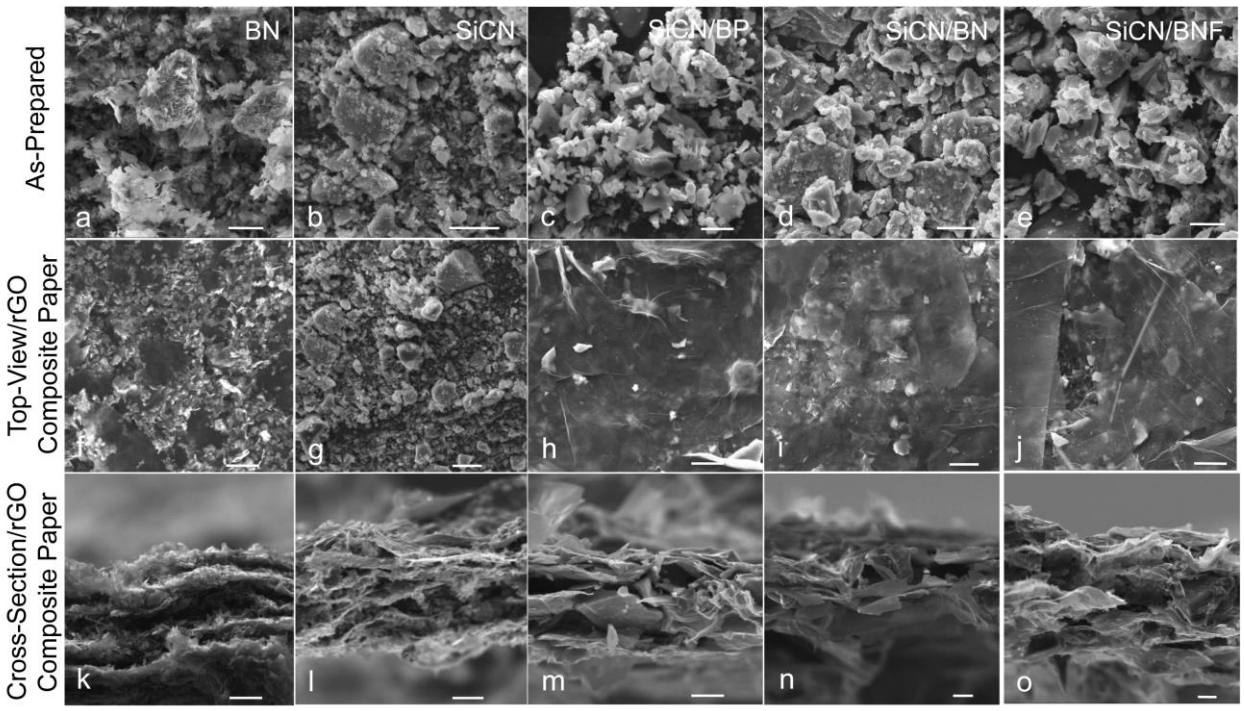

Figure 7-2 (a through e) SEM images of 'as-prepared' BN, SiCN, SiCN/BP, SiCN/BN, and SiCN/BN. (f through j) Top-view images of free-standing paper electrode made with approx. 20 wt.% rGO and (k through o) their corresponding cross-sectional images. The average paper thickness was observed to be approximately 20 to 25 µm. Scale bar is 5 µm in all images.

Further characterization involved X-ray photoelectron spectroscopy (XPS) analysis of SiCN/BN composite as shown in Figure 7.4(a-b), which revealed distinct peaks from which elemental composition of the final material was confirmed. Survey scans in Figure 7.5 of SiCN/BN showed the existence of Si, B, N and C elemental peaks rising from valence energy levels for the respective atoms. Atomic percentage of boron in the composite was 6.8%, which is much higher than other boron-doped SiCN.[40] The peak at approximately 190.5 eV for high resolution B 1s in Figure 7.4b confirmed the presence of B-N bond in the pyrolyzed composite, thereby suggesting successful retention of BN after pyrolysis.[40, 42]

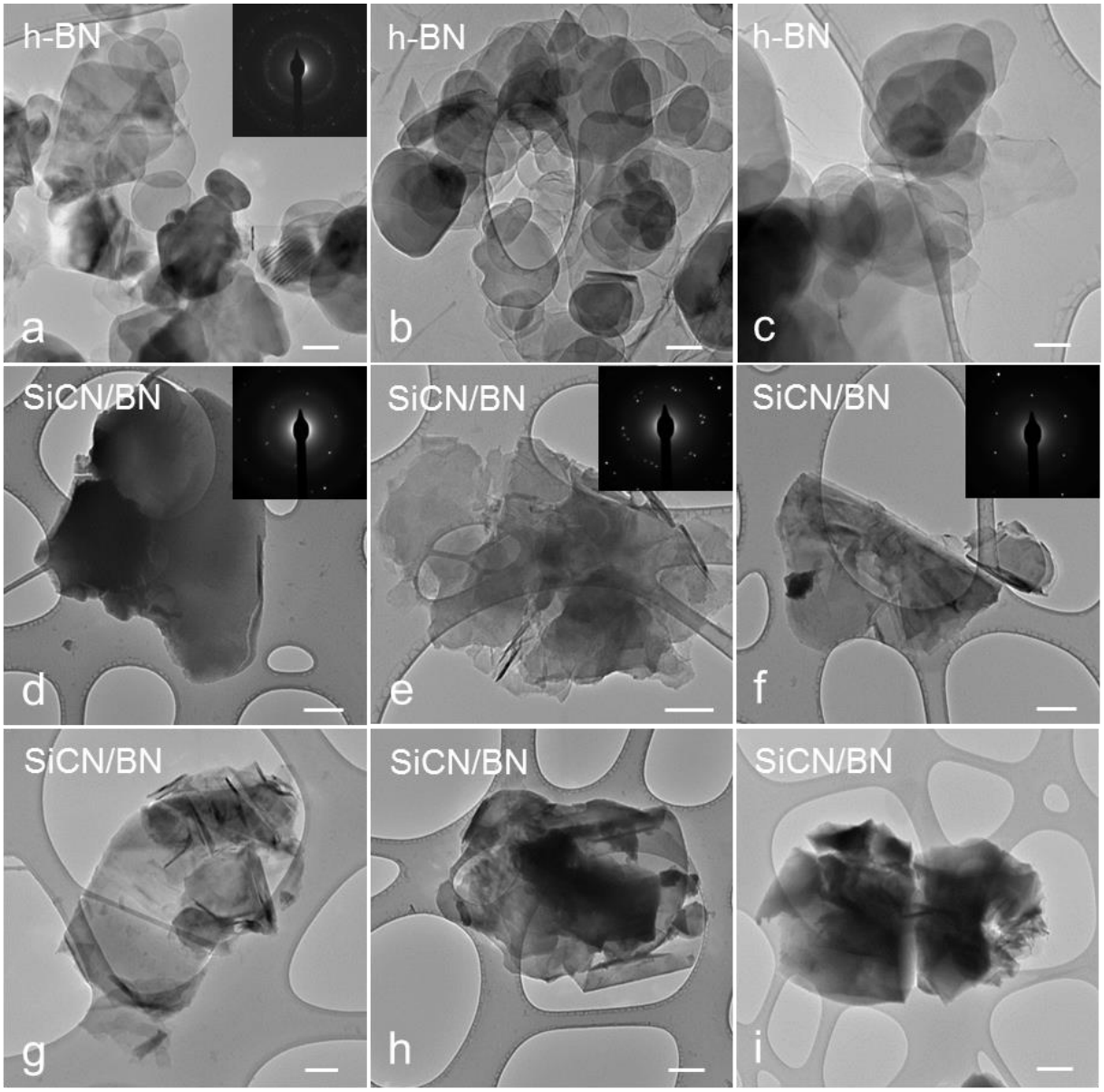

Figure 7-3(a through c): TEM images of as-obtained BN sheets, (d through i): as-synthesized SiCN/BN composite material. The insets show the SAED pattern obtained for the corresponding TEM image. SiCN/BN showed distinct pattern corresponding to BN. Scale bar is 50 nm.

High resolution XPS spectrum of C 1s and N 1s for SiCN and SiCN/BP are included in Figure 7.6. A comparison of C 1s peaks with SiCN/BN revealed that three distinct peaks could

be fitted at 283.4, 284.5, and 288 eV attributed to Si-C, C-C, and C-O bonds, respectively. Closer examination of the area under the peaks revealed a higher percentage of C-C bonds (-sp^2 type carbon) in SiCN/BN (0.14 %) compared to 'neat' SiCN (0.04%) and SiCN/BP (0.1%) specimens. The N 1s spectrum for SiCN/BN specimen could be resolved to Si-N (396.8 eV) and B-N (398.2 eV) while the spectrum for SiCN and SiCN/BP specimens were similar and resolved to two Si-N bonds at (396.8 and 397.1 eV). High-resolution B 1s spectrum (Figure 7.7) of SiCN/BNF was quite different with an emergence of a weak peak at 192.2 eV. That peak was the only observable peak in SiCN/BP.

The chemical bonds present were also characterized using Fourier Transform Infrared (FTIR) spectroscopy which showed that SiCN/BN and SiCN/BNF had strong BN bond vibrations with no obvious presence of B-O bonding (Figure 7.8). Peaks ascribed to vinyl groups are C-H vibrations at 3047 cm^{-1} and C-C stretching at 1591 cm^{-1}. Peaks attributed to Si-NH-Si groups are N-H stretching at 3374 cm^{-1} and Si-N vibration at 1160 cm^{-1}. Si-CH_3 characteristic peaks are at 1253 cm^{-1} and methyl vibrations at 2954 and 2896 cm^{-1}. The large peak at 2111 cm^{-1} is attributed to Si-H and small peaks at 805 and 750 cm^{-1} can be assigned to Si-N and Si-C, respectively.[59-63]

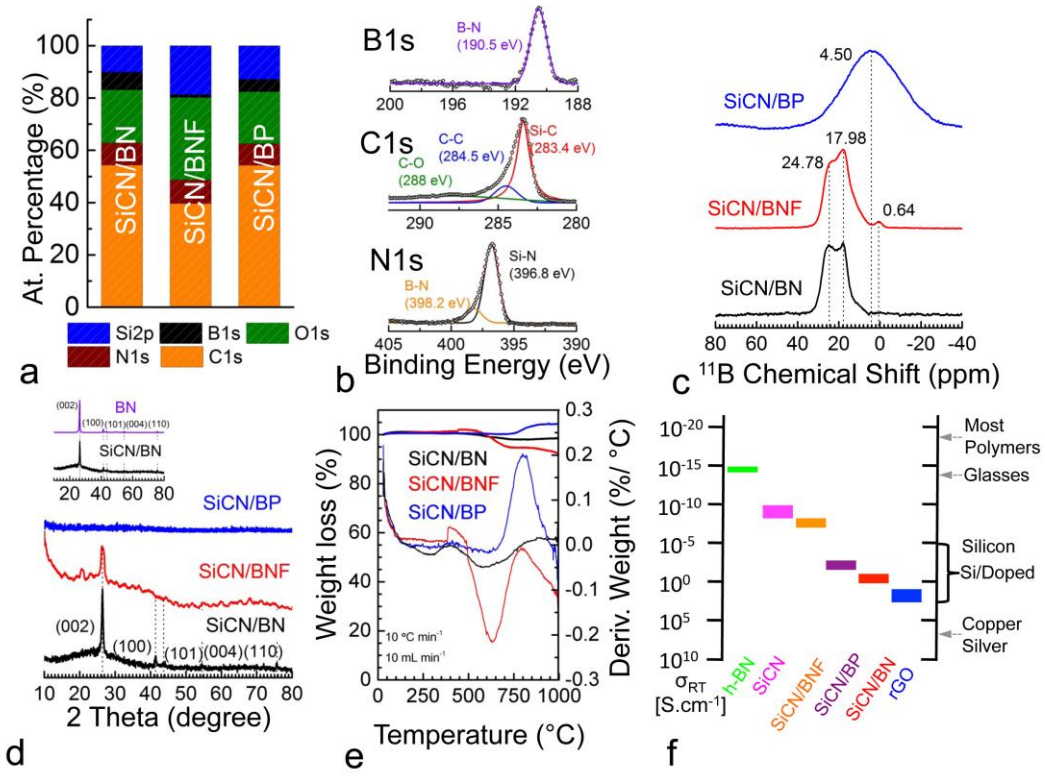

Figure 7-4 (a) Bar chart of atomic percentage of elements present in SiCN/BN, SiCN/BNF and SiCN/BP composites obtained using XPS. (b) High-resolution XPS of B 1s, C 1s and N 1s peaks in SiCN/BN composites. (c) 11B NMR spectra showing B-N bonds in planar BN3 groups in case of SiCN/BN and SiCN/BNF and amorphous boron in SiCN/BP ceramic composites. (d) XRD comparison SiCN/BN, SiCN/BNF and SiCN/BP composites. Inset shows X-ray comparison of 'as-obtained' BN powder and SiCN/BN composite. Characteristic BN peaks were clearly observed in SiCN/BN composite. (e) Thermogravimetric analysis plots of three composites proving SiCN/BN's high thermal stability and oxidation resistance. (f) Electrical conductivity comparison of various SiCN PDCs specimen prepared in this study. rGO and BN are included to demonstrate the wide range in conductivity that can be achieved in these ceramics.

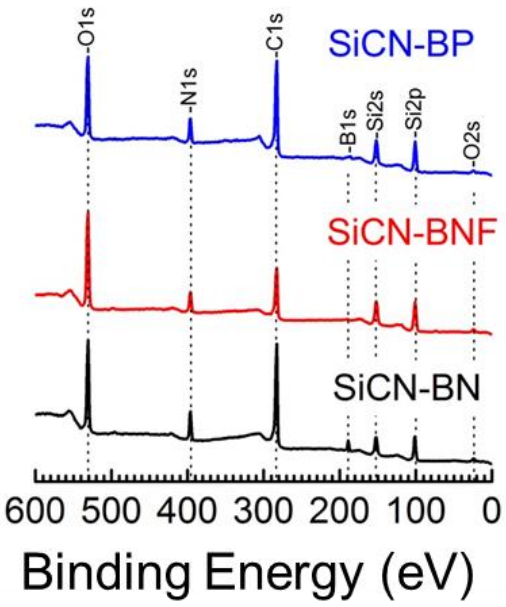

Figure 7-5 XPS (survey scan) comparison SiCN/BN, SiCN/BNF and SiCN/BP composites.

Additional characterization of the composite was carried out by use of solid-state NMR (^{11}B), as shown in Figure 7.4c. ^{11}B solid-state MAS NMR spectra of samples SiCN/BN and SiCN/BNF demonstrated a main signal in the region of tricoordinated boron atoms tentatively simulated with a site at 30 ppm (CQ = 3.0 MHz, η = 0.2) assigned to B-N bonds in planar BN_3 groups within BN graphitic layers. A second small signal at δ_{iso} = 0.6 ppm (no quadrupolar shape) is indicative of the presence of tetragonal BO_4 groups in minor quantity.[54, 55] The ^{11}B spectrum of SiCN/BP showed a shapeless signal centered at 4.5 ppm characteristic of amorphous elemental boron.[64] Chemical characterization of the hybrid matrix involved X-ray diffraction (XRD) to identify crystallinity of the composite material, as shown in Figure 7.4d. SiCN/BN spectrum was comparable to XRD of as-obtained BN powder spectrum (insert in Figure 7.4d) with characteristic 002 peak at 28° 2θ, indicating that BN sheets were primarily intact in the amorphous SiCN ceramic matrix. Very weak but similar spectrum was obtained for SiCN/BNF specimen, while SiCN/BP material was featureless in X-ray.

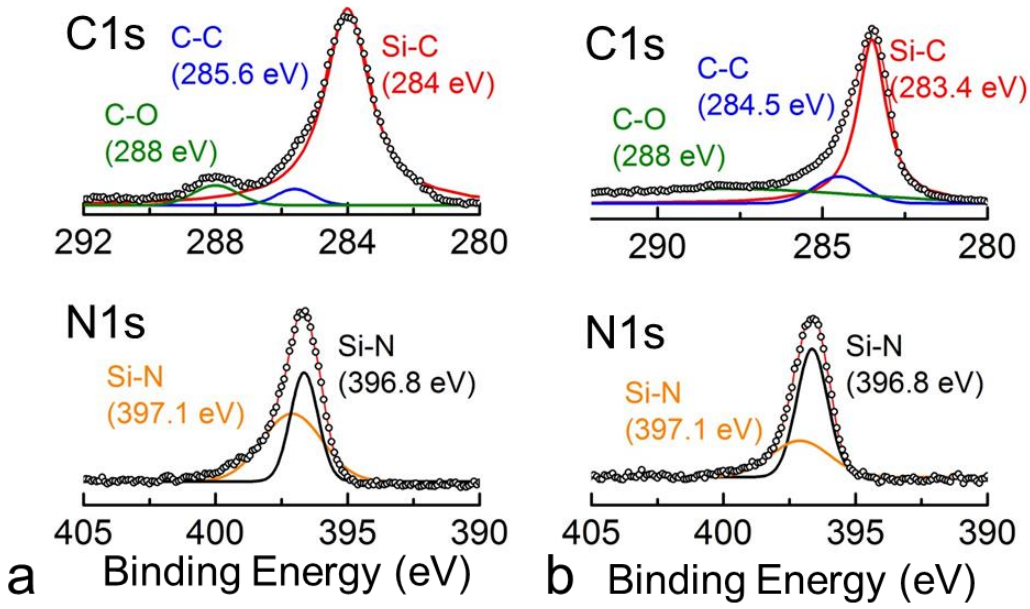

Figure 7-6 High-resolution XPS of C 1s and N 1s spectra of (a) SiCN and (b) SiCN/BP composites, respectively.

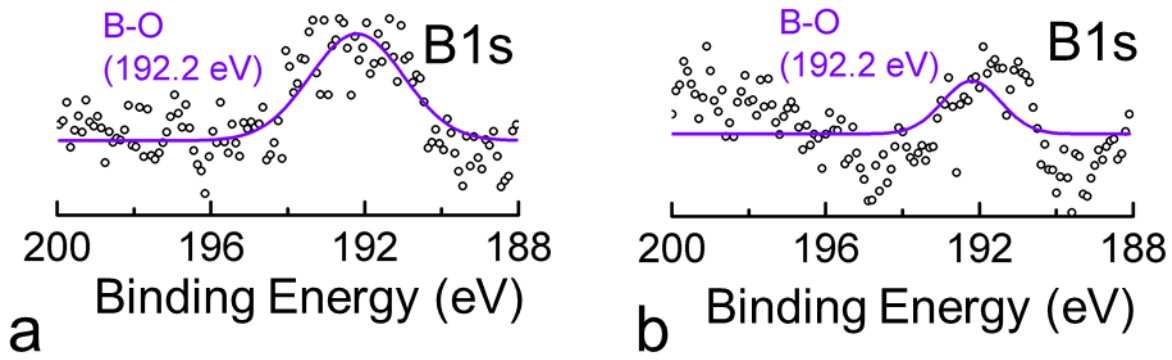

Figure 7-7 High-resolution B 1s spectrum of (a) SiCN/BNF and (b) SiCN/BP composites, respectively.

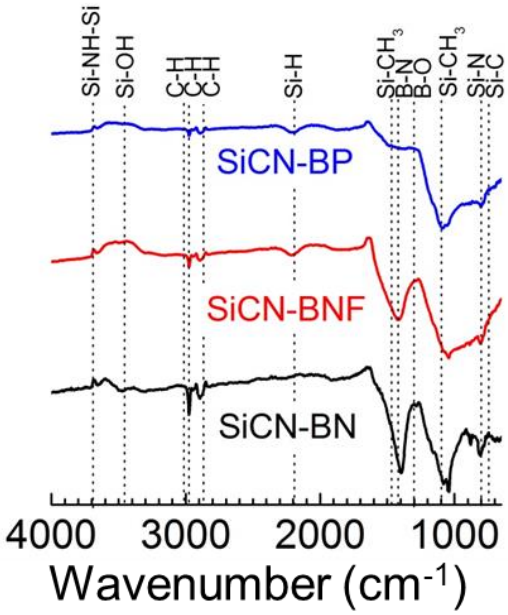

Figure 7-8 FTIR comparison SiCN/BN, SiCN/BNF, and SiCN/BP composites.

In summary, FTIR and XPS characterization of SiCN/BN composite material suggested the presence of only B-N bonding with little or no evidence of damage to BN sheets upon pyrolysis.[42] While NMR data showed that the boron was tricoordinated as planar BN_3 groups. Amorphous nature of Si-C and Si-N groups and crystalline B-N groups were observed using XRD in SiCN/BN composite material. Results confirmed the structure deduced in Figure 7.1.

Thermogravimetric analysis (TGA) plots of all materials were compared (see Figure 7.4e) in order to identify thermal stability. SiCN/BN was extremely stable with no significant weight change even when heated to 1000 °C in flowing air. In contrast, SiCN/BNF composite showed a weight loss attributed to the presence of residual compounds (such as H_2O) in polyborazylene derived BN (BNF) material. SiCN/BP composites had slight weight gain caused by oxidation of boron into boron oxide.

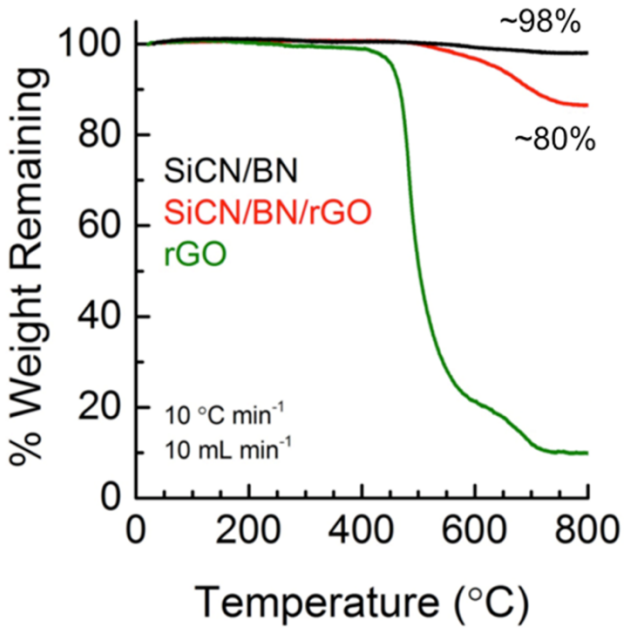

Figure 7-9 Thermogravimetric analysis plots comparing 'neat' SiCN/BN and SiCN/BN/rGO composite paper electrode (in flowing air).

Four-point surface electrical conductivity of various ceramic specimens was also measured and compared. Data presented in Figure 7.4f clearly shows that SiCN/BN displayed highest electrical conductive of any specimens at 0.115±0.005 $S.cm^{-1}$, which is as high as doped silicon but lower than the rGO. SiCN/BP demonstrated the next highest electrical conductivity. Increased conductivity of SiCN/BN composite (compared to other PDCs pyrolyzed under similar conditions) [46,47] is attributed to the increased amounts of C-C bonding character in the composite, which was considerably higher as confirmed by the XPS.

Electrochemical behavior of the SiCN/BN/rGO electrode (with approximately 20 wt.% rGO as mechanical support) was studied by cycling it in a half-cell configuration against pure lithium metal. Mass loading of SiCN/BN in the composite paper was confirmed by use of TGA (see Figure 7.9). Specific capacity values were calculated with respect to total weight of the

electrode and mass of active material. Figures 7.12a and 7.12b show the charge/discharge profile and differential capacity curves of the SiCN/BN electrode's first two cycles. First cycle discharge and charge capacities were observed to be 891 and 517 mAh g^{-1} with a first cycle loss of 58% at current density of 100 mA g^{-1}. This capacity value is one of the highest reported for polysilazane-based anode materials. [34-38] For example, first reversible capacity of SiCN/BN hybrid composite is better than SiCN annealed at 1000 °C (456 mAh g^{-1}), [36] C-rich SiCN (~263 mAh g^{-1}),[37] SiCN-1300 °C (383 mAh g^{-1}), [38] B-doped SiCN (~100 mAh g^{-1}) [47] and SiCN/graphite (~474 mAh g^{-1}).[49] The differential capacity curve showed first cycle lithiation peaks at 50 mV, 150 mV, a weak plateau at ~700 mV, and a delithiation plateau at ~500 mV. From literature, the peak at 50 mV could be attributed to Li intercalation/adsorption in graphitic carbon[32, 34] and the peak at 150 mV corresponds to interaction of Li in nanovoids or interaction with dangling bonds present at Si and C sites in the ceramic.[32, 37, 47] The plateau at ~700 to 800 mV, present only in the first cycle, originated due to formation of passive solid electrolyte interface (SEI) on graphite. This plateau was common to all electrodes including 'neat' rGO electrode and data from the literature (see Figure 7.10 for voltage profiles of BP/rGO, and BN/rGO electrodes). The charge/discharge profile and corresponding differential capacity curves of SiCN/BNF/rGO and SiCN/BP/rGO paper electrodes are shown in Figure 7.11. Lithiation peaks were at 50 mV and ~600 mV with a corresponding delithiation peak at 200 mV (similar to BN/rGO and BP/rGO differential capacity curves). From these results we deduce that the capacity in SiCN/BN originates primarily from BN enhanced SiCN-based Li intercalation sites while it is not the same in other ceramics that we tested. This is even more evident from the first cycle discharge capacities which were at ~531 mAh g^{-1} and 347 mAh g^{-1} for SiCN/BNF/rGO and

SiCN/BP/rGO, respectively. Lower capacity values were observed in subsequent cycles because BN and boron particles have zero or negligible Li cyclability.

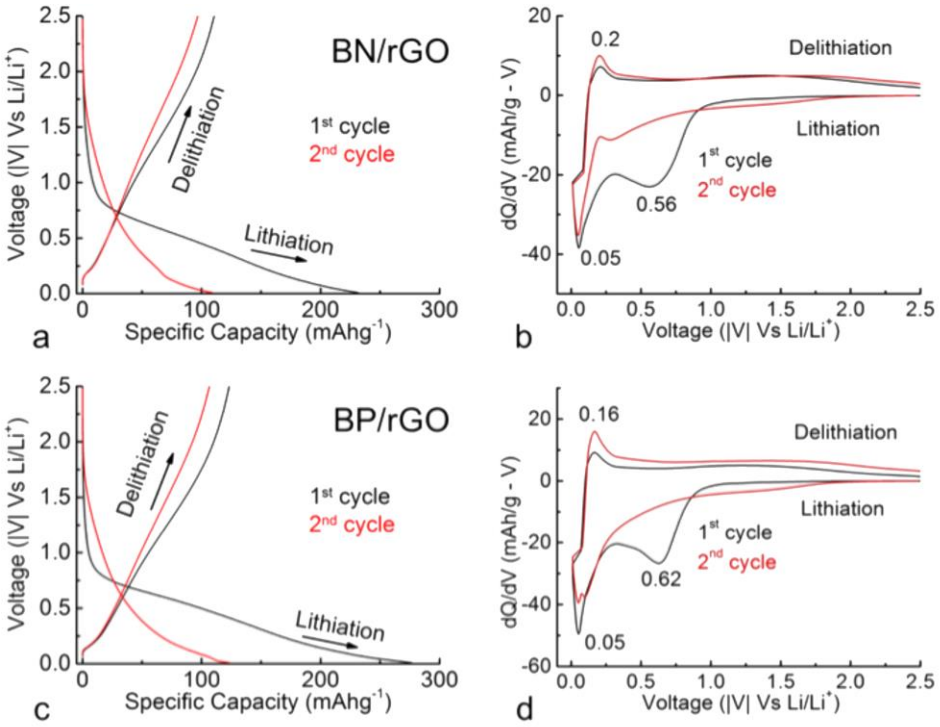

Figure 7-10 1st and 2nd cycle voltage profile and differential capacity curve (a,b) BN/rGO and (c,d) BP/rGO anode.

With additional cycling (Figure 7.12), SiCN/BN/rGO maintained high capacity at 474 mAh g^{-1} (96% of initial capacity retained) which is higher than BN/rGO and SiCN/rGO with charge capacities of 67 and 154 mAh g^{-1}, respectively, after 5 cycles at 100 mA g^{-1}. Current density was gradually increased to 200, 400, 800, 1600 and 2400 mA g^{-1} for each five cycles consecutively. Importantly, SiCN/BN/rGO hybrid composite maintained its reversible capacity of 283 mAh g^{-1} even at 2400 mA g^{-1}. This capacity was 52% of the initial capacity. When the cells were cycled back at 100 mA g^{-1}, all electrodes regained initial charge capacities at 449, 60, and 154 mAh g^{-1} for SiCN/BN/rGO, BN/rGO, and SiCN/rGO, respectively.

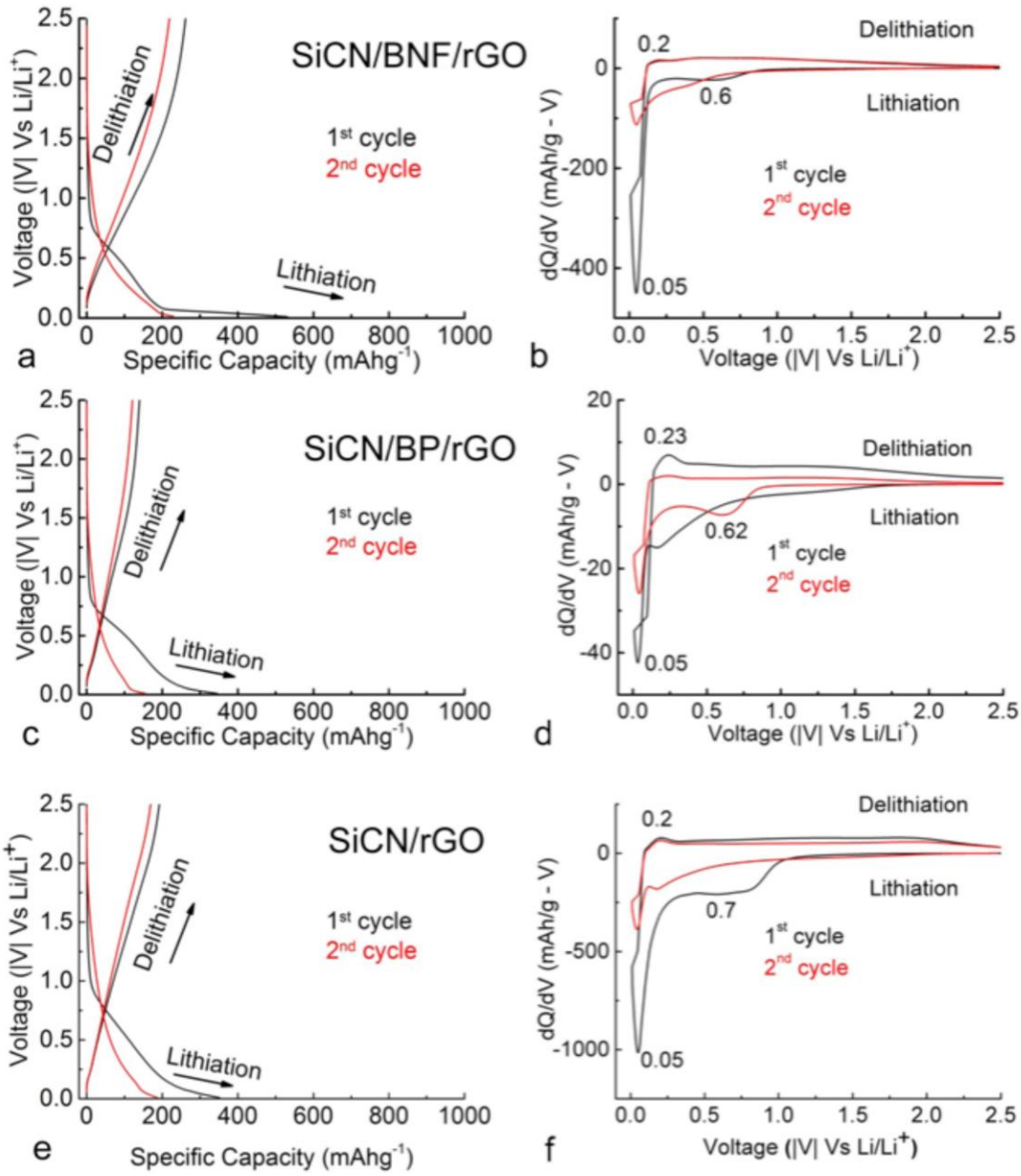

Figure 7-11 1st and 2nd cycle voltage profile and differential capacity curve (a,b) SiCN/BNF/rGO, (c,d) SiCN/BP/rGO and (e,f) SiCN/rGO anode.

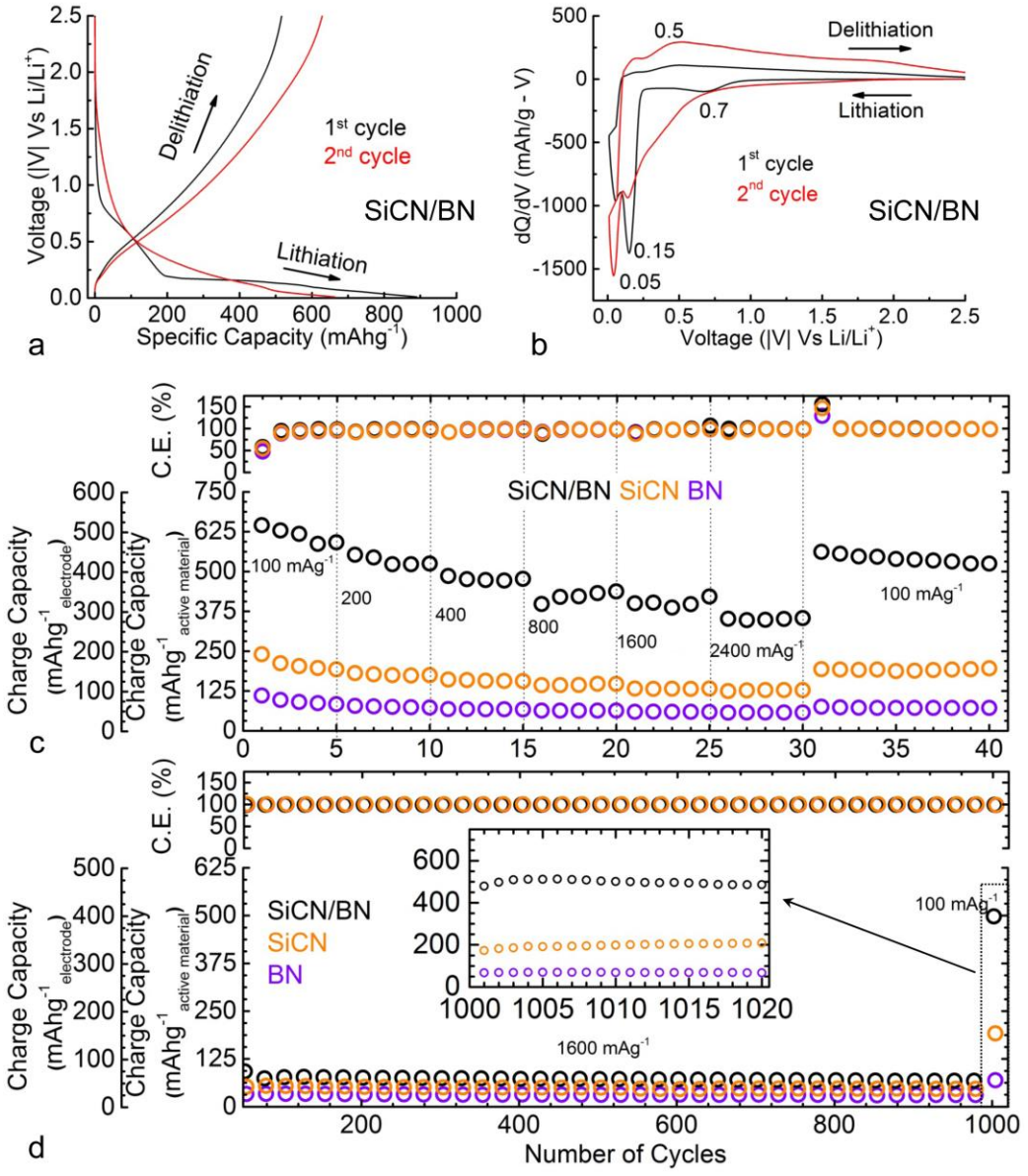

Figure 7-12 1st and 2nd cycle (a) voltage profile and (b) differential capacity curve of SiCN/BN/rGO. (c) Charge capacity of SiCN/BN/rGO with BN/rGO and SiCN/rGO for comparison. Cells were cycled asymmetrically at increasing rates for every five cycles. (d) Charge capacity when symmetrically at 1600 mA g-1 for 1000 cycles and return to 100 mA g-1. Charge capacity of SiCN/BN was more than twice than the capacity of SiCN.

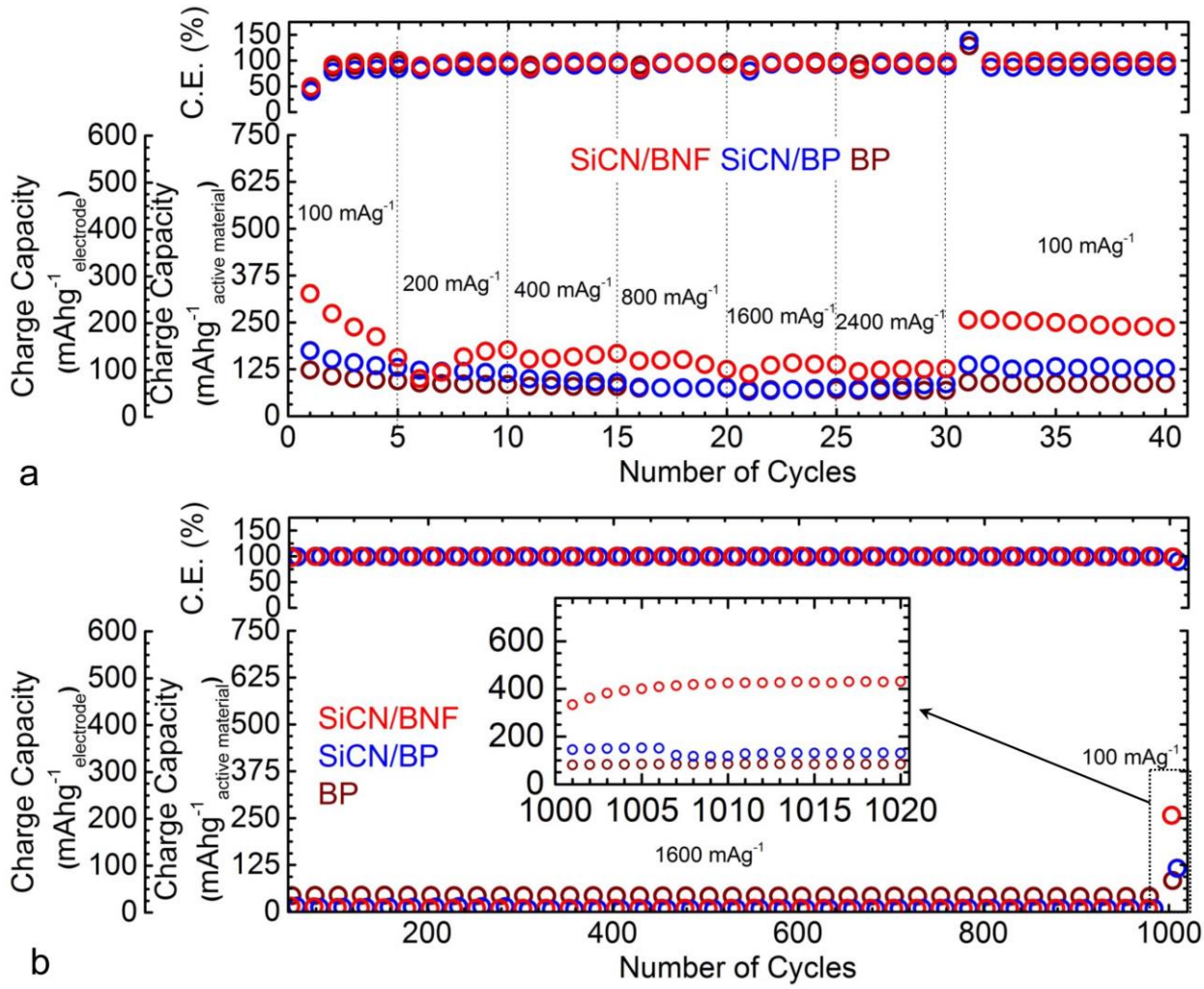

Figure 7-13 Charge capacity of SiCN-BNF/rGO, SiCN/BP/rGO and BP/rGO electrodes: (a) asymmetrically cycled at different rates for every 5 cycles and (b) consecutively cycled symmetrically at 1600 mA g-1 (w.r.t. total weight of the electrode) for 1000 cycles.

However, SiCN/BNF/rGO, SiCN/BP/rGO, and BP/rGO performances, shown in Figure 7.13, were lower than SiCN/BN/rGO. In order to test cell performance during long-term cycling, cells were cycled at 1600 mA g^{-1} during charge and discharge half cycles (see Figure 7.12). SiCN/BN/rGO demonstrated stable and high charge capacity of ~62 mAh.g^{-1} than BN/rGO and SiCN/rGO anode at ~25 and 40 mAh g^{-1}, respectively. All electrodes regained most of initial capacity when they were cycled at 100 mA g^{-1} after 1000 cycles. SiCN/BN/rGO was the best

performing anode with a charge capacity of ~401 mAh g^{-1} at 100 mA g^{-1} even after symmetric cycling at 1600 mA g^{-1} for 1000 cycles. Summary of the electrochemical data and comparison with recent literature (including graphite[65] and rGO paper electrode[66]) is presented in Table 1.

In the galvanostatic intermittent titration technique (GITT) experiment, charge was inserted (or withdrawn) by applying a current pulse of 100 mAh.g^{-1} for 15 min, followed by 8 h of relaxation between pulses during which the change in potential with time was measured. Magnitude of voltage increased during the relaxation period in the insertion half but it decreased in the extraction half of the cycle [69,70].

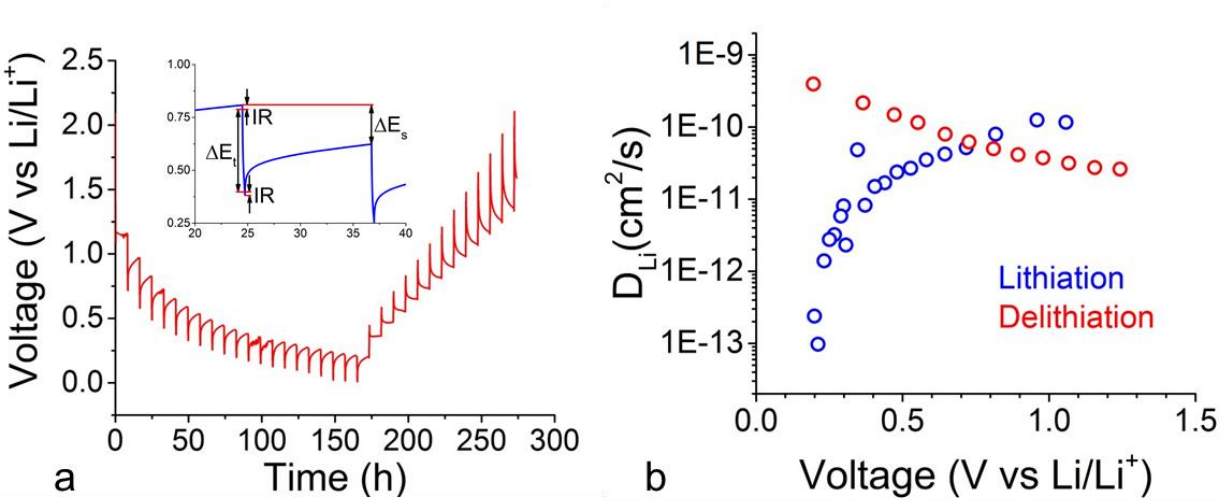

Figure 7-14 GITT Data: (a) Charge and discharge cycles with 15 min of current pulse at 100 mAh.g-1 followed by 8 h of relaxation. (b) Calculated diffusion coefficient based on the relaxation steps at the corresponding voltages.

The solid state lithium ion diffusion coefficients were determined using

Equation 7-1

$$D_{GITT} \approx \frac{4}{\pi\tau}\left(\frac{m_B V_M}{M_B S}\right)^2\left(\frac{\Delta E_S}{\Delta E_T}\right)^2 \quad m^2/s$$

Where τ is pulse time (15 min), m_B is electrode mass, V_M is molar volume, M_B molecular weight, and S is surface area, ΔE_S and ΔE_T are voltage steps as shown in insert in Fig. S10.

Further, Galvanostatic Intermittent Titration Technique (GITT) was performed to obtain the solid state Li-ion diffusion coefficient (D_{Li+}) of SiCN/BN electrode (Figure 7.14). The acquired D_{Li+} varied between approximately (10^{-10} to 1.4 x 10^{-12}) $cm^2.s^{-1}$ and (3.9 x 10^{-10} to 2.6 x 10^{-11}) $cm^2.s^{-1}$ during the insertion and extraction half, respectively. These values are comparable to SiBCN-CNT (~ 10^{-9} to 10^{-12} $cm^2.s^{-1}$) [47] electrodes but lower than the chemical diffusivity of Li-ion in graphite. [67-68]

High charge capacity of SiCN/BN is attributed to the three-fold advantage associated with the addition of boron to SiCN matrix in the form of BN sheets: (1) possible neutralization of nitrogen atoms by boron. SiCN electrodes with higher nitrogen content typically demonstrates lower electrochemical performance, therefore, increased concentration of boron in SiCN neutralized some of the nitrogen dangling bonds in SiCN during pyrolysis, (2) sheet-like morphology, and (3) significant enhancement in electrical conductivity originating from increased C-C bonds of the SiCN/BN hybrid ceramic matrix compared to other PDC material pyrolyzed under similar conditions.[47]

Table 7.1 Summary of electrochemical cycling data for various electrodes used in this study and comparison with data from literature. NOTE: All electrodes in the present study were prepared with approximately 20 wt % rGO. Capacity values are with respect to total electrode weight.

Electrode material	1st Cycle charge, mAh g^{-1}	Capacity at max. current density tested, mAh g^{-1}	Max. number of cycles tested	Charge capacity after 1000 cycles at 100 mA g^{-1}
SiCN/BN	475 ±42 *	283.2 (2400)	1020	400.8
SiCN/BNF	262.4	100.8 (2400)	1020	202.4
SiCN/BP	140	68.8 (2400)	1020	95.2
SiCN	192	102.3 (2400)	1020	159.2
BN	88.8	46.4 (2400)	1020	55.2
BP	99.2	55.2 (2400)	1020	68
SiCN-1000 °C [36]	456	171 (100)	30	-
SiCN-1100 °C[37]	263	100 (36)	50	-
SiCN-1300 °C/O_2[37]	291	250 (72)	60	-
SiCN-1100 °C[38]	254	95 (360)	10	-
Si(B)CN-CNT[47]	362	430 (100)	30	-
SiCN-Graphene[49]	420	440 (40)	50	-
Graphite[65]	298	240 (50)	50	-
rGO-500 °C[66]	292	180 (2400)	1020	190

** Average of three samples. Refer supporting Information Figure 7.15*

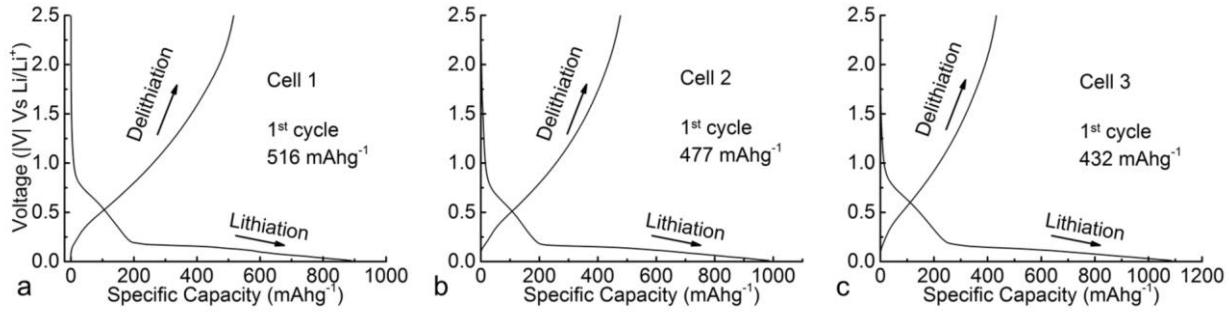

Figure 7-15 Voltage discharge/charge profile of three different SiCN-BN/rGO electrodes. Capacity is w.r.t. total electrode weight.

7.5. Conclusion

Synthesis of a chemically integrated SiCN/BN layered composite is demonstrated for the first time. The composite shows electrical conductivity similar to conductivity of doped-silicon, which is several orders of magnitude higher than that of 'neat' SiCN prepared under similar conditions. Additionally, unlike its individual constituents, the SiCN/BN composite offers high electrochemical activity and stability toward lithium-ions with charge capacity reaching ~517 mAh g^{-1} at 100 mA g^{-1} and ~283 mAh g^{-1} at 2400 mA g^{-1} with respect to total electrode weight. This behavior is attributed to the increased amount of $–sp^2$ carbon in SiCN phase (observed only in presence of BN) that may have exceeded its percolation limit and provided necessary sites for reversible lithium adsorption. Facile synthesis and improved thermal, electrical and electrochemical performance of SiCN/BN composite is expected to open new applications for PDCs and 2-D nanomaterial hybrids.

7.6. Acknowledgements

This research is based on work supported by the National Science Foundation-Chemical, Bioengineering, Environmental, and Transport Systems Division (CBET) under grant no. 1335862 to G. Singh. L.D. Thanks former student Romil and Uriel for assistance with sample

preparation. G. Singh thanks Professor G. Sorarù (University of Trento) and Dr. Yigal Blum (SRI International) for their useful insights.

7.7. References

1. Armand, M.; Tarascon, J. M., Building Better Batteries. *Nature* **2008,** *451*, 652-657.

2. Tarascon, J. M.; Armand, M., Issues and Challenges Facing Rechargeable Lithium Batteries. *Nature* **2001,** *414*, 359-367.

3. Goodenough, J. B.; Kim, Y., Challenges for Rechargeable Li Batteries. *Chem. Mater.* **2010,** *22*, 587-603.

4. Arico, A. S.; Bruce, P.; Scrosati, B.; Tarascon, J. M.; Van Schalkwijk, W., Nanostructured Materials for Advanced Energy Conversion and Storage Devices. *Nat. Mater.* **2005,** *4*, 366-377.

5. Choi, N. S.; Chen, Z.; Freunberger, S. A.; Ji, X.; Sun, Y. K.; Amine, K.; Yushin, G.; Nazar, L. F.; Cho, J.; Bruce, P. G., Challenges Facing Lithium Batteries and Electrical Double-Layer Capacitors. *Angew. Chem., Int. Ed.* **2012,** *51*, 9994-10024.

6. David, L.; Bhandavat, R.; Kulkarni, G.; Pahwa, S.; Zhong, Z.; Singh, G. Synthesis of Graphene Films by Rapid Heating and Quenching at Ambient Pressures and Their Electrochemical Characterization. *ACS Appl. Mater. Interfaces* **2013,** *5*, 546-552.

7. Manthiram, A., Materials Challenges and Opportunities of Lithium Ion Batteries. *J. Phys. Chem. Lett.* **2011,** *2*, 176-184.

8. Hu, L.; Xu, K., Nonflammable Electrolyte Enhances Battery Safety. *Proc. Natl. Acad. Sci. U.S.A.* **2014,** *111*, 3205-3206.

9. Park, C. M.; Kim, J. H.; Kim, H.; Sohn, H. J., Li-Alloy Based Anode Materials for Li Secondary Batteries. *Chem. Soc. Rev.* **2010,** *39*, 3115-3141.

10. Zhang, W. J., A Review of the Electrochemical Performance of Alloy Anodes for Lithium-Ion Batteries. *J. Power Sources* **2011,** *196*, 13-24.

11. Wu, H.; Cui, Y., Designing Nanostructured Si Anodes for High Energy Lithium Ion Batteries. *Nano Today* **2012,** *7*, 414-429.

12. Beaulieu, L. Y.; Eberman, K. W.; Turner, R. L.; Krause, L. J.; Dahn, J. R., Colossal Reversible Volume Changes in Lithium Alloys. *Electrochem. Solid-State Lett.* **2001,** *4*, A137-A140.

13. Nadimpalli, S. P. V.; Sethuraman, V. A.; Dalavi, S.; Lucht, B.; Chon, M. J.; Shenoy, V. B.; Guduru, P. R., Quantifying Capacity Loss Due to Solid-Electrolyte-Interphase Layer

Formation on Silicon Negative Electrodes in Lithium-Ion Batteries. *J. Power Sources* **2012,** *215*, 145-151.

14. Park, M. H.; Kim, M. G.; Joo, J.; Kim, K.; Kim, J.; Ahn, S.; Cui, Y.; Cho, J., Silicon Nanotube Battery Anodes. *Nano Lett.* **2009,** *9*, 3844-3847.

15. Song, T.; Xia, J.; Lee, J. H.; Lee, D. H.; Kwon, M.-S.; Choi, J.-M.; Wu, J.; Doo, S. K.; Chang, H.; Il Park, W. et al. , Arrays of Sealed Silicon Nanotubes as Anodes for Lithium Ion Batteries. *Nano Lett.* **2010,** *10*, 1710-1716.

16. Kasavajjula, U.; Wang, C.; Appleby, A. J., Nano- and Bulk-Silicon-Based Insertion Anodes for Lithium-Ion Secondary Cells. *J. Power Sources* **2007,** *163*, 1003-1039.

17. Liu, B.; Soares, P.; Checkles, C.; Zhao, Y.; Yu, G., Three-Dimensional Hierarchical Ternary Nanostructures for High-Performance Li-Ion Battery Anodes. *Nano Lett.* **2013,** *13*, 3414-3419.

18. Ruvinskiy, P.; Barsukov, I. V.; Mashtalir, O.; Reid, C. M.; Wu, J. J.; Gogotsi, Y., Nano-Silicon Containing Composite Graphitic Anodes with Improved Cycling Stability for Application in High Energy Lithium-Ion Batteries. *ECS J. Solid State Sci. Tech.* **2013,** *2*, M3028-M3033.

19. McDowell, M. T.; Lee, S. W.; Nix, W. D.; Cui, Y., 25th Anniversary Article: Understanding the Lithiation of Silicon and Other Alloying Anodes for Lithium-Ion Batteries. *Adv. Mater.* **2013,** *25*, 4966-4984.

20. Kim, H.; Seo, M.; Park, M. H.; Cho, J., A Critical Size of Silicon Nano-Anodes for Lithium Rechargeable Batteries. *Angew. Chem. Int. Ed.* **2010,** *49*, 2146-2149.

21. Chockla, A. M.; Klavetter, K. C.; Mullins, C. B.; Korgel, B. A., Tin-Seeded Silicon Nanowires for High Capacity Li-Ion Batteries. *Chem. Mater.* **2012,** *24*, 3738-3745.

22. Chan, C. K.; Patel, R. N.; O'Connell, M. J.; Korgel, B. A.; Cui, Y., Solution-Grown Silicon Nanowires for Lithium-Ion Battery Anodes. *ACS Nano* **2010,** *4*, 1443-1450.

23. Deshpande, R.; Cheng, Y. T.; Verbrugge, M. W., Modeling Diffusion-Induced Stress in Nanowire Electrode Structures. *J. Power Sources* **2010,** *195*, 5081-5088.

24. Chockla, A. M.; Panthani, M. G.; Holmberg, V. C.; Hessel, C. M.; Reid, D. K.; Bogart, T. D.; Harris, J. T.; Mullins, C. B.; Korgel, B. A., Electrochemical Lithiation of Graphene-Supported Silicon and Germanium for Rechargeable Batteries. *J. Phys. Chem. C* **2012**, *116*, 11917-11923.

25. Ruffo, R.; Hong, S. S.; Chan, C. K.; Huggins, R. A.; Cui, Y., Impedance Analysis of Silicon Nanowire Lithium Ion Battery Anodes. *J. Phys. Chem. C* **2009,** *113*, 11390-11398.

26. Luo, J.; Zhao, X.; Wu, J.; Jang, H. D.; Kung, H. H.; Huang, J., Crumpled Graphene-Encapsulated Si Nanoparticles for Lithium Ion Battery Anodes. *J. Phys. Chem. Lett.* **2012,** 3, 1824-1829.

27. Fukui, H.; Ohsuka, H.; Hino, T.; Kanamura, K., A Si-O-C Composite Anode: High Capability and Proposed Mechanism of Lithium Storage Associated with Microstructural Characteristics. *ACS Appl. Mater. Interfaces* **2010,** *2*, 998-1008.

28. Shen, J.; Raj, R., Silicon-Oxycarbide Based Thin Film Anodes for Lithium Ion Batteries. *J. Power Sources* **2011,** *196*, 5945-5950.

29. Ahn, D.; Raj, R., Cyclic Stability and C-Rate Performance of Amorphous Silicon and Carbon Based Anodes for Electrochemical Storage of Lithium. *J. Power Sources* **2011**, *196*, 2179-2186.

30. Bhandavat, R.; Singh, G. Stable and Efficient Li-Ion Battery Anodes Prepared from Polymer-Derived Silicon Oxycarbide-Carbon Nanotube Shell/Core Composites. *J. Phys. Chem. C* **2013**, *117*, 11899-11905.

31. Ahn, D.; Raj, R., Thermodynamic Measurements Pertaining to the Hysteretic Intercalation of Lithium in Polymer-Derived Silicon Oxycarbide. *J. Power Sources* **2010,** *195*, 3900-3906.

32. Feng, Y., Electrochemical Properties of Heat-Treated Polymer-Derived SiCN Anode for Lithium Ion Batteries. *Electrochim. Acta* **2010,** *55*, 5860-5866.

33. Fukui, H.; Ohsuka, H.; Hino, T.; Kanamura, K., Polysilane/Acenaphthylene Blends Toward Si-O-C Composite Anodes for Rechargeable Lithium-Ion Batteries. *J. Electrochem. Soc.* **2011,** *158*, A550-A555.

34. Kaspar, J.; Graczyk-Zajac, M.; Riedel, R., Determination of the Chemical Diffusion Coefficient of Li-ions in Carbon-Rich Silicon Oxycarbide Anodes by Electro-Analytical Methods. *Electrochim. Acta.* **2014**, *115*, 665-670.

35. Liebau-Kunzmann, V.; Fasel, C.; Kolb, R.; Riedel, R., Lithium Containing Silazanes as Precursors for SiCN: Li Ceramics - A Potential Material for Electrochemical Applications. *J. Eur. Ceram. Soc.* **2006,** *26*, 3897-3901.

36. Su, D.; Li, Y. L.; Feng, Y.; Jin, J., Electrochemical Properties of Polymer-Derived SiCN Materials as the Anode in Lithium Ion Batteries. *J. Am. Ceram. Soc.* **2009,** *92*, 2962-2968.

37. Graczyk-Zajac, M.; Mera, G.; Kaspar, J.; Riedel, R., Electrochemical Studies of Carbon-Rich Polymer-Derived SiCN Ceramics as Anode Materials for Lithium-Ion Batteries. *J. Eur. Ceram. Soc.* **2010,** *30*, 3235-3243.

38. Kaspar, J.; Mera, G.; Nowak, A. P.; Graczyk-Zajac, M.; Riedel, R., Electrochemical Study of Lithium Insertion into Carbon-Rich Polymer-Derived Silicon Carbonitride Ceramics. *Electrochim. Acta* **2010,** *56*, 174-182.

39. Tamai, H.; Sugahara, H.; Yasuda, H., Preparation of Carbons from Pitch Containing Polysilane and their Anode Properties for Lithium-Ion Batteries. *J. Mater. Sci. Lett.* **2000,** *19*, 53-56.

40. Bhandavat, R.; Singh, G., Synthesis, Characterization, and High Temperature Stability of Si(B)CN-Coated Carbon Nanotubes Using a Boron-Modified Poly(ureamethylvinyl)Silazane Chemistry. *J. Am. Ceram. Soc.* **2012,** *95*, 1536-1543.

41. Sarkar, S.; Gan, Z.; An, L.; Zhai, L., Structural Evolution of Polymer-Derived Amorphous SiBCN Ceramics at High Temperature. *J. Phys. Chem. C* **2011,** *115*, 24993-25000.

42. Hermann, A. M.; Wang, Y. T.; Ramakrishnan, P. A.; Balzar, D.; An, L. N.; Haluschka, C.; Riedel, R., Structure and Electronic Transport Properties of Si-(B)-C-N Ceramics. *J. Am. Ceram. Soc.* **2001,** *84*, 2260-2264.

43. Riedel, R.; Kienzle, A.; Dressler, W.; Ruwisch, L.; Bill, J.; Aldinger, F., A Silicoboron Carbonitride Ceramic Stable to 2,000 Degrees C. *Nature* **1996,** *382*, 796-798.

44. David, L.; Asok, D.; Singh, G., Synthesis and Extreme Rate Capability of Si−Al−C−N Functionalized Carbon Nanotube Spray-on Coatings as Li-Ion Battery Electrode. *ACS Appl. Mater. Interfaces.* **2014**, *6*, 16056-16064.

45. Zimmermann, A.; Bauer, A.; Christ, M.; Cai, Y.; Aldinger, F., High-Temperature Deformation of Amorphous Si-C-N and Si-B-C-N Ceramics Derived from Polymers. *Acta Mater.* **2002,** *50*, 1187-1196.

46. Ramakrishnan, P. A.; Wang, Y. T.; Balzar, D.; An, L. A.; Haluschka, C.; Riedel, R.; Hermann, A. M., Silicoboron-Carbonitride Ceramics: A Class of High-Temperature, Dopable Electronic Materials. *App. Phys. Lett.* **2001,** *78*, 3076-3078.

47. Bhandavat, R.; Singh, G., Improved Electrochemical Capacity of Precursor-Derived Si(B)CN-Carbon Nanotube Composite as Li-Ion Battery Anode. *ACS Appl. Mater. Interfaces* **2012,** *4*, 5092-5097.

48. Feng, Y.; Du, G. X.; Zhao, X. J.; Yang, E. C., Preparation and Electrochemical Performance of SiCN-CNTs Composite Anode Material for Lithium Ion Batteries. *J Appl. Electrochem.* **2011,** *41*, 999-1002.

49. Graczyk-Zajac, M.; Fasel, C.; Riedel, R., Polymer-Derived-SiCN Ceramic/Graphite Composite as Anode Material with Enhanced Rate Capability for Lithium Ion Batteries. *J. Power Sources* **2011,** *196*, 6412-6418.

50. Kolb, R.; Fasel, C.; Liebau-Kunzmann, V.; Riedel, R., SiCN/C-Ceramic Composite as Anode Material for Lithium Ion Batteries. *J. Eur. Ceram. Soc.* **2006,** *26*, 3903-3908.

51. Bechelany, M.; Bernard, S.; Brioude, A.; Cornu, D.; Stadelmann, P.; Charcosset, C.; Fiaty, K.; Miele, P., Synthesis of Boron Nitride Nanotubes by a Template-Assisted Polymer Thermolysis Process. *J. Phys. Chem. C* **2007**, *111*, 13378-13384.

52. Salles, V.; Bernard, S.; Li, J.; Brioude, A.; Chehaidi, S.; Foucaud, S.; Miele, P., Design of Highly Dense Boron Nitride by the Combination of Spray-Pyrolysis of Borazine and Additive-Free Sintering of Derived Ultrafine Powders. *Chem. Mater.* **2009**, *21*, 2920-2929.

53. Termoss, H.; Toury, B.; Pavan, S.; Brioude, A.; Bernard, S.; Cornu, D.; Valette, S.; Benayoun, S.; Miele, P., Preparation of Boron Nitride-Based Coatings on Metallic Substrates Via Infrared Irradiation of Dip-Coated Polyborazylene. *J. Mater. Chem.* **2009**, *19*, 2671-2674.

54. Li, J.; Bernard, S.; Salles, V.; Gervais, C.; Miele, P., Preparation of Polyborazylene-Derived Bulk Boron Nitride with Tunable Properties by Warm-Pressing and Pressureless Pyrolysis. *Chem. Mater.* **2010**, *22*, 2010-2019.

55. Alauzun, J. G.; Ungureanu, S.; Brun, N.; Bernard, S.; Miele, P.; Backov, R.; Sanchez, C., Novel Monolith-Type Boron Nitride Hierarchical Foams Obtained Through Integrative Chemistry. *J. Mater. Chem.* **2011**, *21*, 14025-14030.

56. Schlienger, S.; Alauzun, J.; Michaux, F.; Vidal, L.; Parmentier, J.; Gervais, C.; Babonneau, F.; Bernard, S.; Miele, P.; Parra, J. B., Micro-, Mesoporous Boron Nitride-Based Materials Templated from Zeolites. *Chem. Mater.* **2012**, *24*, 88-96

57. Zhong, W.; Wang, S.; Li, J.; Bechelany, M. C.; Ghisleni, R.; Rossignol, F.; Balan, C.; Chartier, T.; Bernard, S.; Miele, P., Design of Carbon Fiber Reinforced Boron Nitride Matrix

Composites by Vacuum-Assisted Polyborazylene Transfer Molding and Pyrolysis. *J. Eur. Ceram. Soc.* **2013**, *33*, 2979-2992.

58. Hummers, W. S.; Offeman, R. E., Preparation of Graphitic Oxide. *J. Am. Chem. Soc.* **1958**, *80*, 1339-1339.

59. Li, Y. L.; Kroke, E.; Riedel, R.; Fasel, C.; Gervais, C.; Babonneau, F., Thermal Cross-Linking and Pyrolytic Conversion of Poly(Ureamethylvinyl)Silazanes to Silicon-Based Ceramics. *App. Organomet. Chem.* **2001,** *15*, 820-832.

60. Antsiferov, V. N.; Gilyov, V. G.; Karmanov, V. I., IR-Spectra and Phases Structure of Sialons. *Vib. Spectro.* **2002,** *30*, 169-173.

61. Wada, N.; Solin, S. A.; Wong, J.; Prochazka, S., Raman and Ir Absorption Spectroscopic Studies on Alpha, Beta, and Amorphous Si_3N_4. *J. Non-Crystalline Solids* **1981,** *43*, 7-15.

62. Ermer, E.; Ptak, W. S., FTIR Studies of Structural Effects due to Boron Addition in Sintered Silicon Carbide. *Vib. Spectro.* **2002,** *29*, 211-215.

63. Lv, Q.; Cao, C. B.; Li, C.; Zhang, J. T.; Zhu, H. X.; Kong, X.; Duan, X. F., Formation of Crystalline Carbon Nitride Powder by a Mild Solvothermal Method. *J. Mater. Chem.* **2003,** *13*, 1241-1243.

64. Brun, N.; Janot, R.; Sanchez, C.; Deleuze, H.; Gervais, C.; Morcrette, M.; Backov, R., Preparation of $LiBH_4$@carbon Micro-Macrocellular Foams: Tuning Hydrogen Release Through Varying Microporosity. *Energy Environ. Sci.* **2010**, *3*, 824-830.

65. Wang, C.; Li, D.; Too, C. O.; Wallace, G. G. Electrochemical Properties of Graphene Paper Electrodes Used in Lithium Batteries. *Chem. Mater.* **2009,** *21*, 2604.

66. David, L.; Singh, G. Reduced Graphene Oxide Paper Electrode: Opposing Effect of Thermal Annealing on Li and Na Cyclability. *J. Phys. Chem. C* **2014,** *118*, 28401-28408.

67. Yu, P.; Popov, B. N.; Ritter, J. A.; White, R. E. Determination of the Lithium Ion Diffusion Coefficient in Graphite. *J. Electrochem. Soc.* **1999**, *146*, 8-14.

68. Persson, K.; Sethuraman, V. A.; Hardwick, L. J.; Hinuma, Y.; Meng, Y. S.; Ven, A.; Srinivasan, V.; Kostecki, R.; Ceder, G. Lithium Diffusion in Graphitic Carbon. *J. Phys. Chem. Lett.* **2010**, *1*, 1176– 1180.

69. Weppner, W.; Huggins, R. A., Determination of the Kinetic Parameters of Mixed-Conducting Electrodes and Application to the System Li_3Sb. *J. Electrochem. Soc.* **1977,** *124*, 1569-1578.

70. Wen, C. J.; Boukamp, B. A.; Huggins, R. A.; Weppner, W., Thermodynamic and mass transport properties of " LiAl ". *J. Electrochem. Soc.* **1979,** *126*, 2258-2266.

Chapter 8 - CONCLUSION

This dissertation included a demonstration of exfoliation of graphene and MoS_2 by surface functionalization techniques and form large-format freestanding paper composites with PDCs. Detailed characterization was included as well as a description of their testing as anode material in Li-ion and Na-ion batteries. Chapter 1 presented a brief introduction of the motivation behind the study of advanced nanomaterials as alternative or suitable anode materials for Li-ion and Na-ion batteries. The chapter also contextualized results in Chapters 2-7 regarding the overall landscape of battery anodes.

Chapter 2 introduced concepts related to Li-ion and Na-ion batteries, including a brief review of various as anode and cathode materials that have been tested in the literature. The chapter also described various techniques involved in synthesis of graphene and MoS_2 as well as a literature review in battery anode application.

Chapter 3 demonstrated the mechanism of Li and Na storage in graphene sheets exfoliated by graphite oxidation followed by thermal reduction. An opposing effect of thermal annealing and reduction atmosphere was observed on electrochemical Na and Li cycling of reduced graphene oxide paper electrodes. Li charge capacity increased with an increased thermal reduction temperature of GO, reaching a maximum stable value of ~325 $mAh.g^{-1}$ at 900 °C. Negligible Na charge capacity was noted for specimens annealed in NH_3 at 900 °C in Ar. These observations were a direct result of increasing order; decreased interlayer spacing caused complete shutdown of Na's cyclability in the electrode. Results proved that thermal annealing is vital for tailoring of electrochemical metal-ion storage and mechanical properties of chemically

modified graphenes. The potential of rGO in nanostructured electrodes for Li-ion and other large metal-ion battery electrodes was also highlighted.

Exfoliation of MoS_2 by cholorosulfonic acid and subsequent study of its composite with rGO as an Na-ion battery were demonstrated in Chapter 4. The freestanding paper exhibited high static uniaxial fracture strength (~2 MPa) and high failure strain (approximately 1.8%). The composite paper was then directly utilized as a counter electrode in an Na^+ battery half-cell; its performance was evaluated as a potential anode for use in an Na^+ battery full-cell. These tests revealed high first-cycle electrochemical capacity of 338 $mAhg^{-1}$ with respect to total weight of the electrode with excellent cycleability of Na^+ at room temperature. This study provided the first experimental evidence of reversible electrochemical storage of Na in layered self-standing MoS_2 composite electrode at room temperatures. These results are expected to open new avenues for use of large-area freestanding binder-free flexible electrodes for Na-ion battery applications.

Chapter 5 demonstrated the first reported synthesis of an rGO freestanding paper loaded with SiOC amorphous particles as a stable and durable battery anode. The porous 3-D rGO matrix served as an effective current collector and electron conductor with a stable chemical and mechanical structure, while embedded amorphous SiOC particles actively cycled Li-ions with high efficiency. As a result of this unique morphology, the rGO/SiOC composite electrode exhibited stable charge capacity (anode) of approximately 543 $mAh.g^{-1}$ at current densities up to 2400 $mA.g^{-1}$ with ~100% efficiency. At current density of 1600 $mA.g^{-1}$ with symmetric cycling, the anode exhibited stable charge capacity of approximately 200 $mAh.g^{-1}$ after 1000 cycles with approximately 100% efficiency. Postcycle images of the disassembled cell revealed a completely integral electrode, thereby explaining the stable electrochemical performance. Elimination of inactive ingredients such as metal current collector, non-conducting polymeric binder, and

conducting agent reduced the total electrode weight and provided the means to produce highly efficient lightweight batteries.

In Chapter 6, acid-treated MoS_2 was functionalized with liquid polysilazane to prepare polysilazane/MoS_2 composite, which upon pyrolysis in an inert environment, resulted in formation of SiCN-MoS_2 nanosheets. Microscopy and spectroscopy results revealed uniform distribution of SiCN-MoS_2 stacked sheets in the composite. Average sheet size was approximately 3 μm to 5 μm. XPS analysis revealed formation of Mo-C and Mo-O bonds, indicating chemical bonding of the SiCN's carbon phase with molybdenum atoms. Electrochemical performance of the composite was studied as a working electrode in an LIB half-cell, revealing an increasingly stable cycling and higher capacity retention compared to 'neat' MoS_2 after 20 cycles. The contribution of conversion reaction (Phase II) and electrolyte decomposition (Phase III) to overall capacity decreased for SiCN-MoS_2 electrodes. This decrease is one of the reasons for decreased first-cycle loss and increased capacity retention for SiCN-MoS_2 composite. Additionally, the electrically conductive nature of SiCN ceramics may have resulted in enhanced Li-ion diffusion. Post-cycling SEM characterization of the disassembled cells also provided additional evidence for the steep capacity drop observed for case of MoS_2. The cycled MoS_2 electrode surface showed mud-cracks and delamination, whereas the SiCN-MoS_2 and SiCN-MoS_2/paper electrodes showed formation of a uniform SEI layer.

Chapter 7 provided an unprecedented demonstration of the synthesis of a chemically integrated SiCN/BN layered composite. Electrical conductivity was observed to be similar to conductivity of doped-silicon, which is several orders of magnitude higher than 'neat' SiCN prepared under similar conditions. Unlike its individual constituents, the SiCN/BN composite also offered high electrochemical activity and stability toward Li-ions, with charge capacity

reaching ~517 mAh g^{-1} at 100 mA g^{-1} and ~283 mAh g^{-1} at 2400 mA g^{-1} with respect to total electrode weight. This behavior was attributed to the increased amount of $–sp^2$ carbon in the SiCN phase (observed only in the presence of BN) that may have exceeded the percolation limit and provided necessary sites for reversible Li adsorption. Facile synthesis and improved thermal, electrical, and electrochemical performances of SiCN/BN composite are expected to open new applications for PDCs and 2-D nanomaterial hybrids.

In conclusion, although several new findings and substantial conclusions were observed, these results form only the preliminary reports of tests to be conducted in order to fully understand the mechanism behind electrochemical reactions that occur in Li-ion and Na-ion batteries. Further study should test Na insertion behavior in acid exfoliated van der Waals sheets such as WS_2, $MoSe_2$, WSe_2, $MoTe_2$, and WSe_2. Literature of selenide and telluride with insertion mechanisms for Li-ion batteries was described, but further study of their electrochemistry in an Na-ion system could increase understanding of Na-ion chemistry in layered materials. Other method should involve interfacing PDC with other van de Waals sheets, potentially leading to enhanced power density of the anode and prevention of capacity fading due to electrode dissolution over long-term cycling.